



TECHNISCHE
UNIVERSITÄT
WIEN

DISSERTATION

Full-Sphere Antenna Measurements via Pattern Stitching

ausgeführt zum Zwecke der Erlangung des akademischen Grades
eines Doktors der technischen Wissenschaften

unter der Leitung von
Assoc. Prof. Dipl.-Ing. Dr. techn. Holger ARTHABER
Institute of Electrodynamics, Microwave and Circuit Engineering

eingereicht an der Technischen Universität Wien
Fakultät für Elektrotechnik und Informationstechnik

von

Dipl.-Ing. Jure SOKLIČ, dipl. inž. el. (UN)
Matr.Nr. 01432109

Wien, 11. August 2024

Abstract

In the field of antenna measurements, obtaining reliable full-sphere radiation patterns of an antenna under test (AUT) from a single measurement is often impossible, especially in the case of omnidirectional antennas. Since the feeding cable and the support structure interact with the AUT, their presence inevitably distorts the measured fields. In many cases, they also limit the area of the sphere that can be measured.

This work proposes a novel method for full-sphere characterization of antennas called pattern stitching. It is implemented for the case of two truncated patterns, measured in two different AUT orientations, which together cover the entire measurement sphere. Since measurements in different orientations require physically rotating the AUT, the antenna's orientation with regard to the coordinate system of the test range changes as well. To be able to stitch such patterns together, they must be aligned to the same coordinate system, which requires coordinate system translation and rotation.

Translation and rotation operations can be done on spherical wave coefficients (SWCs), which are typically obtained from a full-sphere field pattern via spherical wave expansion. If only a truncated pattern is available, truncated SWCs are computed instead, introducing a truncation error in the reconstructed pattern. Three approaches for reducing the truncation error were investigated in this work, the iterative algorithm, the least squares (LS) matrix method, and the fast Fourier transform (FFT)/Matrix method, where high sensitivity of both matrix methods to noise was observed. By truncating small singular values (SVs), this sensitivity could be contained.

A comparison between the methods has identified the FFT/Matrix method as the fastest and most accurate method to compute truncated SWCs. Using this method, truncated SWCs of several test patterns were tested over a range of translations and rotations, confirming that they can be translated and rotated without introducing large errors and, hence, used for pattern stitching. Keeping one truncated pattern fixed, the alignment procedure of the stitching method manipulates truncated SWCs of the other truncated pattern via translation and rotation operations to minimize the weighted scaled mean square error (wSMSE) in the overlapping range between them. After alignment, the patterns are stitched together using the hemisphere split approach. This involves taking the upper hemisphere of the fixed measurement and combining it with the lower hemisphere of the now aligned measurement, which was found to perform better than blending patterns in the overlapping region.

The stitching method has been validated using synthetic patterns, electromagnetic (EM) simulations, and measurement data. Results of the first two types of test patterns have illustrated the theoretical limits of the pattern stitching method, with scaled mean square error (SMSE) values reaching -50 dB for the former and -40 dB for the latter. An increase in SMSE was observed during tests with measured patterns, where errors between -25 dB and -40 dB were obtained. Using EM simulations, the assumption that the error increase stems from the interaction of the AUT with the feeding cable and the support structure could be confirmed.

Lastly, by comparing simulated full-sphere patterns with those of an antenna model in free space, it was demonstrated that the stitching method has the potential to outperform full-sphere measurements for omnidirectional antennas. This is possible because the method discards parts of the measurement surface most affected by the cable and the support structure from the final stitched patterns.

Kurzfassung

In der Antennenmesstechnik ist es oft unmöglich, die Strahlungscharakteristik einer Testantenne (engl. antenna under test (AUT)) in allen Raumrichtungen, sogenannte “Full-Sphere” Messungen, mit einer einzigen Messung zuverlässig zu erhalten. Insbesondere gilt dies für omnidirektionale Antennen. Da das Antennenkabel und die Montagehalterung mit der AUT interagieren, verzerren sie unvermeidlich die gemessenen Felder. In vielen Fällen begrenzen sie auch den Bereich der messbaren Raumrichtungen.

Diese Arbeit schlägt eine neuartige Methode zur Full-Sphere Charakterisierung von Antennen vor, die als “Pattern Stitching” bezeichnet wird. Die Methode wird dabei für den Fall zweier raumwinkelbeschränkter (“truncated”) Strahlungscharakteristiken implementiert, die in zwei verschiedenen AUT-Ausrichtungen gemessen werden und gemeinsam alle Raumwinkel abdecken. Da Messungen in verschiedenen Ausrichtungen eine physische Drehung der AUT voraussetzen, ändert sich auch die Orientierung der Antenne in Bezug auf das Koordinatensystem der Messung. Um derartige Antennencharakteristiken zusammenzufügen, müssen sie an dasselbe Koordinatensystem ausgerichtet werden, was eine Translation und Rotation erfordert.

Translationen und Rotationen können an sphärischen Wellenkoeffizienten (engl. spherical wave coefficients (SWCs)) durchgeführt werden, die typischerweise aus einer Full-Sphere Strahlungscharakteristik mittels sphärischer Modenzerlegung gewonnen werden. Falls die Strahlungscharakteristik nur raumwinkelbeschränkt bekannt ist, werden stattdessen truncated SWCs berechnet, was zu einem Abschneidefehler in der rekonstruierten Antennencharakteristik führt. In dieser Arbeit wurden drei Ansätze zur Reduktion des Abschneidefehlers untersucht: ein iterativer Algorithmus, die Matrixmethode der kleinsten Quadrate (engl. least squares (LS) matrix method) und die FFT/Matrix-Methode, wobei eine hohe Empfindlichkeit beider Matrixmethoden gegenüber Rauschen beobachtet wurde. Durch das Abschneiden kleiner Singulärwerte konnte ihre Empfindlichkeit gegenüber Rauschen reduziert werden.

Ein Vergleich der Methoden hat die FFT/Matrix-Methode als die schnellstes und genauestes Verfahren zur Berechnung von truncated SWCs identifiziert. Mit dieser Methode wurden truncated SWCs mehrerer Strahlungscharakteristiken über einen Bereich verschiedener Translationen und Rotationen getestet, was bestätigte, dass sie ohne große Fehler verschoben und rotiert werden können und daher für das Pattern Stitching verwendet werden können. Indem eine der raumwinkelbeschränkten Strahlungscharakteristiken fixiert wird, manipuliert das Ausrichtungsverfahren der Stitching-Methode die truncated SWCs der anderen Charakteristik mittels Verschiebungs- und Rotationsoperationen, um den gewichteten skalierten mittleren quadratischen Fehler (engl. weighted scaled mean square error (wSMSE)) im Überlappungsbereich zu minimieren. Nach der Ausrichtung werden die Strahlungscharakteristiken mittels der Hemisphären-Split-Methode zusammengefügt, d.h. durch Übernahme der oberen Hemisphäre der fixierten Charakteristik und der unteren Hemisphäre der nun ausgerichteten Messung. Dieser Ansatz erwies sich besser als Überblenden beider Charakteristiken im Überlappungsbereich.

Die Pattern Stitching Methode wurde anhand von synthetischen Strahlungscharakteristiken, elektromagnetischen (engl. electromagnetic (EM)) Simulationen und Antennenmessungen validiert. Die Ergebnisse der ersten beiden Arten von Strahlungscharakteristiken haben die theoretischen Grenzen der Pattern-Stitching-Methode aufgezeigt, wobei die skalierten mittleren quadratischen Fehler (engl. scaled mean square error (SMSE) values) für

die analytischen gewonnen Strahlungsdiagramme -50 dB und für die EM-Simulationen -40 dB erreichten. Beim Stichting der gemessenen Antennencharakteristiken wurde ein Anstieg des SMSE beobachtet, wobei Fehler zwischen -25 dB und -40 dB erzielt wurden. Mithilfe von EM-Simulationen konnte die Annahme bestätigt werden, dass der Fehleranstieg auf die Interaktion der AUT mit dem Antennenkabel und der Montagehalterung zurückzuführen ist.

Schließlich wurde durch den Vergleich von simulierten Full-Sphere Charakteristiken mit jenen eines Antennenmodells im freien Raum gezeigt, dass die Stitching-Methode das Potenzial hat, Full-Sphere Messungen zu übertreffen. Dies ist möglich, weil die Methode Teile der Messfläche, die am stärksten durch das Antennenkabel und die Montagehalterung beeinflusst werden, aus den endgültigen zusammengesetzten Mustern entfernt.

*at last it is done
thanks to all for their support
antennas are fun*

Table of Contents

1	Introduction	1
1.1	Antenna Measurements	1
1.2	Problem Statement	4
2	Spherical Near-Field Measurements	7
2.1	Spherical Wave Expansion	7
2.2	Rotation and Translation Operators on Spherical Waves	12
2.2.1	Coordinate System Rotation	12
2.2.2	Coordinate System Translation	14
2.3	Scattering Matrix of an Antenna	16
2.4	Transmission Formula	18
2.5	Computation of Spherical Wave Coefficients	20
2.5.1	Analytical Solution	21
2.5.2	Discrete Solution	23
2.6	Transformation Algorithm	26
3	Truncated Pattern Stitching	28
3.1	Pattern Stitching Concept	30
3.2	Spherical Wave Coefficients of Truncated Patterns	30
3.2.1	Iterative Algorithm	32
3.2.2	LS Method	32
3.2.3	FFT/Matrix Method	33
3.2.4	Singular Value Truncation for Computing Pseudoinverses	34
3.2.5	Comparison	41
3.3	Measurement Alignment	50
3.3.1	Rotation and Translation of Truncated SWCs	50
3.3.2	Alignment Algorithm	56
3.4	Aligned Pattern Stitching	58
4	Validation of the Stitching Method	60
4.1	Validation with Synthetic Data	60
4.1.1	Convergence Issues	61
4.1.2	Two-Step Alignment Procedure	62
4.1.3	Frequency Dependency	63
4.2	Validation with EM Simulation Data	66

4.3	Validation with Measurement Data	70
4.3.1	Connectorized AUTs	70
4.3.2	Connectorless Devices	75
5	Practical Limitations of Accuracy	80
5.1	Sources of Error in Spherical Near-Field Measurements	81
5.2	Influence of a Coaxial Cable	83
5.2.1	EM Simulations	83
5.2.2	Measurements	86
5.3	Influence of the Support Structure	88
5.3.1	Support Structures	88
5.3.2	SGH Measurements	89
5.3.3	EM Simulations	91
5.4	Summary	92
6	Conclusion and Outlook	94
	References	97
A	SN2FFT Documentation	102
A.1	Example of Usage	103
A.2	List of Supporting Functions	105
B	Pattern Stitching Method Documentation	114
B.1	Example of Usage	114
B.2	List of Supporting Functions	117
C	Extension of the Stitching Method to Connectorless Devices	130
C.1	Measurement Setup	130
C.2	Magnitude Calibration	132
C.3	Alignment Procedure Adaptation	133

List of Figures

1.1	Field zones of an antenna	2
1.2	Spherical near-field range at TU Wien	5
2.1	Spherical coordinate system (r, θ, ϕ)	8
2.2	Antenna as a $(J + 1)$ -port network	17
2.3	Antenna pair and their coordinate systems	19
3.1	Schematic of a swing arm-over-azimuth range	29
3.2	Pattern stitching concept	31
3.3	Comparison of SVs for different sampling cases	35
3.4	Relation between the condition number κ and the oversampling factor a	36
3.5	Influence of noise on the LS solution	37
3.6	Influence of SV truncation on the LS solution	39
3.7	Influence of SV truncation on radiation patterns	40
3.8	PIFA model	42
3.9	Bowtie antenna model	43
3.10	Measured UWB CMP antenna	43
3.11	Algorithm comparison: computation time (noise-free, random SWCs)	44
3.12	Algorithm comparison: NF SMSE (noise-free, random SWCs)	44
3.13	Algorithm comparison: FF SMSE up to θ_{trunc} (noise-free, random SWCs)	45
3.14	Algorithm comparison: FF SMSE up to θ_{valid} (noise-free, random SWCs)	46
3.15	Algorithm comparison: NF SMSE (100 dB SNR, random SWCs)	46
3.16	Algorithm comparison: FF SMSE up to θ_{trunc} (100 dB SNR, random SWCs)	47
3.17	Algorithm comparison: FF SMSE up to θ_{valid} (100 dB SNR, random SWCs)	47
3.18	Algorithm comparison: computation time over frequency (UWB CMP)	49
3.19	Algorithm comparison: NF SMSE over frequency (UWB CMP)	49
3.20	SMSE sweep over translations in x	52
3.21	SMSE sweep over translations in y	53
3.22	SMSE sweep over translations in z	53
3.23	SMSE sweep over translations in x : frequency comparison	54
3.24	SMSE sweep over translations in y : frequency comparison	55
3.25	SMSE sweep over translations in z : frequency comparison	55
3.26	SMSE over rotations in θ	56
3.27	Stitching approach comparison	59
4.1	SMSE for $40^\circ \leq \theta \leq 180^\circ$ over translation in wavelengths	64

4.2	SMSE for $90^\circ \leq \theta \leq 180^\circ$ over translation in wavelengths	65
4.3	Stitching method computation time	66
4.4	Planar log-spiral antenna model	66
4.5	Vivaldi antenna model	67
4.6	Planar log-spiral antenna field pattern at 16 GHz	69
4.7	Folded dipole measurement orientations	70
4.8	UWB CMP measurement orientations	71
4.9	UWB CMP: SMSE over frequency	73
4.10	DRHA measurement orientations	74
4.11	Scaled square error distribution: top measurement of the DRHA at 7 GHz	74
4.12	ESLs used for validation of the stitching method	76
4.13	ESL 3 measurement orientations	76
4.14	Hearing aid measurement orientations	77
5.1	Influence of a coaxial cable: horizontal orientation	83
5.2	Influence of a coaxial cable: vertical orientation	84
5.3	Influence of a coaxial cable: null-aligned orientation	85
5.4	Connectorized ESL 4	87
5.5	Support structure comparison	89
5.6	Influence of ROHACELL 31 HF: measurements	90
5.7	Influence of ROHACELL 31 HF: simulation model	91
A.1	SN2FFT annotated call graph	106
B.1	Pattern stitching method annotated call graph	117
B.2	Mixed transform annotated call graph	119
B.3	Pattern alignment annotated call graph	121
B.4	Alignment procedure annotated call graph	123
C.1	Placement of the reference antenna, the support structure, the DUT, and the probe antenna when measuring connectorless devices.	131
C.2	Measurement setup for connectorless DUTs: antenna range	132

List of Tables

3.1	Comparison of condition numbers for different sampling cases	36
3.2	Algorithm comparison: EM simulation patterns	48
3.3	Algorithm comparison: UWB CMP antenna	50
4.1	Misalignments used for validation	60
4.2	SWC validation: results	62
4.3	SWC validation: results for random misalignments	63
4.4	SWC validation: frequency variation results	64
4.5	SWC validation: translation in wavelengths	65
4.6	Discrepancy between HFSS patterns	68
4.7	HFSS validation results	69
4.8	Measured data validation: estimated measurement SNR for connectorized AUTs	71
4.9	Validation results for measurements of connectorized AUTs	72
4.10	Validation results for a directive AUT	73
4.11	SMSE results in a reduced θ -range up to $\theta = 90^\circ$	75
4.12	ESL dimensions	76
4.13	Measured data validation: estimated measurement SNR for connectorless DUTs	77
4.14	Validation results of connectorless DUTs	78
4.15	Validation results of connectorless DUTs in a reduced θ -range up to $\theta = 90^\circ$	78
5.1	Sources of error in spherical near-field antenna measurements	82
5.2	Influence of a coaxial cable: simulation results	84
5.3	Influence of a coaxial cable: simulation results	85
5.4	Influence of a coaxial cable: advantage of pattern stitching over full-sphere measurements	86
5.5	Comparison: connectorless and connectorized measurement of ESL 4	87
5.6	Support structure comparison: hearing aid	89
5.7	Influence of ROHACELL 31 HF: SGH measurement results	90
5.8	Influence of ROHACELL 31 HF: simulation results	92

Abbreviations

AUT antenna under test

CATR compact antenna test range

CMP conical monopole

CW continuous wave

DFT discrete Fourier transform

DRHA dual-ridge horn antenna

DUT device under test

EIRP equivalent isotropic radiated power

EM electromagnetic

ESL electronic shelf label

FF far field

FFT fast Fourier transform

FT Fourier transform

GNSS global navigation satellite system

IDFT inverse discrete Fourier transform

IoT internet of things

ISM industrial, scientific, and medical

LS least squares

MRE maximum radial extent

NF near field

NMSE normalized mean square error

PC personal computer

PCB printed circuit board

PIFA planar inverted-F antenna

PosC position controller

RF radio frequency

RFID radio-frequency identification

SA spectrum analyzer

SGH standard gain horn

SMSE scaled mean square error

SN2FFT spherical near-to-far-field transformation

SNR signal-to-noise ratio

SV singular value

SVD singular value decomposition

SWC spherical wave coefficient

TRP total radiated power

UWB ultra-wideband

VNA vector network analyzer

wSMSE weighted scaled mean square error

Symbols and Functions

r	radius
D	largest dimension of an antenna
λ	wavelength
j	imaginary unit
ω	angular frequency
\mathbf{H}	magnetic field
\mathbf{E}	electric field
\mathbf{J}	electric current density
\mathbf{M}	magnetic current density
ε	electric permittivity
μ	magnetic permeability (also used as an index!)
k	wavenumber
c	index of radial function (standing wave, inward/outward traveling wave)
$z_n^{(c)}(kr)$	radial function
$P_n^m(\cos \theta)$	associated Legendre function
e	Euler's number
$\bar{P}_n^{ m }(\cos \theta)$	normalized associated Legendre function

$d\theta$	differential of θ
(s, m, n)	spherical harmonic wave function indices
$F_{smn}^{(c)}(r, \theta, \phi)$	power-normalized spherical harmonic wave function
$Q_{smn}^{(c)}$	spherical wave coefficient
Z_W	wave impedance of the medium
$\sum_s, \sum_{s=1}^2$	summation over s , summation with limits
r_0	maximum radial extent of the AUT
$\lfloor kr_0 \rfloor$	floor function, returns the largest integer smaller or equal to kr_0
N	maximum polar order of n
$(\chi_0, \theta_0, \phi_0)$	Euler angles
(σ, μ, ν)	alternative spherical harmonic wave function indices
$d_{\mu m}^n(\theta)$	rotation coefficient
$\Delta_{m'm}^n$	delta factor
$\binom{2n}{n-m}$	binomial coefficient
A	translation distance
$C_{\sigma\mu\nu}^{sn(c)}(kA)$	translation coefficient
$(n - m)!$	factorial of $(n - m)$
$\delta_{\sigma\sigma}$	Kronecker delta
$a(\mu, n, -\mu, \nu, p)$	linearization coefficient
i, j	single index notation of spherical wave harmonic functions
v, a_j	incoming wave coefficients, $a_j = Q_j^{(3)} = Q_{smn}^{(3)}$
w, b_j	outgoing wave coefficients, $b_j = Q_j^{(4)} = Q_{smn}^{(4)}$
Γ	reflection coefficient

\mathbf{T}	vector containing transmission coefficients $T_i = T_{smn}$
\mathbf{R}	vector containing receiving coefficients $R_j = R_{smn}$
\mathbf{S}	matrix containing scattering coefficients S_{ij}
$P_{s\mu n}(kA)$	probe response constant
DFT{}	discrete Fourier transform
IDFT{}	inverse discrete Fourier transform
$\Delta\chi, \Delta\phi, \Delta\theta$	step size in χ, ϕ, θ
K_χ, K_ϕ, K_θ	number of samples in χ, ϕ, θ
\odot	elementwise vector product
θ_{trunc}	angle θ at which the field is truncated
M	maximum azimuthal order of $ m $
$\max_{\chi, \theta, \phi} f$	maximum value of a function f over χ, θ , and ϕ
$\arg \min_{\mathbf{q}} f$	vector \mathbf{q} at which the function f reaches its minimum
$\ \mathbf{w} - \underline{\Psi}\mathbf{q}\ _2$	Euclidean norm of $\mathbf{w} - \underline{\Psi}\mathbf{q}$
$\underline{\mathbf{V}}^*, \mathbf{v}^*$	conjugate transpose of matrix $\underline{\mathbf{V}}$ and vector \mathbf{v}
$\kappa(\underline{\Psi})$	condition number of matrix $\underline{\Psi}$
$\ \underline{\Psi}\ _\infty$	maximum norm of $\underline{\Psi}$

1 Introduction

The history of antennas dates back to the late 1800s. In 1865, Maxwell’s work titled “A Dynamical Theory of the Electromagnetic Field” was published [1], in which he predicted the existence of propagating electromagnetic waves. Not long after that, Hertz succeeded in proving the existence of such propagating electromagnetic waves [2] and built the first dipole antennas in the process. While building the first antennas has been attributed to Hertz, it was Marconi that recognized the potential of transmitting electromagnetic signals wirelessly over long distances and pioneered the field of wireless telegraphy, for which he was awarded the Nobel prize in 1909 [3]. These discoveries have revolutionized the field of long-distance communications and wireless telegraphy was soon followed by successful broadcasting of audio signals and, later on, also video signals. World War II played a major role in the advancements of antenna technology, when new elements, such as waveguides, horn antennas, and reflectors, were introduced to satisfy the needs of military applications [4]. Throughout the second half of the 20th century, new wireless technologies have continued to emerge, among them, e.g., global navigation satellite systems (GNSSs) [5], radio-frequency identification (RFID) [6], and ultra-wideband (UWB) systems [7]. Over the last couple of decades, a general tendency toward transition from wired to wireless systems can be observed (internet of things (IoT) [8], on-body communication systems [9], etc.), which, along with numerous new emerging wireless applications, requires development of new antennas with various application-specific properties. Validation of antenna performance in terms of its parameters, such as radiation pattern, gain, and polarization [10], is thus inevitable in order to assure correct operation of these systems. To do so, accurate antenna measurements are of utter importance.

1.1 Antenna Measurements

The primary goal of any antenna measurement is the characterization of an antenna under test (AUT) independent of its operational environment. Since the field distribution of an antenna inherently depends on the distance from the antenna, the space surrounding the antenna can be divided into three regions with distinct properties [4]:

- **Reactive near-field region:** The region immediately surrounding the antenna, where the electric and magnetic field components are nearly 90° out of phase, which

means that reactive fields are predominant in this region. The angular field distribution is nearly uniform and depends strongly on the distance from the antenna. Reactive fields cannot propagate in free space and rapidly decay with increasing distance.

- **Radiative near-field (Fresnel) region:** The region where radiating fields are predominant, meaning that the electric field and the magnetic field are already close to being in phase. The angular field distribution still depends on the distance from the antenna.
- **Far-field (Fraunhofer) region:** The region where the angular field distribution is considered independent of the distance from the antenna and the field components are in phase and orthogonal.

Antennas are usually characterized in terms of their behavior in the far field (FF) where angular field distribution becomes distance-independent. Depending on the size of the antenna, the boundaries between the three regions can be determined by one of the two pairs of expressions shown in Figure 1.1. For electrically small antennas, the boundaries are determined by the bottom pair of expressions. Here, the radiative near-field region, the width of which decreases with decreasing antenna dimension D , begins to vanish [11].

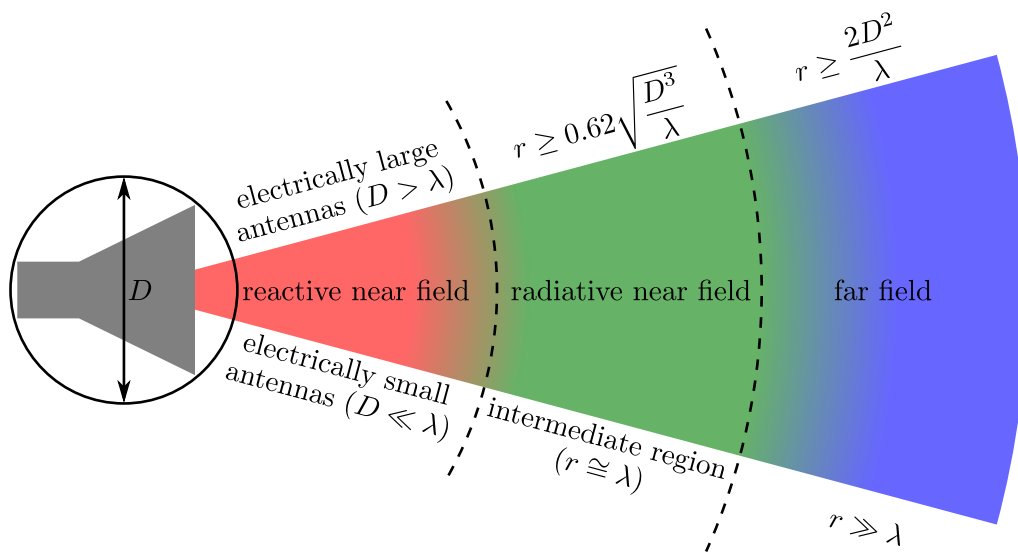


Figure 1.1: Field zones of an antenna

When electrically large antennas are considered, the upper pair of expressions is typically used instead. Due to their size, such antennas cannot be assumed a point source without introducing substantial errors into analytical expressions describing their radiating fields. The changing distance between different positions on the antenna and the observation point can be approximated in order to facilitate analytical descriptions of its radiating fields. The two inequalities represent minimum distances between the observation point and the antenna at which the maximum phase error when using two such approximations is $\pi/8$. These have been derived on the example of a small z -oriented electrical dipole and, for detailed information, the interested reader is referred to [4, Chapter 4]. It should be

noted that the boundaries between these regions are not hard boundaries and, depending on the acceptable error level, many different expressions are used in practice to define them [12].

The measurements are typically done in a well-known environment, called an antenna (test) range. These antenna ranges can be divided into **outdoor ranges** and **indoor ranges**. While outdoor ranges have historically played an important role in antenna testing, they are less common nowadays due to their sensitivity to external influences, such as environmental variations and radio frequency (RF) interference, and strict radiation regulations. For that reason, electromagnetically shielded indoor ranges are the prevailing type of antenna ranges used today. To measure the far-field radiation pattern of an antenna, which is distance-independent, uniform electromagnetic (EM) plane waves should ideally be used. Such plane waves can only be approximated in practice and, based on the approach used, antenna ranges can further be divided into three categories [11]:

- **Free-space ranges:** Designed in a way so that all effects of the surroundings are suppressed to acceptable levels. These include elevated ranges, compact ranges, and far-field anechoic chambers.
- **Ground reflection ranges:** Exploit reflections to produce an approximated plane wave or some predictable combination of waves.
- **Near-field ranges:** Use mathematical transforms to simulate plane waves from measurement samples obtained in the near field (NF).

With the exemption of near-field ranges, measurements are typically done in the far field. Observing the field zone criteria in Figure 1.1, it becomes obvious that near-field ranges allow for field measurements at the shortest distances away from the AUT. This advantage comes at a cost of increased computational complexity. With the high processing power in modern computers, the measurement time supersedes the computation time by far, thus rendering the increased complexity of near-field ranges negligible. In practice, the choice of an antenna range involves trade-offs and the decision requires consideration of various characteristics of the AUT, such as its electrical size, directivity, frequency range, etc. [13]. When a general antenna range capable of covering large frequency spans and measuring antennas of various sizes is sought, near-field ranges have a clear advantage over far-field ranges since they can be substantially more compact and can also be used as a far-field range whenever measuring small antennas which fulfill the far-field condition at the range's measurement distance. In a near-field measurement setup, a separation distance of only a few wavelengths is required between the probe antenna and the AUT in order to avoid coupling effects between them. The exact distance depends on the antennas used, but, as a rule of thumb, a distance of 3λ is commonly used in various types of near-field ranges [14,15]. It should be noted that, aside from near-field ranges, alternative approaches to reducing the measurement distance also exist, for example, the compact antenna test range (CATR), which uses reflectors to approximate plane waves at distances shorter than the FF distance [14]. These tend to be more complex to construct and, thus, more expensive [13]. Moreover, near-field ranges offer the possibility of computing field patterns anywhere in space, which will be exploited throughout this work.

Having shown the advantage of near-field ranges, focus will now be given to the types of near-field ranges and their comparison. In all such ranges, the behavior of the antenna

is characterized on some surface near the antenna and mathematically transformed to far field. The vector wave (Helmholtz) equation, shown in (2.3), serves as the basis of this transformation and it can be solved in various coordinate systems. Typically, one of the following coordinate systems is used, for which the variables in the wave equation are separable and which offer mechanically convenient scanning surfaces with simple orthogonal functions: Cartesian, cylindrical, or spherical coordinate system [16]. Depending on the coordinate system in which the wave equation is solved, the solutions of the equation represent either plane waves, cylindrical waves, or spherical waves. Any field pattern can then be expressed by a combination of solutions in the chosen coordinate system. In accordance with the type of sought solutions, the surface at which the fields are sampled is chosen to be either planar, cylindrical, or spherical to facilitate the computation. Hence, we talk about planar [17], cylindrical [18], and spherical near-field ranges [19]. Some work has also been done on ranges for arbitrary measurement surfaces [15, 20], but such ranges have received little attention due to the challenges in their construction and the computational complexity of transforming the measured data to far field. Each near-field range type comes with its advantages and drawbacks. Among them, the planar near-field ranges have the lowest complexity and cost but can only be used for highly directive AUTs. As a rule of thumb, only AUTs with a directivity greater than 15 dBi should be measured to ensure that all significant radiated energy can be contained within the measurement plane. When antennas with a wide main beam in one plane (but narrow in the other) or a strong back lobe need to be measured, a cylindrical near-field range can be used instead. The most complex among the three standard near-field ranges, the spherical near-field range, can be used even when low-gain omnidirectional AUTs are measured [13]. Here, the measurement samples are obtained on a sphere and all the radiated energy is captured in the measurement. As such, all types of antennas can be measured, regardless of their directivity and radiation pattern. Spherical near-field ranges combine three advantages that no other antenna measurement technique jointly possesses: First, a measurement in an anechoic chamber with electromagnetic (EM) shielding suppresses external interferers and reduces scattered fields. Second, the sphere encloses the AUT and, thus, all radiated energy can be captured during the measurement. And third, the mathematical processing of the near-field data to obtain a far-field radiation pattern, called spherical wave expansion, can reduce the influence of noise errors and scattered fields by truncating higher-order, non-physical solutions of the wave equation. As such, the method is generally considered the state of the art for accurate antenna measurements [21].

1.2 Problem Statement

With the high versatility and comparatively compact size of spherical near-field ranges, it should be easy to understand why this is the range type used at TU Wien. A multitude of configurations for sampling fields over a sphere exist, where either the probe, the AUT, or both have to be moved in space. Spherical near-field ranges can be subdivided into different range types based on the chosen configuration [19]. At TU Wien, the antenna range is realized as a swing arm-over-azimuth range [22]. It can be seen portrayed in Figure 1.2. By simply observing the photograph, it should be evident that it is impossible to cover the whole measurement sphere in a single measurement in this configuration. Since the AUT is mounted on a rotary stage covering rotations in ϕ -axis, the range of θ -angles that can be reached with the swing arm is less than full 180° and we have to deal

with what is termed pattern truncation. The swing arm-over-azimuth range can thus only measure less-than-full-sphere field patterns, commonly called truncated patterns.

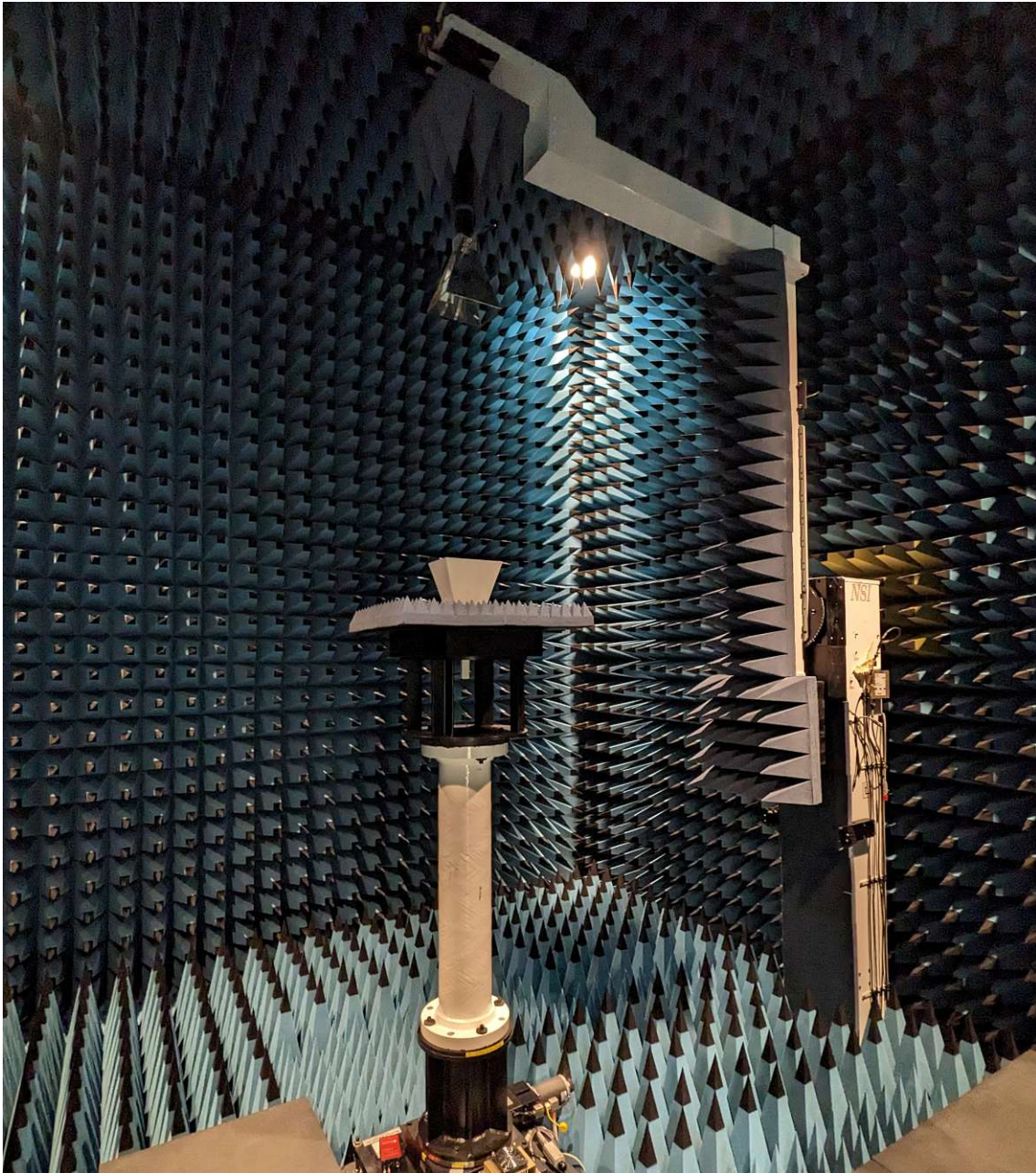


Figure 1.2: Spherical near-field range at TU Wien

Within the Microwave Engineering Group at TU Wien, seminars, theses, and research projects are carried out, requiring measurements of all sorts of antennas with very diverse radiation patterns, both with high and with low directivity. As long as an AUT is oriented in such a way that the amount of energy in the truncated region, i.e., the part of the sphere which cannot be measured, is negligible, truncated patterns obtained at TU Wien's antenna range can be transformed to far-field patterns accurately. While this can be done with high-directivity AUTs, capturing the majority of radiated energy when

measuring low-directivity, omnidirectional antennas becomes impossible. This results in transformation errors when computing the far-field radiation patterns, overestimation of directivity, and underestimation of the total radiated power (TRP).

One method that has been suggested in order to deal with radiation pattern truncation is the reconstruction of full-sphere patterns from truncated measurement data. In [23], the authors have demonstrated a successful reconstruction of the radiation pattern of a sleeve dipole by using an iterative transformation procedure and spatially filtering the computed spherical wave coefficients (SWCs) based on the knowledge of the antenna's maximum radial extent (MRE). Another approach to reconstruct patterns is based on determining a set of equivalent currents with the same radiation pattern as the truncated measurement and extrapolating them to the truncated area. In [24], this approach has been compared to the one mentioned earlier. From the reported results, it becomes apparent that, while these methods are advantageous in terms of determining the directivity, neither of them can accurately describe the radiated fields of an arbitrary antenna in the truncated region. A least-squares-based approach was also proposed for reconstructing full-sphere patterns from truncated data [25, 26], but just like the previous two approaches, the truncated region of an arbitrary antenna could not be reconstructed accurately.

In order to obtain reliable full-sphere radiation patterns, this work pursues the idea of stitching multiple truncated patterns, measured in different orientations of the AUT. Aside from some work on full-sphere characterization by combining multiple planar measurements [27, 28], no work on stitching multiple truncated patterns obtained from near-field antenna ranges has been found. Therefore, to the best of my knowledge, this work introduces a novel method for full-sphere antenna measurements by means of truncated pattern stitching. The stitching method, its performance in terms of accuracy, and the limits thereof will be presented throughout the following chapters.

2 Spherical Near-Field Measurements

As discussed in Chapter 1, measuring antenna radiation patterns in the near field (NF) can substantially reduce the measurement range's size compared to far-field measurement techniques and becomes inevitable when characterizing antennas with physical dimensions much larger than their wavelength. In practice, however, antennas are most commonly used at larger distances, operating in their far field (FF). Moreover, antenna parameters are always defined using FF patterns, where angular distribution becomes independent of the distance. Thus, a transformation to far field is needed when characterizing an antenna in its near field.

The implementation of the near- to far-field transformation algorithm presented in this chapter closely follows the algorithm presented by Hansen [19]. However, there is one major difference between the two: the sign convention of the imaginary unit $i = \sqrt{-1}$, which is typically represented by j in the electrical engineering community. While Hansen follows the $-i\omega t$ time- and ikr distance dependence, the presented algorithm was implemented assuming $j\omega t$ time- and $-jkr$ distance dependence, which is in accordance with the IEEE Std 145-2013 [10]. The latter is the convention typically used in electrical engineering and modern measurement equipment, such as vector network analyzers (VNAs). The simplest solution to ensure interoperability between systems following opposing conventions is phase negation [29].

The algorithm described by Hansen has been defined both for outward and inward traveling waves, which represent a complex conjugated pair of waves. Therefore, most parts of the algorithm could readily be used by interchanging the definitions of the outward and the inward traveling waves. The adapted algorithm will be presented in the following sections, highlighting all the differences between the two conventions.

2.1 Spherical Wave Expansion

Assuming a linear, homogeneous, isotropic medium, an electromagnetic field with $j\omega t$ time dependence satisfies the following two Maxwell's equations, Faraday's law of induction (2.1) and Ampère's circuital law (2.2) [14, 19, 30]:

$$\nabla \times \mathbf{H} = j\omega\varepsilon\mathbf{E} + \mathbf{J} \quad (2.1)$$

$$\nabla \times \mathbf{E} = -j\omega\mu\mathbf{H} \quad (2.2)$$

The electric and magnetic field vectors are represented by \mathbf{E} and \mathbf{H} , respectively, the variable ω stands for the angular frequency, ε and μ represent the permittivity and the permeability of the medium, while \mathbf{J} represents the electric current. **Regardless of the aforementioned sign convention**, in a source-free region where $\mathbf{J} = 0$, both fields satisfy the same vector wave equation,

$$\nabla \times (\nabla \times \mathbf{C}) - k^2 \mathbf{C} = 0, \quad (2.3)$$

where k is the wavenumber, related to the wavelength in the medium by $k = 2\pi/\lambda$.

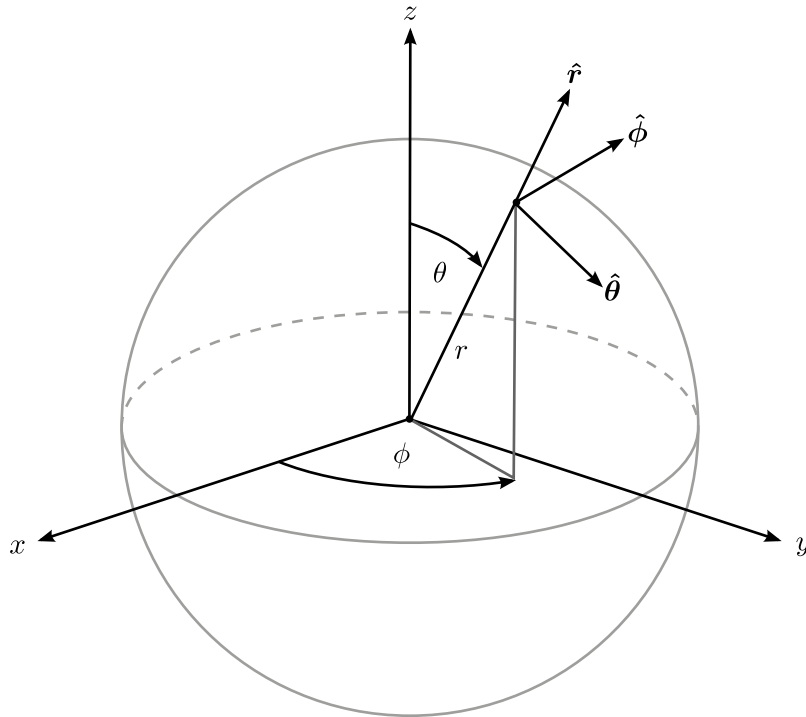


Figure 2.1: Spherical coordinate system (r, θ, ϕ) , as related to the Cartesian coordinate system (x, y, z) , and its unit vectors $\hat{\mathbf{r}}, \hat{\boldsymbol{\theta}}, \hat{\boldsymbol{\phi}}$.

To avoid confusion due to different existing definitions of a spherical coordinate system (r, θ, ϕ) , the definition used throughout this dissertation and its relation to the Cartesian coordinate system (x, y, z) are shown in Figure 2.1. The spherical coordinate variables can take the following range of values: the radial distance $0 \leq r < \infty$, the polar angle $0 \leq \theta \leq 2\pi$, and the azimuthal angle $0 \leq \phi < 2\pi$. In this coordinate system, two independent solutions of the vector wave equation are used to describe an electromagnetic (EM) field:

$$\mathbf{m} = \nabla f \times \mathbf{r} = \frac{1}{k} \nabla \times \mathbf{n} \quad (2.4)$$

$$\mathbf{n} = \frac{1}{k} \nabla \times \mathbf{m} \quad (2.5)$$

By definition, the two vector functions represent solenoidal vector fields ($\nabla \cdot \mathbf{m} = \nabla \cdot \mathbf{n} = 0$) related by curl operations, well suited to represent an electromagnetic field in a source-free homogeneous medium [19]. Function $f = f(r, \theta, \phi)$ is the generating function obtained by solving the scalar wave equation:

$$\nabla^2 f + k^2 f = 0 \quad (2.6)$$

Stratton [31] gives the even and odd generating functions,

$$f_{e,mn}^{(c)}(r, \theta, \phi) = z_n^{(c)}(kr) P_n^m(\cos \theta) \cos m\phi \quad (2.7)$$

and

$$f_{o,mn}^{(c)}(r, \theta, \phi) = z_n^{(c)}(kr) P_n^m(\cos \theta) \sin m\phi, \quad (2.8)$$

where $n = 1, 2, 3, \dots$ and $m = 0, 1, 2, \dots, n$ to generate \mathbf{m} - and \mathbf{n} -functions. The letters e and o in the equation, respectively, signify the even (cos) and odd (sin) trigonometric function in the ϕ -dependence. The θ -dependence of f is described in the associated Legendre function of n^{th} degree and m^{th} order, $P_n^m(\cos \theta)$. **One should note that two different definitions of the associated Legendre functions exist!** Here, the definition by Belousov [32] is used,

$$P_n^m(\cos \theta) = (\sin \theta)^m \frac{d^m P_n(\cos \theta)}{d(\cos \theta)^m}, \quad (2.9)$$

where $P_n(\cos \theta)$ is the Legendre polynomial,

$$P_n(\cos \theta) = \frac{1}{2^n n!} \frac{d^n}{d(\cos \theta)^n} (\cos^2 \theta - 1)^n, \quad (2.10)$$

while an alternative definition including an additional term, $(-1)^m$, called the Condon-Shortley phase [33, 34], has become the most widely used definition nowadays. The radial dependence is confined to the radial function $z_n^{(c)}(kr)$, which, depending on the upper index c , is one of the following functions:

$$z_n^{(1)} = j_n(kr) \quad \text{spherical Bessel function} \quad (2.11)$$

$$z_n^{(2)} = n_n(kr) \quad \text{spherical Neumann function} \quad (2.12)$$

$$z_n^{(3)} = h_n^{(1)}(kr) = j_n(kr) + j_n n_n(kr) \quad \text{spherical Hankel function of the 1st kind} \quad (2.13)$$

$$z_n^{(4)} = h_n^{(2)}(kr) = j_n(kr) - j_n n_n(kr) \quad \text{spherical Hankel function of the 2nd kind} \quad (2.14)$$

The functions with $c = 1$ and $c = 2$ represent standing waves, while $c = 3$ and $c = 4$ correspond to an inward and an outward traveling wave. **For the two traveling waves, the sign convention of the distance dependence determines which Hankel function represents which wave.** Following the $-jkr$ distance dependence (as in [30], in contrast

to [19] and [31]), $c = 4$ will represent the outward traveling wave throughout this dissertation. For the sake of brevity, the derivation of vector wave equation solutions was not included here. The interested reader is referred to Stratton [31] for detailed information.

In his dissertation, Jensen, cited by Hansen in [19], introduced one symbol $\mathbf{f}_{smn}^{(c)}$ to designate both the \mathbf{m} -function ($s = 1$) and the \mathbf{n} -function ($s = 2$). Additionally, he proposed a modified generating function,

$$g_{mn}^{(c)}(r, \theta, \phi) = z_n^{(c)}(kr) P_n^{|m|}(\cos \theta) e^{jm\phi}, \quad (2.15)$$

where the range of n remains the same as in (2.7) and (2.8), while m now takes the values $m = -n, -n + 1, \dots, 0, \dots, n - 1, n$. Using the exponential factor was found to be more convenient for use with mathematical operations required in connection with his proposed near- to far-field transformation algorithm.

Hansen [19], following the notation proposed by Jensen, finally introduced the power-normalized generating function, normalized in such a way that each single spherical wave with amplitude 1 would radiate a power of 0.5 W. This gives the following generating function:

$$F_{mn}^{(c)}(r, \theta, \phi) = \frac{1}{\sqrt{2\pi}} \frac{1}{\sqrt{n(n+1)}} \left(-\frac{m}{|m|}\right)^m z_n^{(c)}(kr) \bar{P}_n^{|m|}(\cos \theta) e^{jm\phi} \quad (2.16)$$

Aside from normalization factors, an additional factor $(-m/|m|)^m$ was added to the function to allow for simplified coordinate rotation operations. This factor is defined to take the value of 1 for $m = 0$. Furthermore, the associated Legendre functions are now replaced with the normalized associated Legendre functions, related by:

$$\bar{P}_n^{|m|}(\cos \theta) = \sqrt{\frac{2n+1}{2} \frac{(n-|m|)!}{(n+|m|)!}} P_n^{|m|}(\cos \theta) \quad (2.17)$$

Using the one-symbol convention and the normalized generating function from (2.16) in (2.4) and (2.5), we obtain the following set of functions, called power-normalized spherical harmonic wave functions:

$$\begin{aligned} \mathbf{F}_{1mn}^{(c)}(r, \theta, \phi) &= \nabla F_{mn}^{(c)}(r, \theta, \phi) \times \mathbf{r} \\ &= \frac{1}{\sqrt{2\pi}} \frac{1}{\sqrt{n(n+1)}} \left(-\frac{m}{|m|}\right)^m \left[z_n^{(c)}(kr) \frac{j m \bar{P}_n^{|m|}(\cos \theta)}{\sin \theta} e^{jm\phi} \hat{\boldsymbol{\theta}} \right. \\ &\quad \left. - z_n^{(c)}(kr) \frac{d \bar{P}_n^{|m|}(\cos \theta)}{d\theta} e^{jm\phi} \hat{\boldsymbol{\phi}} \right] \end{aligned} \quad (2.18)$$

$$\begin{aligned}
 \mathbf{F}_{2mn}^{(c)}(r, \theta, \phi) &= \frac{1}{k} \nabla \times \mathbf{F}_{1mn}^{(c)}(r, \theta, \phi) \\
 &= \frac{1}{\sqrt{2\pi}} \frac{1}{\sqrt{n(n+1)}} \left(-\frac{m}{|m|} \right)^m \left[\frac{n(n+1)}{kr} z_n^{(c)}(kr) \bar{P}_n^{|m|}(\cos \theta) e^{jm\phi} \hat{\mathbf{r}} \right. \\
 &\quad \left. + \frac{1}{kr} \frac{d}{d(kr)} \{kr z_n^{(c)}(kr)\} \frac{d\bar{P}_n^{|m|}(\cos \theta)}{d\theta} e^{jm\phi} \hat{\boldsymbol{\theta}} \right. \\
 &\quad \left. + \frac{1}{kr} \frac{d}{d(kr)} \{kr z_n^{(c)}(kr)\} \frac{j m \bar{P}_n^{|m|}(\cos \theta)}{\sin \theta} e^{jm\phi} \hat{\boldsymbol{\phi}} \right]
 \end{aligned} \tag{2.19}$$

The electric field in a source-free region of space can be written as a weighted sum of functions in (2.18) and (2.19) [19] as

$$\mathbf{E}(r, \theta, \phi) = k \sqrt{Z_W} \sum_{csmn} Q_{smn}^{(c)} \mathbf{F}_{smn}^{(c)}(r, \theta, \phi), \tag{2.20}$$

where Z_W is the wave impedance of the medium, k the wavenumber, and $Q_{smn}^{(c)}$ are the spherical wave coefficients (SWCs), which have the unit of square root of watt (\sqrt{W}). Inserting (2.20) into (2.2), we obtain the relation for the magnetic field:

$$\mathbf{H}(r, \theta, \phi) = \frac{j}{\omega\mu} \nabla \times \mathbf{E}(r, \theta, \phi) = \frac{jk}{\sqrt{Z_W}} \sum_{csmn} Q_{smn}^{(c)} \mathbf{F}_{(3-s)mn}^{(c)}(r, \theta, \phi) \tag{2.21}$$

Having normalized the spherical functions in terms of power, the total power radiated by outward traveling waves can be expressed as a simple summation [19]:

$$P = \frac{1}{2} \sum_{csmn} |Q_{smn}^{(4)}|^2 \tag{2.22}$$

The summation over c , s , m , and n in (2.20) and (2.21) can be understood in the following manner:

$$\sum_{csmn} = \sum_{c=3}^4 \sum_{s=1}^2 \sum_{n=1}^{\infty} \sum_{m=-n}^n \tag{2.23}$$

The sum over c represents summation over both inward ($c = 3$) and outward ($c = 4$) traveling waves and sum over s runs over both vector wave functions ($s = 1$ and $s = 2$). Summation over m is limited by the vanishing nature of the associated Legendre function for $|m| > n$, while n runs from 1 to ∞ . Although n can theoretically extend to infinity, in practice, n is found to be limited. The cause for this limitation will be discussed in the following paragraph.

Spherical wave functions may be thought of as spherical modes, similar to cylindrical modes in a cylindrical waveguide. Thus, spherical wave radiation may be considered as radiation taking place in a spherical waveguide, where counterparts exist for many concepts known from cylindrical waveguides, such as orthogonal modes, cut-off, propagation,

and evanescence [19]. The cross-section of such a spherical waveguide increases with increasing r , allowing a larger number of spherical modes to propagate. From the properties of spherical Hankel functions, the transition between evanescence and propagation of a spherical mode is found to occur at a radial distance $r_t = n/k$. For distances smaller than r_t , the corresponding function decays rapidly, transitions around r_t , and begins to propagate with a comparatively slow decay with a rate of r^{-1} when $r \gg r_t$. Let us now consider a radiating source, i.e., an antenna, placed (not necessarily, but typically) in the center of the spherical coordinate system. The smallest possible spherical surface centered at the origin of the coordinate system and circumscribing antenna's radiating parts is called the maximum radial extent (MRE) of the antenna, denoted by r_0 . Assuming that all outward propagating spherical modes have the same order of magnitude at r_0 , those modes with $n > kr_0$ will still be in the rapidly decaying evanescence region and will become negligible at some distance $r \gg r_0$ where a near- or far-field measurement might take place. Thus, only spherical modes with $n < kr_0$ contribute significantly to the measurement, allowing for a truncation of the polar index at some $n = N$. In practice, the maximum polar index is given by the empirical rule

$$N = \lfloor kr_0 \rfloor + n_1, \quad (2.24)$$

where, typically, $n_1 = 10$. For a more detailed discussion of the topic, supported with graphical examples, the reader is referred to Hansen [19].

2.2 Rotation and Translation Operators on Spherical Waves

Transformations of the coordinate system are of utter importance in near-field spherical measurements, as will be shown later on when talking about transmission between a pair of antennas. Mathematical operators exist, capable of describing a set of spherical waves in one coordinate system as a combination of spherical waves in another coordinate system that is rotated and/or translated. These operators have been studied and documented extensively in existing literature [35–39] and summarized in [19]. An overview of the operators relevant to this work will be presented in the following two subsections.

2.2.1 Coordinate System Rotation

Considering a coordinate system (x, y, z) , any arbitrary orientation (x', y', z') with regard to this fixed coordinate system (where the origin $(0, 0, 0)$ of both coordinate systems lies on the same point in space) can be achieved by a succession of three rotations around its own axes [19]. These rotations by the so-called Euler angles $(\chi_0, \theta_0, \phi_0)$ are done in the following sequence:

- i) A rotation of (x, y, z) by an angle ϕ_0 around the z -axis to (x_1, y_1, z_1)
- ii) A rotation of (x_1, y_1, z_1) by an angle θ_0 around the y_1 -axis to (x_2, y_2, z_2)
- iii) A rotation of (x_2, y_2, z_2) by an angle χ_0 around the z_2 -axis to (x', y', z')

Each of these Cartesian coordinate systems has a unique spherical coordinate system, as defined in Figure 2.1. Spherical waves defined in the unprimed coordinate system may be expressed as a combination of waves in the primed system as

$$\mathbf{F}_{smn}^{(c)}(r, \theta, \phi) = \sum_{\mu=-n}^n e^{jm\phi_0} d_{\mu m}^n(\theta_0) e^{j\mu\chi_0} \mathbf{F}_{s\mu n}^{(c)}(r', \theta', \phi'), \quad (2.25)$$

where rotations in ϕ_0 and χ_0 represent simple phase shifts, while rotation by θ_0 is described with the more complex rotation coefficient $d_{\mu m}^n(\theta_0)$ [19]. To simplify computation, this coefficient can be expanded into a finite Fourier series

$$d_{\mu m}^n(\theta) = j^{m-\mu} \sum_{m'=-n}^n \Delta_{m'\mu}^n \Delta_{m'm}^n e^{jm'\theta} = j^{\mu-m} \sum_{m'=-n}^n \Delta_{m'\mu}^n \Delta_{m'm}^n e^{-jm'\theta}, \quad (2.26)$$

where delta factors $\Delta_{m'\mu}^n$ and $\Delta_{m'm}^n$ represent the rotation coefficients evaluated at $\pi/2$, $d_{m'\mu}^n(\pi/2)$ and $d_{m'm}^n(\pi/2)$ [40]. These delta factors can be computed by using recursion. First, the starting value¹ is computed by

$$\Delta_{nm}^n = \frac{1}{2^n} \sqrt{\binom{2n}{n-m}} = \frac{1}{2^n} \sqrt{\frac{2n \cdot (2n-1) \cdots (n+m+2) \cdot (n+m+1)}{(n-m)!}}. \quad (2.27)$$

Then, the recursion formula is used to obtain values for all $m, m' \geq 0$:

$$\sqrt{(n+m'+1)(n-m')} \Delta_{m'+1,m}^n + \sqrt{(n+m')(n-m'+1)} \Delta_{m'-1,m}^n = -2m \Delta_{m',m}^n \quad (2.28)$$

For computing delta factors of negative modes m or m' , the following identities can be utilized:

$$\Delta_{m'm}^n = (-1)^{n+m} \Delta_{-m',m}^n = (-1)^{n+m'} \Delta_{m',-m}^n = (-1)^{m'+m} \Delta_{-m',-m}^n \quad (2.29)$$

These equations suffice for the computation of any required rotation coefficient. An extensive list of properties, recurrence relations, and identities of delta factors is presented in [19, Appendix A2].

Having established the relationship between spherical harmonic wave functions in two coordinate systems, which are related by $(\phi_0, \theta_0, \chi_0)$ rotations, the last missing information is how SWCs of the rotated coordinate system are related to those of the initial coordinate system. Inserting (2.25) into (2.20), we get the relationship

¹There is an error in the numerator of equation (4.95) in [19], where m is mistakenly subtracted instead of being added. This has been corrected in (2.27) presented here.

$$\begin{aligned}
 \mathbf{E}(r, \theta, \phi) &= k\sqrt{Z_W} \sum_{csmn} Q_{smn}^{(c)} \mathbf{F}_{smn}^{(c)}(r, \theta, \phi) \\
 &= k\sqrt{Z_W} \sum_{csmn} Q_{smn}^{(c)} \sum_{\mu=-n}^n e^{jm\phi_0} d_{\mu m}^n(\theta_0) e^{j\mu\chi_0} \mathbf{F}_{s\mu n}^{(c)}(r', \theta', \phi').
 \end{aligned} \tag{2.30}$$

Considering the fact that indices c , s , and n are independent of the rotation operator, this can be reduced to

$$\begin{aligned}
 \sum_m Q_{smn}^{(c)} \mathbf{F}_{smn}^{(c)}(r, \theta, \phi) &= \sum_m Q_{smn}^{(c)} \sum_{\mu=-n}^n e^{jm\phi_0} d_{\mu m}^n(\theta_0) e^{j\mu\chi_0} \mathbf{F}_{s\mu n}^{(c)}(r', \theta', \phi') \\
 &= \sum_{\mu} Q_{s\mu n}^{(c)} \mathbf{F}_{s\mu n}^{(c)}(r', \theta', \phi'),
 \end{aligned} \tag{2.31}$$

which leads to the final expression for SWCs of the rotated coordinate system:

$$Q_{s\mu n}^{(c)} = e^{j\mu\chi_0} \sum_m Q_{smn}^{(c)} e^{jm\phi_0} d_{\mu m}^n(\theta_0) \tag{2.32}$$

2.2.2 Coordinate System Translation

To be able to describe spherical waves in any arbitrary coordinate system, regardless of its origin, in terms of a combination of waves in another system, the final missing operation is the translation of spherical waves. Translation operators have been developed in [35–38], capable of describing translations in an arbitrary direction. Hansen [19] proposes the use of positive z -axis translation, which allows for a simplified computation with preserved ϕ -dependence of spherical waves. To achieve translation in an arbitrary direction, not aligned with the $+z$ -axis, he suggests a succession of three operations: a rotation, a translation, and an inverse rotation. For the $+z$ -axis translation, the spherical waves in both coordinate systems are, depending on the translation distance A , related by one of the following two expressions:

$$\mathbf{F}_{s\mu n}^{(c)}(r, \theta, \phi) = \begin{cases} \sum_{\sigma=1}^2 \sum_{\substack{\nu=|\mu| \\ \nu \neq 0}}^{\infty} C_{\sigma\mu\nu}^{sn(c)}(kA) \mathbf{F}_{\sigma\mu\nu}^{(1)}(r', \theta', \phi'), & \text{when } r' < |A| \\ \sum_{\sigma=1}^2 \sum_{\substack{\nu=|\mu| \\ \nu \neq 0}}^{\infty} C_{\sigma\mu\nu}^{sn(1)}(kA) \mathbf{F}_{\sigma\mu\nu}^{(c)}(r', \theta', \phi'), & \text{when } r' > |A| \end{cases} \tag{2.33}$$

A translation with $r' = |A|$ is excluded from the equation because such a translation would require an evaluation of spherical waves at the origin of the coordinate system, where they

are not defined. Dependence on the translation distance A is confined in translation coefficients $C_{\sigma\mu\nu}^{sn(c)}(kA)$, which are defined as

$$C_{\sigma\mu\nu}^{sn(c)}(kA) = \frac{1}{2} \sqrt{\frac{(2n+1)(2\nu+1)}{n(n+1)\nu(\nu+1)}} \sqrt{\frac{(\nu+\mu)!(n-\mu)!}{(\nu-\mu)!(n+\mu)!}} (-1)^\mu j^{n-\nu} \sum_{p=|n-\nu|}^{n+\nu} \left[j^{-p} (\delta_{s\sigma} \{n(n+1) + \nu(\nu+1) - p(p+1)\}) + \delta_{(3-s)\sigma} \{2j\mu kA\} a(\mu, n, -\mu, \nu, p) z_p^{(c)}(kA) \right], \quad (2.34)$$

where $a(\mu, n, -\mu, \nu, p)$ is the linearization coefficient [19, Appendix A3] and $z_p^{(c)}(kA)$ the corresponding radial function (see (2.11)–(2.14)). The coefficients $\delta_{s\sigma}$ and $\delta_{(3-s)\sigma}$ are Kronecker deltas, defined by:

$$\delta_{s\sigma} = \begin{cases} 1, & \text{if } s = \sigma \\ 0, & \text{if } s \neq \sigma \end{cases} \quad (2.35)$$

$$\delta_{(3-s)\sigma} = \begin{cases} 1, & \text{if } (3-s) = \sigma \\ 0, & \text{if } (3-s) \neq \sigma \end{cases} \quad (2.36)$$

Symmetry relations listed in equations A3.8–A3.16 in [19, Appendix A3] can be used to reduce the number of computationally very complex translation coefficients that need to be computed.

As for the case of coordinate system rotation, a relation between the SWCs of the original coordinate system's spherical wave coefficients and those of the translated coordinate system can be determined by inserting (2.33) into (2.20). By doing so we obtain:

$$\mathbf{E}(r, \theta, \phi) = \begin{cases} k\sqrt{Z_W} \sum_{c s \mu n} Q_{s\mu n}^{(c)} \mathbf{F}_{s\mu n}^{(c)}(r, \theta, \phi), & \text{when } r' < |A| \\ k\sqrt{Z_W} \sum_{c s \mu n} Q_{s\mu n}^{(c)} \mathbf{F}_{s\mu n}^{(c)}(r, \theta, \phi), & \text{when } r' > |A| \end{cases} \quad (2.37)$$

$$= \begin{cases} k\sqrt{Z_W} \sum_{c s \mu n} Q_{s\mu n}^{(c)} \sum_{\sigma=1}^2 \sum_{\substack{\nu=|\mu| \\ \nu \neq 0}}^{\infty} C_{\sigma\mu\nu}^{sn(c)}(kA) \mathbf{F}_{\sigma\mu\nu}^{(1)}(r', \theta', \phi'), & \text{when } r' < |A| \\ k\sqrt{Z_W} \sum_{c s \mu n} Q_{s\mu n}^{(c)} \sum_{\sigma=1}^2 \sum_{\substack{\nu=|\mu| \\ \nu \neq 0}}^{\infty} C_{\sigma\mu\nu}^{sn(1)}(kA) \mathbf{F}_{\sigma\mu\nu}^{(c)}(r', \theta', \phi'), & \text{when } r' > |A| \end{cases} \quad (2.38)$$

As before, the relation is independent of index c . In the case of a translation in $+z$ direction, index μ also remains unchanged by translation, which brings us to the following relations between waves in the original and the translated coordinate system:

$$\sum_{sn} Q_{s\mu n}^{(c)} \mathbf{F}_{s\mu n}^{(c)}(r, \theta, \phi) = \begin{cases} \sum_{sn} Q_{s\mu n}^{(c)} \sum_{\sigma=1}^2 \sum_{\substack{\nu=|\mu| \\ \nu \neq 0}}^{\infty} C_{\sigma\mu\nu}^{sn(c)}(kA) \mathbf{F}_{\sigma\mu\nu}^{(1)}(r', \theta', \phi'), & \text{when } r' < |A| \\ \sum_{sn} Q_{s\mu n}^{(c)} \sum_{\sigma=1}^2 \sum_{\substack{\nu=|\mu| \\ \nu \neq 0}}^{\infty} C_{\sigma\mu\nu}^{sn(1)}(kA) \mathbf{F}_{\sigma\mu\nu}^{(c)}(r', \theta', \phi'), & \text{when } r' > |A| \end{cases} \quad (2.39)$$

$$= \begin{cases} \sum_{\sigma\nu} Q_{\sigma\mu\nu}^{(c)} \mathbf{F}_{\sigma\mu\nu}^{(1)}(r', \theta', \phi'), & \text{when } r' < |A| \\ \sum_{\sigma\nu} Q_{\sigma\mu\nu}^{(c)} \mathbf{F}_{\sigma\mu\nu}^{(c)}(r', \theta', \phi'), & \text{when } r' > |A| \end{cases} \quad (2.40)$$

Individual SWCs of the translated coordinate system can therefore be expressed as:

$$Q_{\sigma\mu\nu}^{(c)} = \begin{cases} \sum_{s=1}^2 \sum_{\substack{n=|\mu| \\ n \neq 0}}^{\infty} Q_{s\mu n}^{(c)} C_{\sigma\mu\nu}^{sn(c)}(kA), & \text{when } r' < |A| \\ \sum_{s=1}^2 \sum_{\substack{n=|\mu| \\ n \neq 0}}^{\infty} Q_{s\mu n}^{(c)} C_{\sigma\mu\nu}^{sn(1)}(kA), & \text{when } r' > |A| \end{cases} \quad (2.41)$$

It can be seen that the maximum polar order N is theoretically unlimited and infinite spherical harmonic wave functions contribute to the overall field in the translated coordinate system. However, depending on the translation distance A , there is a limited number of translation coefficients $C_{\sigma\mu\nu}^{sn(c/1)}(kA)$ that are nonzero. The maximum polar order N can be obtained from (2.24), when the increase of MRE caused by the translation distance A is considered. A straightforward method to verify if a sufficient number of coefficients has been considered is to compare the total power of both systems, obtained by (2.22), which has to remain unchanged to fulfill the law of conservation of energy.

2.3 Scattering Matrix of an Antenna

Having shown how propagating EM fields may be expanded into a summation of contributions of individual spherical waves and described in an arbitrary spherical coordinate system, it is now time to describe an antenna in terms of these spherical waves. This can be done with the help of scattering matrix theory, which provides the link between quantities measurable in transmission lines and external fields. An antenna can be thought of as a waveguide junction with several ports [19]. One port is the actual physical port, connecting the antenna to a source or a load. Let v and w denote the incoming and outgoing waves on this port, respectively. All remaining ports are radiation ports and can be thought of as modal transmission lines for each individual spherical mode propagating outside the antenna's maximum radial extent (MRE), r_0 . To simplify the notation, the

three indices, s , m , and n , representing individual spherical modes, can be replaced by a single index j by the relation

$$j = 2(n(n+1) + m - 1) + s, \quad (2.42)$$

which, considering the maximum polar index $n = N$ from (2.24), gives the maximum single index $j = J$ as

$$J = 2N(N+2). \quad (2.43)$$

For each radiation port, we have an incoming wave $Q_{smn}^{(3)} = Q_j^{(3)}$, which can also be represented by a_j , as is common in scattering matrices, and an outgoing wave $Q_{smn}^{(4)} = Q_j^{(4)}$, which is commonly represented by b_j in scattering matrices². By separating the antenna's radiation into modal waves, the whole antenna can be understood as a $(J+1)$ -port network. Such a network is illustrated in Figure 2.2.

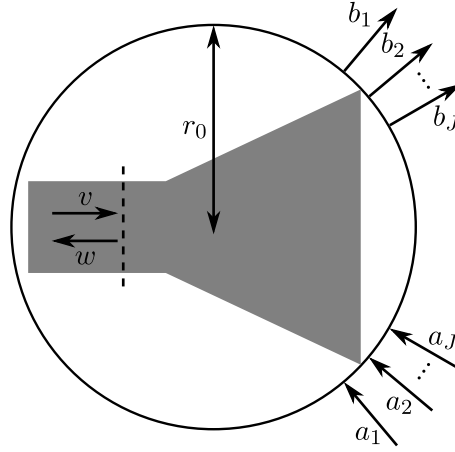


Figure 2.2: Antenna as a $(J+1)$ -port network

This leads to the linear relationship between the incoming and the outgoing waves

$$\begin{bmatrix} \Gamma & \mathbf{R} \\ \mathbf{T} & \mathbf{S} \end{bmatrix} \begin{bmatrix} v \\ \mathbf{a} \end{bmatrix} = \begin{bmatrix} w \\ \mathbf{b} \end{bmatrix}, \quad (2.44)$$

where Γ is the reflection coefficient of the antenna, \mathbf{R} a row vector of size $1 \times J$ containing the antenna receiving coefficients R_j , \mathbf{T} a column vector of size $J \times 1$ containing the antenna transmitting coefficients T_i , and \mathbf{S} the square matrix of size $J \times J$ containing the scattering coefficients of the antenna. The column vectors \mathbf{a} and \mathbf{b} contain as their elements the incoming and outgoing wave coefficients a_1, a_2, \dots, a_J and b_1, b_2, \dots, b_J . The matrix equation in (2.44) can be rewritten as a set of $J+1$ equations,

²Note that, compared to [19], the role of the coefficients is swapped here, as discussed in Section 2.1.

$$w = \Gamma v + \sum_{j=1}^J R_j a_j \quad \text{and} \quad (2.45)$$

$$b_i = T_i v + \sum_{j=1}^J S_{ij} a_j, \quad i = 1, 2, \dots, J. \quad (2.46)$$

With this set of equations, the behavior of the antenna can be described completely in terms of incoming and outgoing waves on all its ports. When the antenna is used to transmit in a reflectionless environment, no incoming inward traveling waves a_j exist and (2.45) and (2.46) reduce to

$$\Gamma v = w \quad \text{and} \quad (2.47)$$

$$T_i v = b_i = Q_i^{(4)}, \quad i = 1, 2, \dots, J. \quad (2.48)$$

2.4 Transmission Formula

Having established how an antenna can be described in terms of its scattering matrix (in an arbitrary coordinate system), the last remaining information required for developing a transmission formula capable of describing a measurement between a pair of antennas is the coupling between them. Consider the situation shown in Figure 2.3 where we have a pair of antennas: the antenna under test (AUT) and the probe antenna. Here, the AUT is fixed in its coordinate system (x, y, z) , while the probe antenna, along with its coordinate system (x', y', z') , is moved on a sphere of radius A and the origin of (x', y', z') lies in (A, θ, ϕ) in the coordinate system of the AUT. Regardless of θ and ϕ , the probe is always pointing towards the origin of the unprimed coordinate system. Additionally, rotation of the probe antenna around the z' -axis by an angle χ is typically required in antenna measurements to cover both field polarizations.

When the AUT is used as a transmitting antenna, the radiated electric field can be expressed by (2.20) in a free-space environment under the condition that r is outside of the AUT's MRE, $r > r_0$. The equations for rotation (2.30) and translation (2.37) can be utilized to express this electric field in the coordinate system of the probe antenna, (r', θ', ϕ') . This gives the expression

$$\mathbf{E}(r', \theta', \phi') = k\sqrt{Z_W} \sum_{\substack{smn \\ \sigma\mu\nu}} Q_{smn}^{(4)} e^{jm\phi_0} d_{\mu m}^n(\theta_0) e^{j\mu\chi_0} C_{\sigma\mu\nu}^{sn(4)}(kA) \mathbf{F}_{\sigma\mu\nu}^{(1)}(r', \theta', \phi'), \quad (2.49)$$

where standing waves, corresponding to spherical Bessel functions, are used in accordance with the condition in (2.37). Per definition, these waves may be replaced by a sum of an inward and an outward traveling wave of amplitude $\frac{1}{2}$ [19] and (2.49) may be rewritten as

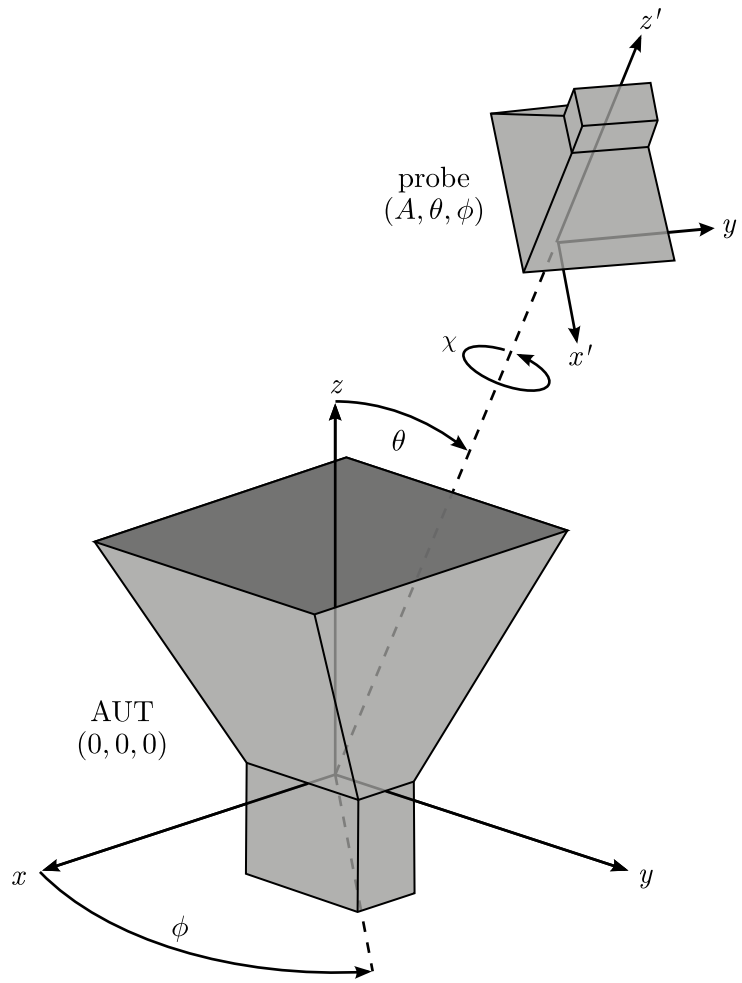


Figure 2.3: Probe antenna and AUT, each with their corresponding coordinate system.

$$\mathbf{E} = k\sqrt{Z_W} \sum_{\substack{smn \\ \sigma\mu\nu}} vT_{smn} e^{jm\phi_0} d_{\mu m}^n(\theta_0) e^{j\mu\chi_0} C_{\sigma\mu\nu}^{sn(4)}(kA) \frac{1}{2} (\mathbf{F}_{\sigma\mu\nu}^{(3)} + \mathbf{F}_{\sigma\mu\nu}^{(4)}), \quad (2.50)$$

where the (r', θ', ϕ') dependence of \mathbf{E} , $\mathbf{F}_{\sigma\mu\nu}^{(3)}$, and $\mathbf{F}_{\sigma\mu\nu}^{(4)}$ has been omitted for compactness and the identity in (2.48) has been used. With this expression, the electric field at the position of the probe can be described and the question that remains to be answered is how the probe antenna interacts with this field. Assuming that the influence of probe insertion on the spherical waves incident onto the probe antenna is negligible³ and that the probe antenna is connected to a perfectly matched receiver⁴, the signal received at the

³The assumption that the influence of scattering due to probe insertion is negligible is common in near-field spherical measurements and will be used hereafter. Nevertheless, consideration of scattering effects is possible and the interested reader is referred to [19] for detailed information.

⁴A receiver mismatch would influence the absolute signal level and the reflection coefficients would need to be measured to correct for it. However, a VNA is typically used for antenna measurements and the absolute signal levels are obtained by an additional standard gain horn (SGH) measurement, thus allowing us to neglect this mismatch.

probe antenna can be expressed from (2.44) and (2.45) using the three-index notation as

$$w = \mathbf{R}^p \mathbf{a} = \sum_{\sigma\mu\nu} R_{\sigma\mu\nu}^p a_{\sigma\mu\nu}. \quad (2.51)$$

The incoming wave coefficients, $a_{\sigma\mu\nu}$, are the coefficients of the modes traveling towards the probe antenna, i.e., $\mathbf{F}_{\sigma\mu\nu}^{(3)}$

$$a_{\sigma\mu\nu} = \frac{1}{2} \sum_{smn} v T_{smn} e^{jm\phi_0} d_{\mu m}^n(\theta_0) e^{j\mu\chi_0} C_{\sigma\mu\nu}^{sn(4)}(kA), \quad (2.52)$$

while $R_{\sigma\mu\nu}^p$ represent the probe receiving coefficients. Inserting (2.52) into (2.51) and omitting the subscript 0 of the probe angles relative to AUT position, the transmission equation can be written as

$$w(A, \chi, \theta, \phi) = \frac{1}{2} \sum_{\substack{smn \\ \sigma\mu\nu}} v T_{smn} e^{jm\phi} d_{\mu m}^n(\theta) e^{j\mu\chi} C_{\sigma\mu\nu}^{sn(4)}(kA) R_{\sigma\mu\nu}^p. \quad (2.53)$$

Note that, in contrast to Hansen [19], translation coefficients for spherical Hankel functions of the second order ($c = 4$) are used here. A similar transmission formula can be derived for the inverse case where the probe antenna is used to transmit a signal and the AUT is used to receive it, where the rotation by Euler angles and translation by translation distance A are done in the opposite direction. For the case where both antennas are reciprocal, their receiving and transmitting coefficients are related by [19]

$$R_{smn} = (-1)^m T_{s,-m,n}. \quad (2.54)$$

In this (very common) case, the received signal w is identical regardless of the mode of operation as long as the transmit signal v remains unchanged.

2.5 Computation of Spherical Wave Coefficients

The transmission formula presented in (2.53) can be used to compute the transmitting coefficients T_{smn} of an AUT if the received signal w is measured at sufficient positions of the probe antenna (A, χ, θ, ϕ) and its receiving coefficients $R_{\sigma\mu\nu}^p$ are known. At least J (2.43) measurement positions are required for an antenna with maximum polar order N (2.24). This results in a system of linear equations, the solution of which has been addressed by various approaches, including matrix-based methods [43], a Fourier transform (FT)-based approach [39], and an iterative method [41]. In 1976, a comparison of these approaches has been done for electrically large antennas in terms of computation time and required resources, demonstrating the superiority of the FT-based approach [42]. Due to low computational power and computer storage at that time, the FT-based transformation algorithm has become the *de facto* standard used in most, if not all, available commercial applications. This approach requires equidistant sampling in χ , θ , and ϕ and measured data over the whole measurement sphere with radius A .

It is important to note that matrix-based approaches do not require equidistant sampling nor measurement points covering the whole sphere. For that reason and due to rapid advancements in computer technology, which reduced computation times significantly, matrix-based methods have been receiving more attention in the last few decades. Different matrix-based approaches for solving the system of linear equations have been investigated in [43] and their solving times compared to a FT-based solution presented by Hansen [19]. It can be seen that even the simplest matrix-inversion computation for a practical measurement with a relatively low maximum polar order $N = 30$ takes more than 23 times longer than the FT-based approach. For this reason, the FT-based approach will be presented in detail in the following but the topic will be revisited later in Chapter 3 when talking about truncated (non-full-sphere) measurements.

2.5.1 Analytical Solution

The analytical solution of the transmission formula, described in detail in [19], is presented in the following. By introducing probe response constants,

$$P_{s\mu n}(kA) = \frac{1}{2} \sum_{\sigma\nu} C_{\sigma\mu\nu}^{sn(4)}(kA) R_{\sigma\mu\nu}^p, \quad (2.55)$$

and separating the summations over the four remaining variables, the transmission formula in (2.53) can be rewritten as

$$w(A, \chi, \theta, \phi) = v \sum_{\mu=-\nu_{\max}}^{\nu_{\max}} \sum_{m=-N}^N \sum_{\substack{n=|m| \\ n \neq 0}}^N \sum_{s=1}^2 T_{smn} e^{jm\phi} d_{\mu m}^n(\theta) e^{j\mu\chi} P_{s\mu n}(kA). \quad (2.56)$$

The number of both the probe receiving coefficients, $R_{\sigma\mu\nu}$, and the AUT transmitting coefficients, T_{smn} , is limited by their maximum polar orders, ν_{\max} and N , obtained from (2.24) for their corresponding MRE. To solve the transmission equation, the FT-based approach exploits the orthogonality of the exponential function,

$$\int_0^{2\pi} e^{j(m-m')\psi} d\psi = 2\pi\delta_{mm'}, \quad (2.57)$$

and the orthogonality of the rotation coefficient [40],

$$\int_0^\pi d_{\mu m}^n(\theta) d_{\mu m'}^{n'}(\theta) \sin\theta d\theta = \frac{2}{2n+1} \delta_{nn'}. \quad (2.58)$$

Here, $\delta_{mm'}$ and $\delta_{nn'}$ represent Kronecker deltas. The solution can then be obtained by sequentially solving for each of the variables in (2.56). In the first step, (2.56) is rewritten as a summation dependent solely on μ ,

$$w(A, \chi, \theta, \phi) = \sum_{\mu=-\nu_{\max}}^{\nu_{\max}} w_\mu(A, \theta, \phi) e^{j\mu\chi}, \quad (2.59)$$

with all other summations contained in $w_\mu(A, \theta, \phi)$. This corresponds to an expansion of w into a finite Fourier series in χ and the coefficients $w_\mu(A, \theta, \phi)$ are obtained by multiplying both sides of the equation by $e^{-j\mu\chi}$ and integrating from 0 to 2π with respect to χ , which allows to express coefficients $w_\mu(A, \theta, \phi)$ in terms of a Fourier transform,

$$w_\mu(A, \theta, \phi) = \frac{1}{2\pi} \int_{\chi=0}^{2\pi} w(A, \chi, \theta, \phi) e^{-j\mu\chi} d\chi. \quad (2.60)$$

In the second step, the same procedure can be repeated for summation over m , expressing $w_\mu(A, \theta, \phi)$ as

$$w_\mu(A, \theta, \phi) = \sum_{m=-N}^N w_{\mu m}(A, \theta) e^{jm\phi}, \quad (2.61)$$

which leads to the FT expression for $w_{\mu m}(A, \theta)$,

$$w_{\mu m}(A, \theta) = \frac{1}{2\pi} \int_{\phi=0}^{2\pi} w_\mu(A, \theta, \phi) e^{-jm\phi} d\phi. \quad (2.62)$$

In the third step, the twice transformed transmission formula is expressed as a summation over n as

$$w_{\mu m}(A, \theta) = \sum_{\substack{n=|m| \\ n \neq 0}}^N w_{\mu m}^n(A) d_{\mu m}^n(\theta), \quad (2.63)$$

and the orthogonality of the rotation coefficient (2.58) is exploited to obtain

$$w_{\mu m}^n(A) = \frac{2n+1}{2} \int_{\theta=0}^{\pi} w_{\mu m}(A, \theta) d_{\mu m}^n(\theta) \sin \theta d\theta. \quad (2.64)$$

The remaining summation of the three-times transformed $w_{\mu m}^n(A)$ over s is then

$$w_{\mu m}^n(A) = v \sum_{s=1}^2 T_{smn} P_{s\mu n}(kA) = v T_{1mn} P_{1\mu n}(kA) + v T_{2mn} P_{2\mu n}(kA). \quad (2.65)$$

In contrast to directly solving the linear system of equations from the transmission formula (2.56), which has a large number of unknowns, exploitation of orthogonality in (2.57) and (2.58) leads to a linear system of equations with only two unknowns, T_{1mn} and T_{2mn} , for each (μ, m, n) combination. To further reduce the number of equations and measurements, Wacker [39] proposed using circularly symmetric probes, such as a small dipole or a circular waveguide, where only $\mu = \pm 1$ spherical modes exist. In this case, (2.59) reduces to a system of two equations with two unknowns and only two measurements in χ are required to compute w_μ . If the field is measured in $\chi = 0$ and $\chi = \frac{\pi}{2}$, the Fourier transform for obtaining $w_\mu(A, \theta, \phi)$ reduces to the simple relation

$$w_{\mu=\pm 1}(A, \theta, \phi) = \frac{1}{2} \left[w(A, \chi = 0, \theta, \phi) \mp jw(A, \chi = \frac{\pi}{2}, \theta, \phi) \right]. \quad (2.66)$$

Hansen [19] suggests that, even for antennas which are not perfectly rotationally symmetric, such as rectangular horn antennas, the $\mu = \pm 1$ modes are dominating at a sufficient distance from the AUT. This approximation has become common practice in commercial solutions.

2.5.2 Discrete Solution

The presented analytical solution requires triple (or double, for the special case where only $\mu = \pm 1$ modes exist) integration of w to compute the transmission coefficients of the AUT, which requires continuous data over χ , ϕ , and θ . In practice, this information is not available, and we have to make use of discrete sampling over all three variables and numerically integrate over them. The discrete Fourier transform (DFT) and its inverse, the inverse discrete Fourier transform (IDFT), can be used for evaluating Fourier integrals of bandlimited, periodic functions. For DFT, the definition that will be used throughout this work is

$$X[l] = \sum_{k=0}^{K-1} x[k] e^{-j \frac{2\pi kl}{K}}, \quad (2.67)$$

while its inverse, IDFT, will be defined as

$$x[k] = \frac{1}{K} \sum_{l=0}^{K-1} X[l] e^{j \frac{2\pi kl}{K}}. \quad (2.68)$$

In both equations, K represents the total number of samples both in x and in X . These definitions are the most common definitions in engineering and are also the ones used in Matlab [44]. **A different definition is used by Hansen [19], where the sign of the exponential functions in both equations is interchanged.**

The first integral in the analytical solution of the transmission formula, (2.60), is periodic with a period of 2π and bandlimited, where, in accordance with (2.59), μ takes the values $\mu = -\nu_{\max}, \dots, 0, \dots, \nu_{\max}$. By obtaining sufficient equidistant samples of the function w in χ , the integral can be solved by applying a DFT. A sufficient number of samples, K_χ , in this context means that the number has to fulfill the condition $K_\chi \geq 2\nu_{\max} + 1$. The maximum sample spacing still fulfilling this condition is then $\Delta\chi = 2\pi/K_\chi$, for which the transformation over μ can be computed as

$$w_\mu(A, \theta, \phi)[\mu] = \frac{1}{K_\chi} \sum_{k=0}^{K_\chi-1} w(A, k\Delta\chi, \theta, \phi) e^{-jk\Delta\chi\mu}. \quad (2.69)$$

Due to the different sign convention used by Hansen [19], his use of an IDFT is replaced by a DFT that additionally needs to be scaled by $1/K_\chi$. The first integration is thus computed by

$$w_\mu(A, \theta, \phi) = \frac{1}{K_\chi} \text{DFT}\{w(A, k\Delta\chi, \theta, \phi)\}. \quad (2.70)$$

As mentioned earlier, the computation of this integral can be reduced to a simple summation, (2.66), when a circularly symmetric probe containing only $\mu = \pm 1$ modes is used.

A similar approach can be used for computing the second integral in (2.62). For each probe mode μ , a Fourier transform of a periodic, bandlimited function with $K_\phi \geq 2N + 1$ samples, where $m = -N, \dots, 0, \dots, N$, and a measurement step $\Delta\phi = 2\pi/K_\phi$, can be computed via DFT:

$$w_{\mu m}(A, \theta) = \frac{1}{K_\phi} \text{DFT}\{w_\mu(A, \theta, k\Delta\phi)\} \quad (2.71)$$

Having computed $w_{\mu m}(A, \theta)$ for all μ and m , it is now time to solve the θ -integral in (2.64). While the function to be integrated is again bandlimited with $n \leq N$, integration over θ is only done in the range $0 \leq \theta \leq \pi$ and the integrand cannot be assumed a periodic function. However, per definition, rotation coefficients $d_{\mu m}^n(\theta)$ are periodic with a period of 2π and are either even or odd functions about π depending on the parity of $(\mu - m)$. This allows $w_{\mu m}(A, \theta)$ to be extended to the whole 2π range with the same parity as the corresponding rotation coefficients [19], resulting in:

$$\tilde{w}_{\mu m}(A, \theta) = \begin{cases} w_{\mu m}(A, \theta), & 0 \leq \theta \leq \pi \\ w_{\mu m}(A, 2\pi - \theta), & \pi \leq \theta < 2\pi \quad \text{for } (\mu - m) \text{ even} \\ -w_{\mu m}(A, 2\pi - \theta), & \pi \leq \theta < 2\pi \quad \text{for } (\mu - m) \text{ odd} \end{cases} \quad (2.72)$$

This extended sequence may then be expanded into a finite Fourier series

$$\tilde{w}_{\mu m}(A, \theta) = \sum_{l=-N}^N b_l^{\mu m} e^{jl\theta}. \quad (2.73)$$

By expanding the rotation coefficient into a finite Fourier series, as was shown in (2.26), and inserting the finite Fourier series (2.73) of the extended twice-transformed sequence $\tilde{w}_{\mu m}(A, \theta)$, (2.64) can be rewritten as

$$w_{\mu m}^n(A) = \frac{2n+1}{2} j^{\mu-m} \sum_{l=-N}^N b_l^{\mu m} \sum_{m'=-n}^n \Delta_{m'\mu}^n \Delta_{m'm}^n \int_{\theta=0}^{\pi} e^{j(l-m')\theta} \sin \theta \, d\theta. \quad (2.74)$$

The integral takes the values

$$\int_{\theta=0}^{\pi} e^{j(l-m')\theta} \sin \theta \, d\theta = \begin{cases} \pm j \frac{\pi}{2}, & (l - m') = \pm 1 \\ 0, & |l - m'| = 3, 5, 7, \dots \\ \frac{2}{1 - (l - m')^2}, & |l - m'| = 0, 2, 4, \dots \end{cases} \quad (2.75)$$

and the only remaining unknowns in (2.78) are the coefficients $b_l^{\mu m}$, which can be computed from the extended sequence $\tilde{w}_{\mu m}(A, \theta)$ utilizing a DFT as

$$b_l^{\mu m}(A) = \frac{1}{K_\theta} \text{DFT}\{\tilde{w}_{\mu m}(A, k\Delta\theta)\}. \quad (2.76)$$

In this equation, K_θ represents the number of measurement samples in the extended range, $K_\theta = 2N + 1$. This integral can be further reduced to obtain an efficient algorithm for its evaluation by considering steps presented in the following, described in detail in [19]. First, from the definition of the extended function $\tilde{w}_{\mu m}(A, \theta)$, it can be shown that

$$b_l^{\mu m} = (-1)^{\mu+m} b_{-l}^{\mu m}. \quad (2.77)$$

From this property of the sequence $b_l^{\mu m}$, the identities in (2.29), and the values of the integral (2.75), it can be shown that the terms for $(l - m') = \pm 1$ cancel out. Equation (2.78) may thus be rewritten as

$$w_{\mu m}^n(A) = \frac{2n+1}{2} j^{\mu-m} \sum_{m'=-n}^n \Delta_{m'\mu}^n \Delta_{m'm}^n \sum_{l=-N}^N \Lambda(l - m') b_l^{\mu m}, \quad (2.78)$$

where

$$\Lambda(l - m') = \begin{cases} 0, & (l - m') \text{ odd,} \\ \frac{2}{1 - (l - m')^2}, & (l - m') \text{ even.} \end{cases} \quad (2.79)$$

Then, the summation over l first has to be done for each m' in order to compute $w_{\mu m}^n(A)$:

$$G(m') = \sum_{l=-N}^N \Lambda(m' - l) b_l^{\mu m} \quad (2.80)$$

Here, $\Lambda(l - m')$ was replaced by $\Lambda(m' - l)$ to indicate the resemblance to a convolution. A fast computation of $G(m')$ coefficients is possible by taking the following steps. First, a periodic sequence $\tilde{\Lambda}(k)$ is obtained by truncating the infinite sequence $\Lambda(m' - l = k)$ to the range between $-2N < k \leq 2N$ and defining it to be periodic with a period of $4N$. The sequence $b_l^{\mu m}$, defined in the range between $-N \leq l \leq N$, can also be extended to the range between $-2N < k \leq 2N$ by assigning the missing values to be zero and defining it to be periodic with a period of $4N$, thus obtaining the sequence $\tilde{b}_l^{\mu m}$. The sequences in (2.80) can then be replaced by their periodic counterparts,

$$G(m') = \sum_{l=0}^{4N-1} \tilde{\Lambda}(m' - l) \tilde{b}_l^{\mu m}, \quad (2.81)$$

without changing the results of the summation over l for m' in the interval $-N \leq m' \leq N$. This summation of a product of two periodic sequences represents a cyclic convolution, which can be computed as a DFT of an elementwise product, \odot , of two IDFTs as

$$G(m') = \frac{1}{4N} \text{DFT}\{4N \text{IDFT}\{\tilde{\Lambda}(k)\} \odot 4N \text{IDFT}\{\tilde{b}_l^{\mu m}\}\}, \quad (2.82)$$

where additional multiplications of both IDFTs with $4N$ and DFT with $1/4N$ are done to correct for the different definitions of these two transforms in comparison to the definitions used by Hansen [19]. It is possible to reduce the number of computations further by exploiting the fact that the function in (2.79) is an even function and the extended $\tilde{b}_l^{\mu m}$ retains the property of $b_l^{\mu m}$ shown in (2.77). These properties are retained under DFT and IDFT operations, leading to the conclusion that

$$G(m') = (-1)^{\mu+m} G(-m'). \quad (2.83)$$

From this property and the identities in (2.29), it can be seen that

$$\Delta_{m'\mu}^n \Delta_{m'm}^n G(m') = \Delta_{-m'\mu}^n \Delta_{-m'm}^n G(-m'). \quad (2.84)$$

Due to this identity, the summation over m' in (2.78) can be reduced further to

$$w_{\mu m}^n(A) = \frac{2n+1}{2} j^{\mu-m} \left(\Delta_{0\mu}^n \Delta_{0m}^n G(0) + \sum_{m'=1}^n 2\Delta_{m'\mu}^n \Delta_{m'm}^n G(m') \right). \quad (2.85)$$

This step concludes the triple integration of the transmission formula and the linear system of equations in (2.65) can be solved to compute the SWCs of the antenna under test (AUT).

2.6 Transformation Algorithm

Once the spherical wave coefficients ($Q_{smn} = vT_{smn}$) are obtained, the radiation pattern can be evaluated anywhere in space outside of the AUT's MRE. A straightforward approach to computing the electric field pattern would be to compute the spherical wave functions in (2.18) and (2.19) and then compute the sum of these spherical wave functions with their corresponding SWCs (2.20). An alternative approach to this tedious computation procedure is to reuse the transmission formula and compute the received signal $w'(A', \chi, \theta, \phi)$ on a sphere with radius A' , which circumscribes the AUT, from

$$w'(A', \chi, \theta, \phi) = \sum_{\mu=-\nu_{\max}}^{\nu_{\max}} e^{j\mu\chi} \sum_{m=-N}^N e^{jm\phi} \sum_{m'=-N}^N e^{jm'\theta} \sum_{n=\max(|m'|, |m|, 1)}^N j^{m-\mu} \Delta_{m'\mu}^n \Delta_{m'm}^n \sum_{s=1}^2 vT_{smn} P'_{s\mu n}(kA'). \quad (2.86)$$

The computation can be done by first computing the summations in the second line of (2.86) for each μ, m', m combination,

$$b_{m'}^{\prime\mu m} = \sum_{n=\max(|m'|, |m|, 1)}^N j^{m-\mu} \Delta_{m'\mu}^n \Delta_{m'm}^n \sum_{s=1}^2 v T_{smn} P'_{s\mu n}(kA'), \quad (2.87)$$

succeeded by a series of IDFTs:

$$\tilde{w}'_{\mu m}(A', k\Delta\theta) = K_\theta \text{IDFT}\{b_{m'}^{\prime\mu m}\} \quad (2.88)$$

$$w'_\mu(A', k\Delta\theta, k\Delta\phi) = K_\phi \text{IDFT}\{w'_{\mu m}(A, k\Delta\theta)\} \quad (2.89)$$

$$w'(A', k\Delta\chi, k\Delta\theta, k\Delta\phi) = K_\mu \text{IDFT}\{w'_\mu(A', k\Delta\theta, k\Delta\phi)\} \quad (2.90)$$

The sequence in (2.88) is the extended sequence from (2.72) which has to be truncated to the range of $0 \leq \theta \leq \pi$ before computing the IDFT in (2.89). For all three angles, θ , ϕ , and χ , an arbitrary number of samples (and the corresponding sampling step) can be achieved by zero padding the sequences before transformation. The probe response constants $P'_{s\mu n}(kA')$ can be defined to evaluate the signal that a chosen probe antenna would receive from the transmitting AUT. Typically, an x-directed electric dipole is used as the transformation probe antenna, which has two nonzero probe receiving coefficients, $R_{211}^p = -R_{2,-1,1}^p = -\sqrt{2}/2$, since the signals received by such a probe are directly proportional to the incident electric field parallel to the dipole [19]. From signals received by a dipole probe, the electric field can be expressed by

$$E'_\theta(A', \theta, \phi) = \sqrt{Z_w} \frac{2k}{\sqrt{6\pi}} w'(A', 0, \theta, \phi), \quad (2.91)$$

$$E'_\phi(A', \theta, \phi) = \sqrt{Z_w} \frac{2k}{\sqrt{6\pi}} w'(A', \frac{\pi}{2}, \theta, \phi). \quad (2.92)$$

The presented discrete solution of the transmission formula and the computation of a radiation pattern on an arbitrary sphere, whether in the near field or far field, have been implemented in Matlab [44] and named spherical near-to-far-field transformation (SN2FFT). The collection of scripts and functions used by SN2FFT has been documented in Appendix A with commentary.

3 Truncated Pattern Stitching

In Chapter 2, the theoretical background of spherical near-field measurements and the subsequent transformation of such measured antenna near-field patterns into far-field patterns has been discussed in detail. Assuming perfect field-pattern measurements, this transformation is considered exact and its accuracy is limited only by the numerical precision of the discrete transformation algorithm and the maximum considered polar order N . At this point, it is necessary to transition from theoretical concepts to practical applications. Thus, it is important to consider the practical methods for measuring near-field (NF) patterns.

As discussed in the previous chapter, aside from the antenna under test (AUT) itself, a second (probe) antenna is required, capable of measuring electric fields at all points on a sphere which circumscribes the AUT. The interaction between both antennas is described by the transmission formula, which relates the received signal at one antenna to the signal transmitted by the other one. To measure the transmission between them, one antenna must be connected to a signal generator, while the other must be connected to a vector signal receiver. Alternatively, a single two-port vector network analyzer (VNA) is commonly used in place of these two devices. Since measured fields have to be unaffected both by external interfering signal sources and reflections, the measurements are normally carried out in an electromagnetically shielded anechoic chamber. As already stated in Chapter 1, different approaches to measuring fields on the whole measurement sphere exist and measurement ranges can be divided into different range types depending on the implementation [15, 19]. Since the antenna range installed at TU Wien, which was shown in Figure 1.2, is a swing arm-over-azimuth range, this work mainly focuses on this type of ranges.

A simple schematic of a swing arm-over-azimuth range can be seen in Figure 3.1, where all the rotation axes have been marked. The probe antenna is mounted onto the swing arm and covers the θ -axis of the sphere, while the AUT is mounted onto a rotary stage which covers the ϕ -axis. Additionally, the probe antenna is also mounted on a rotary stage which covers the χ -axis, i.e., the two orthogonal polarizations. As mentioned in Chapter 1, a glance at either Figure 1.2 or Figure 3.1 suffices to see that covering the whole sphere in a single measurement with this range type is impossible. The rotary stage on which the AUT is mounted limits the range of θ -angles to less than full 180° , necessitating the use of truncated field patterns. Just like the transformation algorithm presented in Chapter 2, the majority of commercially available near-to-far-field transformation algorithms are Fourier-transform (FT)-based. They require equidistant sampling

over the whole sphere, so missing points have to be assigned some value, typically zero. If directive antennas are used, errors caused by truncation can be kept low by orienting the antenna in such a way that radiated fields in the range not covered by the measurement are small. With omnidirectional antennas, however, this is not possible and truncation results in nonzero higher-order spherical wave coefficients (SWCs) or ripple effects in the transformed patterns.¹

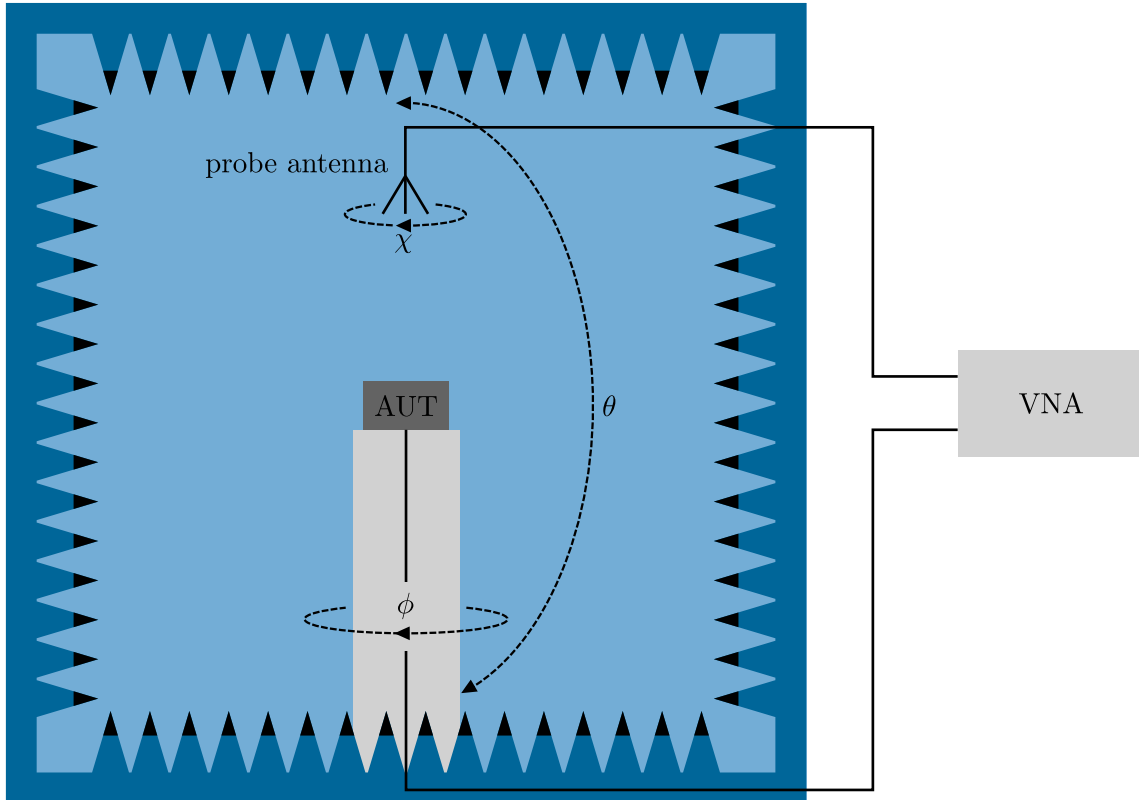


Figure 3.1: Schematic of a swing arm-over-azimuth range

Many approaches capable of reducing the truncation error exist. A least-squares (LS) approach was proposed in [26], which only uses measurements of the forward hemisphere, with the number of samples doubled compared to the sampling theorem. An energy constraint is specified for the backward hemisphere to prevent the method from overestimating the radiation in the backward hemisphere. In [23], the authors proposed an iterative procedure for the spherical near-to-far-field transformation (SN2FFT) algorithm, where the values in the truncated region are set to zero, and the algorithm is used to obtain the SWCs. After filtering the SWCs above maximal polar order N , the field is reconstructed and the newly computed field values are used in the truncated region, while the values in the measured region are replaced with the actual measured values. This is done iteratively until the reconstructed fields match the measured fields up to a defined maximal error. This approach was further simplified in [45] by strictly limiting SWCs to N , thus avoiding the need for SWC-filtering. This method computes a possible combination of SWCs

¹It should be noted at this point that some spherical near-field ranges are constructed in a way which allows for full-sphere measurements. However, the presence of a support structure on which the AUT is mounted is inevitable. This support structure directly interacts with the radiating antenna, thus causing errors in the field pattern.

capable of describing the pattern in the measured range, but the solution does not provide reliable information on the behavior in the range above truncation angle θ_{trunc} . With the constantly increasing available computing power, matrix-solver-based approaches have also been gaining popularity [43]. These approaches are not constrained by equidistant sampling or the full-sphere requirement. However, they are slower than the FT-based algorithms and the processing time increases rapidly for higher maximum polar order problems. Caution has to be taken to define a well-conditioned matrix of linear equations.

While these methods tackle truncation errors in the covered range, they all share one limiting factor. They represent a possible combination of SWCs capable of describing the pattern in the measured range up to the angle of truncation ($0^\circ \leq \theta \leq \theta_{\text{trunc}}$), but above truncation angle ($\theta > \theta_{\text{trunc}}$) no reliable information is given. To obtain reliable full-sphere radiation patterns, the idea of stitching multiple truncated patterns is proposed, the details of which will be discussed in this chapter.

3.1 Pattern Stitching Concept

As already stated, it is generally impossible to compute full-sphere radiation patterns from a single truncated measurement and samples over the whole sphere are required for an accurate near-to-far-field transformation. In order to overcome limitations stemming from pattern truncation, which is inevitable in most antenna ranges, our proposed method exploits the fact that an antenna can readily be measured in multiple orientations. By doing so, measurement points over the whole sphere are obtained, extending the range of the measurement system to full 180° in θ . Throughout this work, two measurement orientations are considered, which suffice for stitching measurement data obtained in the spherical near-field range at TU Wien. However, there is no indication that it would be impossible to generalize the approach to include more than two measurement orientations if necessary. With two measurements, the intuitive approach is to rotate the antenna by 180° in one measurement, thus obtaining measurements of two hemispheres. It has to be taken into account that, in practice, the measured antenna is unlikely to be placed exactly in the origin of the measurement system. Moreover, any additional physical manipulation of the antenna will likely result in some relative offset between the measurements. In order to stitch the measured patterns together, the coordinate systems of both measurements have to be aligned by comparing measured field values, for which an overlapping region is needed. In Figure 3.2, the concept of the pattern stitching procedure is illustrated. Two antenna measurements are done, where the antenna has been rotated by 180° around the x - or y -axis for measurement 2. The measurement points of both measurements are shown along with the truncated region marked in green (top). When measurement 2 is rotated by 180° , the points from the two measurements are most likely misaligned and need to be adjusted (upper middle). After the coordinate systems have been successfully aligned, the measurement points from the two datasets coincide (lower middle) and can be stitched together to generate a full-sphere pattern (bottom).

3.2 Spherical Wave Coefficients of Truncated Patterns

As mentioned in the previous section, the partial truncated measurements need to be aligned to the same coordinate system before they can be stitched together. To do so, the

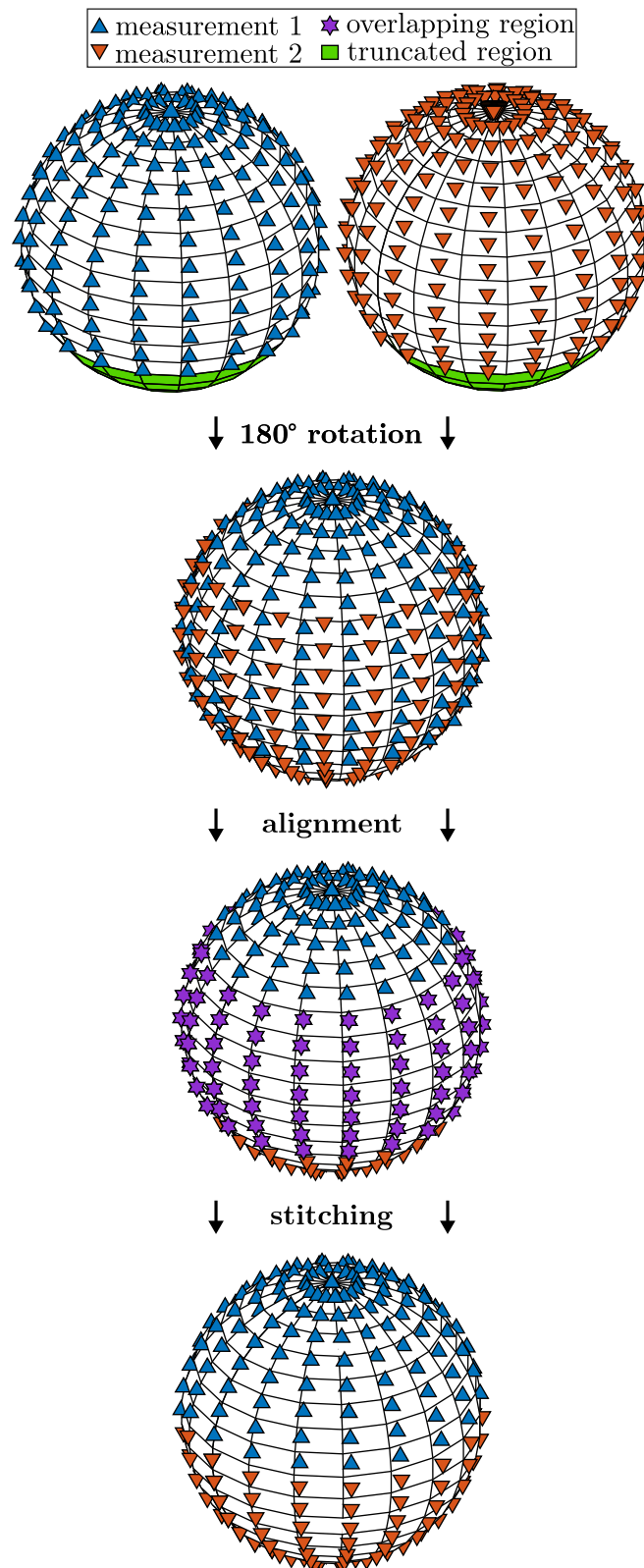


Figure 3.2: Pattern stitching concept

coordinate system of one measurement needs to be rotated and translated to match the coordinate system of the second measurement. These manipulations of the coordinate system can be done by using the mathematical operators presented in Section 2.2. Equations for rotation, (2.32), and translation, (2.41), can be used to rotate and translate the coordinate system to any arbitrary point and orientation in space. However, these equations require the knowledge of SWCs. When processing truncated patterns with the SN2FFT algorithm presented in Chapter 2, truncation causes errors in the computed SWCs and, especially in the case of omnidirectional antennas, large errors in the transformed field pattern. Therefore, an approach for computing SWCs which can accurately describe the measured field pattern is required. Hereinafter, such SWCs will be called truncated SWCs and three different approaches for their computation have been investigated: the iterative algorithm [45], the least squares (LS) method [43], and the FFT/Matrix method [42, 46].

3.2.1 Iterative Algorithm

An iterative algorithm similar to the one presented in [45] was the first of the three methods to be implemented. As its input, the algorithm takes the truncated field pattern in two orthogonal linear polarizations, maximum polar and azimuthal orders N and M , a maximum-error goal, and a limit on the number of iterations. The field points in the truncated region are set to their respective last measured point in θ , which was found to allow for faster convergence of the algorithm than when setting them to zero. In each iteration, a same-distance near-to-near-field transformation is done on the field pattern using SN2FFT, computing a combination of SWCs and their corresponding field pattern. This pattern is compared to the original measured data in terms of a scaled mean square error (SMSE), which is defined as

$$\text{SMSE} = \frac{1}{K} \frac{\sum_{\chi, \theta, \phi} |w(\chi, \theta, \phi) - \hat{w}(\chi, \theta, \phi)|^2}{\max_{\chi, \theta, \phi} |w(\chi, \theta, \phi)|^2}, \quad (3.1)$$

where $K = K_\chi \cdot K_\theta \cdot K_\phi$ is the total number of points, w the array containing the measured field pattern, and \hat{w} the array containing the estimated field pattern obtained from expansion of computed SWCs. Error normalization in relation to the maximum field value is done in order to prioritize measurement points with large fields as they are less sensitive to both measurement and numerical noise. The algorithm then constructs a new field pattern from the original truncated pattern by substituting the values in the truncated region with those from the current iteration pattern. Previous steps are repeated using this updated pattern, including the computation of new SWCs and their corresponding pattern, and the evaluation of the SMSE once more. This iterative procedure is continued until the SMSE goal is achieved or the maximum number of iterations is reached.

3.2.2 LS Method

Using the iterative algorithm to obtain SWCs, the time efficiency of the FT-based transformation algorithm is significantly impaired since hundreds or even thousands of iterations are required to reach the desired SMSE goal. For that reason, a least squares (LS) matrix method had also been implemented and tested. While this method underperforms the

Fourier-transform-based method in terms of computational efficiency when a full-sphere pattern is available, as demonstrated, e.g., in [43], it does not require equidistant sampling in θ and ϕ . This means that, in contrast to the iterative algorithm presented earlier, truncated SWCs accurately describing the field pattern in the measured range can be obtained directly from a single computation step.

For the LS method, the transmission formula (2.53) can be rewritten in matrix form as

$$\mathbf{w} = \underline{\Psi}\mathbf{q}, \quad (3.2)$$

where \mathbf{w} is the vector containing measured fields in all measurement points, \mathbf{q} the vector containing all sought SWCs, $q_j = Q_{smn} = vT_{smn}$, and $\underline{\Psi}$ the matrix containing all remaining elements of (2.53), computed for each (A, χ, θ, ϕ) and (s, m, n) combination. The LS objective is then to minimize the square difference between measured and estimated fields,

$$\arg \min_{\mathbf{q}} \|\mathbf{w} - \underline{\Psi}\mathbf{q}\|_2. \quad (3.3)$$

In general, the number of measurement points is not equal to the number of SWCs and the matrix $\underline{\Psi}$ is a nonsquare matrix, therefore an inverse matrix $\underline{\Psi}^{-1}$ cannot exist. In [43], the authors suggest solving this system of linear equations by computing the Moore-Penrose pseudoinverse [47] of $\underline{\Psi}$, represented here by $\underline{\Xi}$.² Using singular value decomposition (SVD) of $\underline{\Psi} = \underline{U}\underline{\Sigma}\underline{V}^*$, the expression for the pseudoinverse is $\underline{\Xi} = \underline{V}\underline{\Sigma}^{-1}\underline{U}^*$ [44, 48]. The vector containing all the SWCs can then be expressed as

$$\mathbf{q} = \underline{\Xi}\mathbf{w}. \quad (3.4)$$

For the general case where $M = N$, this gives a linear system with $J = 2N(N + 2)$ unknowns in accordance with (2.43). To solve this system, $K \geq J$ measurement points are needed, resulting in a $J \times K$ matrix $\underline{\Xi}$.

3.2.3 FFT/Matrix Method

In an attempt to combine the benefits of the FT-based algorithm with those of the matrix-based approach, a third approach was implemented, discussed already in [42] and, more recently, in [46]. Exploiting the fact that the variables are separable due to the orthogonality of the exponential coefficients, integrations in χ and ϕ can be computed with a two-dimensional fast Fourier transform (FFT), since full angular range is measured for both variables. This is done by using (2.70) first and then (2.71), which gives us the twice-transformed transmission formula [42],

$$w_{\mu m}(A, \theta) = \sum_{s=1}^2 \sum_{\substack{n=|m| \\ n \neq 0}}^N Q_{smn} d_{\mu m}^n(\theta) P_{s\mu n}(kA). \quad (3.5)$$

²A large number of alternative methods for solving the least squares system exist, e.g., QR decomposition, modified Gram-Schmidt, or normal equations [48], and SVD is used here mainly because of its robustness and ease of singular value (SV) truncation when dealing with rank-deficient coefficient matrices.

At this point, the FT-based SN2FFT algorithm presented in Chapter 2 would exploit the orthogonality of the rotation coefficient $d_{\mu m}^n(\theta)$, (2.58), to integrate over θ by using another DFT. However, when dealing with truncated patterns, the pattern is not periodic in θ and using a DFT is not possible without introducing a truncation error. Therefore, a system of linear equations is constructed from the twice-transformed transmission formula instead. Similar to the least squares method presented in the previous section, this system of equations can be written in matrix form as

$$\mathbf{w}_{\mu m} = \underline{\Psi}_m \mathbf{q}_m, \quad (3.6)$$

and solved independently for each polar index m by computing the pseudoinverse of the coefficient matrix $\underline{\Psi}_m$, $\underline{\Xi}_m$ and inverting (3.6) to express \mathbf{q}_m :

$$\mathbf{q}_m = \underline{\Xi}_m \mathbf{w}_{\mu m} \quad (3.7)$$

By doing so, the number of unknowns is reduced from J to the m -dependent $J_m = 2(N + 1 - |m|)$ with the special case, valid for $|m| = 0$, where $J_m = 2N$. This substantially reduces the complexity of the pseudoinverse computation, as well as high memory requirements connected with the large system of linear equations from (3.4).

3.2.4 Singular Value Truncation for Computing Pseudoinverses

During preliminary testing, it was observed that coefficient matrices (either $\underline{\Psi}$ or $\underline{\Psi}_m$, depending on the method) describing the linear system of equations in the least squares (LS) method and the FFT/Matrix method are rank deficient³ when field patterns are sampled with the minimum number of samples required by a full-sphere SN2FFT⁴ and the range of measured θ -angles is less than 180° . As a consequence of rank deficiency, an infinite number of solutions to the transmission equation exists. In [49], authors claimed that this issue can be solved by increasing the number of sampling points in the allowable range of scan angles, thus obtaining a full-rank coefficient matrix which would allow computing a unique solution of the transmission formula. This would mean that radiation patterns over the whole sphere could be reconstructed from a small subsurface of the sphere as long as sufficient independent samples were obtained. Tests on coefficient matrices $\underline{\Psi}$ from the LS method⁵ have demonstrated that increasing the number of samples in θ —such that the number of samples in the truncated region, $K_{\theta_{\text{trunc}}}$, equals the minimum number of samples in the full θ -range in Chapter 2, $K_\theta = N + 1$ —can indeed contribute to achieving full rank when the maximum polar order N is low. This can be seen on an example shown in Figure 3.3, where $N = 20$ and the measurement distance $A = N/k$.

³Due to limited numerical precision and roundoff error, none of the singular values are actually zero and numerical rank is evaluated based on a chosen tolerance related to machine precision [48]. By default, Matlab [44] uses $\max(\text{size}(\underline{\Psi})) * \text{eps}(\text{norm}(\underline{\Psi}))$ as a tolerance for computing the rank of matrix $\underline{\Psi}$.

⁴The minimum required number of samples, discussed already in Chapter 2, is $K_\chi \cdot K_\theta \cdot K_\phi$, where $K_\chi = 2$, $K_\theta = N + 1$, and $K_\phi = 2M + 1$. With no knowledge of the AUT, M has to be assumed equal to N , i.e., $M = N$.

⁵Due to lower complexity of the LS method (only one coefficient matrix instead of $2N + 1$ smaller coefficient matrices), the findings in this chapter are presented only with examples using the LS method. The same behavior could be observed when using the FFT/Matrix method and all presented findings can be applied to the FFT/Matrix method as well.

This measurement distance was chosen since it is the shortest distance for which the transmission formula is valid and, as such, represents the worst-case scenario. In the graph, singular values (SVs) σ_j , sorted from largest to smallest, are plotted for three distinct sampling cases: (a) pattern samples over the full 180° -range of θ available, (b) pattern truncated at $\theta_{\text{trunc}} = 135^\circ$ with the minimum number of samples required by SN2FFT, and (c) pattern truncated at $\theta_{\text{trunc}} = 135^\circ$ with the increased number of samples $K_{\theta_{\text{trunc}}} = N + 1$. One can observe that the tail of small singular values in (b) around 10^{-15} , which is in the range of numerical precision, disappears with increased sampling in (c), thus resulting in a matrix with full numerical rank. However, the large variation between

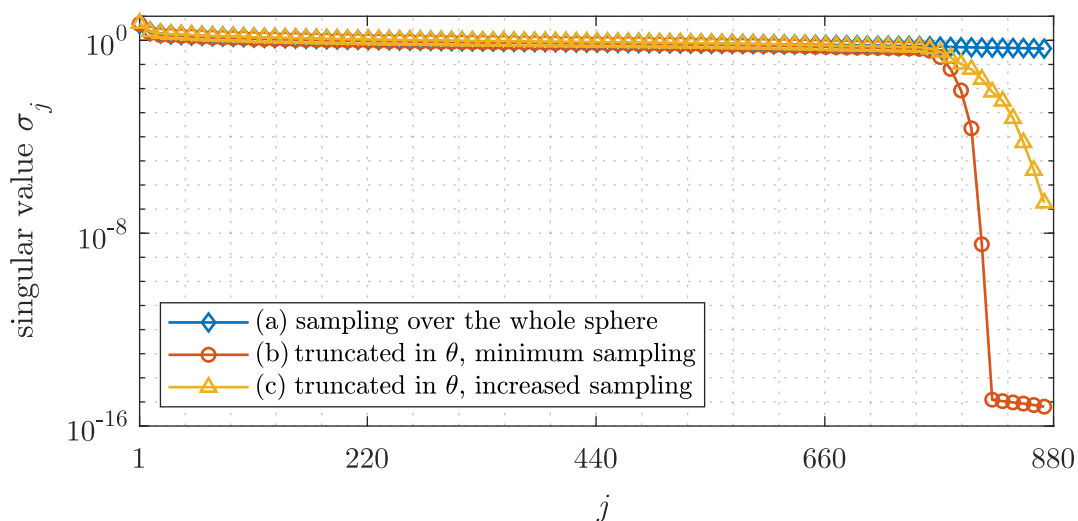


Figure 3.3: Comparison of singular values σ_j ⁶ for different sampling cases: Polar order $N = 20$, evaluation distance $A = N/k$, $\theta_{\text{trunc}} = 135^\circ$

SVs indicates that this linear system of equations is highly sensitive to small variations in the data, e.g., simulation or measurement noise. This can best be demonstrated by computing the condition number of the matrix $\underline{\Psi}$, which is expressed as the ratio between the largest and the smallest singular value [50],

$$\kappa(\underline{\Psi}) = \frac{\sigma_{\max}(\underline{\Psi})}{\sigma_{\min}(\underline{\Psi})}. \quad (3.8)$$

The condition number $\kappa(\underline{\Psi})$ for each of the sampling cases is listed in Table 3.1. It can be seen that the condition number in the case of full theta range (a) is substantially lower than those of the two truncated-pattern cases, (b) and (c). While the distinction between small and large condition numbers is rarely quantified in the literature, in [50] the author states that $\kappa > 30$ implies severe multicollinearity and, thus, an ill-conditioned system.

For this reason, further oversampling in θ was investigated, where the number of samples was multiplied by a factor, a , such that $K_{\theta_{\text{trunc}}} = a \cdot (N + 1)$. The results are shown in Figure 3.4. One can see that doubling the number of samples by using the factor $a = 2$ decreases the condition number κ and using the factor $a = 5$ decreases it even further.

⁶For the purpose of readability, only every 10th singular value is displayed in the plot.

Table 3.1: Comparison of condition numbers $\kappa(\underline{\Psi})$ for different sampling cases: Polar order $N = 20$, evaluation distance $A = N/k$, $\theta_{\text{trunc}} = 135^\circ$

sampling case	condition number $\kappa(\underline{\Psi})$
(a) full theta range	10.72
(b) truncated, minimum sampling ($K_\theta = N + 1$)	9.84×10^{15}
(c) truncated, increased sampling ($K_{\theta_{\text{trunc}}} = N + 1$)	3.5×10^{10}

Observing the results for $a = 10$ and $a = 20$, it becomes clear that this reduction is limited and κ converges to some value, which is still very large. Moreover, for maximum polar order $N = 50$, increasing the number of samples by multiplication with $a = 20$ results in a problem so large that the used personal computer (PC) with 32 GB RAM runs out of available memory. This leads to the conclusion that increasing the number of samples in θ is an unfeasible approach for reducing the condition number $\kappa(\underline{\Psi})$. For the sake of thoroughness, increasing the number of samples in both θ and ϕ simultaneously has also been tested. As predicted, no evident improvement in comparison to increasing the number of samples solely in θ has been identified since a sufficient number of independent samples in the nontruncated ϕ -axis is obtained already with the usual SN2FFT sampling scheme. As such, increasing the number of samples in ϕ can be considered superfluous.

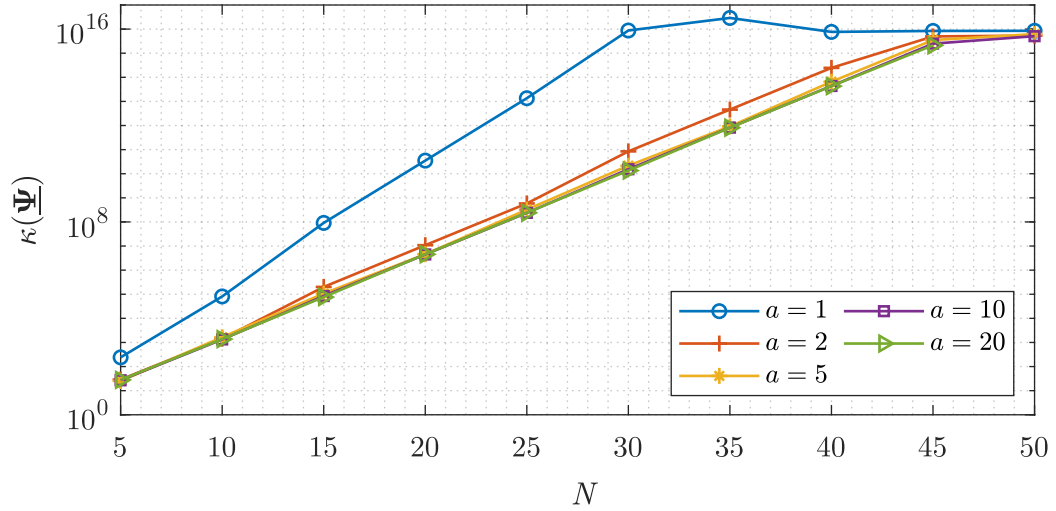


Figure 3.4: Relation between the condition number κ and the oversampling factor a

In this work, only equidistant sampling in χ , ϕ , and θ has been considered. Existence of an alternative sampling scheme capable of forming a well-conditioned linear system of equations therefore cannot be disproved with absolute certainty. However, no written work suggesting that such a scheme exists has been found. Based on the findings presented in [51] for various sampling schemes with samples obtained over the full sphere, there is no indication that an alternative sampling scheme could give a sufficient number of independent samples and, with it, assure full-rankness in the general case and bring the reduction of the condition number required for a well-conditioned system of equations.

The question at hand thus becomes whether or not, and to what extent, matrix methods can be used to solve the transmission formula if only a truncated field pattern is available. Since the coefficient matrices are, in general, rank deficient, an infinite number of solutions to the problem exists. Singular value decomposition (SVD) can be used to obtain the minimum norm solution to this problem by computing the Moore-Penrose pseudoinverse. By default, SVs smaller than the numerical precision tolerance⁷ are excluded from the computation of the pseudoinverse in Matlab [44]. When an ideal, noise-free radiation pattern is known, a (possible) set of SWCs can be computed from either (3.4) or (3.7), capable of describing the field pattern in the measured points over the truncated range with high accuracy even for systems of equations with a large condition number κ . However, when computing SWCs from noisy data, this can cause the method to return an unrealistic set of SWCs which cannot be used neither for estimating a far-field pattern nor for further use with the pattern stitching algorithm presented in this chapter. To illustrate the problem, a random set of SWCs with $N = 20$ was used to compute a radiation pattern at a distance $A = N/k$ with the minimum number of samples required to assure full-rankness when truncated at $\theta_{\text{trunc}} = 135^\circ$ (example (c) in Figure 3.3). SWCs were computed using the LS method, first from a noiseless truncated pattern, then Gaussian white noise with 100 dB signal-to-noise ratio (SNR) was added to the initial pattern and SWCs were computed again. The results can be seen in Figure 3.5, where the magnitudes

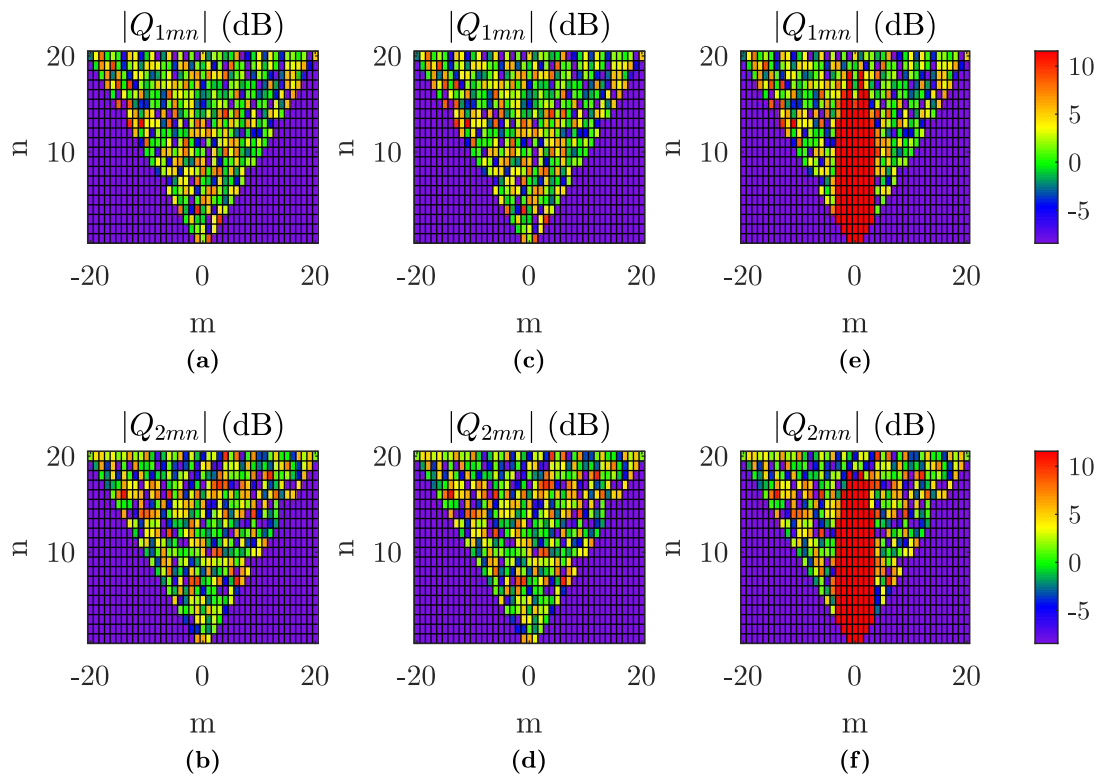


Figure 3.5: Influence of noise on the LS solution: (a) and (b) original SWCs, (c) and (d) SWCs obtained from a noiseless pattern, and (e) and (f) SWCs obtained from a noisy pattern with SNR = 100 dB

⁷See footnote 3.

of original spherical wave coefficients, $|Q_{smn}|$, divided into two two-dimensional plots for $s = 1$ and $s = 2$, respectively, are shown on the left. Plots of the noiseless solution, limited only by numerical precision, are shown in the middle, while the two plots on the right represent the solution when noisy data are used. Sensitivity of the least squares method to noise results in an overestimation of many SWCs. This issue is far more severe than Figure 3.5 might reveal at first sight, since all SWCs larger than the largest SWC in the original set of coefficients have been colored with the same red color. In fact, they are much larger than the original SWCs, which can be shown by evaluating the total power of the system per (2.22). The total power of the original SWCs and the total power of those obtained from a noiseless truncated pattern (at $N = 20$ this system has full rank as shown in Figure 3.3) is approximately equal, $P \approx 866.4$ W. The total power of SWCs obtained from noisy data is more than 10 000 000 times larger than that, $P_{\text{noisy}} \approx 10^{10}$ W. While this solution best describes the field pattern in the provided sampling points in the LS sense, it yields extremely large, physically infeasible field strengths in the truncated range ($\theta > \theta_{\text{trunc}}$) and fails entirely when operations such as translation or rotation are applied. Similar behavior was observed in all tests, where radiation patterns of random sets of SWCs with varying order N were used. In any realistic measurement setup, measurement data will be distorted by measurement noise. As demonstrated in Figure 3.5, this results in failure of the LS method even for a very high signal-to-noise ratio (SNR). The method thus cannot be used with noisy data without modifications, which will be discussed in the following paragraph.

The pseudoinverse $\underline{\Xi}$ of the coefficient matrix $\underline{\Psi}$ can be expressed by the three matrices obtained by SVD as $\underline{\Xi} = \underline{\mathbf{V}}\underline{\Sigma}^{-1}\underline{\mathbf{U}}^*$. This product can be expressed as a summation over SVs,

$$\underline{\Xi} = \sum_{j=1}^J \mathbf{v}_j \sigma_j^{-1} \mathbf{u}_j^*, \quad (3.9)$$

where \mathbf{v}_j and \mathbf{u}_j are vectors extracted from the matrices $\underline{\mathbf{V}}$ and $\underline{\mathbf{U}}$, corresponding to the singular value σ_j from the diagonal matrix $\underline{\Sigma}$. Taking limited numerical precision into account, the numerical rank \hat{r} can be determined and SVs smaller than some tolerance $\delta > 0$ are discarded from the computation of $\underline{\Xi}$, giving an approximation

$$\underline{\Xi} \approx \sum_{j=1}^{\hat{r}} \mathbf{v}_j \sigma_j^{-1} \mathbf{u}_j^*, \quad \hat{r} \leq J. \quad (3.10)$$

As mentioned earlier, this tolerance is related to the numerical precision of the used PC and software when noise-free data are available. When dealing with noisy coefficient matrix data, the following example for adapting the tolerance δ is given in [48]. If entries in $\underline{\Psi}$ are correct to two digits, the authors suggest using the tolerance $\delta = 10^{-2} \|\underline{\Psi}\|_{\infty}$ as the criterium for discarding small SVs, where $\|\underline{\Psi}\|_{\infty}$ is the infinity norm of the coefficient matrix $\underline{\Psi}$. It is unclear why the authors in [48] use the maximum norm in their example, presumably because of its ease of computation in comparison to the Euclidean norm. However, using the Euclidean norm is by far more intuitive, since the resulting value directly corresponds to the maximum SV of the coefficient matrix, $\underline{\Psi}$, and limits the minimum SV with regard to σ_{max} . The Euclidean norm is also the norm used in the

default tolerance computation in Matlab's `pinv` function [44]. In our specific case, the coefficient matrix $\underline{\Psi}$ is considered noise-free and thus limited solely by numerical precision. Nevertheless, this does not hold true for measured data points, which are contained in the observation vector \mathbf{w} . Following the assumption that increasing the tolerance factor δ can be used analogously when noisy measurement data are available, δ is defined as

$$\delta = 10^{-\frac{\text{SNR}}{20}} \cdot \|\underline{\Psi}\|_2 = 10^{-\frac{\text{SNR}}{20}} \cdot \sigma_{\max}(\underline{\Psi}), \quad (3.11)$$

which requires the knowledge of measurement SNR for its computation. Instead of using the maximum norm, as suggested in [48], Euclidean norm was used in (3.11).⁸ The noisy radiation pattern with SNR = 100 dB, the SWCs of which were shown in Figure 3.5, have now been processed with the LS method again, using the tolerance factor δ obtained by (3.11). To demonstrate the improvement of the LS method when small singular values are truncated, a comparison of computed SWCs between the actual coefficients on the left, the nonoptimized SV solution in the middle, and the solution obtained using the modified tolerance factor δ according to (3.11) is shown in Figure 3.6. It can be seen that the overestimated coefficients in Figures 3.6c and 3.6d are dealt with by truncating small SVs. Of course, some difference between the original SWCs and the

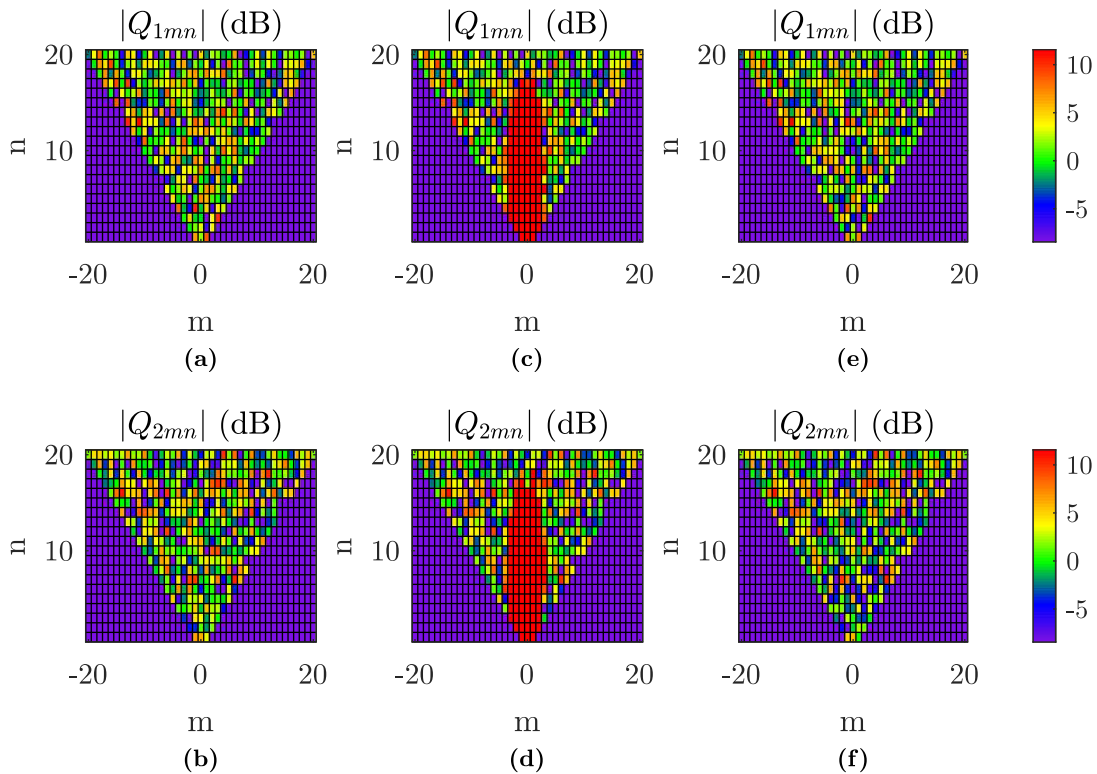


Figure 3.6: Influence of SV truncation on the LS solution: (a) and (b) original SWCs, (c) and (d) SWCs obtained from a noisy pattern (SNR = 100 dB) without SV truncation, and (e) and (f) SWCs obtained from a noisy pattern with SV truncation

⁸A series of evaluations of the SMSE was done using both norms to determine the tolerance factor δ . These tests have confirmed the advantage of using the Euclidean norm over using the maximum norm.

SWCs obtained from the LS method with modified tolerance factor is expected since noisy (and truncated) data have been used for its computation. The total power contained in these coefficients is $P_\delta \approx 830.2 \text{ W}$, showing a decrease of approximately 4% compared to the original SWCs, $P \approx 866.4 \text{ W}$. The field patterns corresponding to these sets of spherical wave coefficients are shown in Figure 3.7. Both polarizations of the original noiseless radiation pattern are depicted in Figures 3.7a and 3.7b, followed in Figures 3.7c and 3.7d by the pattern obtained from the non-SV-truncated solution of the LS method, and finally, in Figures 3.7e and 3.7f, pattern obtained by the LS method when SVs smaller than the tolerance factor δ are discarded from the computation.

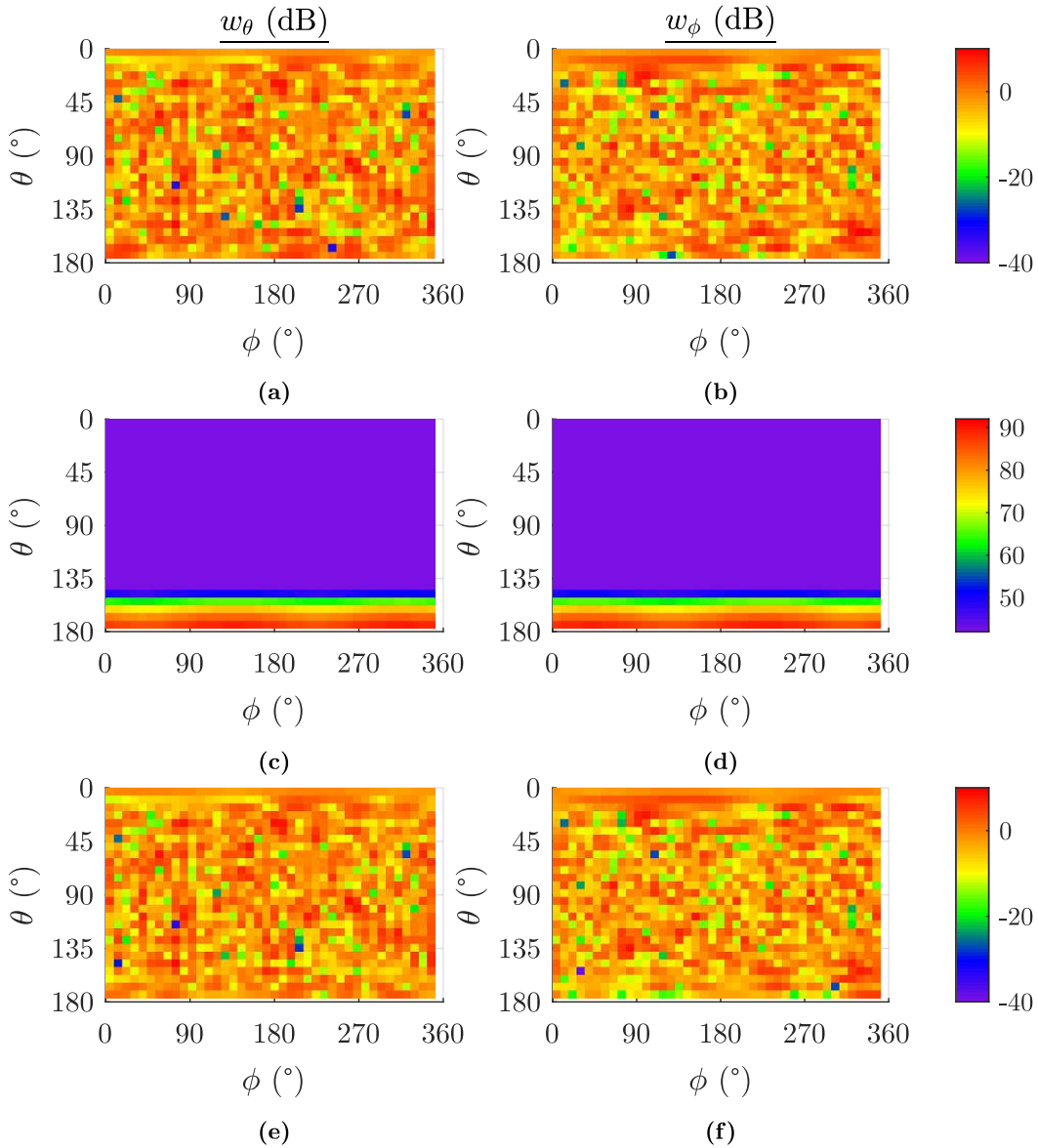


Figure 3.7: Influence of SV truncation on radiation patterns: (a) and (b) original pattern, (c) and (d) pattern from SWCs computed without SV truncation, (e) and (f) pattern obtained from SWCs computed with SV truncation

The results clearly demonstrate the extreme increase of field strengths for θ -angles larger than the truncation angle θ_{trunc} when small SVs are not truncated. When SVs smaller than δ are truncated, these overestimated fields are suppressed while the field pattern up to θ_{trunc} still bears a close resemblance to the original pattern. A quantification of how well the patterns match will follow in the next section, where results of an SMSE analysis will be given.

3.2.5 Comparison

All three presented methods for computing SWCs from truncated patterns have been implemented in Matlab [44] and tested extensively. Three parameters were used for evaluating their performance: their respective computation time, the error in calculated near field (NF) patterns, determined by computing the NF SMSE, and the error in calculated far field (FF) patterns, computed via FF SMSE. It should be noted that the computation time was defined as the time needed to both compute the SWCs and expand them into a field pattern at the desired distance, which was done by the same procedure as in SN2FFT, using the three IDFTs listed in (2.88), (2.89), and (2.90). Results of all methods have been compared to each other, as well as to the FT-based SN2FFT, where missing data points were assigned to be zero, which represents results without truncation error correction. Results of this comparison have partially been reported already in [52].

Radiation Patterns for Testing

For testing purposes, three types of test objects were used to obtain radiation patterns: sets of random SWCs, EM simulation models, and a real measured antenna. Detailed information on all test patterns is given in the following list:

- Synthetic radiation patterns, computed from sets of random SWCs with different maximum polar orders N , ranging from 5 to 200, at $f = 2.4$ GHz. In an attempt to make a fair comparison, the measurement distance was varied along with N to match the theoretical minimum measurement distance, $A = N/k$, which equals the MRE. Patterns were truncated at $\theta_{\text{trunc}} = 135^\circ$ and sampled equidistantly. In ϕ , the smallest number of samples required by SN2FFT was used, $K_\phi = 2N + 1$, while an increased number of samples, discussed in Section 3.2.4, was used in θ , such that $K_{\theta_{\text{trunc}}} = N + 1$. The patterns were first processed with all three methods to compute SWCs and their respective near- and far-field patterns. Then, white Gaussian noise with an SNR of 100 dB was added to the patterns and all three methods were retested with noisy truncated data.
- Simulated radiation patterns of two antennas, a planar inverted-F antenna (PIFA) and a bowtie antenna, designed for operation at $f = 2.4$ GHz, obtained by electromagnetic (EM) simulations in HFSS [53]. Simulation models of both antennas can be seen in Figures 3.8 and 3.9. Evaluating electric fields at the minimum distance, i.e., MRE, as in the case of random SWC patterns, was not possible due to simulation constraints. Specifically, the field evaluation sphere overlapped with the simulation domain boundaries in that case, resulting in errors in the evaluated fields. Therefore, the patterns were computed at a measurement distance of $A = 1.31$ m

instead, which corresponds to the measurement distance at the near-field range at TU (already in far field as per Figure 1.1), and in normalized far field, as defined by HFSS. The maximum polar order N was determined by (2.24) with $n_1 = 10$ based on their MRE, which gave $N = 14$ for PIFA and $N = 12$ for the bowtie antenna. Simulated patterns were stored with equidistant sampling steps of 2° , out of which the minimum number of steps required to fulfill the conditions $K_\phi \geq 2N + 1$ and $K_{\theta_{\text{trunc}}} \geq N + 1$ were extracted for testing. Just as the random SWCs patterns, they were truncated at $\theta_{\text{trunc}} = 135^\circ$.

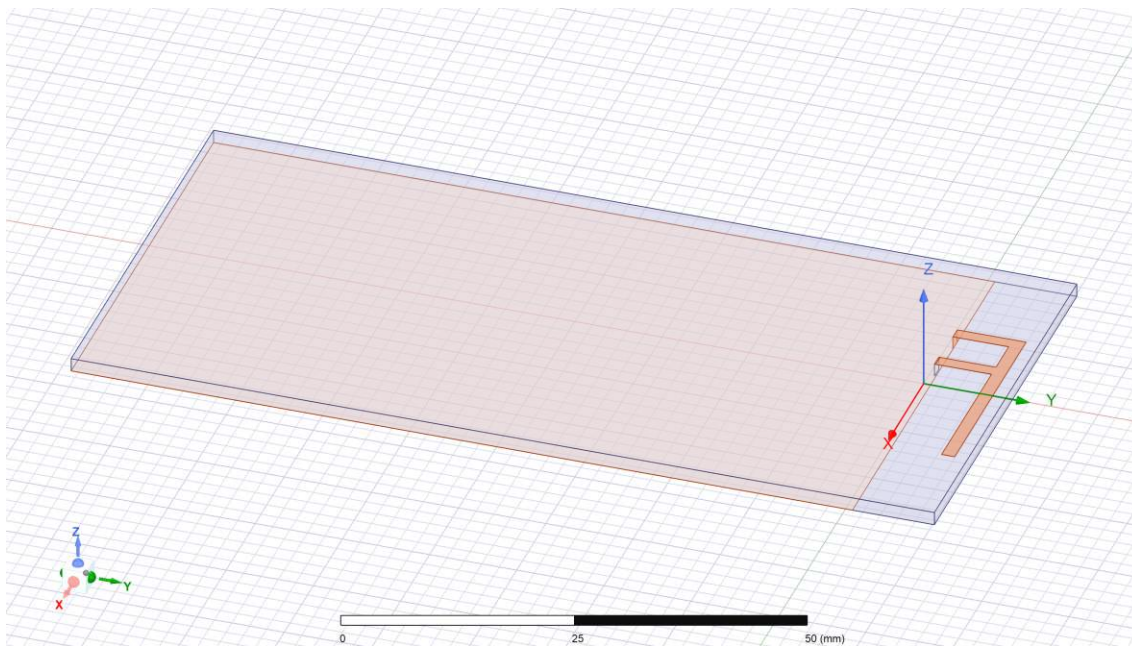


Figure 3.8: PIFA model

- Measured radiation pattern of an ultra-wideband (UWB) conical monopole (CMP) antenna manufactured according to [54], with a simplified ground plane. The antenna is shown in Figure 3.10. It was measured in a single measurement in the near-field range at TU Wien, spanning the range from 4 GHz to 16 GHz in 250 MHz steps (frequencies below 4 GHz would require a different probe antenna). Due to the large frequency range, the maximum polar order N varied from 16 to 35 and sampling was chosen based on the largest among them, which, including some over-sampling to assure the sampling step to be a rational number, resulted in a sampling step of 4° in both θ and ϕ . Using additional absorbers at the ϕ -axis rotary stage, the maximum θ -angle that could be measured was $\theta_{\text{trunc}} = 140^\circ$.

Comparison Results

The first series of tests was carried out on radiation patterns obtained from random sets of SWCs. For comparison purposes, the iterative approach was limited by the maximum number of iterations, which was set to 500. For noise-free radiation patterns of random SWCs, the computation time, the NF SMSE, and the FF SMSE are shown in Figures 3.11

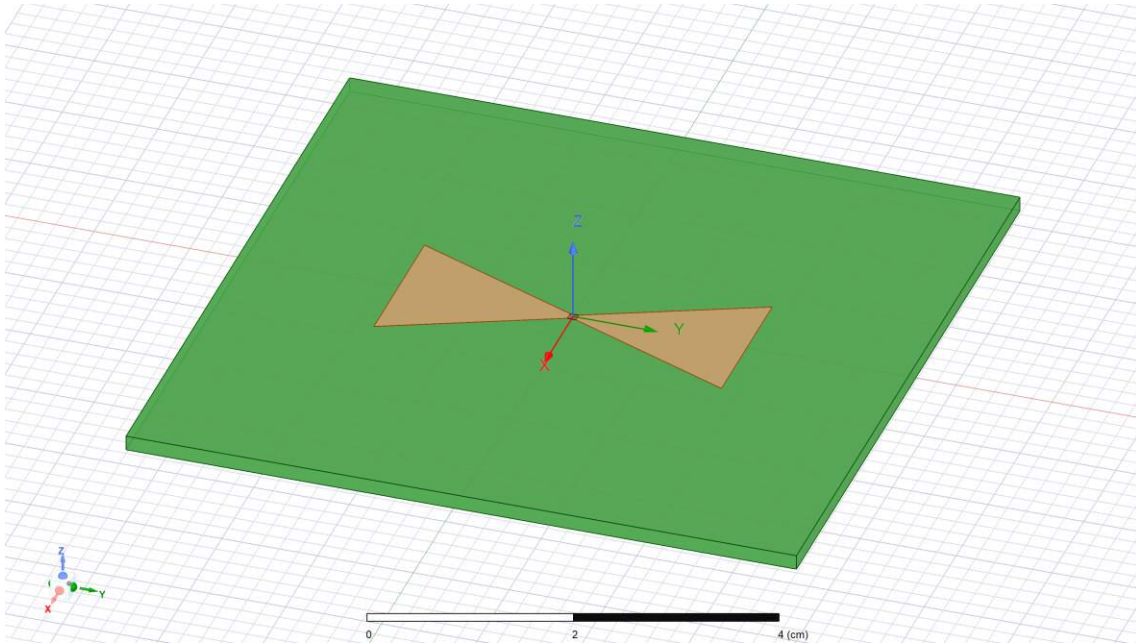


Figure 3.9: Bowtie antenna model



Figure 3.10: Measured UWB CMP antenna

to 3.14. The least squares (LS) method could only be used up to $N = 80$ due to memory limits of the PC, which, as stated earlier, had 32 GB RAM available. Observing the computation times in Figure 3.11, it can be seen that the computation time of the LS method increases rapidly with increasing order N and already exceeds the computation time of the iterative algorithm at $N = 80$. The computation time of the iterative algorithm rises proportionally to the computation time of SN2FFT and can be estimated by $t_{\text{iterative}} \approx N_{\text{iterations}} \cdot t_{\text{SN2FFT}} = 500 \cdot t_{\text{SN2FFT}}$. As can be seen, compared to SN2FFT, the FFT/Matrix method demonstrates the best performance in terms of computation time.

This was expected since the method makes use of the fast Fourier transform to break down the coefficient matrix $\underline{\Psi}$ of the LS method into smaller submatrices, while still allowing for a single-step solution in contrast to the iterative algorithm. At $N = 200$, the FFT/Matrix method needed approximately 1.6 min to compute the spherical wave coefficients (SWCs) and the corresponding pattern, while the computation time of the SN2FFT was approximately 0.9 min.

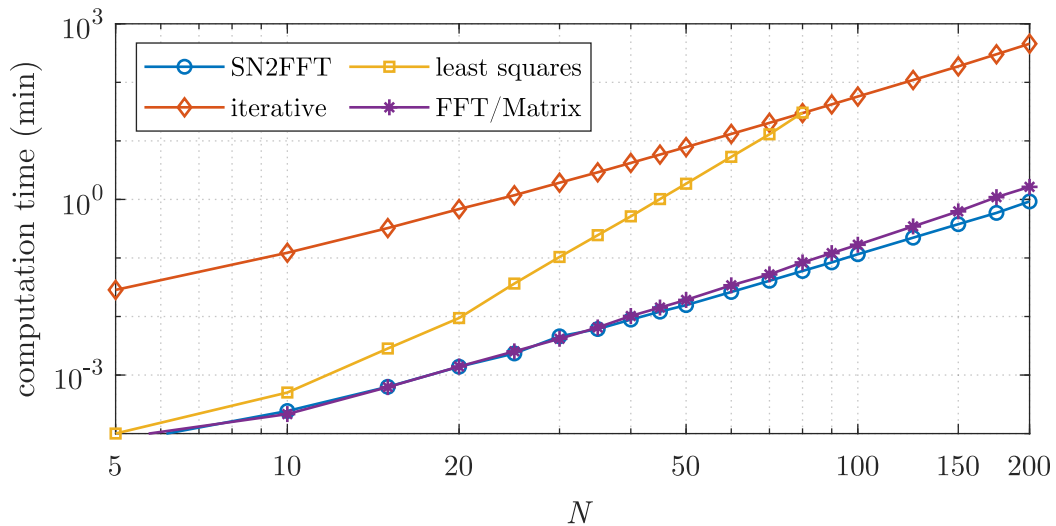


Figure 3.11: Algorithm comparison: computation time (noise-free, random SWCs)

The results in Figure 3.12 show how well the truncated near-field patterns are matched by the same-distance patterns computed from SWCs obtained by each of the methods. It can be seen that, after 500 iterations, the iterative algorithm achieves an improvement of about 30 dB compared to SN2FFT. The error is reduced even further when using

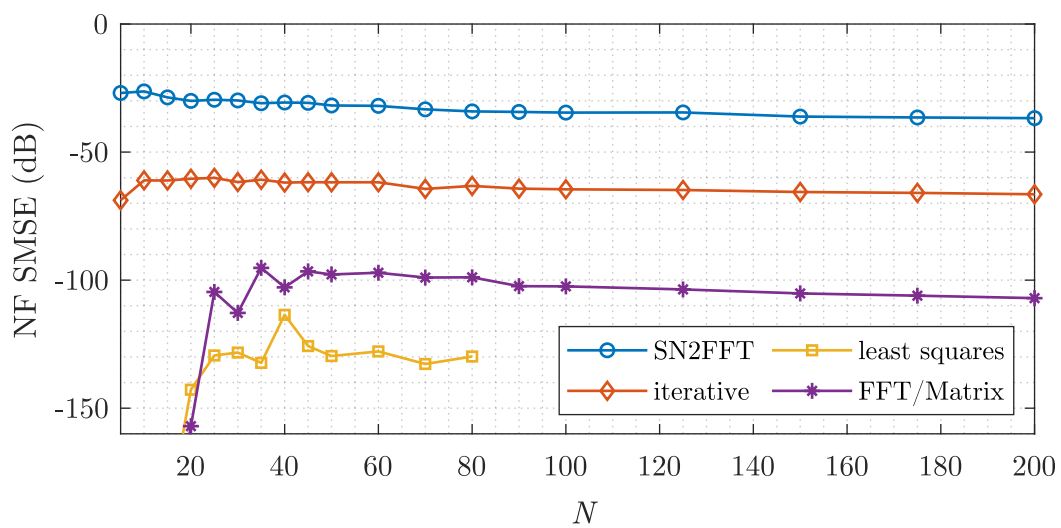


Figure 3.12: Algorithm comparison: NF SMSE (noise-free, random SWCs)

matrix methods, with the least squares method showing an NF SMSE below -110 dB over the whole range and the FFT/Matrix method showing a maximum NF SMSE just above -100 dB. Also here, the fact that the LS-based methods outperform the iterative algorithm does not come as a surprise since they represent the least squares fit and SMSE evaluates the error in terms of weighted squared differences. Furthermore, the LS method outperforms the FFT/Matrix method since it represents the pure LS fit. Nevertheless, due to computational limits of the LS method, the FFT/Matrix method can be identified as the best method in terms of NF SMSE.

In Figure 3.13, the FF SMSE was evaluated over the whole range of θ -angles up to θ_{trunc} . All three methods result in an SMSE reduction compared to SN2FFT, with both matrix methods outperforming the iterative algorithm, just as was observed already in the NF SMSE case. This confirms that the LS solutions provide reliable sets of SWCs which, even after transformation to far field, give more accurate results than the iterative algorithm. Even though a general improvement in comparison to SN2FFT can be observed, the overall FF SMSE values are substantially larger than those of the same-distance NF SMSE and cannot be considered an accurate representation of the corresponding far field radiation pattern. Since truncation effects are generally most severe near the angle of truncation,

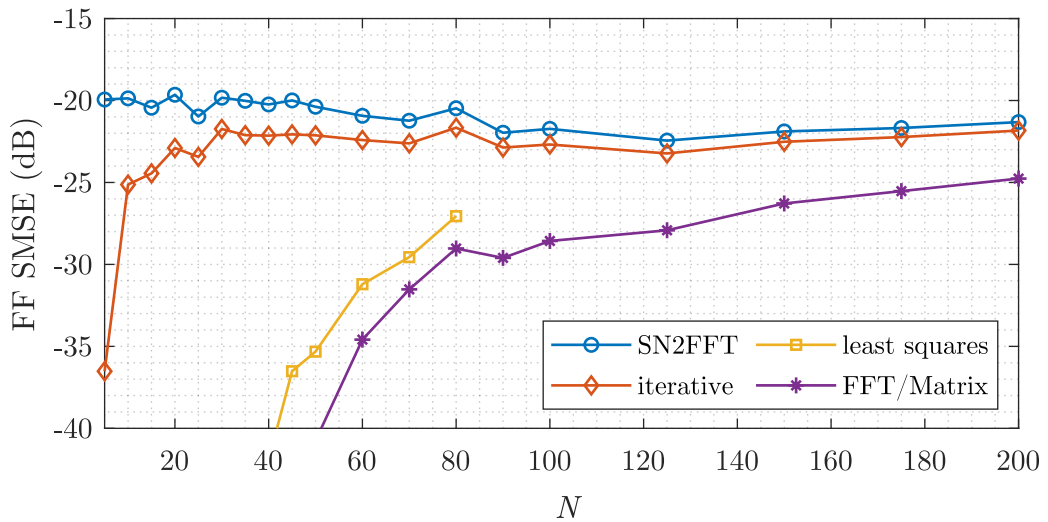


Figure 3.13: Algorithm comparison: FF SMSE up to θ_{trunc} (noise-free, random SWCs)

evaluating the FF SMSE over the entire range yields very pessimistic results. To gain a better insight into the distribution of SMSE, the FF SMSE was evaluated for a reduced range of θ -angles as well. This reduced range was defined up to $\theta_{\text{valid}} = \theta_{\text{trunc}} - \arcsin(r_0/A)$ [19], where r_0 represents the MRE of the AUT and A the distance for which the radiation patterns were computed. As stated earlier, the patterns were evaluated at the minimum possible distance, $A = r_0$. For a truncation angle $\theta_{\text{trunc}} = 135^\circ$, this gives the maximum valid angle $\theta_{\text{valid}} = 45^\circ$. From the results in Figure 3.14, it can be seen that, for all methods, the error in this range is substantially smaller than that of the full range up to θ_{trunc} . A large jump in error between $N = 100$ and $N = 125$ is observed for the FFT/Matrix method. Comparing the results to those of the full range up to θ_{trunc} , it can be seen that this error increase must stem from a change in error distribution with regard to the θ -angle. Indeed, by investigating the computed truncated patterns, this could be

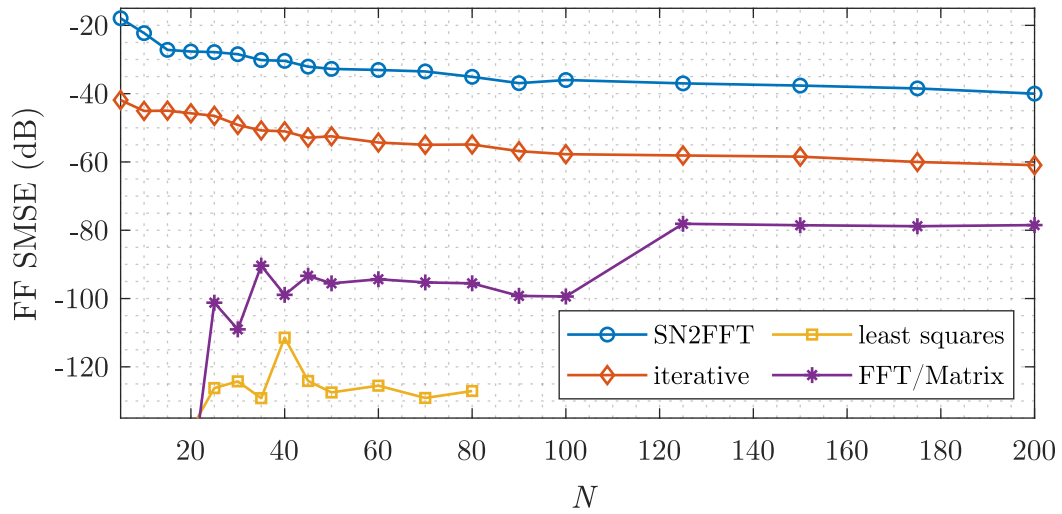


Figure 3.14: Algorithm comparison: FF SMSE up to θ_{valid} (noise-free, random SWCs)

confirmed and a larger error was observed for θ -angles near $\theta = 0^\circ$. The reason for this behavior could not be identified based on the results of these tests. Since this work focuses on pattern stitching in the near field, where such behavior was not observed, an in-depth analysis was not included at this stage.

Next, these tests were repeated for the case of noisy radiation patterns with an SNR of 100 dB. For the two matrix methods using SVD, SV truncation was done according to (3.11). Since adding noise to radiation patterns does not influence the computation time of the algorithms, similar computation times as in Figure 3.11 were observed. It does, however, influence the SMSE results. Compared to Figure 3.12, the NF SMSE results of SN2FFT and the iterative algorithm in Figure 3.15 show no change in error.

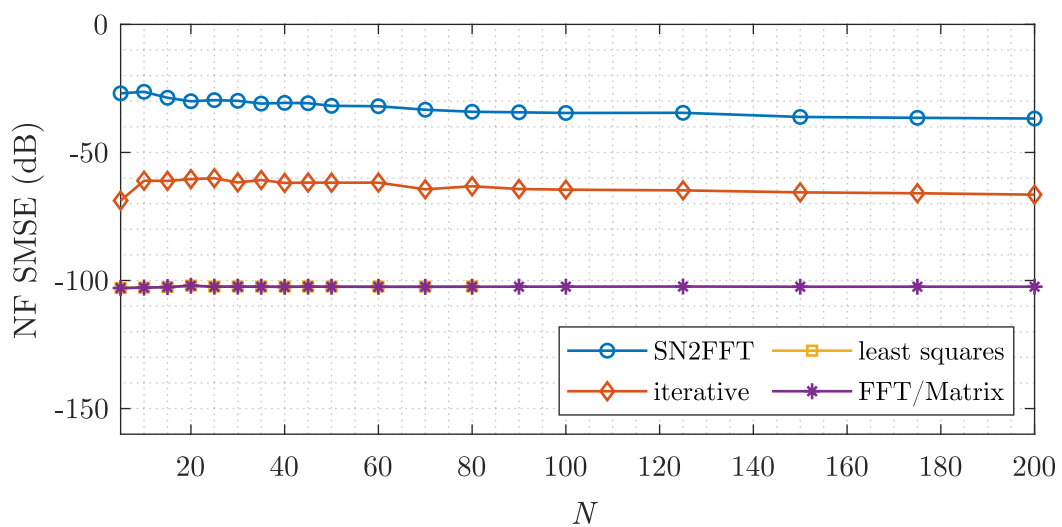


Figure 3.15: Algorithm comparison: NF SMSE (100 dB SNR, random SWCs)

This indicates that truncation error dominates the overall error and the influence of high-SNR noise is negligible. The two matrix methods, on the other hand, show identical NF SMSE values just below 100 dB and are clearly limited by noise. The FF SMSE results for noisy patterns in the two considered ranges are shown in Figures 3.16 and 3.17.

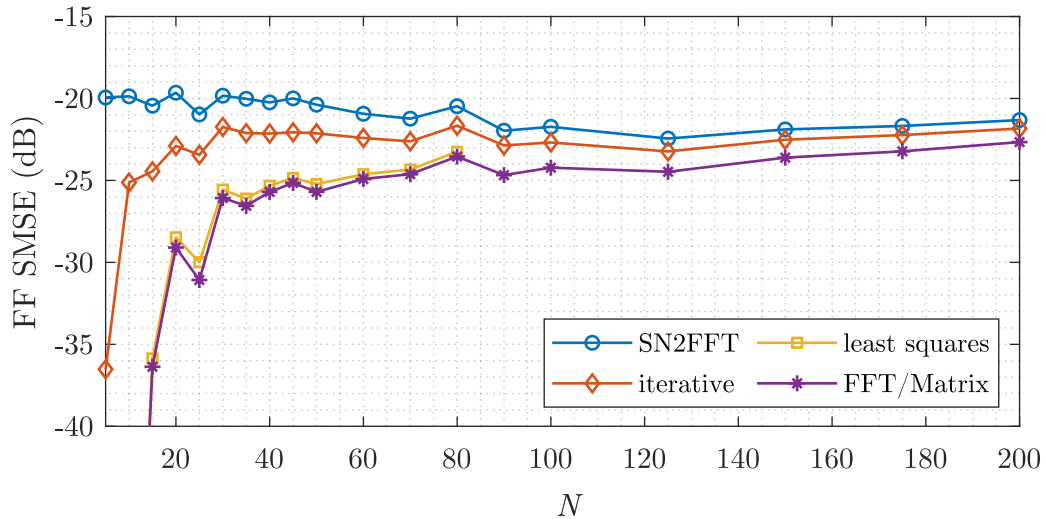


Figure 3.16: Algorithm comparison: FF SMSE up to θ_{trunc} (100 dB SNR, random SWCs)

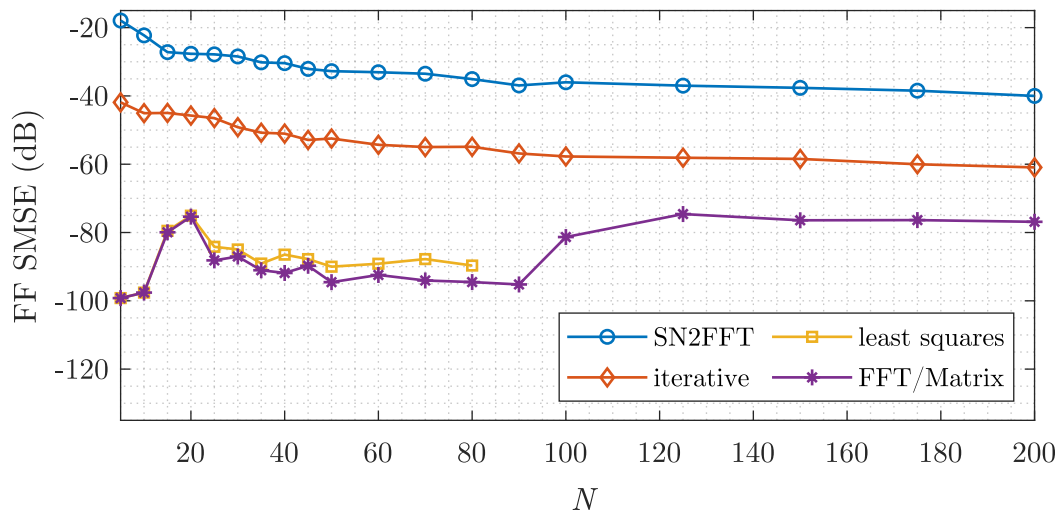


Figure 3.17: Algorithm comparison: FF SMSE up to θ_{valid} (100 dB SNR, random SWCs)

Comparing these results to the noise-free case in Figures 3.13 and 3.14, it can be seen that, just as in the case of NF SMSE, the FF SMSE values for the two FT-based algorithms remain unchanged and noise plays a negligible role in their overall error. This does not hold true for the LS method and the FFT/Matrix method, where the overall error has become larger. One can see that SV truncation causes the two matrix methods to yield results that are more consistent with each other compared to the case where noiseless

data with standard, numerical-precision-based SV truncation are used. Even with the increase in error compared to the noiseless case, the FFT/Matrix method delivers the lowest SMSE values in both ranges and shows an error reduction of more than 30 dB compared to SN2FFT in the range up to θ_{valid} .

After comparing results obtained from theoretical data sets, where the field distributions were completely random, the methods had to be tested on test objects with somewhat more realistic radiation patterns. Results of EM simulations were used for this purpose. Since every EM simulation tool introduces some error to the resulting patterns—caused by discrete meshing as well as numerical precision—an estimate of added noise was needed for the two matrix methods. This was computed by using a same-distance SN2FFT and evaluating the SMSE between the original data, obtained by HFSS [53], and the radiation pattern obtained by the transformation. The resulting value, which was around 80 dB in both examples, was then used as the SNR estimate for computing the tolerance factor δ . In Table 3.2, the computation time, NF SMSE, and FF SMSE values for the two EM simulation antenna patterns are listed. The results demonstrate a large advantage of all

Table 3.2: Algorithm comparison: EM simulation patterns

algorithm	PIFA			bowtie		
	<i>time</i>	<i>NF SMSE</i>	<i>FF SMSE</i>	<i>time</i>	<i>NF SMSE</i>	<i>FF SMSE</i>
SN2FFT	0.03 s	−31.27 dB	−27.50 dB	0.02 s	−30.15 dB	−27.44 dB
iterative	15.79 s	−70.25 dB	−49.06 dB	10.04 s	−78.81 dB	−52.55 dB
LS	0.18 s	−84.93 dB	−57.92 dB	0.10 s	−83.83 dB	−55.75 dB
FFT/Matrix	0.03 s	−85.01 dB	−59.89 dB	0.02 s	−83.84 dB	−55.54 dB

three methods compared to SN2FFT, with the two matrix methods outperforming the iterative method both in terms of computation time and resulting field pattern errors. The FF SMSE in this case was evaluated for the whole range up to θ_{trunc} .

Finally, the methods had to be tested with actual measurement data as well. As mentioned earlier, the ultra-wideband (UWB) conical monopole (CMP) antenna was measured over a wide frequency range from 4 GHz to 16 GHz. The measurement software of the near-field range, NSI2000 [55], provides an estimate for measured SNR values which can readily be used for determining the tolerance factor δ (3.11). Alternatively, the signal-to-noise ratio can be estimated by first using the matrix method without SV truncation and evaluating the NF SMSE compared to measurement data. This value indicates the theoretical lower bound of how well the measured radiation pattern can be described by a spherical wave expansion and can be used as an SNR estimate. It should be noted that this overall estimate includes not only random errors but also unwanted reflections and other measurement inaccuracies. For the used measured pattern, noise values over the whole frequency range were between −40 dB and −45 dB and an SNR of 45 dB was set for further processing. In Figure 3.18, the computation time over the frequency range is shown for SN2FFT and the three presented methods. Similar to previous examples, one can see that the FFT/Matrix method closely follows the computation time of the FT-based SN2FFT regardless of the frequency, while the computation times of the iterative method and the LS method are longer by a factor of 100 or more.

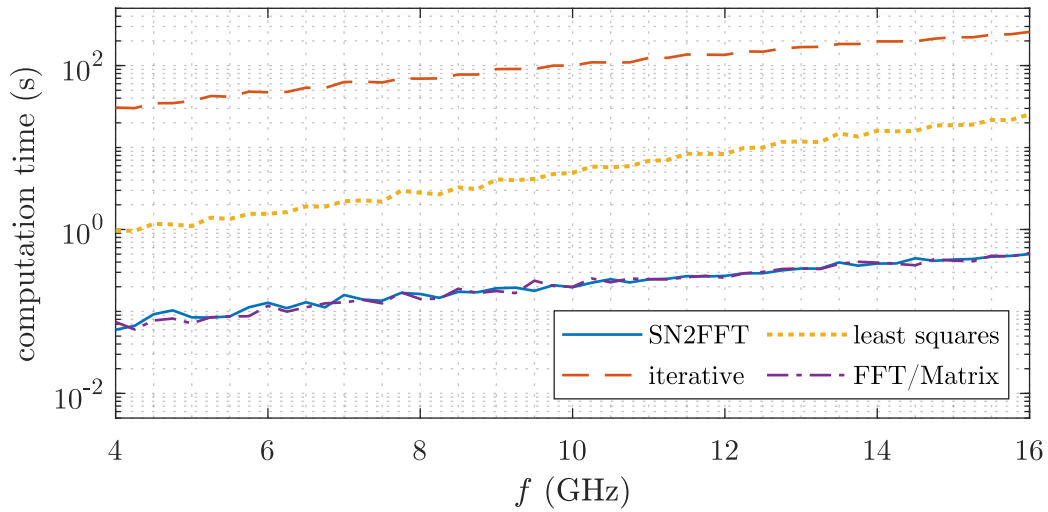


Figure 3.18: Algorithm comparison: computation time over frequency (UWB CMP)

Shown in Figure 3.19 are the same-distance NF SMSE values. An advantage of methods for reducing truncation error over the classical SN2FFT can be seen, however, this improvement is small due to measurement errors in the measured pattern. Moreover, a ripple in error over frequency can be observed from the figure, as well as a clear decrease of the SMSE with increasing frequency. It should be noted that this behavior has no theoretical background in the computation of truncated SWCs and presumably stems from measurement errors. At this stage, no further attention was given to observed errors. An analysis of sources of errors and the potential for their minimization will follow later in Chapter 5.

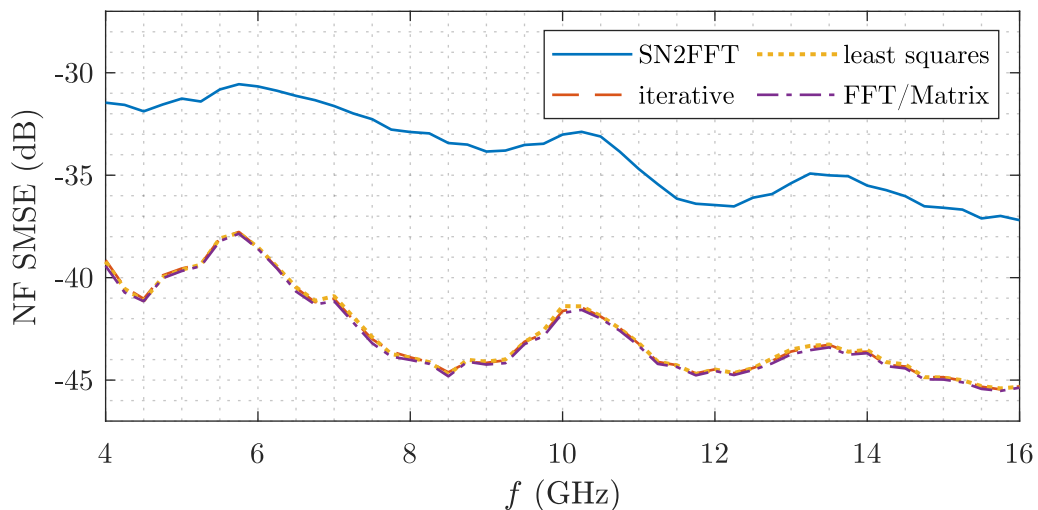


Figure 3.19: Algorithm comparison: NF SMSE over frequency (UWB CMP)

Marginal differences between the three methods were observed, which can best be seen by the maximum, minimum, and mean NF SMSE values over all frequencies, listed in

Table 3.3. Overall, the mixed FFT/Matrix method exhibits superior performance even with practical measurement results, offering computation times comparable to those of SN2FFT and an error reduction of approximately 6 dB.

Table 3.3: Algorithm comparison: UWB CMP antenna

algorithm	NF SMSE		
	<i>max</i>	<i>min</i>	<i>mean</i>
SN2FFT	−30.56 dB	−37.19 dB	−33.87 dB
iterative	−37.77 dB	−45.45 dB	−42.73 dB
LS	−37.82 dB	−45.40 dB	−42.71 dB
FFT/Matrix	−37.86 dB	−45.53 dB	−42.85 dB

This comparison has shown that all three truncation error reduction methods offer a significant error reduction compared to the commonly used zero-padded SN2FFT. In terms of computation time, the FFT/Matrix method is the fastest among them, with computation time increasing by less than a factor of 2 even for very high polar orders N . Consequently, this method was identified as the most effective of the three presented methods and is utilized in subsequent steps of the pattern stitching method proposed in this work.

3.3 Measurement Alignment

Looking back at the pattern stitching procedure shown in Figure 3.2, one of the key steps of the procedure is the alignment of coordinate systems of both partial measurements. Only once this is done can the truncated patterns be stitched together to describe the whole sphere. In the previous section, the best algorithm for computing truncated spherical wave coefficients (SWCs) was identified, which can accurately describe the AUT's field pattern in the truncated range covered by the measurement. Using this algorithm on truncated field patterns obtained by measuring the AUT in two different orientations, a distinct set of truncated SWCs can be obtained for each measurement. In order to align them, the goal was to implement an error minimization procedure which searches for the optimum misalignment in a defined range of misalignments, resulting in the smallest mismatch in the overlapping region between both measurements. To do so, rotation and translation operations presented in Section 2.2 must be used on these truncated SWCs.

3.3.1 Rotation and Translation of Truncated SWCs

While translation and rotation operations have been well-defined for spherical waves and their corresponding SWCs, no published research has been found on how accurately a set of truncated SWCs, capable of describing an arbitrary antenna in its truncated range, can represent that same antenna in some translated and rotated coordinate system. We have done a series of tests to determine whether such truncated SWCs can arbitrarily be rotated and translated accurately using the operations in (2.32) and (2.41) and the results

were presented in [56].⁹ These tests have been conducted using the iterative algorithm for obtaining patterns from truncated SWCs. In accordance with findings presented in the previous section, which showed that the FFT/Matrix method outperforms the iterative algorithm, the analysis had to be repeated for the case where truncated SWCs are computed using the FFT/Matrix method.

Test Objects

For comparability, the same test objects as in [56] have also been used for testing the FFT/Matrix method. Four synthetic test objects were generated using different combinations of SWCs. From their respective set of SWCs, radiation patterns for a frequency of 2.4 GHz were then computed using the SN2FFT algorithm at a distance of 1.31 m, matching the measurement distance of the NF test range at TU Wien. For the first test object, SWCs representing an x-oriented dipole were used. For remaining objects, matrices of random SWCs with maximum polar orders $N_{\text{set}} \in \{4, 19, 34\}$ were generated, where coefficients were weighted by $1/n$ to imitate the decay of SWCs with increasing order n , as is common for realistic antennas. The orders N_{set} represent the product of MRE and the wavenumber k . In [56], following the typically used empirical formula for maximum polar order, $N = \lfloor k \cdot \text{MRE} \rfloor + 10$ (2.24), the matrices were assigned to be of the order $N_{\text{set}} + 10$ with other SWCs set to 0. In this work, the extension of the order N by 10 with zero-valued spherical wave coefficients was omitted because it is redundant when the actual order is known. Finally, radiation patterns, computed from these sets of SWCs using SN2FFT, were truncated at $\theta_{\text{trunc}} = 120^\circ$.

In addition to the test objects used in [56], a test object with a random set of SWCs of the order $N_{\text{set}} = 40$ was also considered here, generated earlier for tests in Section 3.2.5. This was the highest order N which could be translated 0.5 m away from the origin of the coordinate system and still have a theoretical MRE smaller than the radius of the measurement sphere, $A = 1.31$ m, assuming that the theoretical MRE is determined by $r_0 = N_{\text{set}}/k + 0.5$ m. It should be noted that, in contrast to other used test objects with random SWCs, the coefficients were not weighted by $1/n$ in this example. As such, the example represents the absolute worst case for the given parameters. Since the FFT/Matrix method can find the exact solution for very low orders of N , as was shown in Figure 3.12, also the translation and rotation operations on such truncated SWCs will be identical to those of their full-range counterparts. For this reason, random Gaussian noise with an SNR of 80 dB was added to radiation patterns for comparability with the results in [56]. Initial SWCs and their truncated counterparts, obtained from noisy radiation patterns by the FFT/Matrix method, were then used for translation and rotation sweeps. For each sweep step, radiation patterns were computed both from the translated/rotated SWCs and translated/rotated truncated SWCs. By comparing the two, the SMSE could be evaluated for each translation/rotation step.

⁹In [56], normalized mean square error (NMSE) was used to represent $\frac{1}{N} \sum_{\chi, \theta, \phi} |x - x_{\text{est}}|^2 / \max_{\chi, \theta, \phi} |x|^2$, which is not the standard definition. To avoid using conflicting definitions, this same metric has been called scaled mean square error (SMSE) in this work, but results reported as NMSE in [56] can be directly compared to SMSE values listed here.

Effects of Translation

A sweep over translations in each of the directions, x , y , and z , was done in the range from -0.5 m to 0.5 m or, expressed in wavelengths, in the range between -4λ and 4λ . It is important to note that the maximum radial extent (MRE) of the antenna will increase with translation away from the origin of the coordinate system and care has to be taken to keep N large enough to contain all nonzero SWCs after translation. According to (2.41), the order N of translated SWCs extends to infinity and any translation theoretically results in an infinite set of coefficients. However, the coefficients tend to zero with increasing polar index n and can be truncated at a certain finite N . As mentioned earlier, the MRE of translated coefficients was determined by $r_0 = N_{\text{set}}/k + d_{\text{trans}}$, where d_{trans} is the translation distance. According to the empirical formula in (2.24), the maximum polar order N of the translated coefficients is then given by

$$N = \lceil r_0 \cdot k \rceil + n_1 = N_{\text{set}} + \lceil d_{\text{trans}} \cdot k \rceil + n_1, \quad (3.12)$$

where $n_1 = 10$ was chosen for the computation, as is common practice. During evaluation, a bug was discovered in the evaluation procedure script used in [56]. The script discarded some of the higher-order SWCs and caused an increased error and ripple effects in Fig. 1 of [56]. This bug was fixed for the reevaluation stage presented here, and the SMSE results of translation sweeps over x , y , and z are shown in Figures 3.20 to 3.22. For all three translation directions, the SMSE has been computed in two different ranges of θ -angles. Results over the whole range up to θ_{trunc} are shown in Figures 3.20a to 3.22a, where it can be seen that, for larger orders of N_{set} , SMSE increases rapidly when moving away from the origin of the coordinate system. However, it was found that this error increase is mainly contained in the region near the angle of truncation and SMSE was evaluated once more, now for a reduced θ -range up to $\theta_{\text{reduced}} = 90^\circ$. These results are shown in Figures 3.20b to 3.22b.

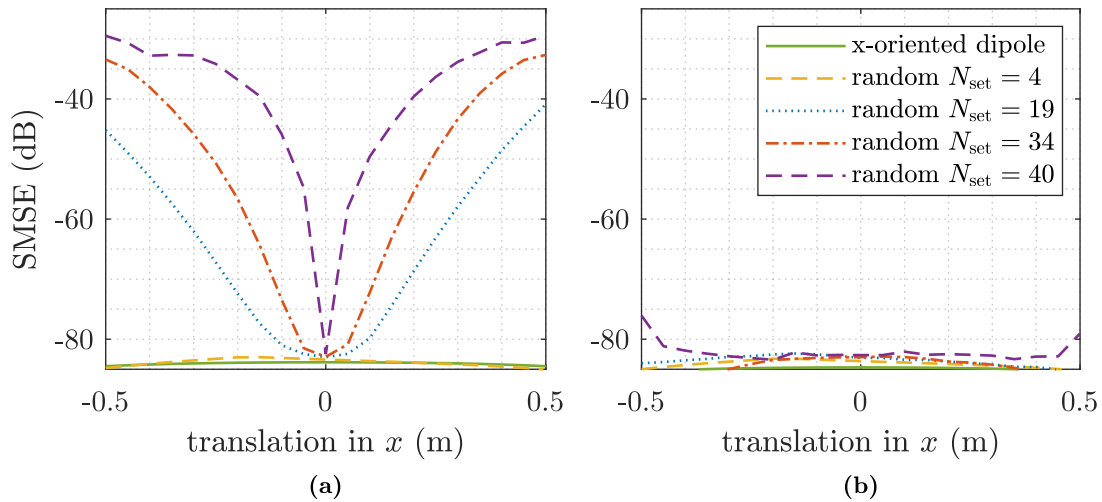


Figure 3.20: SMSE sweep over translations in x : (a) whole $\theta \leq \theta_{\text{trunc}} = 120^\circ$ range and (b) reduced $\theta \leq \theta_{\text{reduced}} = 90^\circ$ range

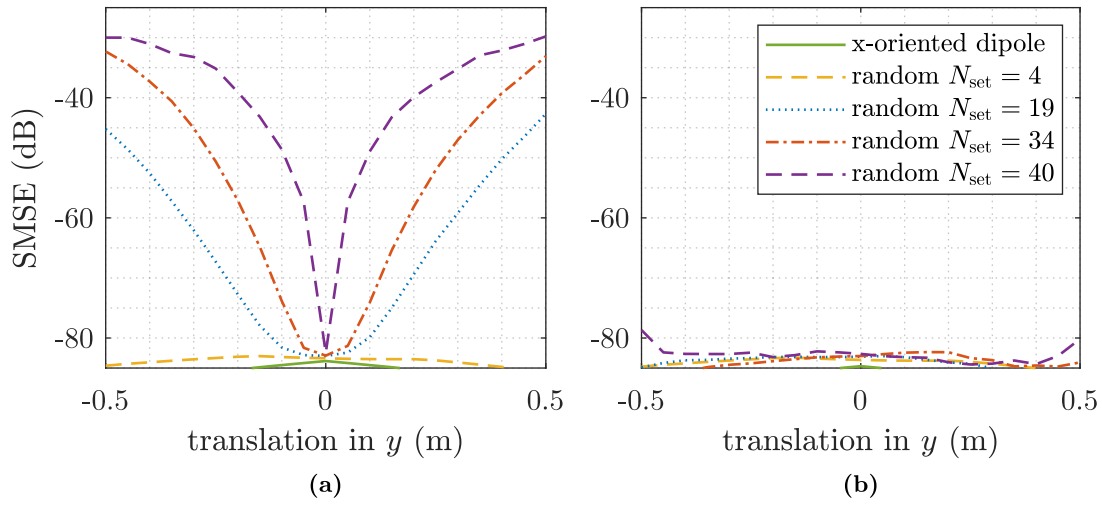


Figure 3.21: SMSE sweep over translations in y : (a) whole $\theta \leq \theta_{\text{trunc}} = 120^\circ$ range and (b) reduced $\theta \leq \theta_{\text{reduced}} = 90^\circ$ range

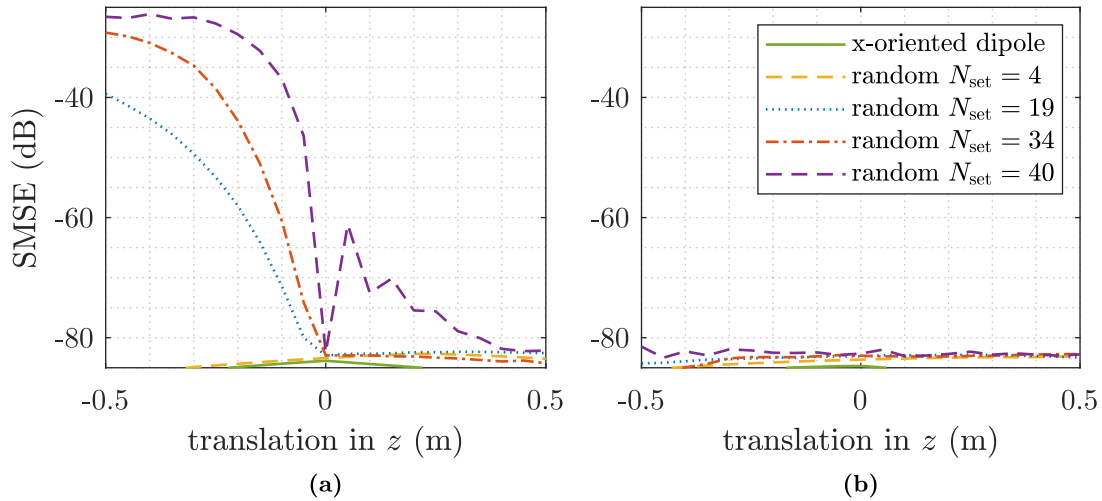


Figure 3.22: SMSE sweep over translations in z : (a) whole $\theta \leq \theta_{\text{trunc}} = 120^\circ$ range and (b) reduced $\theta \leq \theta_{\text{reduced}} = 90^\circ$ range

For the x-oriented dipole and the random set of SWCs with $N_{\text{set}} = 4$, both ranges show almost identical results. This indicates that the FFT/Matrix solution is distorted only by the added noise and no additional error is introduced by translation of their respective SWCs. The reduced θ -range was chosen to see how well translated truncated SWCs can describe the radiation patterns of the upper hemisphere. One can observe that the SMSE in this reduced range of θ -angles remains appreciably low over all translation distances with a negligible increase of error compared to nontranslated SWCs. The one exemption to this observation is the example with random coefficients of $N_{\text{set}} = 40$, where an error increase of approximately 5 dB can be seen for translations of ± 0.5 m away from the origin of the

coordinate system. An investigation has shown that this can directly be related to the large MRE relative to the measurement distance A and translation error could be reduced by increasing the measurement distance. Since it is common practice to keep the distance between the probe antenna and the AUT at 3λ or more to avoid coupling effects between them [14, 15], this extreme result has no impact on practical measurements. The example with random coefficients of $N_{\text{set}} = 34$ represents the largest order N where the minimum distance between the AUT and the probe antenna after translation is larger than 1λ . This example shows no increase of error, suggesting that already this distance is sufficient from the theoretical point of view. These results imply that, for a frequency of 2.4 GHz, translated fields are accurate up to a reduced angle $\theta = 90^\circ$ and can therefore be used for accurate pattern stitching. Since the increase of the order N depends on the wavenumber k , which in turn depends on the frequency, the question that remained unanswered was whether higher frequencies demonstrate the same behavior. For that reason, the same sets of SWCs were also tested at a frequency of 4.8 GHz. Compared to tests at 2.4 GHz, the results, shown in Figures 3.23 to 3.25 for the x-oriented dipole and patterns of random sets of SWCs with $N_{\text{set}} = 34$ and $N_{\text{set}} = 40$, show minor differences in computed SMSE values. For the reduced θ -range, SMSE over the whole translation sweep range remains at the noise level, which suggests that the translation of truncated SWCs delivers accurate results regardless of the frequency. Due to the rapidly increasing computation times with increasing maximum polar order N , higher frequencies were not considered at this stage.

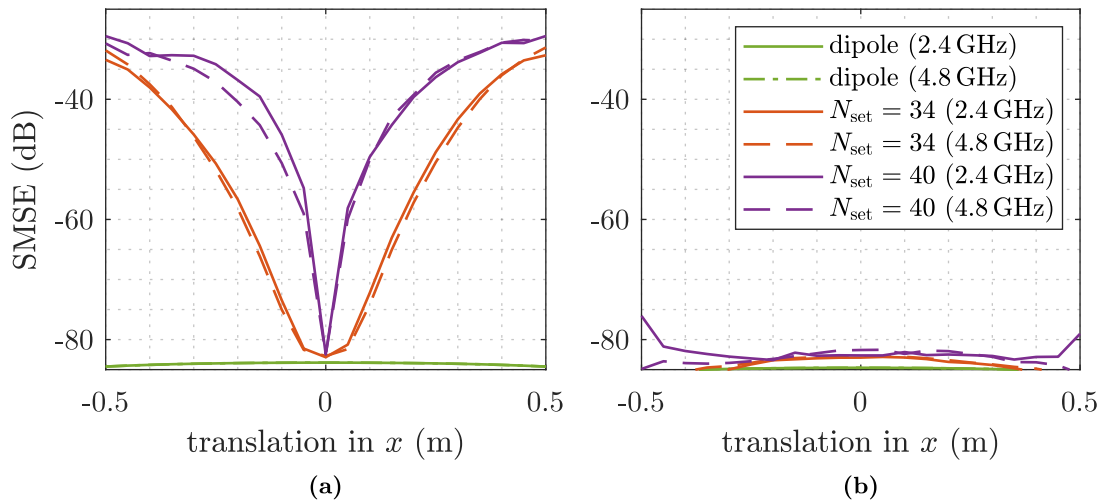


Figure 3.23: SMSE sweep over translations in x : (a) frequency comparison over the whole $\theta \leq \theta_{\text{trunc}} = 120^\circ$ range and (b) reduced $\theta \leq \theta_{\text{reduced}} = 90^\circ$ range

Effects of Rotation

After investigating the effects of translation, the same test objects were used for testing the effects of rotation. As discussed in Section 2.2, an arbitrary rotation in (2.32) can be represented by a sequence of Euler angles, φ_0 , ϑ_0 , and χ_0 , where the rotations are done around the z -, y -, and z' -axis, respectively. If $\vartheta_0 = 0$, the axes z and z' are aligned and φ_0 and χ_0 are interchangeable. The rotation is then obtained by multiplying the coefficients

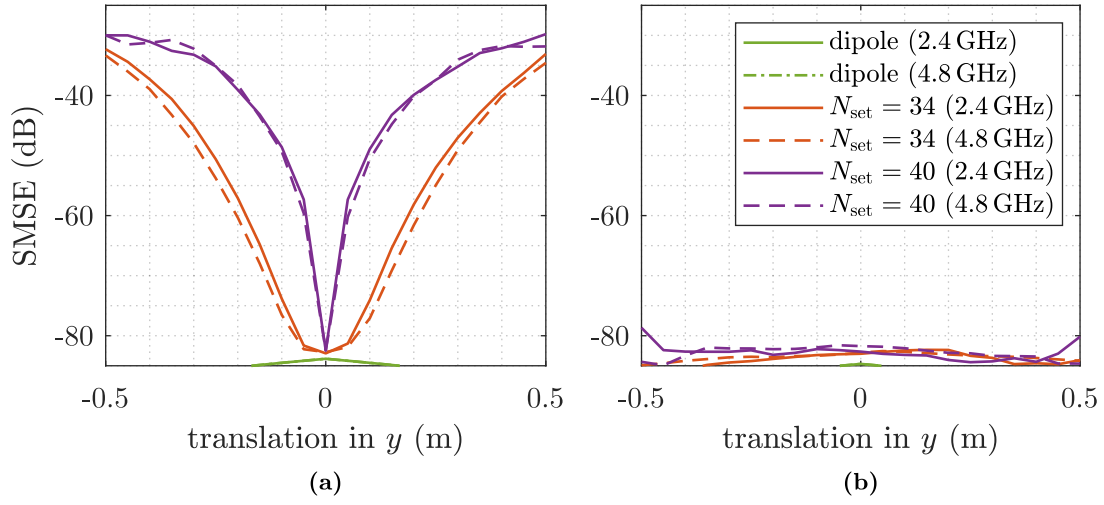


Figure 3.24: SMSE sweep over translations in y : (a) frequency comparison over the whole $\theta \leq \theta_{\text{trunc}} = 120^\circ$ range and (b) reduced $\theta \leq \theta_{\text{reduced}} = 90^\circ$ range

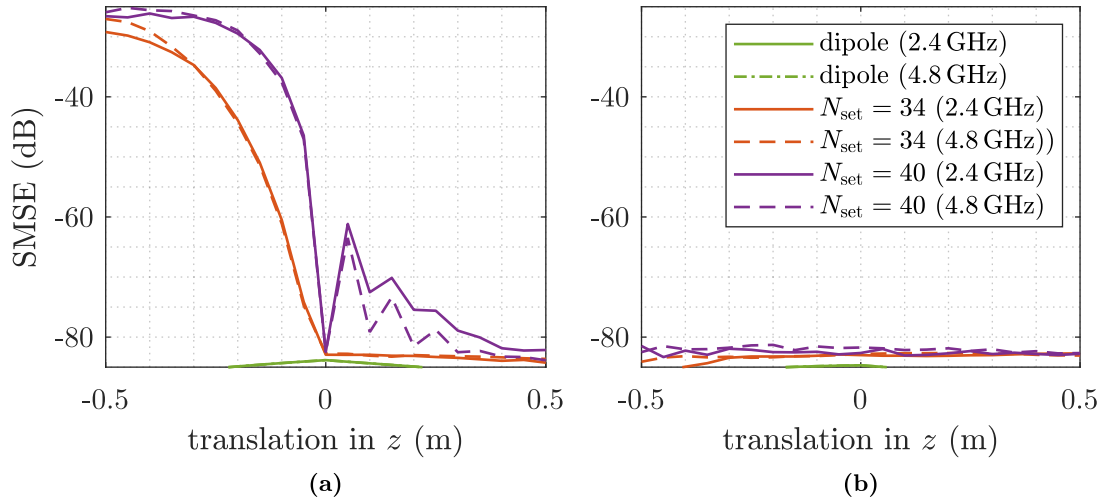


Figure 3.25: SMSE sweep over translations in z : (a) frequency comparison over the whole $\theta \leq \theta_{\text{trunc}} = 120^\circ$ range and (b) reduced $\theta \leq \theta_{\text{reduced}} = 90^\circ$ range

with a complex exponential term

$$Q_{smn,\text{rotated}}^{(4)} = e^{jm(\chi_0 + \varphi_0)} Q_{smn}^{(4)}, \quad (3.13)$$

which represents a simple pattern shift in ϕ . Ideally, rotation in ϕ or χ should have no impact on the accuracy. Nevertheless, a minor ripple has been observed in the SMSE results, demonstrating a periodic behavior over the range of rotation angles with a period that is equal to the sampling step Δ_ϕ . This suggests that truncated SWCs describe the radiation patterns with a variable accuracy depending on the chosen sampling points. However, the observed ripple was below 0.5 dB for all tested examples and can thus be

considered negligible compared to the errors introduced by translations, as well as by rotation in θ . Since ϑ_0 represents a rotation in θ , where the patterns are truncated at θ_{trunc} , larger errors can be observed in the sweep in Figure 3.26a. The sweep over ϑ_0 was only done in the range $-90^\circ \leq \vartheta_0 \leq 90^\circ$. Analyzing this range was found to be sufficient because rotation in θ is symmetric about $\vartheta_0 = \pm 90^\circ$ and the results for angles below -90° and above 90° are the mirrored versions of the results between -90° and 90° . Limiting the range to

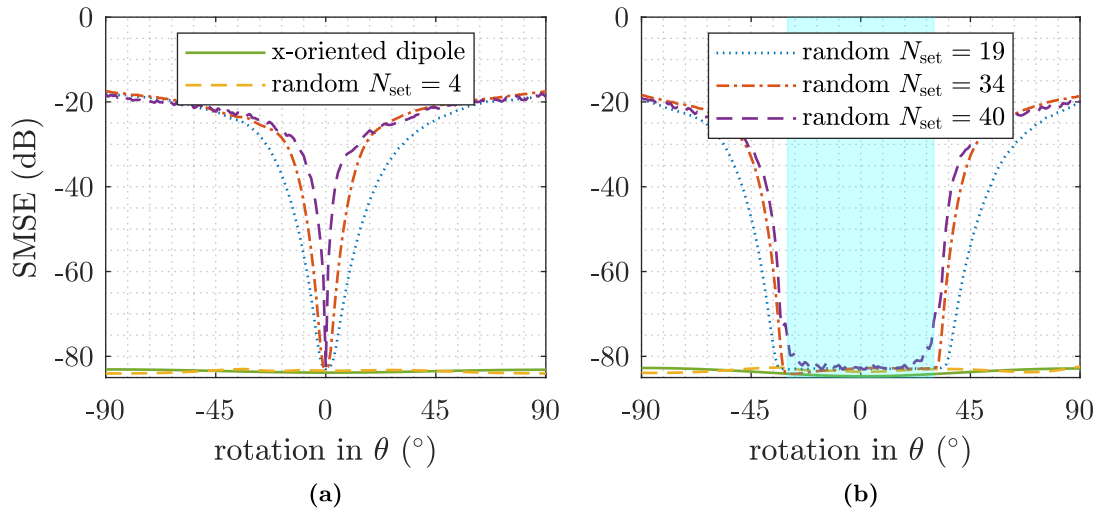


Figure 3.26: SMSE over rotations in θ : (a) whole $\theta \leq \theta_{\text{trunc}} = 120^\circ$ range and (b) reduced $\theta \leq \theta_{\text{reduced}} = 90^\circ$ range

$\theta = 90^\circ$ again, a range of rotation angles $\vartheta_0 = \pm 30^\circ$ has been found, marked in light blue in Figure 3.26b, where accurate results can be obtained from rotated truncated SWCs. It can be seen that this resulting range directly relates to the difference between the truncation angle and accurate-region angle as $\vartheta_0 = \pm(\theta_{\text{trunc}} - \theta_{\text{accurate}}) = \pm(120^\circ - 90^\circ)$. While rotation in θ is found to be the limiting factor for accurate representation of truncated fields, it should be noted that misalignment errors larger than a few degrees in θ are unlikely in practice.

This leads to the conclusion that, regardless of the chosen order N_{set} , SWCs obtained from truncated field patterns using the FFT/Matrix method can be both translated and rotated to a different coordinate system with negligible loss of accuracy in a reduced range of θ -angles for which $\theta \leq \theta_{\text{accurate}}$. This maximum θ -angle depends on the translation and rotation at hand, and, for all tested translations and θ -rotations up to $\vartheta_0 = \pm 30^\circ$, accurate results could be obtained in the range of the upper hemisphere, i.e., $0^\circ \leq \theta \leq \theta_{\text{accurate}} = 90^\circ$. It was thus confirmed that translation and rotation operations on such truncated SWCs can be used as a basis for stitching multiple truncated field patterns together.

3.3.2 Alignment Algorithm

Having confirmed that truncated fields can indeed be translated and rotated accurately up to an angle smaller than θ_{trunc} , the next task is to align the partial patterns to the same coordinate system. The intuitive approach for aligning multiple patterns is to fix one

pattern and consider this pattern aligned. This measurement orientation will hereafter be referred to as the top measurement. To avoid having a nonphysical field distribution in the top measurement pattern, which is caused by pattern inaccuracies due to noise and other measurement uncertainties, the pattern is processed once with the FFT/Matrix method to obtain a field pattern that can be described by SWCs of the given order N . The coordinate system of the other partial radiation pattern, referred to as the bottom measurement in the remainder of this work (assuming two measurement orientations), must then be transformed to match the coordinate system of the processed top measurement. First, the SWCs of the bottom measurement must be rotated by 180° in θ , as indicated in Figure 3.2. Then, the misalignment in translation and rotation between the two patterns must be found. To do so, an alignment algorithm has been devised, first presented in [57].¹⁰

For the alignment algorithm to work, there must be an overlap between the two measurements, i.e., each measurement needs to cover more than a hemisphere. The goal is then to minimize the error in the overlapping region, which can be evaluated using (3.1) for this reduced region of θ -angles,

$$\text{SMSE} = \frac{1}{K_{\text{overlap}}} \frac{\sum_{\chi, \theta_{\text{overlap}}, \phi} |w(\chi, \theta, \phi) - \hat{w}(\chi, \theta, \phi)|^2}{\max_{\chi, \theta_{\text{overlap}}, \phi} |w(\chi, \theta, \phi)|^2}. \quad (3.14)$$

Due to the distribution of the sample points over the sphere—the density of sample points in ϕ increases when approaching the z -axis (the pole of the coordinate system)—the SMSE in the overlapping region can further be weighted by $\sin^2 \theta$ to account for the surface area covered by each point, leading to the expression for the weighted scaled mean square error:

$$\text{wSMSE} = \frac{1}{K_{\text{overlap}}} \frac{\sum_{\chi, \theta_{\text{overlap}}, \phi} \sin^2 \theta |w(\chi, \theta, \phi) - \hat{w}(\chi, \theta, \phi)|^2}{\max_{\chi, \theta_{\text{overlap}}, \phi} |w(\chi, \theta, \phi)|^2} \quad (3.15)$$

This assures a fair comparison of the error between all points in the overlapping region. Additionally, knowing that the misalignment error is largest near the angle of truncation, θ_{trunc} , and becomes negligible at angles sufficiently distant from θ_{trunc} , the region in which the SMSE is evaluated can be reduced to discard erroneous data. The extent of θ -angles at which data are erroneous directly depends on the translation and rotation misalignment. The worst-case scenario can be estimated using the misalignment bounds of the alignment algorithm. This, of course, is measurement-specific and a single value cannot be applied as a universal rule.

The algorithm takes six variables, the three Euler rotation angles, $(\varphi_0, \vartheta_0, \chi_0)$, and the three translation components, (x, y, z) . Lower and upper bounds are defined for each variable and a bounded error minimization technique is then used to find the combination of rotation and translation parameters for which the error in the overlapping region is the smallest. The function `fmincon`, which is part of Matlab's Optimization Toolbox [44], is used for error minimization. Various parameters of the `fmincon` function were tested during validation, more information on this topic will follow in Chapter 4. At this stage, the alignment procedure served as a proof of concept and the potential of using alternative error minimization techniques to assure either faster or more reliable performance of the stitching method has not been investigated.

¹⁰Footnote 9 also applies to results presented in [57].

3.4 Aligned Pattern Stitching

Once the misalignment error minimization procedure converges, SWCs representing the bottom measurement, i.e., the measurement which was rotated and translated during the alignment procedure, are aligned with those of the fixed top measurement using the obtained optimal translation vector, $(x_{\text{opt}}, y_{\text{opt}}, z_{\text{opt}})$, and optimal rotation vector, $(\vartheta_{\text{opt}}, \varphi_{\text{opt}}, \chi_{\text{opt}})$. Then, radiation patterns of these aligned SWCs, computed using a same-distance SN2FFT, need to be stitched together.

This brings the method to the final stage, i.e., the pattern stitching stage. Looking back at the third stage in Figure 3.2, which follows after the coordinate system alignment, it should be evident that only data from **measurement 1** are available for θ -angles up to $\pi - \theta_{\text{trunc}}$, and only data from **measurement 2** are available for θ -angles larger than θ_{trunc} . Therefore, data in these ranges can be used in the final stitched pattern without modifications. The last question that needs to be answered is how to use the data in the overlapping region between $\pi - \theta_{\text{trunc}}$ and θ_{trunc} , where data from both measurements are available. Two different approaches were considered:

- **Pattern blending:** Radiation patterns of both measurements are blended together in the overlapping region. The mean value of both patterns is computed for each data point, i.e., $w_{\text{stitched}} = (w_1 + w_2)/2$ and the resulting value is used to represent this data point in the stitched field pattern.
- **Hemisphere split:** The range representing the bottom hemisphere ($\theta > 90^\circ$) is extracted from the aligned patterns and appended to the upper hemisphere radiation pattern of the top measurement ($\theta < 90^\circ$). If data at the equator, i.e., at the center of the θ -range ($\theta = 90^\circ$), have been obtained during measurements, the mean value of both measurements is used to represent the data in the stitched field pattern.

To determine which of these approaches returns more accurate results, sets of random SWCs with different maximum polar orders from $N = 5$ to $N = 200$, which were introduced in Section 3.2.5, were used to generate field patterns in two different coordinate systems. For the pattern representing the measurement of the top hemisphere, the initial SWCs were used, while the bottom hemisphere patterns were obtained by misaligning the SWCs by a translation of (10 cm, 10 cm, 10 cm), a rotation of $(10^\circ, 5^\circ, 10^\circ)$, and a consecutive rotation of 180° around the y -axis. The patterns representing both measurements were evaluated at a distance of 3λ away from the MRE of the misaligned bottom hemisphere. Patterns of both measurements were truncated at 135° and then truncated SWCs were computed for each. Next, the truncated SWCs of the bottom hemisphere were transformed back to the coordinate system of the top hemisphere (the alignment procedure was skipped for this evaluation), which led to the final stage of the stitching algorithm. Both stitching methods listed above, i.e., pattern blending and hemisphere split, were used in this stage to obtain stitched patterns for all test objects. The stitched patterns were then processed with the FT-based SN2FFT using a same-distance near-to-near-field transformation to obtain the final stitched patterns. These patterns were then compared to the aligned untruncated patterns of the respective test object and the SMSE was computed for both methods. From the SMSE results, shown in Figure 3.27, it can be seen that both methods perform almost identically for lower polar orders up to $N = 30$. Increasing the

order further, the SMSE values begin to drift apart. The results using the **hemisphere split** approach remain stable at error levels around -100 dB, showing even a slight error decrease. On the other hand, the SMSE values using the **pattern blending** approach increase rapidly and reach -50 dB at $N = 200$. Looking back at the results from the analysis of translation and rotation effects in Section 3.3.1, a logical explanation for the increased error when using **pattern blending** becomes apparent. While exact SWCs can accurately be determined from a noiseless truncated pattern for low orders N without an increase in error due to translation and rotation, it was shown that translating and rotating truncated SWCs with higher orders N results in increased error contained primarily in the vicinity of the truncation angle θ_{trunc} . When the two patterns in the overlapping region are blended together, these errors find their way into the final pattern. Using the **hemisphere split** approach, both patterns are cut at 90° , discarding the range of θ -angles near θ_{trunc} , where these errors are contained. Therefore, it is the better-performing stitching approach and will be used hereafter.

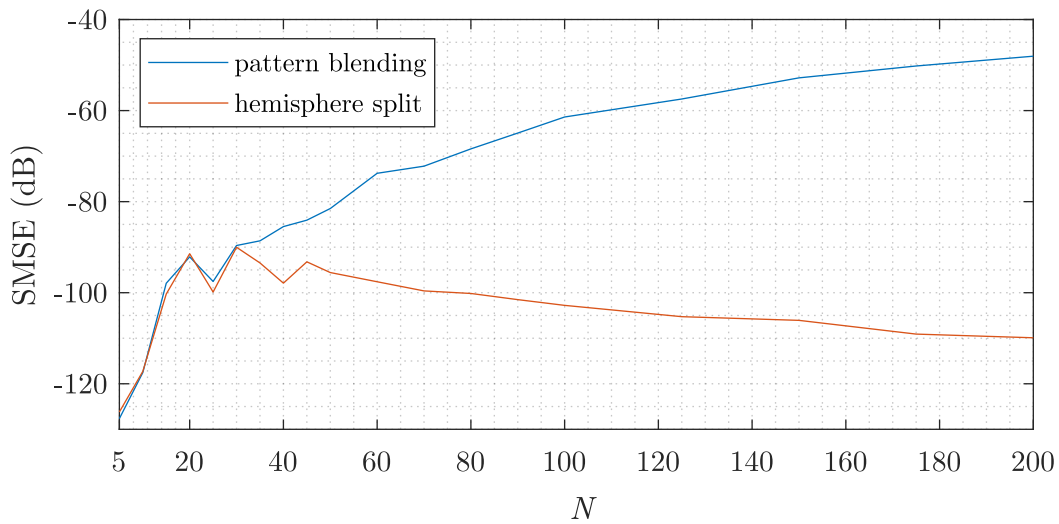


Figure 3.27: Stitching approach comparison: SMSE comparison between pattern blending and the hemisphere split approach

By stitching the patterns together using the **hemisphere split** approach, a full-sphere near-field radiation pattern of the AUT is obtained. However, truncation errors, noise, and other potential differences between both partial measurements might result in nonphysical discontinuities in the resulting pattern. To obtain a physically plausible radiation pattern that can be described by a combination of spherical wave coefficients, a same-distance near-to-near-field transformation using the FT-based SN2FFT is done on the stitched pattern, as was briefly mentioned when stitching approaches were compared. This gives us the final stitched NF pattern, as well as a set of SWCs that can describe the AUT anywhere in space. Once the pattern stitching procedure is done, the stitched full-sphere pattern can be processed with the SN2FFT to obtain the AUT's full-sphere far-field radiation pattern. The pattern stitching method was implemented in Matlab [44] and the used functions are documented in Appendix B along with a demonstration of their application. The complete method along with its validation and practical limitations, which will be presented in the following chapters, has been summarized in [58].

4 Validation of the Stitching Method

In the previous chapter, the proposed truncated pattern stitching method was presented in detail. It was shown that spherical wave coefficients (SWCs) can be obtained from truncated measurements, patterns of which can be rotated and translated with a tolerable increase in error in an attempt to align partial measurements. The stitching method was implemented in Matlab [44] and, now, it had to be validated. The validation procedure was done in three steps. First, the method was tested with noiseless synthetic data and the results of this validation step will be presented in Section 4.1. This was followed by validation with data obtained from electromagnetic (EM) simulations using HFSS [53], the results of which will be shown in Section 4.2. Lastly, the stitching method needed to be validated with actual measurement data, as will be demonstrated in Section 4.3. In each of the validation steps, attention was given to the resulting scaled mean square error (SMSE) as a measure of how well the stitching method can describe the field pattern of the antenna under test (AUT).

4.1 Validation with Synthetic Data

In the first validation step, synthetic spherical wave coefficients (SWCs) were used to compute noiseless field patterns. Specifically, coefficients representing an x-oriented dipole with $N_{\text{set}} = 1$ and sets of random complex coefficients with the order N_{set} in the range between 5 and 35. Two combinations representing an AUT placement misalignment between the two partial measurements were chosen, defined by a translation vector (x, y, z) and a rotation vector $(\varphi_0, \vartheta_0, \chi_0)$. They are listed in Table 4.1. The smaller of the two, denoted as **misalignment 1**, represents a realistic positioning precision achievable without expensive equipment, such as laser positioners. In contrast, the larger **misalignment 2** is considered to be within the range of positioning precision that can be achieved with the

Table 4.1: Misalignments used for validation

	translation			rotation		
	x	y	z	φ_0	ϑ_0	χ_0
misalignment 1	2 cm	-2 cm	4 cm	10°	-2°	0°
misalignment 2	10 cm	10 cm	10 cm	10°	5°	10°

naked eye. For all examples, the unrotated SWCs were chosen to represent the measurement of the upper hemisphere, while the misaligned SWCs, offset using the rotation and translation combination from either **misalignment 1** or **misalignment 2** and rotated by 180° around the y -axis, were used to represent the measurement of the bottom hemisphere. During the initial analysis, a frequency of 2.4 GHz was chosen for validation and, for each misalignment, the maximum radial extent (MRE) of the AUT was obtained by computing the MRE of the aligned AUT, r_0 , as discussed in Section 3.3, and adding the total translation distance of the respective misalignment,

$$\text{MRE} = r_0 + \sqrt{x^2 + y^2 + z^2} = N_{\text{set}}/k + \sqrt{x^2 + y^2 + z^2}. \quad (4.1)$$

Knowing the MRE, the maximum polar order N follows from (2.24):

$$N = \lfloor (r_0 + \sqrt{x^2 + y^2 + z^2}) \cdot k \rfloor + 10 = N_{\text{set}} + \lfloor \sqrt{x^2 + y^2 + z^2} \cdot k \rfloor + 10 \quad (4.2)$$

For each example, the number of samples in ϕ was set such that $K_\phi = 2N + 1$ and the number of samples in θ was set such that $K_{\theta_{\text{trunc}}} \geq N + 1$ while simultaneously fulfilling the requirement that the measurement points of both truncated measurements used for stitching must coincide. The measurement radius A was defined to change along with r_0 in order to maintain a constant distance of 3λ away from the AUT's MRE, $A = r_0 + 3\lambda$. Radiation patterns representing the sets of SWCs were then computed using the spherical near-to-far-field transformation (SN2FFT) algorithm, which generates noiseless radiation patterns limited only by the numerical precision of Matlab [44]. The patterns were truncated at $\theta_{\text{trunc}} = 140^\circ$, corresponding to the maximum θ -angle that can be covered in a single measurement in the near field (NF) range at TU Wien when additional absorbers are used, designed for reflection suppression when measuring omnidirectional antennas. It should be noted that other truncation angles were not tested in the validation process. Assuming a sufficient overlap between the measurements to be stitched, varying truncation angle is not expected to play a significant role on the performance of the stitching method.

These truncated radiation patterns were then provided to the pattern stitching algorithm in an attempt to obtain full-sphere radiation patterns. As discussed in Section 3.3.2, the alignment was done using a bounded SMSE-minimization procedure, for which the bounds were chosen slightly larger than the estimated naked-eye alignment precision, i.e., $\pm 11^\circ$ for all Euler rotations and ± 11 cm for all translation directions.

4.1.1 Convergence Issues

Unfortunately, initial tests have shown poor performance of the pattern alignment procedure since the misalignment vector was often not converging towards the optimum solution, instead getting stuck in local minima of the SMSE objective function. The convergence was found to deteriorate with increasing misalignment between the two patterns. Countless attempts have been made in order to improve the performance of the method, such as swapping the underlying minimization algorithm used by Matlab's `fmincon` [44] from the default 'interior-point' to 'active-set', increasing or decreasing the bounds, and changing the starting misalignment vector for the algorithm. These attempts were found to be beneficial for solving specific examples, but none of them could be used as a universal solution with which convergence could be achieved for all test examples. A brute force approach using multiple start points was considered as a possible solution, but the

computational complexity and duration of such an approach even for relatively low orders N would limit the method to the point of uselessness. Investigating the observed poor convergence of the problem further, the realization was made that its source must lie in the periodic nature of the complex-valued field patterns—an offset Δr from the coordinate system’s origin causes a wavelength-dependent phase change ($2\pi\Delta r/\lambda$)—which results in countless local minima of the SMSE function. It was found that this local minima vanish when the SMSE is evaluated using only the magnitude of the field patterns. This led to the implementation of the two-step alignment procedure.

4.1.2 Two-Step Alignment Procedure

Due to stitching method convergence issues when the SMSE in the overlapping range is computed from complex-valued radiation patterns, the alignment procedure was split into two consecutive steps. Only the magnitude of the radiation patterns is used in the first step of the procedure, using large bounds of $\pm 11^\circ$ for all Euler rotations and ± 11 cm for all translation directions. The constrained minimization function, `fmincon`, is set to use the ‘active-set’ algorithm, which can take large steps and was thus found to work more efficiently within this large range of rotation angles and translation distances than the default option, the ‘interior-point’ algorithm. By minimizing the SMSE based solely on the magnitude, a good starting point for the second step can be found. In the second step, SMSE minimization of complex-valued patterns is then carried out in order to also match the phase between both measurements. The starting point for the second step of the minimization procedure, i.e., the vector of rotation angles and translation distances representing the misalignment, is already expected to be near the optimum solution because the field magnitude distributions of both measurements already closely resemble each other in the overlapping range. Therefore, the ‘interior-point’ algorithm is utilized instead of the ‘active-set’ algorithm. A smaller range of misalignment vectors could thus theoretically be defined, but (at this stage) it was found that the stitching method was converging to the correct solution even if large bounds were used.

The pattern stitching algorithm following this two-step alignment procedure was tested on all synthetic test objects presented earlier and the results are shown in Table 4.2. For

Table 4.2: SWC validation: results

	N_{set}	misalignment 1		misalignment 2	
		<i>NF SMSE</i>	<i>FF SMSE</i>	<i>NF SMSE</i>	<i>FF SMSE</i>
dipole	1	−106.7 dB	−106.7 dB	−114.0 dB	−114.5 dB
random SWCs	5	−122.7 dB	−122.7 dB	−124.1 dB	−124.3 dB
	10	−122.5 dB	−122.7 dB	−118.5 dB	−119.4 dB
	15	−118.3 dB	−119.0 dB	−102.9 dB	−103.6 dB
	20	−121.4 dB	−121.7 dB	−113.9 dB	−113.8 dB
	25	−120.5 dB	−120.7 dB	−8.6 dB	−9.4 dB
	30	−106.3 dB	−106.9 dB	−9.6 dB	−10.4 dB
	35	−9.2 dB	−9.7 dB	−10.2 dB	−10.4 dB

all, both the near field (NF) SMSE and the far field (FF) SMSE were evaluated to confirm that the results are valid also after transformation to far field. Marked in red, one can observe that the stitching method has failed to find the solution for the largest tested orders of N . Although this might appear concerning at first sight, an investigation of the results has shown that it is in fact irrelevant when measuring actual antennas. Concretely, the reason that the method fails with higher orders N of random SWCs is the fact that the radiation pattern has an increasing resemblance to noise with increasing N , which in turn increases the probability that already the first, magnitude-based minimization step of the alignment procedure will get stuck in a local minimum. Of course, the radiation pattern of any practical antenna will not resemble noise, and failure in the first alignment step is not anticipated in realistic scenarios. This will be confirmed in subsequent validation steps.

To verify that the two-step alignment procedure does not only converge for the two specific misalignment combinations from Table 4.2, a set of one hundred random misalignment combinations with translations in the range between -10 cm and 10 cm and rotations in the range between -10° and 10° has been generated. These were used to further test the stitching method using SWCs representing an x-oriented dipole and random SWCs with $N = 5$ and $N = 10$. The mean and the maximum SMSE were evaluated using both NF and FF patterns and the results, shown in Table 4.3, confirm the general validity of the stitching method within this range of misalignments for low-order field patterns.

Table 4.3: SWC validation: results for random misalignments

	N_{set}	NF SMSE		FF SMSE	
		<i>mean</i>	<i>max</i>	<i>mean</i>	<i>max</i>
dipole	1	-115.8 dB	-99.6 dB	-115.8 dB	-99.6 dB
random SWCs	5	-122.4 dB	-87.8 dB	-122.3 dB	-87.8 dB
	10	-123.2 dB	-83.7 dB	-123.5 dB	-84.1 dB

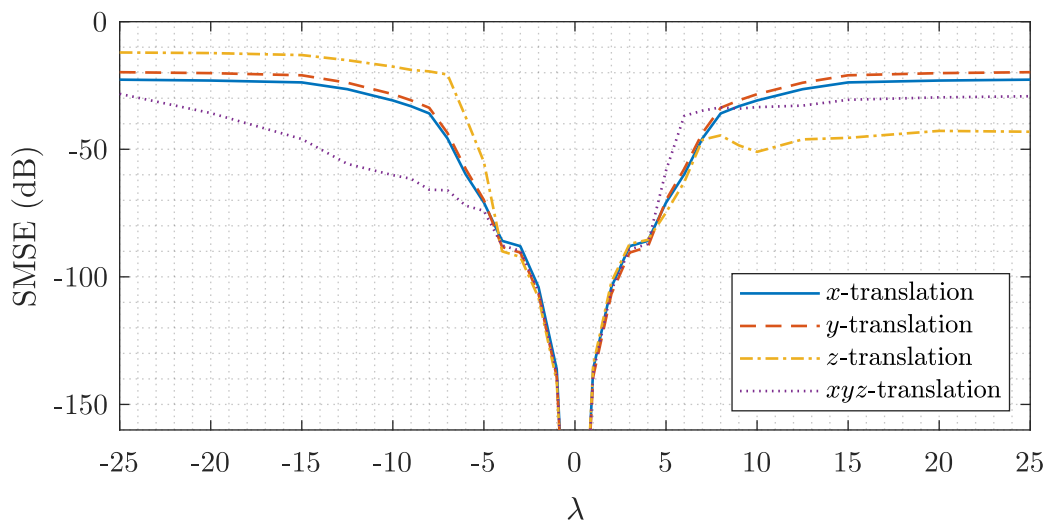
4.1.3 Frequency Dependency

So far, all validation has been performed at a frequency of 2.4 GHz, showing promising results for low-order SWCs for misalignments up to $\pm 10^\circ$ and ± 10 cm where the maximum misalignment values were defined under the assumption that they represent the worst-case scenario when aligning an AUT with the naked eye. To test how the stitching method performs at other frequencies, the SWCs of the x-oriented dipole were used to compute radiation patterns at various frequencies following the same procedure as was described at the beginning of this chapter, i.e., always at a measurement range A defined by $A = r_0 + 3\lambda$ and offset using the misalignments from Table 4.1. The results of this analysis can be seen in Table 4.4, where a deterioration of the method's performance with increasing frequency can be observed. This deterioration was unexpected and thus thoroughly investigated, which led to the conclusion that the increased error does not stem from a failure of the alignment procedure. Surprisingly, contrary to the findings presented in Section 3.3.1, the source of error could be traced back to the translation of truncated SWCs. While translations in Section 3.3.1 were carried out starting with SWCs aligned with the origin of

Table 4.4: SWC validation: frequency variation results

	<i>frequency</i>	misalignment 1		misalignment 2	
		<i>NF SMSE</i>	<i>FF SMSE</i>	<i>NF SMSE</i>	<i>FF SMSE</i>
dipole	1.2 GHz	-112.1 dB	-112.1 dB	-116.0 dB	-116.0 dB
	2.4 GHz	-106.7 dB	-106.7 dB	-114.0 dB	-114.5 dB
	4.8 GHz	-106.2 dB	-106.2 dB	-97.7 dB	-97.3 dB
	9.6 GHz	-102.4 dB	-102.2 dB	-56.4 dB	-57.1 dB
	19.2 GHz	-90.7 dB	-91.2 dB	-51.2 dB	-51.3 dB
	38.4 GHz	-56.9 dB	-57.1 dB	-43.2 dB	-43.2 dB

the coordinate system and translating in all directions away from it, the inverse procedure is done here. The coordinate system is translated in order to align itself with the initially severely offset SWCs, which, in turn, should minimize the number of nonzero SWCs. Using truncated SWCs results in artifacts in translated SWCs, which are the cause for errors in the radiation pattern. As can be seen in (4.2), the order N of the translated SWCs depends on the wavenumber k , which itself is inversely proportional to the wavelength λ (and proportional to the frequency f). Moreover, the computation of translation coefficients, as defined in (2.34), depends solely on the product of the wavenumber k and the translation distance A . This indicates that the observed translation error can be related to the translation distance in terms of wavelengths. Using the x-oriented dipole example, the SMSE between its actual pattern and the pattern obtained from truncated misaligned SWCs after coordinate-system alignment was computed for different initial misalignments in terms of λ , considering translations in x , y , z , and a combined xyz -translation, where the translation distance in each direction is $A/\sqrt{3}$. The results, shown in Figure 4.1, indicate that the SMSE in the θ -range representing the truncated bottom hemisphere measurement increases rapidly with increasing translation distance. Already at a distance of 5λ , an

**Figure 4.1:** SMSE for $40^\circ \leq \theta \leq 180^\circ$ over translation in wavelengths

SMSE between -50 dB to -70 dB can be observed for all tested translation directions, approaching -10 dB at 25λ in the worst case. These SMSE values are much larger than the overall error of stitched patterns reported in Table 4.4, since only the bottom hemisphere range above $\theta = 90^\circ$ is used for pattern stitching. Thus, it is informative to evaluate the SMSE also in this reduced range of θ -angles.¹ The SMSE results, which can be seen in Figure 4.2, show a significant error reduction for large translation distances when compared to Figure 4.1.

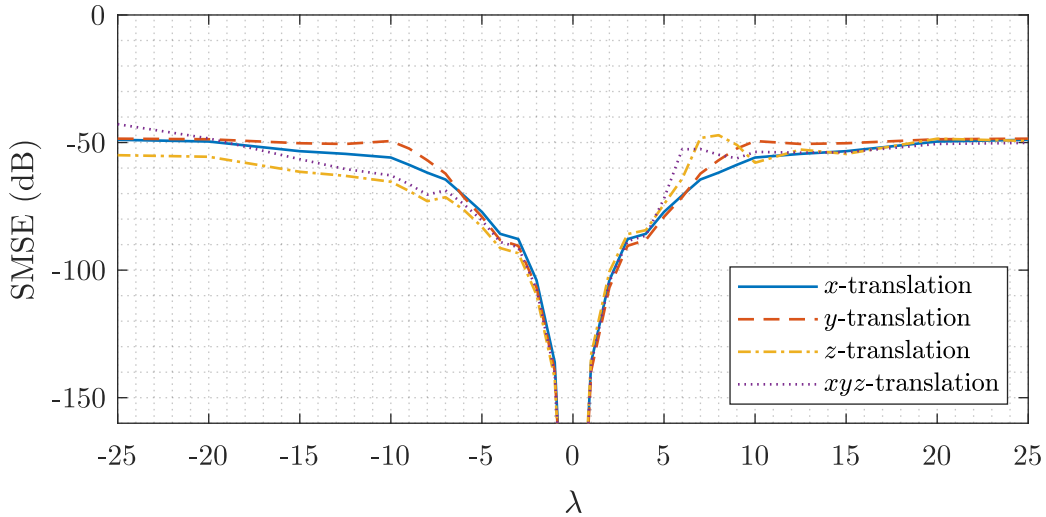


Figure 4.2: SMSE for $90^\circ \leq \theta \leq 180^\circ$ over translation in wavelengths

Up to approximately 3λ , the SMSE due to translation errors stays below -90 dB and stabilizes at around -50 dB when increasing translation distance further, except for the xyz -translation, where it reaches -42 dB at -25λ . To relate the results of Table 4.4 with the results from Figure 4.2, the combined xyz -translation distances of both misalignments, expressed for each respective frequency in terms of wavelengths, are shown in Table 4.5. The required alignment precision in terms of wavelengths can thus be estimated based on the chosen maximum acceptable noise level goal.

Table 4.5: SWC validation: translation in wavelengths

	dipole					
frequency	1.2 GHz	2.4 GHz	4.8 GHz	9.6 GHz	19.2 GHz	38.4 GHz
misalignment 1	0.2λ	0.4λ	0.8λ	1.6λ	3.1λ	6.3λ
misalignment 2	0.7λ	1.4λ	2.8λ	5.5λ	11.1λ	22.2λ

Aside from the error itself, it should also be noted that the computation time of the pattern stitching method rises rapidly with increasing order of N . For every 4λ increase

¹While the stitching method successfully aligned both truncated patterns in all examples presented in Table 4.4, it is important to note that the large errors observed in Figure 4.1 could cause severe differences between the two truncated patterns in the overlapping region ($40^\circ \leq \theta \leq 140^\circ$), which might result in failure of the stitching method.

in translation distance, the order N increases by approximately 25. In Figure 4.3, the computation times for the x-oriented dipole examples at different frequencies were related to their respective translation distances expressed in wavelengths, listed above in Table 4.5. One can see that even for the simplest antenna with the lowest order $N = 1$, large misalignments result in long computation times of the stitching method. For the largest translation, 22.2λ away from the center of the coordinate system, the stitching procedure took more than 2 days. From these results, the strict placement precision requirements, especially when dealing with higher frequencies, should become evident.

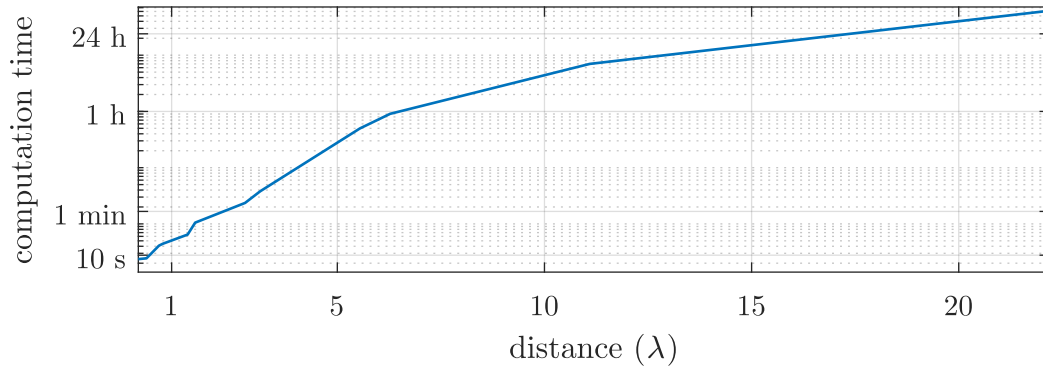


Figure 4.3: Stitching method computation time over translation in wavelengths

4.2 Validation with EM Simulation Data

In the second validation step, antenna radiation pattern examples obtained via electromagnetic (EM) simulation were used. Four different antennas were modeled in Ansys HFSS [53]. The planar log-spiral antenna can be seen in Figure 4.4, where the orienta-

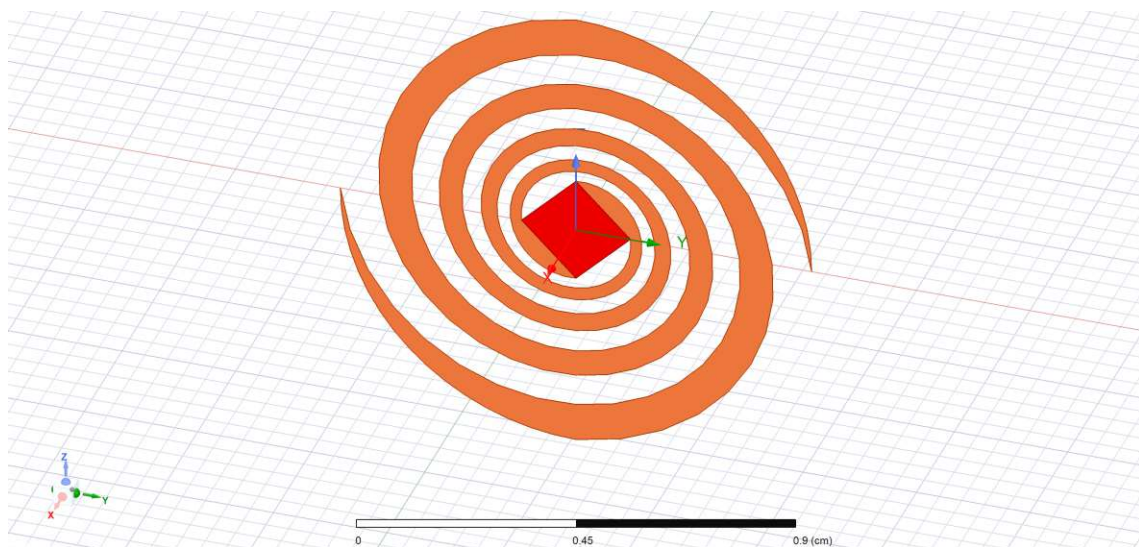


Figure 4.4: Planar log-spiral antenna model

tion of the aligned coordinate system is drawn in the bottom left corner. This antenna was modeled to operate in a very wide frequency range between 16 GHz and 40 GHz.

The second test object was a Vivaldi antenna, shown in Figure 4.5. It was designed for operation in the frequency range from 8 GHz to 21 GHz. In contrast to other test objects, this antenna is directional with a gain between 7.8 dBi and 9.8 dBi, depending on the frequency. It was used to verify how the stitching method performs in the case of directional antennas.

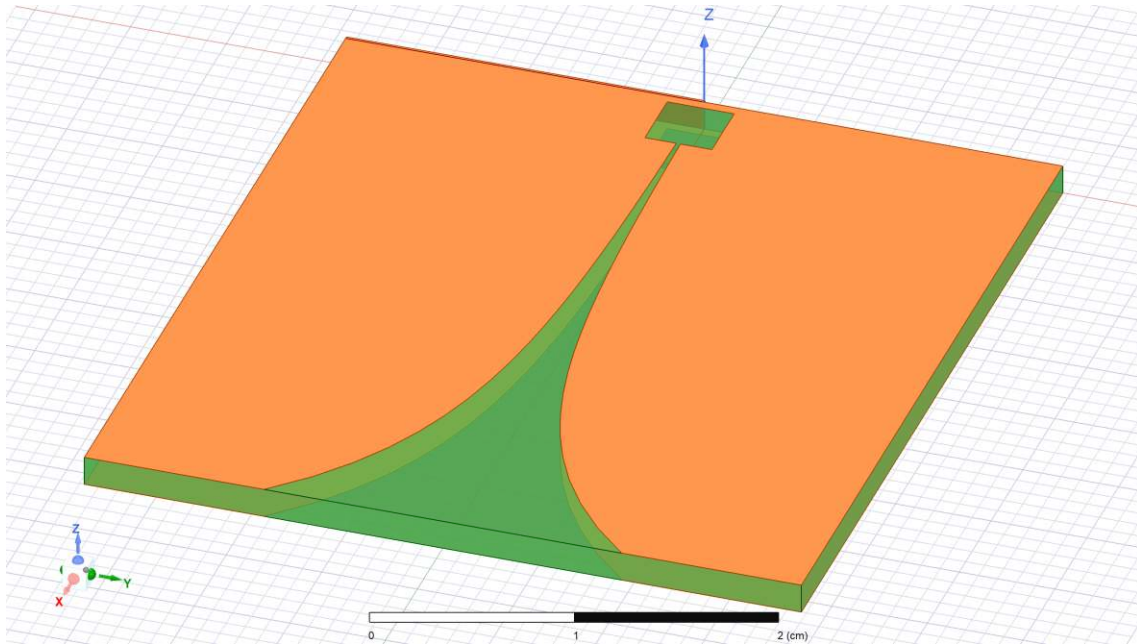


Figure 4.5: Vivaldi antenna model

The remaining two test objects were a planar inverted-F antenna (PIFA) and a bowtie antenna, both designed to operate at the frequency of 2.4 GHz. These antennas were already used in Chapter 3 as test objects for comparisons between different methods for computation of truncated SWCs, where their models were shown in Figures 3.8 and 3.9.

EM simulation results of all four test objects were used to obtain their radiation patterns both at $A = 1.31$ m, corresponding to the measurement distance in the NF test range at TU Wien, and in far field. The patterns of all antennas were computed in the software's global coordinate system, which is marked in Figures 3.8, 3.9, 4.5, and 4.4 for each respective antenna. This was considered to represent the orientation of the top hemisphere measurement. Two additional coordinate systems were defined in HFSS, representing the two misalignments in Table 4.1, and antennas' radiation patterns were computed in both to represent the two misaligned orientations of the bottom hemisphere measurement. The number of samples in θ and ϕ for each of the antennas was determined in a similar fashion as in Section 4.1, using the largest order N , computed at the highest frequency and for the larger of the two misalignments, i.e., **misalignment 2**.

Since simulation noise is an inherent part of any numerical simulation, the accuracy of the EM simulation data was briefly investigated before using the stitching method to establish what the theoretical best accuracy of the stitching method would be. First, a same distance transformation was done on all patterns using spherical near-to-far-field transformation (SN2FFT) with the order N , determined based on the dimensions of the

AUT and misalignment of each respective pattern. These maximum polar orders of the aligned patterns (N_0), the patterns offset by **misalignment 1** (N_1), and the patterns offset by **misalignment 2** (N_2) are listed in Table 4.6 for all test objects. The SMSE between the original patterns and their transforms was then computed to see how well SWCs can describe each pattern. It was found that all except the log-spiral antenna at **misalignment 2** match up to an error of around -80 dB, whereas the SMSE in that case showed increased values of about -65 dB. Then, differences between patterns expressed in different coordinate systems were analyzed. This discrepancy can be quantified by computing the SWCs of the untruncated pattern of the bottom hemisphere measurement, rotating it to match the coordinate system of the upper hemisphere, and then evaluating the SMSE between the so obtained pattern and the pattern representing the upper hemisphere extracted from HFSS. This was done for all test objects and the results are shown in Table 4.6. These results can be interpreted as an approximate lower bound for the error obtained when stitching patterns together. While a somewhat larger error can be observed for the Vivaldi antenna at 21 GHz, it should be noted that no effort was made to further reduce the error levels since robustness against noise itself is also an important factor for a reliable stitching method.

Table 4.6: Discrepancy between HFSS patterns

	<i>frequency</i>	N_0	misalignment 1		misalignment 2	
			<i>discrepancy</i>	N_1	<i>discrepancy</i>	N_2
PIFA	2.4 GHz	14	-76.8 dB	17	-69.8 dB	23
bowtie	2.4 GHz	12	-70.1 dB	14	-61.3 dB	21
Vivaldi	8.0 GHz	17	-74.8 dB	25	-65.7 dB	46
	14.5 GHz	23	-71.1 dB	38	-61.4 dB	76
	21.0 GHz	29	-64.0 dB	51	-53.4 dB	106
planar log-spiral	16.0 GHz	11	-76.9 dB	28	-66.1 dB	69
	28.0 GHz	13	-73.3 dB	41	-63.1 dB	114
	40.0 GHz	14	-69.9 dB	55	-61.8 dB	159

All near-field patterns were then truncated at $\theta_{\text{trunc}} = 140^\circ$, discarding the data points where $\theta > \theta_{\text{trunc}}$, and processed using the pattern stitching method with the two-step alignment procedure presented in the previous section. When computing truncated SWCs from noisy data, singular value (SV) truncation is required to assure correct operation of the FFT/Matrix method. In order to determine the tolerance factor δ from (3.11), a signal-to-noise ratio (SNR) estimate is thus needed. The SNR can be estimated by first computing the truncated SWCs without SV truncation and then evaluating the SMSE between the original pattern and the FFT/Matrix result, which represents the optimum fit in the least squares (LS) sense for the given order N . This SMSE value can then be used as the SNR level for SV truncation.

After stitching, the NF SMSE and the FF SMSE were evaluated for all tested antennas at all simulated frequencies. Obtained values for all AUTs are listed in Table 4.7. One can observe that the results of all test objects for **misalignment 1** and those test objects for **misalignment 2** with a frequency of 14.5 GHz or less are below -50 dB while the

Table 4.7: HFSS validation results

	frequency	misalignment 1		misalignment 2	
		NF SMSE	FF SMSE	NF SMSE	FF SMSE
PIFA	2.4 GHz	-78.5 dB	-75.6 dB	-65.5 dB	-65.0 dB
bowtie	2.4 GHz	-72.6 dB	-66.3 dB	-56.5 dB	-56.1 dB
Vivaldi	8.0 GHz	-67.7 dB	-67.5 dB	-60.3 dB	-60.2 dB
	14.5 GHz	-64.4 dB	-64.0 dB	-52.4 dB	-52.3 dB
	21.0 GHz	-58.0 dB	-57.4 dB	-49.5 dB	-49.4 dB
planar log-spiral	16.0 GHz	-54.3 dB	-54.4 dB	-44.0 dB	-44.0 dB
	28.0 GHz	-55.9 dB	-56.0 dB	-38.1 dB*	-38.2 dB*
	40.0 GHz	-57.5 dB	-57.5 dB	-38.2 dB*	-38.3 dB*

* Patterns were aligned using the optimum misalignment vector obtained from the results at 16 GHz.

Vivaldi antenna at 21 GHz is just barely above it. The worst results were observed for the planar log-spiral antenna, where **misalignment 2** resulted in an SMSE of -44 dB for the 16 GHz pattern. Due to the long computation time, already observed when stitching the Vivaldi antenna at 21 GHz (more than 16 h), an alternative approach was chosen for stitching patterns of the planar log-spiral antenna at 28 GHz and 40 GHz. Here, the wideband nature of the antenna was exploited and the optimized alignment vector found when stitching the 16 GHz patterns was reused to align and stitch the patterns at 28 GHz and at 40 GHz. By doing so, the NF SMSE and the FF SMSE, marked with a “*” in Table 4.7, were obtained. To determine the cause for this worsened performance when stitching patterns of the planar log-spiral antenna, the patterns at 16 GHz, misaligned by **misalignment 2**, were aligned again with the known misalignment vector and stitched together. The obtained SMSE values were -58.5 dB for the NF and -58.6 dB for the FF, an improvement of more than 14 dB, which indicates that the increased error is caused by the alignment procedure. The cause for poor alignment could be traced back to the nature of the AUT. Looking at the radiation pattern shown in Figure 4.6, one can see that the field distribution in the overlapping range between $\theta = 40^\circ$ and $\theta = 140^\circ$ remains rather

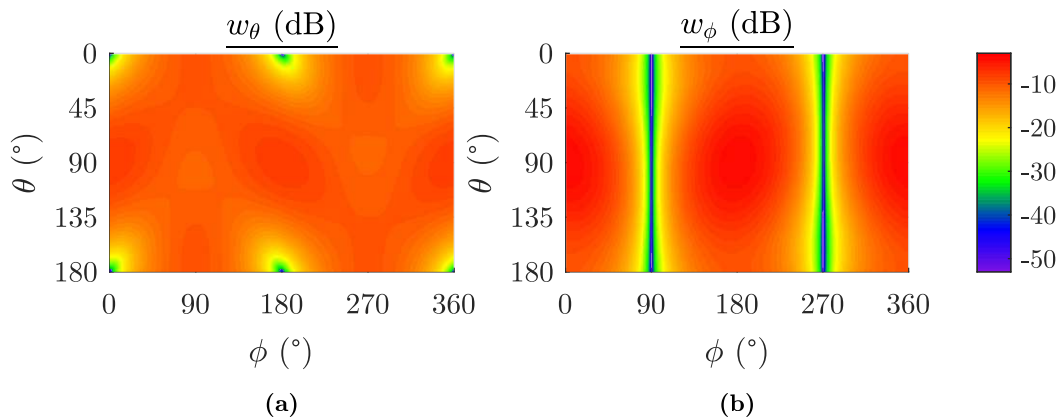


Figure 4.6: Planar log-spiral antenna field pattern at 16 GHz

constant over θ . As such, the elevational alignment becomes difficult and prone to errors in the radiation patterns, which cause the procedure to get stuck in a local minimum. An alternative measurement orientation would thus be beneficial for the planar log-spiral antenna; however, this possibility was not explored at this stage.

4.3 Validation with Measurement Data

In the final step, the method had to be validated using measurement data. In addition to validation with data from measurements of conventional connectorized antennas, where the antenna under test (AUT) is equipped with a coaxial connector that can be accessed during the measurement, validation using measurement data of connectorless devices was also carried out in order to gain more insight about the error introduced by the coaxial cable. Here, the antenna is integrated onto a device under test (DUT) and cannot be accessed via a coaxial connector. A measurement setup was devised for this purpose and the pattern stitching method had to be adapted accordingly. This procedure, which we first presented in [59], is documented in Appendix C. Measurement data for test objects of both types were obtained in the test range at TU Wien and processed with the proposed pattern stitching method.

4.3.1 Connectorized AUTs

Two low-directivity test antennas with coaxial connectors were measured in the NF test range, a folded dipole antenna and an ultra-wideband (UWB) conical monopole (CMP) antenna, similar to the one presented in [54] but with a simplified ground plane structure. The folded dipole antenna was measured in 100 MHz steps in the range between 1.8 GHz and 2 GHz. The AUT was first measured in the orientation shown in Figure 4.7a, which represents the upper hemisphere measurement. Then, it was rotated by 180° around the y -axis and measured again to obtain the truncated pattern covering the bottom hemisphere. This measurement orientation is shown in Figure 4.7b.

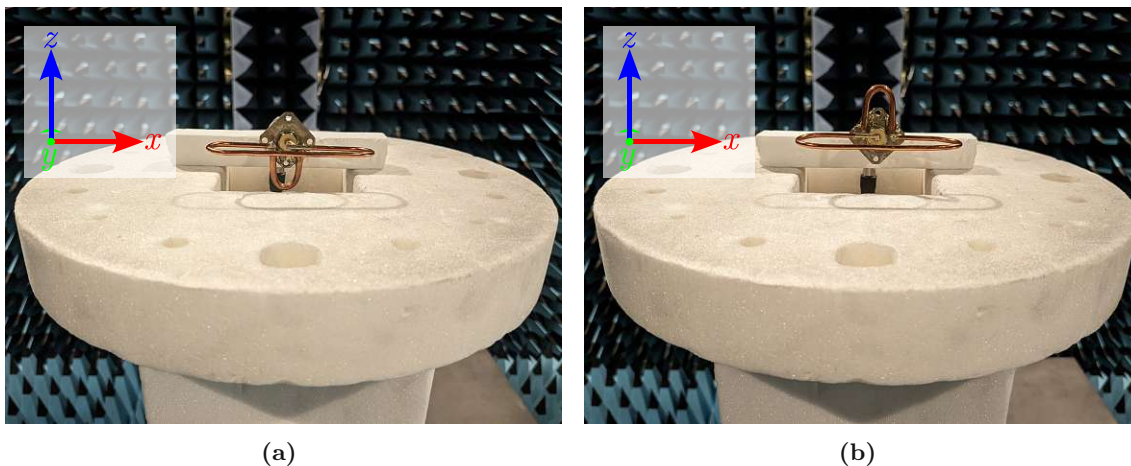


Figure 4.7: Folded dipole in (a) top and (b) bottom measurement orientation

Similarly, the UWB CMP was measured in the two measurement orientations seen in Figures 4.8a and 4.8b, where it was rotated by 180° around the x -axis for the second measurement. It was measured in 250 MHz steps in the range from 4 GHz to 20 GHz.

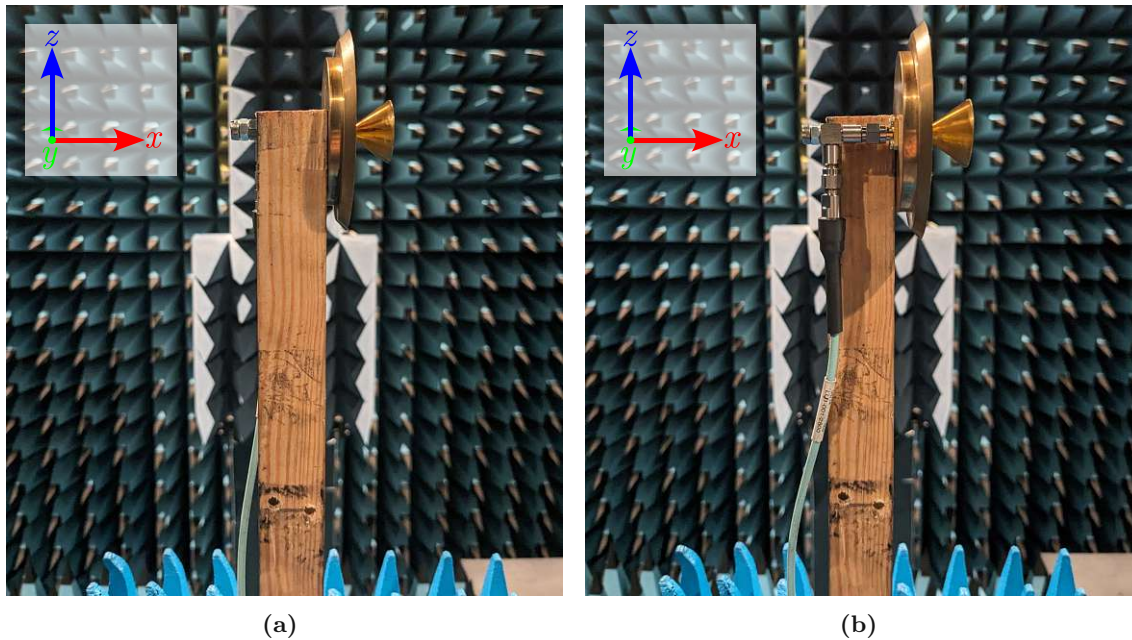


Figure 4.8: UWB CMP in (a) top and (b) bottom measurement orientation

Just as for the EM simulation examples, the noise level in both measurement orientations was estimated by computing an FFT/Matrix transform without SV truncation before proceeding with the pattern stitching method. Besides giving an SNR estimate for SV truncation, these SMSE values also give a good indication of the theoretically achievable accuracy of the full-sphere pattern. For that reason, the mean and maximum estimated SNR values over frequency for each antenna/orientation combination have been listed in Table 4.8 along with the range of computed maximum polar orders N over all frequencies. These results already suggest that the introduced measurement noise and measurement uncertainties limit the potential accuracy of the radiation pattern more than the error levels introduced by the stitching method reported in previous validation steps.

Table 4.8: Measured data validation: estimated measurement SNR for connectorized AUTs

	<i>frequency range</i>	N	SNR (top)		SNR (bottom)	
			<i>mean</i>	<i>min</i>	<i>mean</i>	<i>min</i>
folded dipole	1.8 GHz – 2.0 GHz	13 – 14	46 dB	43 dB	45 dB	42 dB
UWB CMP	4 GHz – 20 GHz	16 – 41	42 dB	37 dB	43 dB	37 dB

The patterns were then processed with the pattern stitching method. At this point, it was found that the alignment procedure does not always converge to the global minimum.²

²Whether the resulting misalignment vector represents the global minimum or just a local one can easily be determined by comparing the phase information of the final aligned bottom hemisphere pattern to that of the upper hemisphere. In the global minimum, patterns in the overlapping range will show a strong resemblance, whereas the differences between them directly relate to measurement and processing errors.

However, since a common misalignment vector should ideally be obtained for all frequencies, a single measured frequency where the alignment procedure converges was found to be sufficient for the pattern stitching method. It should be noted that, due to measurement noise, this converged solution will generally not minimize the SMSE at other measured frequencies. Nevertheless, it provides a good starting point for the alignment procedure at all remaining measured frequencies. The alignment procedure can then be repeated with this starting misalignment vector. Following this procedure, truncated patterns of both tested AUTs were successfully stitched. An SMSE analysis was then carried out to evaluate how well the stitched full-sphere patterns match the measurement data. Since radiation patterns obtained with a single full-sphere measurement were not available for our AUTs, the following approach was used for the analysis:

- **top (hemisphere):** These patterns were fixed (neither translated nor rotated) during the stitching procedure and stitched patterns up to θ_{trunc} could be compared with the measured truncated patterns of the top hemisphere directly to compute the SMSE.
- **bottom (hemisphere):** These patterns were translated and rotated during the stitching procedure. The SWCs representing the stitched patterns thus had to be reversed back to the initial coordinate system of the bottom hemisphere measurement before computing the SMSE up to θ_{trunc} .

The so-obtained mean and maximum SMSE values over all measured frequencies are shown in Table 4.9, where it can be seen that the error levels are 20 dB and more larger than those reported in the first two validation steps. Aside from measurement noise and other measurement uncertainties common with NF testing, the extent of which was already implied by the SNR values in Table 4.8, two sources of error which inevitably cause differences in field patterns measured in different orientations could be identified: The interaction of the support structure with the AUT and the coaxial cable routing—the change in position of the support structure and the coaxial cable relative to the antenna is inevitable between measurements in different AUT orientations. To gain better understanding of the reported

Table 4.9: Validation results for measurements of connectorized AUTs

	<i>frequency range</i>	SMSE (top)		SMSE (bottom)	
		<i>mean</i>	<i>max</i>	<i>mean</i>	<i>max</i>
folded dipole	1.8 GHz – 2.0 GHz	–29.6 dB	–25.4 dB	–28.5 dB	–25.2 dB
UWB CMP	4 GHz – 20 GHz	–31.2 dB	–24.8 dB	–31.2 dB	–25.0 dB

increased SMSE levels, it is insightful to look at Figure 4.9, where the achieved error levels are plotted over the whole measured frequency range for both partial measurements of the UWB CMP antenna. Firstly, the figure reveals a ripple in SMSE levels which might give the impression that the method performs better at some frequencies than at others. When investigating this behavior, the ripple over frequency was compared to SNR estimates of the respective measurements, which showed that those frequencies where the SMSE is larger correspond to the frequencies where the SNR estimates were lower. This led to the conclusion that the worsened performance stems from measurement inaccuracies and not from the pattern stitching method. Whether this is caused by interaction of the AUT with

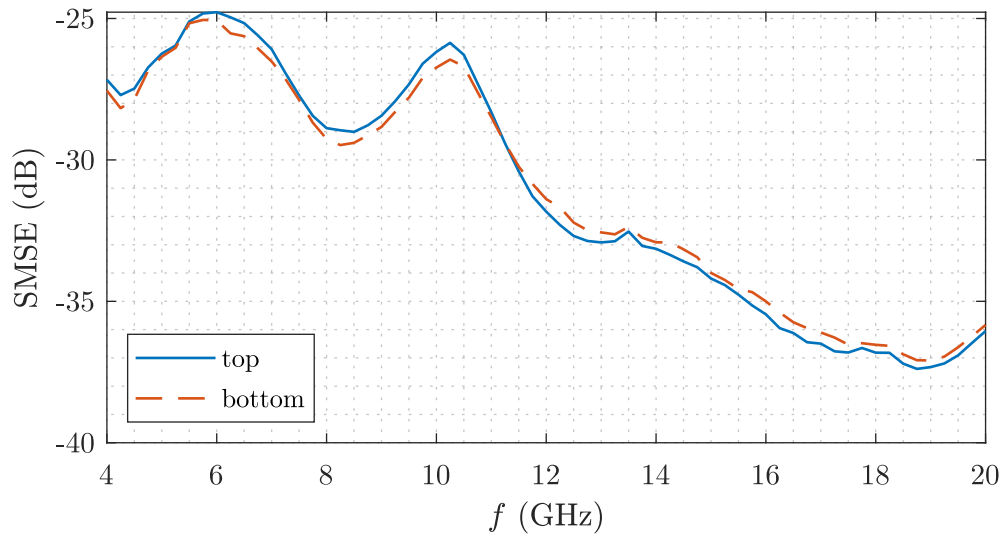


Figure 4.9: UWB CMP: SMSE over frequency

the coaxial cable, interaction with the support structure, or other sources of error, e.g., effects of rotary joints, cable mismatches, chamber reflections, etc., was not investigated at this point, but the topic will be revisited later. In addition to the discussed ripple, a general decrease of SMSE values with increasing frequency can be seen in Figure 4.9. Investigating the radiation patterns of the antenna over frequency, it was found that the back lobe of the antenna decreases in gain with increasing frequency, in turn increasing the antenna's directivity. Looking back at measurement orientations of the UWB CMP antenna in Figure 4.8, the reason for better performance at higher frequencies should become clear. Since the UWB CMP antenna radiates chiefly in the $+x$ -direction, the influence of both the cable and the support structure on the radiation patterns is reduced. In order to confirm that this is indeed the source of the observed performance improvement, a high-directivity dual-ridge horn antenna (DRHA) was also measured and processed with the pattern stitching method. In the two orientations shown in Figure 4.10, the DRHA was measured in steps of 100 MHz in the frequency range from 4 GHz to 10 GHz. The SMSE results, shown in Table 4.10, which were obtained in the same way as for the other two antennas, confirmed the expected improvement. Concretely, a mean SMSE reduction of about 6 dB was observed compared to the measurement results of the folded dipole antenna. Compared to the UWB CMP antenna, the average improvement was around 4 dB, and this lower observed improvement is mainly due to the impact of measurement results at higher frequencies, where the UWB CMP has higher directivity. Since the SMSE values

Table 4.10: Validation results for a directive AUT

	<i>frequency range</i>	SMSE (top)		SMSE (bottom)	
		<i>mean</i>	<i>max</i>	<i>mean</i>	<i>max</i>
DRHA	4 GHz – 10 GHz	-35.0 dB	-29.5 dB	-34.9 dB	-29.6 dB

of the DRHA were still relatively large compared to previous validation steps, the distribution of error over the measurement sphere was investigated to gain further insight. It was

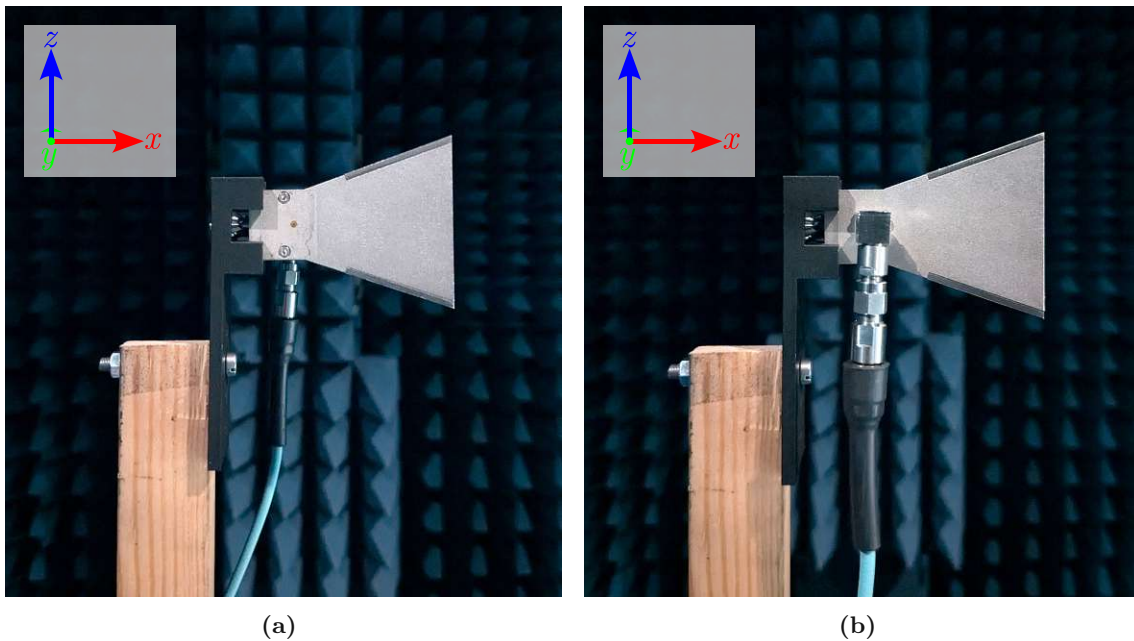


Figure 4.10: DRHA in (a) top and (b) bottom measurement orientation

found that larger errors are concentrated predominantly in the measurement range above $\theta = 90^\circ$, the range which is discarded in the final stitched patterns. An exemplary plot can be seen in Figure 4.11, where the scaled square error (ϵ) distribution (normalized by the largest measured field value as in the case of SMSE) for the upper measurement of the DRHA at 7 GHz is shown for both measurement polarizations. This finding implies that the final SWCs can describe the measured patterns in the upper measurement hemisphere rather well, but a mismatch between the top and bottom AUT orientation measurements exists, which deteriorates the performance of the pattern stitching method. Having in

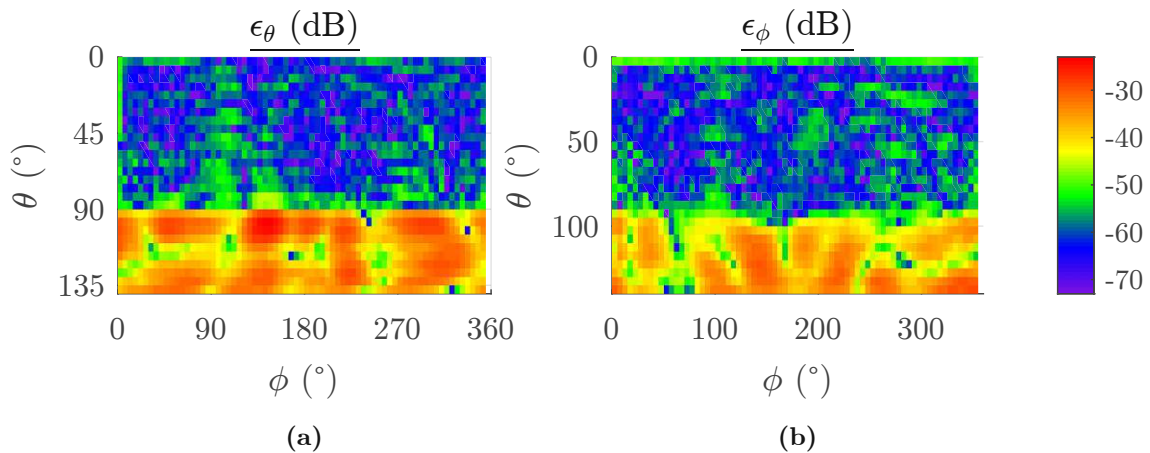


Figure 4.11: Scaled square error distribution: top measurement of the DRHA at 7 GHz

mind that the bottom part of the measurement is the part where the coaxial cable and the support structure are located, it is reasonable to expect that the largest distortions in the measured pattern due to their presence will also be located in the lower measurement hemisphere. For this reason, an additional SMSE evaluation approach was implemented,

following the same procedure as before but considering only measurement data from the upper measurement hemisphere (up to $\theta = 90^\circ$) for each respective measurement. The SMSE values obtained using this approach are listed in Table 4.11 for all three tested antennas, along with the approximate error reduction compared to SMSE values obtained for the whole measured θ -range, listed in Tables 4.9 and 4.10. Looking at the results, it can be seen that the SMSE values in this reduced range are 9 dB or more below those reported for the full measurement range. Overall, the stitched patterns match the measured hemisphere patterns up to SMSE values between -35 dB and -44 dB. It should be noted

Table 4.11: SMSE results in a reduced θ -range up to $\theta = 90^\circ$

	<i>mean error reduction (top/bottom)</i>	SMSE (top)		SMSE (bottom)	
		<i>mean</i>	<i>max</i>	<i>mean</i>	<i>max</i>
folded dipole	9 dB/9 dB	-38.7 dB	-36.3 dB	-37.4 dB	-35.2 dB
UWB CMP	10 dB/12 dB	-41.6 dB	-36.0 dB	-43.0 dB	-37.1 dB
DRHA	13 dB/11 dB	-48.1 dB	-43.9 dB	-46.0 dB	-42.1 dB

that the directive dual-ridge horn antenna was measured in different configurations using different support structures, the detailed results of which were omitted from this dissertation for the sake of conciseness. In an attempt to minimize the effects of the support structure, it was also measured using a block of low-permittivity material instead of the wood structure shown in Figure 4.10. However, regardless of the configuration, especially at frequencies where the SMSE was the largest, the changes in SMSE values were found to be negligible. This led to the conclusion that the impact of the support structure was not a dominant source of error, which must thus come either from the effects of the coaxial cable or general inaccuracies of the NF test range. While further investigation of these sources of error and the potential approaches for their mitigation will be discussed in Chapter 5, a reduction of error can intuitively be expected by simply excluding the coaxial cable from the measurement setup. This is possible when measuring connectorless active devices, which will be discussed in the remainder of this chapter.

4.3.2 Connectorless Devices

As already mentioned earlier, a measurement procedure was devised, capable of characterizing battery-powered connectorless devices under test (DUTs). The procedure requires the DUTs to transmit a CW signal at the frequency of interest, includes an additional reference antenna which maintains a constant orientation with regard to the DUT, and necessitates a calibrated received power measurement at the probe antenna. The pattern stitching method also had to be extended to work with measurement results of connectorless devices, which was achieved by including two additional parameters into the alignment procedure for compensation of the magnitude and phase offset between partial measurements stemming from the modified measurement procedure. Both the measurement procedure and the extension of the pattern stitching method are discussed in detail in Appendix C. By using such devices, the influence of the coaxial cable on the radiation pattern can be omitted and, therefore, an error reduction compared to connectorized AUTs was expected in this validation step. Five connectorless test devices were used for validation of the stitching method. The first four were electronic shelf labels (ESLs) of different sizes, shown in

Figure 4.12. They are equipped with a planar inverted-F antenna (PIFA), designed for operation in the industrial, scientific, and medical (ISM) band between 2.4 GHz and 2.5 GHz. All four were programmed to transmit a sequence of CW signals at the frequencies of interest after receiving a wake-up pulse, as described in Appendix C. Due to an unknown



Figure 4.12: ESLs used for validation of the stitching method: (a) ESL 1, (b) ESL 2, (c) ESL 3, and (d) ESL 4

misalignment, which was inevitable when placing the antenna onto the support structure, the maximum radial extents (MREs) used for computing the maximum polar order N were larger than the theoretical MREs obtained when considering only their dimensions. Their actual dimensions as well as the MREs used for computing N are listed in Table 4.12.

Table 4.12: ESL dimensions

	length	width	height	MRE
ESL 1	48 mm	36 mm	11 mm	50 mm
ESL 2	67 mm	34 mm	12 mm	100 mm
ESL 3	104 mm	82 mm	13 mm	125 mm
ESL 4	175 mm	123 mm	14 mm	150 mm

Before being stitched with the extended stitching algorithm from Appendix C, the DUTs were measured in two different orientations, similar to the case of connectorized AUTs. The first orientation, shown on the example of **ESL 3** in Figure 4.13a, was used to represent the top hemisphere measurement. Then, the DUTs were rotated by 180° around the x -axis to obtain the second orientation for the bottom hemisphere, shown in Figure 4.13b.

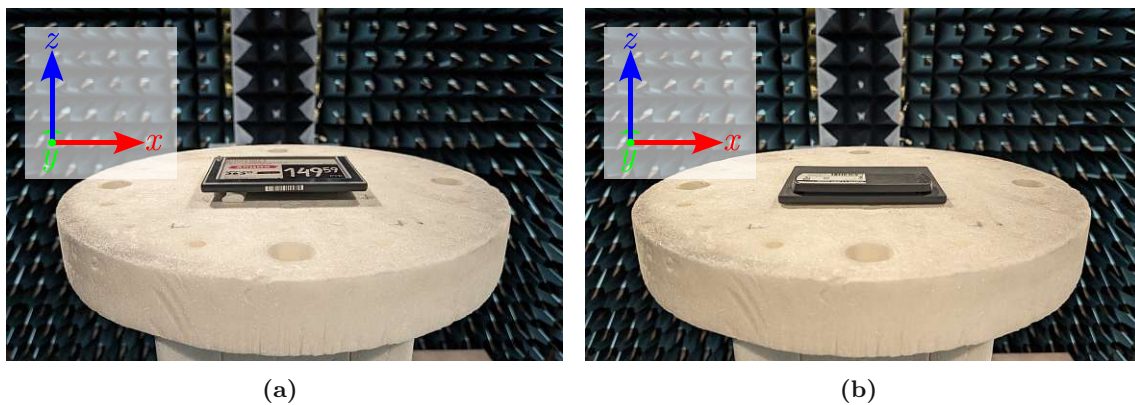


Figure 4.13: ESL 3 measurement in (a) top and (b) bottom orientation

The fifth test object was a commercial hearing aid equipped with a custom-designed antenna, also operating in the 2.4 GHz ISM band. This DUT, measured in the two orientations shown in Figures 4.14a and 4.14b, has a length of 52 mm, a width of 40 mm, and a height of 9.5 mm. For processing purposes, a slightly larger MRE of $r_0 = 50$ mm was selected.

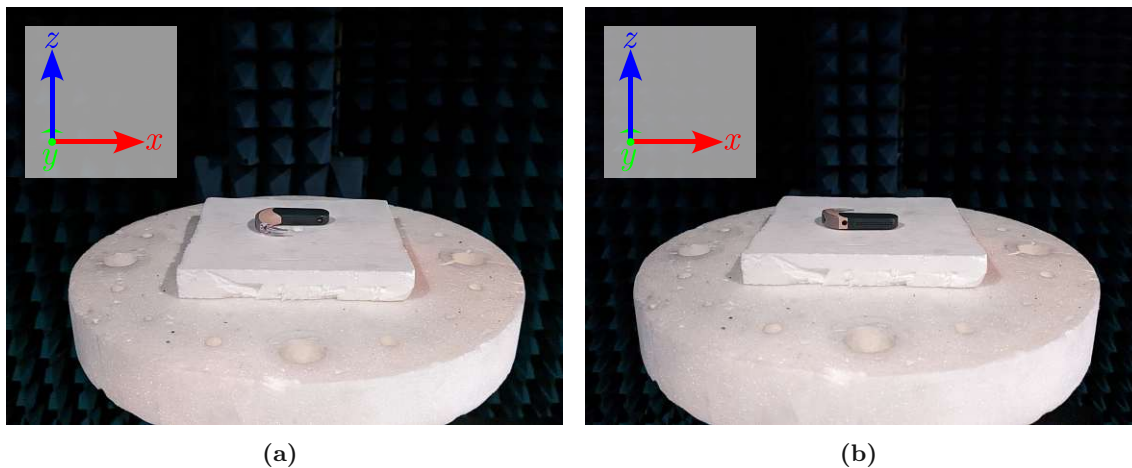


Figure 4.14: Hearing aid in (a) top and (b) bottom orientation

As with connectorized AUTs, SNR estimates were first computed for all test objects. For each of the DUTs, the SNR values are documented in Table 4.13, along with the order N used for computing them. Large differences between the two partial measurements could be observed especially for **ESL 4**, where this difference was more than 10 dB. These variations could be traced back to differences in the received signal strength at the reference antenna in different measurement orientations (see Appendix C), where lower signal strength resulted in increased noise in the pattern of the bottom measurement orientation.

Table 4.13: Measured data validation: estimated measurement SNR for connectorless DUTs

	<i>frequency range</i>	N	SNR (top)		SNR (bottom)	
			<i>mean</i>	<i>min</i>	<i>mean</i>	<i>min</i>
ESL 1	2.404 GHz – 2.479 GHz	12	38 dB	38 dB	38 dB	37 dB
ESL 2	2.404 GHz – 2.479 GHz	15	50 dB	47 dB	46 dB	43 dB
ESL 3	2.404 GHz – 2.479 GHz	16	47 dB	45 dB	43 dB	41 dB
ESL 4	2.404 GHz – 2.479 GHz	17	50 dB	47 dB	38 dB	36 dB
hearing aid	2.402 GHz – 2.480 GHz	12	40 dB	38 dB	41 dB	40 dB

The truncated patterns were then stitched together. As already observed with measurement results of connectorized AUTs, the alignment procedure did not always converge to the global minimum due to the high measurement noise levels and other measurement inaccuracies. Nevertheless, by using all available information on the measured antenna's position and exploiting the advantage of using multiple measurement frequencies, a good starting point could be found for all DUTs, which in turn led to successful convergence of the stitching method. Since full-sphere radiation patterns were not known for connec-

torless DUTs either, the same procedure as in the case of connectorized AUTs was used to evaluate the error of the final stitched results, observing errors in the top hemisphere measurement and errors in the bottom hemisphere measurement separately. With connectorless DUTs, the bottom hemisphere measurement correction includes an additional phase and magnitude correction according to (C.3) during the stitching procedure. Along with the translation and rotation to the bottom hemisphere measurement's coordinate system, these changes had to be reverted for SMSE evaluation on data from the bottom hemisphere measurement. The mean and maximum SMSE values over frequency were then found for both partial measurements, shown in Table 4.14. Compared to the re-

Table 4.14: Validation results of connectorless DUTs

	<i>frequency range</i>	SMSE (top)		SMSE (bottom)	
		<i>mean</i>	<i>max</i>	<i>mean</i>	<i>max</i>
ESL 1	2.404 GHz – 2.479 GHz	−30.1 dB	−29.3 dB	−30.4 dB	−30.2 dB
ESL 2	2.404 GHz – 2.479 GHz	−30.9 dB	−30.0 dB	−31.4 dB	−31.0 dB
ESL 3	2.404 GHz – 2.479 GHz	−27.3 dB	−26.3 dB	−27.4 dB	−26.6 dB
ESL 4	2.404 GHz – 2.479 GHz	−26.9 dB	−25.6 dB	−27.2 dB	−26.7 dB
hearing aid	2.402 GHz – 2.480 GHz	−29.4 dB	−28.9 dB	−29.2 dB	−29.0 dB

sults of connectorized AUTs from Table 4.9, **ESL 1**, **ESL 2**, and the **hearing aid** show marginally better SMSE results, while results of **ESL 3** and **ESL 4** are slightly worse than those of the tested low-directivity connectorized AUTs. As was done during validation with connectorized antennas, the errors were also evaluated in a reduced θ -range up to $\theta = 90^\circ$. The results are listed in Table 4.15, where it can be seen that a lesser improvement was typically achieved compared to the results of connectorized antennas shown in Table 4.11. Further, the results show that the differences in SNR between the top and

Table 4.15: Validation results of connectorless DUTs in a reduced θ -range up to $\theta = 90^\circ$

	<i>mean error reduction (top/bottom)</i>	SMSE (top)		SMSE (bottom)	
		<i>mean</i>	<i>max</i>	<i>mean</i>	<i>max</i>
ESL 1	5 dB/4 dB	−35.1 dB	−34.7 dB	−34.2 dB	−33.6 dB
ESL 2	9 dB/5 dB	−39.4 dB	−38.2 dB	−36.8 dB	−35.9 dB
ESL 3	10 dB/7 dB	−37.2 dB	−35.6 dB	−34.6 dB	−34.4 dB
ESL 4	9 dB/5 dB	−36.2 dB	−34.7 dB	−32.4 dB	−31.6 dB
hearing aid	6 dB/5 dB	−35.8 dB	−35.1 dB	−34.5 dB	−34.3 dB

bottom measurement orientation translate to differences in the error reduction achieved by observation in the reduced range of θ -angles. This could be expected since the weak signal received at the reference antenna, which was the identified source of lower SNR values for bottom hemisphere measurements for some DUTs, uniformly distorts measured ratioed field readings over the whole measurement surface. In turn, this causes larger mismatch between measured patterns and the physically permissible patterns which can be described by a set of SWCs of the given maximum polar order N .

In conclusion, the SMSE results from Tables 4.14 and 4.15 show similar values as the results of the omnidirectional folded dipole antenna from Tables 4.9 and 4.11, while results of the UWB CMP showed lower mean SMSE values due to the increased directivity at higher frequencies. The expected improvement of results due to exclusion of the coaxial cable from the measurement environment could thus not be confirmed. However, caution should be taken when directly comparing the reported results of connectorized AUTs and connectorless DUTs since the test objects are of different sizes and operating at different frequencies. Moreover, replacing a dedicated measurement device, i.e., vector network analyzer (VNA), with an active device's consumer electronics RF transmitter chip inevitably deteriorates the accuracy of the measured patterns in terms of both magnitude and phase errors. Overall, validation results using measurement data have shown a large performance deterioration compared to the validation results using synthetic data and EM simulation data, which required further analysis of the various error sources present in practical measurements. This analysis deserves special attention and will be presented in the following chapter, dedicated to the practical limitations of accuracy in pattern stitching.

5 Practical Limitations of Accuracy

In Chapter 4, large differences between the error levels for tests on synthetic data, electromagnetic (EM) simulation data, and measurement data could be observed during the validation process. By stitching noiseless synthetic radiation patterns, the error introduced by the stitching method itself could be quantified, which remained below -80 dB for all realistic test cases with misalignments up to 3λ , reaching -43 dB in the extreme case where a misalignment distance of more than 20λ was used. The introduction of simulation noise, inherent to any field pattern obtained via numerical EM simulation, resulted in an increase of error levels for test objects at higher frequencies, however, the largest observed error levels were still in the range of -38 dB. Up to this point, an ideal measurement environment was considered, where the antenna under test (AUT) is located in free space and can be enclosed by a sphere with a radius of r_0 , which represents the maximum radial extent (MRE) of the antenna.

Considering a realistic measurement environment, such as the near-field test range at TU Wien shown earlier in Figure 1.2, it is impossible to meet these conditions in practice. Various sources of uncertainties, stemming predominantly from mechanical, electrical, and computational inaccuracies, are inherent to any spherical near-field antenna measurement. These inevitably distort measured radiation patterns and result in deviations from a theoretical solution of the wave equation which can be represented as a series of spherical wave coefficients (SWCs). Among these sources of error, there are two that have an especially significant impact on the proposed pattern stitching method. Firstly, the support structure onto which the antenna to be measured is mounted, which is the reason for having to work with truncated field patterns in the first place, also directly interacts with the AUT's radiated fields, inevitably changing their spatial distribution. Secondly, cable-connected AUT measurements require a connection between the vector network analyzer (VNA) and the AUT by means of a coaxial cable, which again interacts with the radiated fields and distorts the measured field pattern. When the AUT is measured in multiple orientations in an attempt to characterize its behavior on the whole sphere surface, the relative position of the support structure and the coaxial cable with regard to the antenna is changed between these measurements. These issues cause disagreements between partial truncated measurements to be stitched, ultimately resulting in an increased error in the stitched pattern and, in extreme cases, its failure.

Due to these imperfections compared to a perfect free-space environment, much larger mismatches between measured patterns and the final stitched patterns have been observed during the validation step in which actual measurement data were used. Here, the errors

were found to be in the range between -35 dB and -25 dB. This chapter is dedicated to the analysis of these practical limitations and the possibilities for their mitigation.

5.1 Sources of Error in Spherical Near-Field Measurements

As mentioned above, a variety of sources of error common to all spherical near-field measurements exist, originating from either mechanical, electrical, or computational inaccuracies. They will be discussed here briefly for the sake of completeness, while an in-depth analysis of these sources of error was out of scope of this work. Generally, the sources of error involved in a spherical near-field antenna measurement can be divided into six distinct categories: mechanical errors, electrical errors, probe-related errors, stray signal errors, acquisition errors, and processing errors. According to [60, Chapter 9], there are 21 individual sources of error within these six categories, as listed in Table 5.1. Error source 18, scan area truncation, of course, has been the main motivation for the research done in this dissertation. The influence of the support structure, which has been mentioned earlier in this chapter and plays a significant role in pattern stitching, is listed under 17. Errors due to the coaxial cable have not been included in this extensive list of errors, presumably due to its negligible effect when measuring directive antennas and because the cable is often considered part of the AUT. It belongs in the same category of error sources as AUT support scattering, i.e., stray signal errors. One should note that not all listed sources of error are applicable in all measurement systems and configurations. The probe-related errors 12 and 13, for example, are only applicable when using dual polarized probe antennas, which are not used in the NF range at TU Wien. Furthermore, the sampling point offset under 19 can be excluded from measurements by stopping at each measurement point to measure the signals, coming at the cost of increased measurement times. Lastly, the total radiated power computation, listed in processing errors under 21, is a specific computation not generally required when gain calibration is done by substitution with a standard gain horn (SGH) antenna.

All remaining error sources listed in Table 5.1 contribute to the overall measurement error in the NF range at TU Wien and also affect the accuracy of the pattern stitching method. To determine the level of inaccuracy that each of these terms can cause, an uncertainty analysis would be required, which is not a trivial task in practice. Since the far-field pattern is obtained by transformation from sampled near-field data, a direct evaluation of uncertainties based on observed errors, as can be done in the case of far-field measurements, is not possible. In [19], the authors therefore suggest the use of EM simulations for their assessment. They emphasize the dependency of such an analysis on the nature of the AUT, indicating that it should be done for the given antenna under test of interest. This procedure could also be extended to test the impact of these error sources on final stitched patterns, which was not done at this point due to time constraints. Instead, the signal-to-noise ratio (SNR) level estimates reported in Tables 4.8 and 4.13 for validation measurements were used to obtain an estimate for the overall measurement error containing all individual contributions from Table 5.1. These estimates, ranging from 36 dB to 50 dB, give an indication that the overall measurement error is lower than the error levels of final stitched patterns reported in Chapter 4. This suggests that the errors attributed to the coaxial cable and the support structure are indeed the limiting factors of accuracy of the pattern stitching method and thus deserve further attention.

Table 5.1: Sources of error in spherical near-field antenna measurements [60, Chapter 9]

	error source		description
mechanical errors	1	axes intersection	<i>lateral displacement between the horizontal and vertical axes</i>
	2	axes orthogonality	<i>horizontal and vertical axes not perfectly orthogonal</i>
	3	horizontal pointing	<i>the horizontal axis not pointing to the probe antenna at $\theta = 0^\circ$</i>
	4	probe vertical position	<i>vertical displacement of the probe from the horizontal axis</i>
	5	probe horizontal and vertical pointing	<i>horizontal and vertical mispointing of the probe's z-axis</i>
	6	measurement distance	<i>inaccurate distance between the AUT and the probe</i>
electrical errors	7	amplitude and phase drift	<i>systematic amplitude and phase change at still AUT</i>
	8	amplitude and phase noise	<i>random amplitude and phase change at still AUT</i>
	9	leakage and crosstalk	<i>interfering extraneous signals on channel paths</i>
	10	amplitude nonlinearity	<i>nonlinear relationship between measured values and input signal level</i>
	11	amplitude and phase shift in rotary joints	<i>systematic amplitude and phase change in rotary joints at different angles</i>
probe-related errors	12	amplitude and phase channel balance	<i>amplitude and phase imbalance when using two polarization channels</i>
	13	polarization amplitude and phase	<i>amplitude and phase differences when using dual-polarized probes</i>
	14	pattern knowledge	<i>deviations from the known/assumed probe pattern</i>
stray signal errors	15	multiple reflections	<i>changes in the received signal due to interactions between the AUT and the probe</i>
	16	room scattering	<i>changes in the received signal due to finite reflectivity of the anechoic chamber</i>
	17	AUT support scattering	<i>changes in the received signal due to scattering from the support structure</i>
acquisition errors	18	<u>scan area truncation</u>	<i>errors due to acquisition only on a partial sphere surface</i>
	19	sampling point offset	<i>position offset when the positioner continuously rotates during measurement</i>
processing errors	20	spherical mode truncation	<i>changes in patterns due to SWC truncation at the calculated maximum polar order N</i>
	21	total radiated power	<i>total radiated power (TRP) numerical integration errors</i>

5.2 Influence of a Coaxial Cable

Following the conclusions drawn in the previous section, the first limiting source of inaccuracy when using the pattern stitching method to be investigated was the influence of a coaxial cable on stitched patterns, where major differences between measured field patterns of different antenna orientations can be expected. In order to analyze the severity of its impact, comparative EM simulations and measurements have been done, the results of which will be presented in the following two subsections.

5.2.1 EM Simulations

In the first step, analysis using EM simulations was done by including a simplified cable model to a model of an antenna standing in free space. Under the assumption that radiating fields interact only with the outer conductor of a cable, a simple rod with a diameter of 5 mm and a length of 20 cm was modeled to represent the coaxial cable. Here, it should be noted that an imbalance between current flowing on the inner conductor and current flowing on the outer conductor of a coaxial cable can lead to sheath currents and cable radiation in practice. The analysis on the influence of a coaxial cable on radiation patterns considered in this section has been reduced to scattering effects under the assumption that potential sheath currents can be suppressed using common countermeasures, such as a balun, ferrite beads, or similar.

The metal rod representing the simplified cable model was added to the antenna model of a planar inverted-F antenna (PIFA) shown earlier in Figure 3.8, designed for operation at 2.4 GHz, which was already used for tests in previous chapters of this work. The cable was routed such that it points downwards from the antenna, in the negative z -direction, as would be the case during a measurement in the near-field test range at TU Wien. This orientation is shown in Figure 5.1a. For the second antenna orientation, shown in Figure 5.1b, the antenna was rotated by 180° around the y -axis while the cable remained fixed in its position. To avoid meshing changes between the two configurations, both coaxial cable models were included in both configurations and the material of the one

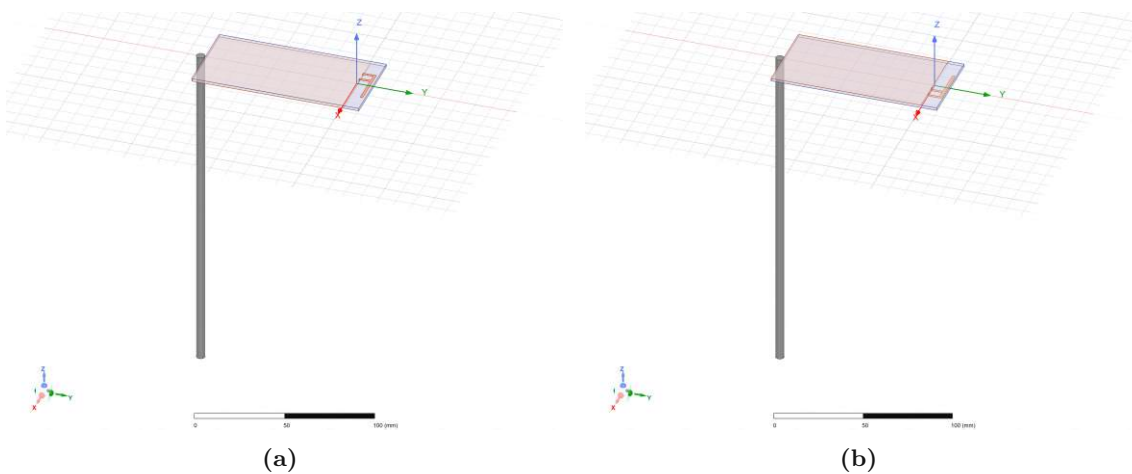


Figure 5.1: Influence of a coaxial cable: (a) simulation of the top hemisphere measurement and (b) bottom hemisphere measurement when the antenna is oriented horizontally

unused in the given configuration was assigned to be vacuum. To allow for a comparison with a free-space cableless configuration, an additional simulation was carried out where both cable models were set to vacuum.

In the above example, the antenna was oriented horizontally with its ground plane lying in the xy -plane. Considering the dimensions of the PIFA and the coordinate system of the antenna range in Figure 3.1, this is the natural orientation where the AUT is laid on the support structure. As an alternative orientation, the PIFA was rotated by 90° around the y -axis into a vertical orientation with regard to the coordinate system, resulting in the two simulation configurations shown in Figure 5.2. This way, the cable is aligned with the current flow in the main part of the antenna as well as with the strongest radiation null. As for the horizontal case, three simulations were carried out, two with the presence

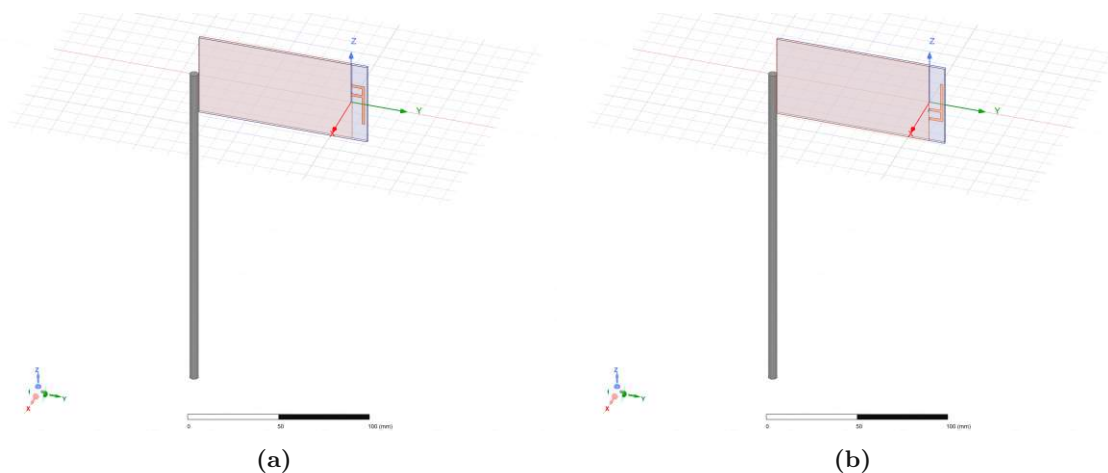


Figure 5.2: Influence of a coaxial cable: (a) simulation of the top hemisphere measurement and (b) bottom hemisphere measurement when the antenna is oriented vertically

of a coaxial cable and one where both cables were excluded. To determine to what extent the presence of a coaxial cable in the measurement environment influences stitched patterns, simulated patterns of the antenna with a cable in both considered configurations, shown in Figure 5.1 for the horizontal antenna orientation and in Figure 5.2 for the vertical orientation, were first processed with the **pattern stitching method**. Then, these stitched patterns were compared to the free-space patterns and the scaled mean square error (SMSE) values were computed both for near-field patterns and for far-field patterns. The results are listed in Table 5.2, where it can be seen that results of both test cases show large discrepancies compared to the free-space pattern. For the horizontal antenna orientation, the errors are of the same order as the largest measurement errors reported in Table 4.9, where SMSE levels for validation measurements of connectorized AUTs were

Table 5.2: Influence of a coaxial cable: simulation results

	pattern stitching method		full-sphere measurement	
	<i>NF SMSE</i>	<i>FF SMSE</i>	<i>NF SMSE</i>	<i>FF SMSE</i>
horizontal	-25.7 dB	-25.5 dB	-20.5 dB	-20.5 dB
vertical	-18.5 dB	-18.3 dB	-14.1 dB	-14.1 dB

shown. Results for the vertical antenna orientation show even higher error levels that are about 7 dB larger than those of the horizontal orientation. Investigating this large difference in error levels between the two orientations, its origin could be traced back to the larger coupling between the antenna and the cable model in the vertical case, inducing stronger currents on the ungrounded cable model, which, in turn, resulted in stronger pattern distortions. Inspecting the radiation pattern, it became clear that neither of these cable routings is located within the radiation nulls of the antenna and significant interaction of the antenna's radiated fields with the cable model could be observed. In an attempt to reduce this interaction as much as possible, an alternative cable routing was chosen where the cable models were aligned with the radiation nulls. The chosen two simulation orientations along with the radiation pattern of the antenna in free space are shown in Figure 5.3. Simulation patterns of these two null-aligned cable routing models

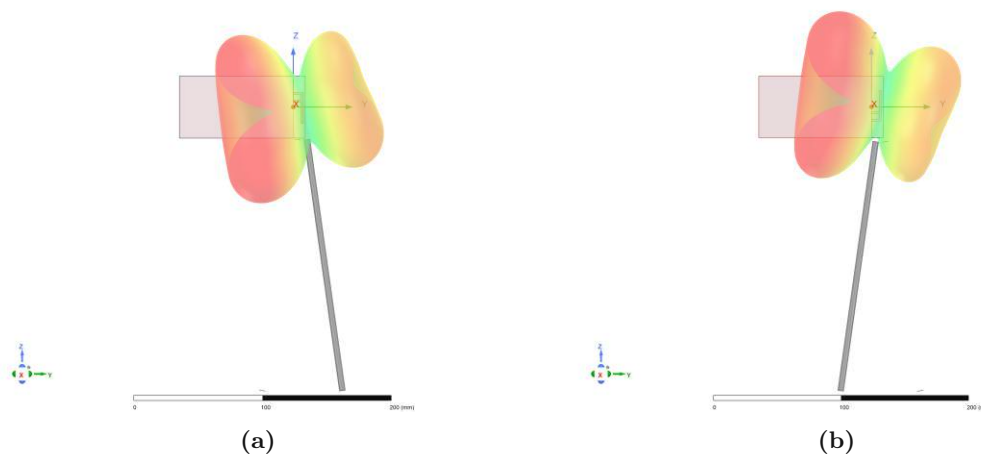


Figure 5.3: Influence of a coaxial cable: (a) simulation of the top hemisphere measurement and (b) bottom hemisphere measurement when the cable is aligned with the radiation null

were then processed in the same way as previous models and the results are shown in Table 5.3. An improvement of about 11.5 dB compared to the results of the vertical orientation model and about 4.5 dB compared to the results of the horizontal orientation model, reported in Table 5.2, could be observed. These findings demonstrate the importance of cable routing for error reduction in pattern stitching and care should be taken to route the measurement cable in such a way that its interaction with the antenna is minimal, which is a task that needs to be done individually for each AUT.

Table 5.3: Influence of a coaxial cable: simulation results

	pattern stitching method		full-sphere measurement	
	<i>NF SMSE</i>	<i>FF SMSE</i>	<i>NF SMSE</i>	<i>FF SMSE</i>
null-aligned	-30.3 dB	-29.9 dB	-26.2 dB	-26.3 dB

In order to put results of the pattern stitching method into perspective, untruncated simulation patterns from configurations in Figures 5.1a and 5.3a were also compared to those of the antenna in free space. Here, the untruncated simulated pattern in the presence

of a cable was used to represent a simplified measurement environment with a measurement cable but without a support structure. NF and FF SMSE were evaluated to estimate how well such a **full-sphere measurement** can represent the antenna’s radiation pattern in free space. The results have also been listed in Tables 5.2 and 5.3, where one can observe an error increase of 4 dB – 5 dB compared to the **pattern stitching method** for both antenna orientation pairs. This indicates that, when using the pattern stitching method, antenna radiation patterns can be obtained which resemble free-space radiation patterns of an antenna more closely than those of a classical full-sphere measurement. Considering the nature of the stitching procedure, this does not come as a surprise. Since only the upper hemisphere data of both truncated measurements are used, the part of the radiation pattern most influenced by the coaxial cable is discarded in the stitched patterns. This can best be demonstrated by comparing the stitched pattern SMSE of the horizontally oriented antenna from Figure 5.1 to the SMSE of the stitched pattern using the same simulation data where, instead of stitching the hemispheres opposite from the cable model (**stitched tops**), hemispheres containing the cable model (**stitched bottoms**) were used for pattern stitching. The results of this comparison, presented in Table 5.4, demonstrate an error increase of approximately 7 dB when stitching bottom hemispheres instead of top hemispheres. Further, a full-sphere measurement simulation in this case outperforms the pattern stitching method, which is not surprising considering that stitching the bottom hemispheres can be interpreted as stitching those parts of both radiation patterns which are most distorted by their respective coaxial cables.

Table 5.4: Influence of a coaxial cable: advantage of pattern stitching over full-sphere measurements

	pattern stitching method		full-sphere measurement	
	NF SMSE	FF SMSE	NF SMSE	FF SMSE
stitched tops	–25.7 dB	–25.5 dB	–20.5 dB	–20.5 dB
stitched bottoms	–18.4 dB	–18.4 dB	–20.5 dB	–20.5 dB

Regardless of the measurement orientation, relatively high errors were observed both for pattern stitching and conventional full-sphere measurements. These error levels can be considered an approximate level of achievable accuracy when omnidirectional antennas are measured. In practice, error levels will depend both on the type of the AUT and the routing of the coaxial cable. To minimize the impact of the cable, optimal routing thus has to be considered separately for each case.

5.2.2 Measurements

In Section 4.3, two connectorized AUTs were measured and processed with the stitching method along with several active connectorless DUTs which were measured and processed with an adapted approach (presented in Appendix C) devised specifically for connectorless DUTs. Contrary to expectations, the observed scaled mean square error (SMSE) levels of connectorless DUTs were in the same order as those reported for connectorized AUTs, which could give the misleading impression that the influence of a coaxial cable is negligible in the overall error of the pattern stitching method. However, as already

demonstrated with the help of EM simulations, large variations in error levels can be observed between simulations with different cable routings. This directly relates to the electric field distribution of a given AUT, which is a unique property of the antenna at hand. As such, the measurement data results in Appendix C are not directly comparable. To be able to quantify the influence of a coaxial cable on the measurement accuracy, a direct comparison of results of the same AUT measured with and without a cable was needed. For this purpose, the same device had to be measured and stitched both with the classical connectorized pattern stitching method and with the adapted method for connectorless DUTs. To do so, a coaxial connector was soldered onto the printed circuit board (PCB) of **ESL 4**, which was previously measured as a connectorless device. The connector was placed directly at the feed of the PIFA, as shown in Figure 5.4a. A short cable was attached to the connector and routed out of the housing through a small cutout, after which the complete DUT including batteries was reassembled. The connectorized **ESL 4**, which can be seen in Figure 5.4b, was then measured at the same frequencies as in Section 4.3 and in the same two measurement orientations as shown on the example of **ESL 3** in Figure 4.13, this time as a connectorized device. The measured patterns



Figure 5.4: Connectorized ESL 4: (a) PCB and (b) assembled device

were then processed with the stitching method and SMSE values of partial measurements were computed in the same way as in Section 4.3. In Table 5.5, the SMSE values of this remeasured *connectorized* **ESL 4** are listed along with SMSE values of the *connectorless* **ESL 4**, which were presented already in Table 4.14. These results clearly demonstrate the

Table 5.5: Comparison: connectorless and connectorized measurement of ESL 4

		SMSE (top)		SMSE (bottom)	
		<i>mean</i>	<i>max</i>	<i>mean</i>	<i>max</i>
ESL 4	<i>connectorless</i>	-26.9 dB	-25.6 dB	-27.2 dB	-26.7 dB
ESL 4	<i>connectorized</i>	-19.9 dB	-19.7 dB	-20.3 dB	-20.1 dB

severity of the influence of the coaxial cable, which was found to cause an error increase of approximately 6 dB to 7 dB, and the results are within the range of EM simulation results in Tables 5.2 and 5.3. Measurements of active connectorless DUTs therefore have a clear advantage in terms of accuracy when compared to measurements of connectorized AUTs and should therefore be the preferred measurement method for pattern stitching whenever

the DUT permits it. At this stage, it should also be noted that, in contrast to the EM simulations, the results in Table 5.5 also include potential cable radiation due to sheath currents, which was not investigated in this work, as well as the influence of the support structure, which will be discussed in the remainder of this chapter.

5.3 Influence of the Support Structure

The second source of error to be investigated was the influence of the support structure. Depending on the nature of the AUT, different materials can be used for the support structure. If high-gain antennas are measured, oriented away from the support structure with their main radiation beam, the material used for the support structure plays a lesser role, allowing for materials with arbitrary electromagnetic properties, i.e., arbitrary electric permittivity ε and magnetic permeability μ . If, on the other hand, low-gain, omnidirectional antennas are measured, the interaction between the radiated fields and the support structure becomes important. In order to mimic free-space conditions, the obvious choice thus become materials with EM properties closely resembling those of air.

5.3.1 Support Structures

To the best of my knowledge, the best choice for materials with EM properties closely imitating air are foams from the ROHACELL family [61]. During measurements used for pattern stitching method validation (Chapter 4), a support structure made from discontinued ROHACELL 31 IG foam was used, shown in Figure 5.5a. The supplier reported measured values of $\varepsilon_r = 1.05$ and $\tan \delta = 0.0006$ at 2.8 GHz [62]. This structure had an unnecessarily large surface and, furthermore, its performance was influenced by impurities, such as layers of glue and carbon dust from the absorbers used in the anechoic chamber. A new, more compact support structure was thus built using ROHACELL 31 HF, which offers the best dielectric performance, with reported dielectric constant of $\varepsilon_r' = 1.05$ and a loss tangent of $\tan \delta < 0.0002$ at 2.5 GHz [61]. This structure is shown in Figure 5.5b and was constructed specifically for use with connectorless DUTs, where no coaxial cable is attached to the device under test.

The hearing aid connectorless DUT, which was shown earlier in Figure 4.14, was remeasured in the same two measurement orientations using the new support structure and processed with the stitching method. Just as in Section 4.3, the final stitched patterns for all frequencies were compared to measurement data to determine how well they match. Mean and maximum SMSE values over frequency are listed in Table 5.6 for both the old ROHACELL 31 IG support structure and the new ROHACELL 31 HF support structure. As can be seen, an improvement of approximately 3 dB could be achieved by using the new support structure. This comparison should not be interpreted as a direct comparison between the two materials used since impurities of the old support structure and the differing dimensions also have an impact on the reported error values. Instead, it is a comparison between the existing support structure that was generally used for measurements at TU Wien and the optimized support structure, designed to minimize its impact on the overall error of the pattern stitching method. Even with the observed improvement, the reported error levels are relatively high considering that ROHACELL 31 HF is the material that resembles

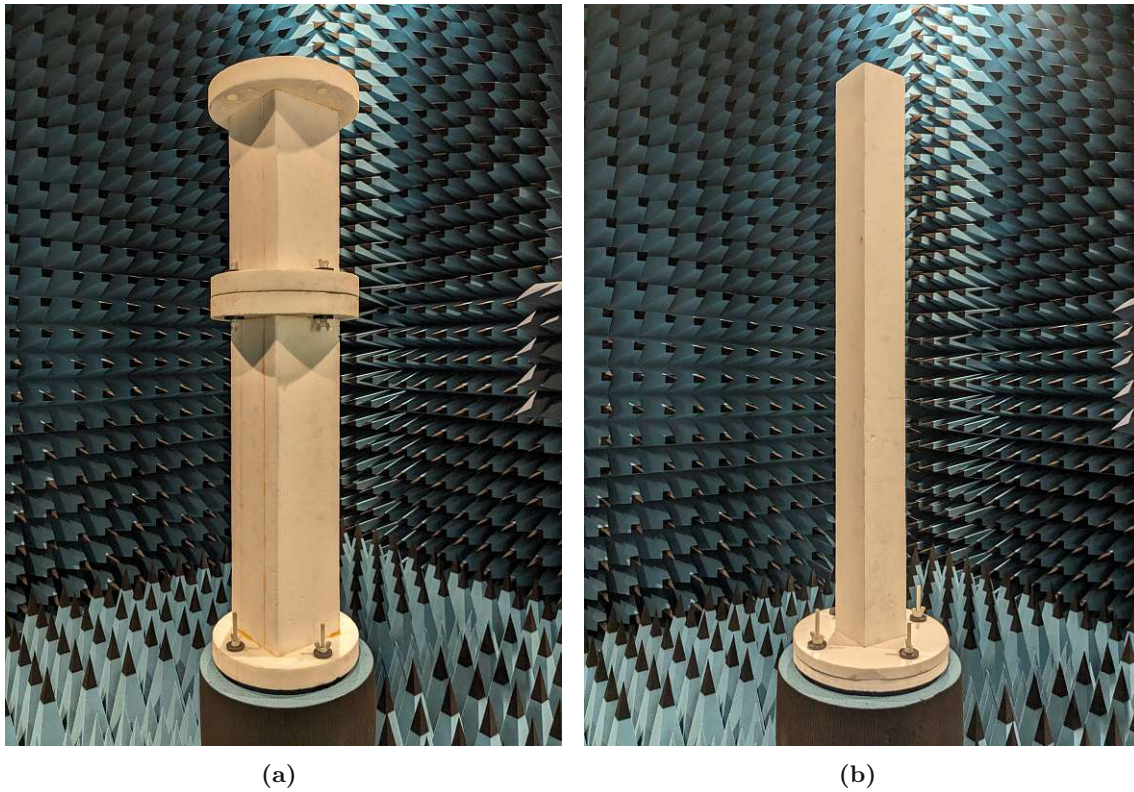


Figure 5.5: Support structure comparison: (a) the old structure made from ROHACELL 31 IG and (b) the new ROHACELL 31 HF structure

Table 5.6: Support structure comparison: hearing aid

	<i>frequency range</i>	SMSE (top)		SMSE (bottom)	
		<i>mean</i>	<i>max</i>	<i>mean</i>	<i>max</i>
31 IG	2.402 GHz – 2.48 GHz	−29.4 dB	−29.0 dB	−29.2 dB	−29.0 dB
31 HF	2.402 GHz – 2.48 GHz	−32.7 dB	−32.4 dB	−31.4 dB	−31.2 dB

air the closest in terms of its EM properties and, as such, is the most suitable material for constructing a support structure. To verify whether these are indeed the practical limits due to the support structure when measuring omnidirectional antennas, further measurement and EM simulation tests have been carried out, presented in the following sections.

5.3.2 SGH Measurements

While the overall stitching errors reported in Table 5.6 gave an indication of the achievable SMSE levels, it is impossible to confirm whether these stem from the support structure, other measurement uncertainties, or the stitching method itself. To analyze the influence of ROHACELL on measured field patterns while excluding potential errors introduced by the stitching method, further measurements were done using a standard gain horn (SGH) antenna, SGH430, operating in the frequency range between 1.7 GHz and 2.6 GHz. Two disks of ROHACELL 31 HF [61] with a diameter of 47 cm, which just covers the physical

aperture of the antenna, were used for testing. One disk had a thickness of 2 cm and the other was 10 cm thick. The antenna was measured in the near-field test range at TU Wien three consecutive times, once without ROHACELL, once covered with the thinner of the two disks and once with the thicker disk, as shown in Figures 5.6a to 5.6c. To estimate the

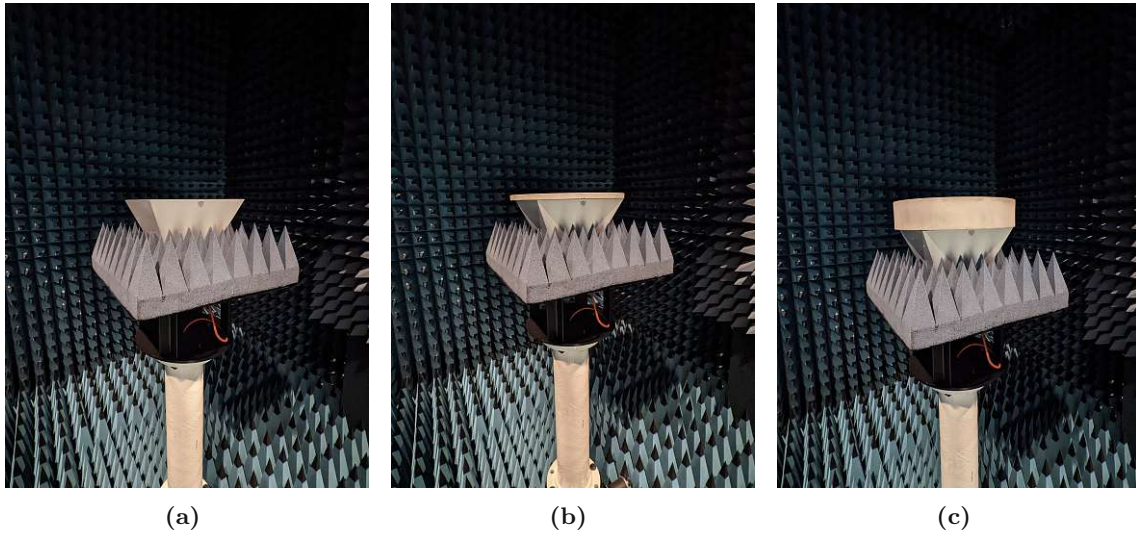


Figure 5.6: Influence of ROHACELL 31 HF: (a) antenna measurement without ROHACELL, (b) with a 2 cm thick disk, and (c) with a 10 cm thick disk

level of error that these two disks introduce, the patterns of both cases where the AUT was covered with a ROHACELL 31 HF disk were then compared to those of the uncovered antenna. In both cases, the scaled mean square error (SMSE) between measured patterns of the uncovered antenna and measured patterns with the respective ROHACELL 31 HF disk were computed for all measured frequencies, once using only magnitude information of the measured patterns and once using measured complex field values. The results are listed in Table 5.7, where the mean SMSE over all frequencies and the maximum observed deviation from the mean value are given for both cases.¹ Considering only magnitude

Table 5.7: Influence of ROHACELL 31 HF: SGH measurement results

	magnitude SMSE	total SMSE
ROHACELL disk: 2 cm	$-54.2 \text{ dB} \pm 4.3\%$	$-45.3 \text{ dB} \pm 2.5\%$
ROHACELL disk: 10 cm	$-51.6 \text{ dB} \pm 6.9\%$	$-31.9 \text{ dB} \pm 3.1\%$

information, one can see that the SMSE values remain below -50 dB for both disks, while the total SMSE values are significantly larger. This suggests that the observed errors caused by the inclusion of ROHACELL 31 HF disks mainly stem from phase distortion of measured patterns and less from dielectric losses. Furthermore, the total SMSE of the 2 cm

¹It is important to note that the only changing parameter between the three measurements shown in Figure 5.6 was the introduction of the ROHACELL 31 HF disks. Thus, all systematic errors remained unchanged between consecutive measurements and cancel out during comparison. Random errors, on the other hand, which originate from positioning repeatability, thermal noise, etc., could not be excluded from the measurement and inevitably influence the results. However, it was found that their influence is negligible compared to the large increase of error between results of the two test disks reported in Table 5.7.

thick disk is more than 13 dB lower than that of the 10 cm disk, demonstrating the expected relation of the phase distortion with the thickness of the dielectric material. The severity of the influence of a support structure, even when using the low-loss, low-permittivity ROHACELL 31 HF, could therefore be confirmed, limiting the accuracy of measured radiation patterns of omnidirectional antennas. Since propagation in a dielectric medium causes a phase delay compared to propagation in free space, and this phase delay increases proportionally to the frequency, the impact of the support structure on the SMSE will also increase at higher frequencies. Even larger errors must therefore be expected at higher frequencies, which will limit the achievable accuracy of the pattern stitching method.

5.3.3 EM Simulations

In an attempt to mimic the influence of the manufactured ROHACELL 31 HF support structure on stitched truncated patterns and compare it to measured full-sphere patterns with that same support structure, two cubes with a 10 cm edge length were added to the simulation model of the planar inverted-F antenna (PIFA) from Figure 3.8, covering its top and bottom surface, to obtain the model shown in Figure 5.7. To avoid errors due to

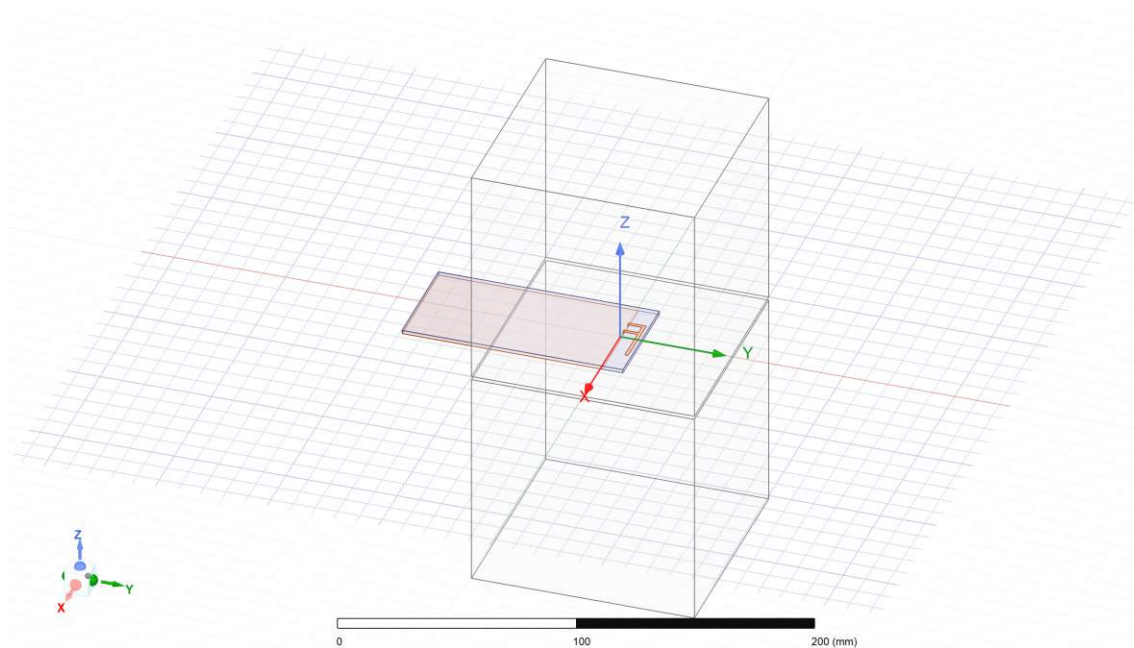


Figure 5.7: Influence of ROHACELL 31 HF: simulation model

differences in meshing, this structure was simulated thrice while maintaining a constant mesh. First, it was simulated with vacuum assigned to both cubes to represent the AUT in free space. Then, the bottom cube was assigned to have the electromagnetic properties of ROHACELL 31 HF, representing the top hemisphere measurement. Lastly, the bottom cube was changed back to vacuum and the top cube was assigned to be ROHACELL 31 HF, representing the bottom hemisphere measurement. Field patterns of all were exported and processed in the following manner:

- **truncated pattern stitching:** For pattern stitching, the top and bottom hemisphere simulated patterns were first truncated at $\theta_{\text{trunc}} = 140^\circ$ and then stitched

together, thus giving the stitched NF and FF patterns.

- **full-sphere simulation:** Even in NF ranges capable of full-sphere measurements, the support structure is an inevitable part of any practical measurement. The simulated pattern with the bottom cube made from ROHACELL 31 HF was used to compute the NF and FF patterns using SN2FFT.

These patterns were then compared to the free-space patterns obtained with the same mesh by computing the NF SMSE and the FF SMSE. Results are shown in Table 5.8, where it can be seen that error levels when using the **truncated pattern stitching** method are at approximately -26.5 dB. These are somewhat larger than the results for the hearing aid presented in Table 5.6, but are in the same range with errors reported for larger electronic shelf labels (ESLs) in Table 4.14, leading to the conclusion that, also here, the type and orientation of the AUT have a significant impact on the results. Looking at FF SMSEs obtained from **full-sphere simulations** in the presence of a support structure, the results for the stitched patterns show a marginal error increase of 0.4 dB to 0.6 dB. This confirms that the limitations of the support structure when measuring omnidirectional antennas are inherent to any antenna measurement and are not an issue specific to pattern stitching.

Table 5.8: Influence of ROHACELL 31 HF: simulation results

	NF SMSE	FF SMSE
truncated pattern stitching	-26.6 dB	-26.4 dB
full-sphere measurement	-27.0 dB	-27.0 dB

5.4 Summary

The analysis of practical limitations of accuracy of the proposed pattern stitching method confirmed that, especially for omnidirectional antennas, the coaxial cable and support structure play a dominant role in the accuracy of the final stitched pattern. They were shown to limit the accuracy of stitched patterns to an SMSE range between -20 dB and -30 dB. Other sources of error commonly present in spherical near-field measurements were also briefly discussed, but their impact was estimated to be well below the aforementioned SMSE levels and an extensive analysis of each source was not done at this stage.

While large variations in SMSE were observed between different coaxial cable routing schemes, the simulation results were generally found to match well with the results obtained during method validation with measurement data, presented in Section 4.3. For the chosen test antenna, the best cable routing practice was demonstrated, where the cable was aligned with the radiation nulls of the antenna. By doing so, scaled mean square error (SMSE) levels of approximately -30 dB could be achieved. Moreover, comparing simulation data containing a coaxial cable model to those of an antenna in free-space, it was shown that the stitching method can outperform the classical full-sphere measurement due to the fact that the partial patterns stitched together represent areas of the measurement sphere that are least influenced by the coaxial cable. When comparing measurement results of the same AUT, first measured as an active connectorless DUT and then with

a coaxial connector attached to the DUT's antenna, an SMSE increase of 6 dB was observed in the connectorized measurement results. This highlights the benefit of avoiding cable-connected measurements whenever permissible by the DUT at hand.

By measuring connectorless DUTs, the coaxial cable can be omitted, allowing to evaluate the influence of the support structure on accuracy. A connectorless DUT was first measured using a support structure made from the discontinued ROHACELL 31 IF foam (assembled with glue of unknown electrical properties and covered with carbon dust from the absorbers), which is typically used in the NF range at TU Wien. To minimize the influence of the support structure, a new structure was constructed using the high-performing ROHACELL 31 HF foam, which was the material found to resemble air the closest in terms of its electromagnetic properties. Using this material can be considered best practice when measuring omnidirectional antennas. Comparing the results to those of the old support structure, this has brought an improvement of 3 dB, leading to SMSE values around -32 dB. Further tests have confirmed that these SMSE values are indeed realistic, even with an antenna support made from ROHACELL 31 HF. They reflect the accuracy limitations imposed by the support structure. As with the coaxial cable, test simulations were also done to compare the accuracy of the pattern stitching method to the accuracy of a classical full-sphere measurement. These tests have shown negligible differences between the two approaches.

Lastly, it should be noted that all values reported in this chapter were example-specific and can only serve as a rough estimation of the general achievable accuracy. As such, best cable routing and measurement orientations should be determined separately for each AUT/DUT of interest.

6 Conclusion and Outlook

This dissertation addressed the conceptualization and implementation of field pattern stitching as a potential approach for tackling a common issue in the field of spherical antenna measurements, pattern truncation, which arises from the physical impossibility of placing an antenna independently and unobstructed in free space during measurement. The antenna under test (AUT) is inevitably mounted on some support structure, which limits the validity of the measurement data and often prevents measurements in certain areas of the measurement sphere. This issue is particularly problematic when measuring omnidirectional antennas, where it is impossible to orient the AUT such that the energy radiated in the area not covered by the measurement is negligible. Besides missing information, truncation also causes errors in the area of the sphere covered by the measurement when the AUT is measured in near field (NF) and transformed to far field (FF) by the commonly used Fourier transform (FT)-based near-to-far-field transformation technique. While some research on truncation error reduction has been done in [23–26], none of these approaches can accurately extrapolate field patterns to the missing, truncated area of the measurement sphere in the general case.

The proposed pattern stitching method makes use of two measurements of the AUT in different measurement orientations, which must then be aligned to the same coordinate system. To do so, the method uses spherical wave coefficients (SWCs) and the underlying theory of spherical wave expansion, commonly used in spherical near-field measurements, which requires both magnitude and phase information of measured fields. The theoretical foundation of spherical near-field measurements was thus introduced in Chapter 2, with particular emphasis on the sign convention for the time/space dependency of electromagnetic waves. A transformation algorithm following the sign convention commonly used in electrical engineering was implemented in Matlab [44], named spherical near-to-far-field transformation (SN2FFT), which uses $\exp(j\omega t)$ for time dependency and $\exp(-jkr)$ for space dependency.

Building on the theory of spherical waves, the concept of pattern stitching was then presented in Chapter 3, where the implementation of all three fundamental steps in the stitching procedure was discussed in detail for the case of truncated patterns obtained from two measurement orientations. The first step focuses on the computation of SWCs from truncated measurements, named truncated SWCs, which must accurately represent the measured truncated fields. Since the common, Fourier transform (FT)-based technique for computing SWCs requires full-sphere patterns and leads to truncation error when full-sphere information is not available, truncation error reduction techniques must be used.

Three approaches capable of reducing truncation errors were implemented and evaluated extensively, the iterative algorithm [23], the least squares (LS) matrix method [43], and the FFT/Matrix method [42,46]. It was found that the coefficient matrices of both matrix methods, which are used to compute the LS solution, are in general ill-conditioned when using truncated patterns, which leads to high noise sensitivity. By introducing a tolerance factor δ for singular value (SV) truncation, computed using either known or estimated signal-to-noise ratio (SNR), this sensitivity was managed, enabling the methods to be effectively applied to noisy data. While an expansion of computed truncated SWCs to far field results in large errors in radiation patterns for all methods, they can accurately describe field patterns in the initial measurement range at the measurement distance, fulfilling the requirements for the pattern stitching method. A comparison of computation times and scaled mean square errors (SMSEs) has shown that the FFT/Matrix method outperforms other methods in terms of both time and error levels and, thus, was the preferred method chosen for pattern stitching. In the second step, truncated SWCs need to be aligned. To achieve this, the performance of mathematical operations for translations and rotations of SWCs [19] when using truncated SWCs needed to be investigated first. Analysis in a wide range of translations and rotations has shown that these introduce increased errors in truncated patterns, which, however, are contained mainly near the truncation angle θ_{trunc} . In a reduced range of θ -angles, accurate pattern representation was observed, confirming the possibility of aligning truncated SWCs for pattern stitching. Relying on the existence of an overlap between the two truncated patterns to be stitched, a pattern alignment procedure was then implemented, which aims to minimize the weighted scaled mean square error (wSMSE) in the overlapping region within a plausible bounded range of translation and rotation combinations. Once the alignment procedure finishes, the final, third step of the stitching method is needed in order to obtain full-sphere radiation patterns. Two approaches were investigated to determine how to obtain the most accurate radiation patterns from aligned patterns with an overlapping region: pattern blending and hemisphere split. Due to the increased error in truncated patterns observed near the truncation angle θ_{trunc} , the hemisphere split was identified as the more accurate approach, where only the upper hemisphere of each measurement is used for stitching. Once stitched, the patterns are processed using the classical SN2FFT to obtain a single set of SWCs and to compute the far-field radiation patterns of the AUT.

The pattern stitching method was implemented in Matlab [44] and thoroughly validated in Chapter 4 using three different types of test patterns: patterns generated from synthetic SWCs, patterns obtained from electromagnetic (EM) simulations, and patterns obtained from measurements in the near-field test range at TU Wien. During validation with synthetic data, poor convergence of the alignment procedure was observed due to the numerous local SMSE minima caused by the periodic nature of propagating EM waves. A two-step alignment procedure was therefore implemented to assure convergence. In the first alignment step, only magnitudes of both patterns in the overlapping range are used to obtain a good starting point for the alignment procedure using complex data in the second step. For translation misalignments larger than 5λ , an increase of error was observed, indicating higher placement precision requirements especially when measuring antennas operating at higher frequencies. Nevertheless, SMSE values below -50 dB were observed for all translations below 20λ when comparing stitched patterns of synthetic patterns to their original nontruncated counterparts. Validation results obtained using patterns from EM simulations have shown a slight increase of error in the stitched patterns, which can

be attributed to the introduction of simulation noise into the pattern stitching method. The worst observed SMSE values in this case reached -40 dB. Lastly, the pattern stitching method was tested on real measurement data. In addition to connectorized AUTs, equipped with a coaxial connector, the method has also been tested on measurements of connectorless devices under test (DUTs), for which a special acquisition procedure was devised, presented in Appendix A. Results have shown a substantial error increase compared to other types of test patterns, with reported SMSE values between -25 dB and -40 dB, where better results could be obtained for antennas with higher directivity.

In Chapter 5, the sources of error in practical measurements and the extent of their impact on stitched full-sphere patterns were discussed. By comparing stitched patterns to free-space patterns excluding the investigated sources of error, it was shown that both the coaxial cable attached to the AUT and the support structure holding it play a dominant role in the overall error, limiting the accuracy of stitched patterns of omnidirectional antennas, resulting in scaled mean square errors of approximately -25 dB to -30 dB. These estimates coincide with the errors reported during the validation procedure to a great extent. Additionally, a comparison was made between the radiation patterns of an antenna simulated in free-space and full-sphere patterns of that same antenna in the presence of a coaxial cable/support structure. It was shown that the impact of the coaxial cable is even more severe in that case, suggesting that the stitching method can provide results more closely resembling a free-space environment than a full-sphere measurement when measuring omnidirectional antennas.

Future work should include a detailed uncertainty analysis of the stitching method in terms of all error sources, as well as an investigation of possibilities to further reduce their impact. One approach to potentially reduce the influence of both the support structure and the coaxial cable, for example, would be to use support structures made from absorbing materials. While this would certainly decrease the overall accuracy of the measurement sphere covered in a single measurement, the absorbing properties of the support structure might be beneficial for the accuracy of measured patterns in some reduced range. By measuring the AUT in more than two measurement orientations and extending the algorithm to align all of them to a common coordinate system based on their respective overlapping junctions, such patches of the measurement sphere could then be stitched together into a full-sphere pattern with increased accuracy. Furthermore, the focus should be put on reducing the computation time required by the stitching method, especially the time required to align the truncated patterns. This includes the optimization of translation coefficients' computation, as well as investigating alternative alignment procedures.

References

- [1] J. C. Maxwell, “A dynamical theory of the electromagnetic field,” *Philosophical Transactions of the Royal Society of London*, vol. 155, pp. 459–513, 1865.
- [2] H. Hertz, “The forces of electrical oscillations, treated according to Maxwell’s theory (in German),” *Annalen der Physik und Chemie*, vol. 36, pp. 1–22, 1889.
- [3] G. Marconi, “Wireless Telegraphic Communication,” in *Nobel Lectures: Physics. 1901-1921*, pp. 196–222. Elsevier Publishing Company, 1967.
- [4] C. Balanis, *Antenna Theory: Analysis and Design*. John Wiley & Sons, 2005.
- [5] J. J. H. Wang, “Antennas for global navigation satellite system (GNSS),” *Proceedings of the IEEE*, vol. 100, no. 7, pp. 2349–2355, 2012.
- [6] K. Rao, P. Nikitin, and S. Lam, “Antenna design for UHF RFID tags: a review and a practical application,” *IEEE Transactions on Antennas and Propagation*, vol. 53, no. 12, pp. 3870–3876, 2005.
- [7] H. Schantz, “A brief history of UWB antennas,” *IEEE Aerospace and Electronic Systems Magazine*, vol. 19, no. 4, pp. 22–26, 2004.
- [8] A. Al-Fuqaha, M. Guizani, M. Mohammadi, M. Aledhari, and M. Ayyash, “Internet of things: A survey on enabling technologies, protocols, and applications,” *IEEE Communications Surveys and Tutorials*, vol. 17, no. 4, pp. 2347–2376, 2015.
- [9] P. S. Hall, Y. Hao, Y. I. Nechayev, A. Alomainy, C. C. Constantinou, C. Parini, M. R. Kamarudin, T. Z. Salim, D. T. Hee, R. Dubrovka, A. S. Owadally, W. Song, A. Serra, P. Nepa, M. Gallo, and M. Bozzetti, “Antennas and propagation for on-body communication systems,” *IEEE Antennas and Propagation Magazine*, vol. 49, no. 3, pp. 41–58, 2007.
- [10] “IEEE standard for definitions of terms for antennas,” *IEEE Std 145-2013 (Revision of IEEE Std 145-1993)*, pp. 1–50, 2014.
- [11] “IEEE recommended practice for antenna measurements,” *IEEE Std 149-2021 (Revision of IEEE Std 149-1977)*, pp. 1–207, 2022.
- [12] C. Capps, “Near field or far field?,” *EDN*, vol. 46, no. 18, pp. 95–99, 2001.

- [13] D. Gray, “How to choose an antenna range configuration,” in *2002 Antenna Measurement Techniques Association Symposium (AMTA)*, pp. 1–6, 2002.
- [14] C. Parini, S. Gregson, J. McCormick, D. Janse van Rensburg, and T. Eibert, *Theory and Practice of Modern Antenna Range Measurements*, vol. 1. London: SciTech Publishing, an imprint of The Institution of Engineering and Technology, 2nd ed., 2020.
- [15] C. Parini, S. Gregson, J. McCormick, D. Janse van Rensburg, and T. Eibert, *Theory and Practice of Modern Antenna Range Measurements*, vol. 2. London: SciTech Publishing, an imprint of The Institution of Engineering and Technology, 2nd ed., 2020.
- [16] A. Yaghjian, “An overview of near-field antenna measurements,” *IEEE Transactions on Antennas and Propagation*, vol. 34, no. 1, pp. 30–45, 1986.
- [17] S. Gregson, J. McCormick, C. Parini, I. of Engineering, and Technology, *Principles of Planar Near-Field Antenna Measurements*. IET electromagnetic waves series, Institution of Engineering and Technology, 2007.
- [18] A. Yaghjian and I. for Basic Standards (U.S.). Electromagnetics Division, *Near-field antenna measurements on a cylindrical surface: a source scattering-matrix formulation*. No. Bd. 13 in NBS technical note, Department of Commerce, National Bureau of Standards, Institute for Basic Standards, Electromagnetics Division, 1977.
- [19] J. Hansen, ed., *Spherical Near-field Antenna Measurements*. IET Electromagnetic Waves Series, The Institution of Engineering and Technology, hardcover ed., 6 1988.
- [20] D. Leatherwood, “Conical near-field antenna measurement system,” *IEEE Antennas and Propagation Magazine*, vol. 50, no. 6, pp. 212–218, 2008.
- [21] O. Breinbjerg, “Spherical near-field antenna measurements — The most accurate antenna measurement technique,” in *2016 IEEE International Symposium on Antennas and Propagation (APSURSI)*, pp. 1019–1020, 2016.
- [22] NSI-MI Technologies, “Swing Arm-over-Azimuth Systems.” <https://www.nsi-mi.com/products/system-solutions/near-field-systems/spherical-near-field-scanner-systems/swing-arm-over-azimuth-systems>, Accessed: 01.01.2024.
- [23] E. Martini, S. Maci, and L. J. Foged, “Spherical near field measurements with truncated scan area,” in *Proceedings of the 5th European Conference on Antennas and Propagation (EUCAP)*, pp. 3256–3258, 2011.
- [24] L. J. Foged, L. Scialacqua, F. Saccardi, F. Mioc, J. L. A. Quijano, E. Martini, S. Maci, M. Sabbadini, and G. Vecchi, “Comparative investigation of methods to reduce truncation errors in partial spherical near-field antenna measurements,” in *2012 6th European Conference on Antennas and Propagation (EUCAP)*, pp. 2533–2537, 2012.
- [25] R. C. Wittmann, C. F. Stubenrauch, and M. H. Francis, “Spherical scanning measurements using truncated data sets,” in *2002 Antenna Measurement Techniques Association Symposium (AMTA)*, pp. 1–5, 2002.

- [26] R. C. Wittmann, C. F. Stubenrauch, and M. H. Francis, “Using truncated data sets in spherical-scanning antenna measurements,” *International Journal of Antennas and Propagation*, vol. 2012, pp. 1–6, 2012.
- [27] A. C. Newell and G. Hindman, “Antenna spherical coordinate systems and their application in combining results from different antenna orientations,” in *1999 ESA ESTEC Workshop on Antenna Measurements*, pp. 1–6, 1999.
- [28] S. Gregson, C. Parini, and J. McCormick, “Full sphere far-field antenna patterns obtained using a small planar scanner and a poly-planar measurement technique,” in *2006 Antenna Measurement Techniques Association Symposium (AMTA)*, pp. 1–5, 2006.
- [29] “IEEE recommended practice for near-field antenna measurements,” *IEEE Std 1720-2012*, pp. 1–102, 2012.
- [30] V. Kalashnikov, M. Ponomarev, O. Platonov, V. Shubnikov, M. Rivkin, A. Shatrakov, I. Shatrakov, Y. Shatrakov, and O. Zavalishin, *Near-Field Antenna Measurements: Calculations and Facility Design*. Springer aerospace technology, Springer Singapore, 2021.
- [31] J. Stratton, *Electromagnetic Theory*. IEEE Press Series on Electromagnetic Wave Theory, Wiley, 2007.
- [32] S. Belousov and D. Brown, *Tables of Normalized Associated Legendre Polynomials*. Mathematical tables series, Pergamon Press, 1962.
- [33] M. Abramowitz and I. Stegun, *Handbook of Mathematical Functions: With Formulas, Graphs, and Mathematical Tables*. Applied mathematics series, Dover Publications, 1965.
- [34] G. Arfken, H. Weber, and F. Harris, *Mathematical Methods for Physicists: A Comprehensive Guide*. Elsevier Science, 2013.
- [35] B. Friedman and J. Russek, “Addition theorems for spherical waves,” *Quarterly of Applied Mathematics*, vol. 12, no. 1, pp. 13–23, 1954.
- [36] S. Stein, “Addition theorems for spherical wave functions,” *Quarterly of Applied Mathematics*, vol. 19, no. 1, pp. 15–24, 1961.
- [37] O. R. Cruzan, “Translational addition theorems for spherical vector wave functions,” *Quarterly of Applied Mathematics*, vol. 20, no. 1, pp. 33–40, 1962.
- [38] J. Bruning and Y. Lo, “Multiple scattering of EM waves by spheres part I—multipole expansion and ray-optical solutions,” *IEEE Transactions on Antennas and Propagation*, vol. 19, no. 3, pp. 378–390, 1971.
- [39] P. Wacker, *Non-Planar Near-Field Measurements: Spherical Scanning*. U.S. Department of Commerce, National Institute of Standards and Technology, 6 1975.
- [40] A. Edmonds, *Angular Momentum in Quantum Mechanics*. CERN [Reports], CERN, 1955.

- [41] A. Ludwig, “Calculation of orthogonal-function expansion from imperfect data,” *Electromagnetics Institute Technical University of Denmark, Lyngby, Tech. Rep.*, vol. 15, p. 16, 1972.
- [42] F. Jensen and F. H. Larsen, “Spherical near-field far-field techniques,” in *1976 6th European Microwave Conference*, pp. 98–102, 1976.
- [43] R. Cornelius, A. A. Bangun, and D. Heberling, “Investigation of different matrix solver for spherical near-field to far-field transformation,” in *2015 9th European Conference on Antennas and Propagation (EuCAP)*, pp. 1–4, 2015.
- [44] MathWorks, “MATLAB R2023b.” <https://www.mathworks.com/products/matlab.html>, Accessed: 13.01.2024.
- [45] R. Cornelius, H. Shakhtour, and D. Heberling, “Extrapolation of truncated spherical near-field measurements,” in *2012 42nd European Microwave Conference*, pp. 301–304, 2012.
- [46] T. Laitinen, S. Pivnenko, J. M. Nielsen, and O. Breinbjerg, “Theory and practice of the FFT/Matrix inversion technique for probe-corrected spherical near-field antenna measurements with high-order probes,” *IEEE Transactions on Antennas and Propagation*, vol. 58, no. 8, pp. 2623–2631, 2010.
- [47] R. Penrose, “A generalized inverse for matrices,” *Mathematical Proceedings of the Cambridge Philosophical Society*, vol. 51, no. 3, p. 406–413, 1955.
- [48] G. Golub and C. Van Loan, *Matrix Computations*. Johns Hopkins Studies in the Mathematical Sciences, Johns Hopkins University Press, 2013.
- [49] T. Yang and W. A. Davis, “A direct matrix approach to 3-d antenna radiation-pattern estimation from partially-scanned spherical near-field data,” in *2011 XXXth URSI General Assembly and Scientific Symposium*, pp. 1–4, 2011.
- [50] A. Khuri, *Advanced Calculus with Applications in Statistics*. Wiley Series in Probability and Statistics, Wiley, 2003.
- [51] R. Cornelius and D. Heberling, “Analysis of sampling grids for spherical near-field antenna measurements,” in *2015 Progress in Electromagnetics Research Symposium (PIERS)*, pp. 923–927, 2015.
- [52] J. Soklič and H. Arthaber, “Comparison of methods for computing spherical wave coefficients from truncated measurements,” in *2023 IEEE Conference on Antenna Measurements and Applications (CAMA)*, pp. 790–794, 2023.
- [53] Ansys, “HFSS 2022 R2.” <https://www.ansys.com/products/electronics/ansys-hfss>, Accessed: 19.12.2022.
- [54] T. Mikulasek, J. Blumenstein, and A. Prokes, “Antennas utilized for intra-vehicle 3–11GHz and 55–65GHz channel measurement,” in *2016 Progress in Electromagnetics Research Symposium (PIERS)*, pp. 4258–4262, 2016.
- [55] NSI-MI Technologies, “NSI2000 Professional Edition 4.8.6.” <https://www.nsi-mi.com/products/software-products/nsi2000-professional-edition-upgrade>.

- [56] J. Soklič and H. Arthaber, “Investigation of coordinate system rotation and translation on iteratively reconstructed truncated antenna field patterns,” in *2022 IEEE International Symposium on Antennas and Propagation and USNC-URSI Radio Science Meeting (AP-S/URSI)*, pp. 631–632, 2022.
- [57] J. Soklič and H. Arthaber, “Full-sphere characterization of low-gain antennas via truncated field pattern stitching,” in *2022 Antenna Measurement Techniques Association Symposium (AMTA)*, pp. 1–6, 2022.
- [58] J. Soklič and H. Arthaber, “Antenna characterization using the truncated pattern stitching method and its practical limitations of accuracy,” *IEEE Transactions on Antennas and Propagation*, Manuscript in preparation.
- [59] J. Soklič and H. Arthaber, “Full-sphere radiation pattern characterization of IoT devices via pattern stitching,” in *2023 XXXVth General Assembly and Scientific Symposium of the International Union of Radio Science (URSI GASS)*, pp. 1–4, 2023.
- [60] M. Z. Haq, *Advanced Topics in Measurements*. Rijeka: IntechOpen, Mar 2012.
- [61] Evonik Industries, “ROHACELL[®] HF.” <https://performance-foams.evonik.com/en/products-and-solutions/rohacell/rohacell-hf-170037.html>, Accessed: 13.01.2024.
- [62] Suter Kunststoffe AG, “Technical datasheet: ROHACELL.” <https://www.swiss-composite.ch/pdf/t-Rohacell-d-f.pdf>, Accessed: 13.01.2024.

A SN2FFT Documentation

The Matlab [44] implementation of the Fourier transform based spherical near-to-far-field transformation (SN2FFT) algorithm, the theory of which has been discussed in Chapter 2, will be presented in this appendix. First, an example of usage will be introduced, giving detailed information on the required input data of the main function of the algorithm. This will be followed by an overview of all the implemented supporting functions that are used for the transformation of an input field pattern into the desired output field pattern, which may generally be either a near- or a far-field pattern.

It should be noted at this point that the implementation of the spherical near-to-far-field transformation (SN2FFT) algorithm and of all the supporting functions was done under the following assumptions:

- A1 The probe antenna was assumed to be rotationally symmetric, possessing only spherical wave modes with azimuthal indices $\mu = \pm 1$. Using this assumption, sampling in χ can be reduced to two orthogonal probe orientations: $\chi = 0^\circ$ and $\chi = 90^\circ$. The extension to circularly asymmetric probe antennas, which contain also SWC modes for $\mu \neq \pm 1$, was not done at this stage due to the increased computational complexity that such a generalization brings. As discussed at the end of Section 2.5.1, this assumption is commonly applied in practice even when probe antennas which are not perfectly rotationally symmetric are used, such as dual-ridge horn antennas (DRHAs). The reasoning behind it is that, at a sufficient distance from the AUT, the probe antenna can be approximated well using only coefficients with $\mu = \pm 1$. This approximation is also used by the NSI software [55] which is employed in the NF test range at TU Wien. The software does not permit defining more than two measurement steps in χ .
- A2 The maximum azimuthal order M is always set to be equal to the maximum polar order N . In practice, M could sometimes be reduced below N to reduce computational complexity, for example, when the antenna can be enclosed in a cylinder with a base diameter smaller than its height or rotational symmetries in the pattern exist [19]. Since the implemented SN2FFT algorithm can solve problems even for very high orders N in the matter of seconds, the benefit of reducing the azimuthal order further was found to be negligible.
- A3 It was assumed that measurements will always take place in free space, not in some dielectric media. Following this assumption, the wavelength λ and the wavenumber

k are derived directly from the measurement frequency f and the speed of light in vacuum, c_0 : $\lambda = c_0/f$ and $k = 2\pi/\lambda$.

A.1 Example of Usage

In order to accurately determine the far-field (FF) radiation pattern¹ of an arbitrary antenna under test (AUT) at a given frequency f from full-sphere field data obtained in the near field (NF), sufficient samples of the NF data must first be acquired. These samples must be taken in equidistant steps over the whole measurement sphere with radius A_{in} , which corresponds to the distance between the AUT and the probe. The meaning of sufficient in this context was discussed in Section 2.5.2 and follows from the electrical size of the AUT and the probe antenna, as well as their radiation characteristics. To summarize, the minimum number of required samples in χ depends on the maximum azimuthal order of the probe antenna. Taking into account the assumption of rotational symmetry of the probe antenna (A1), only two sampling points are required in χ , $\chi = 0^\circ$ and $\chi = 90^\circ$. In ϕ , the minimum number of equidistant samples in the range $0^\circ \leq \phi < 360^\circ$ can be determined by the maximum azimuthal order M as $K_\phi = 2M + 1$. Since the general case is assumed, where $M = N$ (A2), this can be rewritten as $K_\phi = 2N + 1$. Lastly, in θ , the minimum number of required samples in the range $0^\circ \leq \theta \leq 180^\circ$ is governed by the maximum polar order N , where $K_\theta = N + 1$.² One can see that the minimum number of samples in both θ and ϕ depends on the maximum polar order N , which can be determined from the wavenumber k and the size of the AUT—described by the radius r_0 of the smallest sphere circumscribing the AUT—using (2.24). Considering the free-space assumption (A3), the wavenumber k is given as $k = 2\pi/\lambda = 2\pi f/c_0$. With this knowledge, the field pattern $w(A_{\text{in}}, \chi, \theta, \phi)$ can be measured (or otherwise obtained) at all sampling positions necessary for successful transformation into FF.³ It should be noted that the algorithm was designed to handle radiation patterns that are truncated in θ as well. Truncation at some angle $\theta_{\text{trunc}} \leq 180^\circ$ is inevitable when measuring patterns in a swing arm-over-azimuth range, such as the test range at TU Wien. In case of truncated patterns, the missing θ -samples are assigned to be zero during the transformation to allow for a transformation in θ using a fast Fourier transform (FFT). This comes at the cost of introducing truncation errors.

Aside from the sampled field pattern $w(A_{\text{in}}, \chi, \theta, \phi)$, information on the probe antenna is also required for an accurate transformation into far field since probe correction must be done when the AUT is measured in near field. Concretely, the transformation algorithm requires the probe receiving coefficients $R_{\sigma\mu\nu}^p$. These have been precomputed for all probe antennas used at the NF range at TU Wien from radiation patterns provided by the supplier and are stored together with the scripts used by the algorithm. They are loaded by providing the name of the probe antenna, as will be shown in the description of the main function of the transformation algorithm. In addition to the available probe antennas, the receiving coefficients of an x-directed dipole have also been defined since a dipole is

¹Typically, the far field (FF) is sought, but the algorithm allows for transformations into any measurement distance outside of the minimum sphere circumscribing the complete AUT.

²The field pattern is extended to the whole 360° -range during transformation. Measuring the field exactly at $\theta = 180^\circ$ is not necessary as long as the number of samples in the extended θ -range is greater or equal to $2N + 1$.

³The algorithm is, of course, capable of performing the transformation also in the case where the number of samples exceeds the minimum sampling requirements.

typically used as the receiving probe of the output transformed FF radiation pattern. As explained in Section 2.6, the x-directed dipole is used due to the simple relations between the resulting transmission coefficients $w'(A', \chi, \theta, \phi)$ and the electric field values $E'_\theta(A', \theta, \phi)$ and $E'_\phi(A', \theta, \phi)$, defined by (2.91) and (2.92).

With information about the probe and all the necessary NF pattern samples $w(A_{\text{in}}, \chi, \theta, \phi)$ measured, the transformation into far field can be done by calling the main function of the algorithm, **SN2FFT**. This function will be discussed in the remainder of this section, where its syntax, required input variables, and resulting output variables will be explained.

SN2FFT

Description:

The main function of the spherical near-to-far-field transformation (SN2FFT) algorithm. It takes the input field pattern, $w(A_{\text{in}}, \chi, \theta, \phi)$, obtained in sampling points in χ , θ , and ϕ , at a distance A_{in} between the probe and the antenna under test (AUT), and computes the spherical wave coefficients (SWCs) of the AUT, Q_{smn} . Within the function, the range of θ -values is checked and, if samples in the range $0^\circ \leq \theta \leq 180^\circ$ are missing, extended to the whole range by assigning missing field pattern samples to be zero. This must be done to ensure equidistant sampling over the whole range, which is needed when using FFT transformations. In order to compensate for the influence of a realistic probe antenna, which measures a field average over its aperture rather than the exact field in the specified measurement point, probe correction is done during transformation. The name of the used probe antenna must be input for this purpose, while the precomputed probe receive coefficients $R_{\sigma\mu\nu}^p$ for the chosen probe antenna at the given frequency are loaded within a supporting function, which will be described at a later stage. These SWCs are then used to compute the output field pattern, $w_T(A_{\text{out}}, \chi, \theta_T, \phi_T)$, as it would be received by a chosen output probe antenna at a chosen distance A_{out} (which must be larger than the AUT's MRE) and for an arbitrary number of equidistant samples in θ and ϕ .

Syntax:

```
[wT, thetaT, phiT, Q, d_m, d_mu] = SN2FFT(w, f, theta, phi, NthT, NphT,
inpr, A_in, outpr, A_out, N)
```

Inputs:

- **w(chi, theta, phi)** → 3D array containing the input field pattern $w(\chi, \theta, \phi)$, obtained at a constant distance A_{in} , ordered in an array using indices of vectors **chi** (1st dimension), **theta** (2nd dimension), and **phi** (3rd dimension) as array indices
- **f** → frequency in Hz
- **theta** → θ -steps for the corresponding pattern, ordered in a vector of length K_θ ; it must start with $\theta = 0^\circ$ but can be truncated at some $\theta_{\text{trunc}} < 180^\circ$
- **phi** → ϕ -steps for the corresponding pattern, ordered in a vector of length K_ϕ ; it must contain equidistant samples over the whole range
- **NthT** → desired number of θ -steps in $[0, \pi]$ after transformation

- **NphT** → desired number of ϕ -steps in $[0, 2\pi)$ after transformation
- **inpr** → input probe name (the following probe antennas have been implemented): 'dipole' (ideal x-oriented dipole) or 'RGP10_187' (RGP10 with 187 mm mast) or 'RGP10_527' (RGP10 with 527 mm mast) or 'RGP40' (RGP40 dual ridge horn probe antenna)
- **A_in** → input AUT-to-probe distance A_{in} in meters
- **outpr** → output probe name, where the same probes are available as for the input probe name
- **A_out** → output AUT-to-probe distance A_{out} in meters, for far field (FF) **Inf** must be set
- **N** → maximum polar order N

Outputs:

- **wT(chi, theta, phi)** → output field pattern, ordered in an array using indices of vectors **chi** (1st dimension), **theta** (2nd dimension), and **phi** (3rd dimension) as array indices
- **thetaT** → θ -steps for the output pattern, ordered in a vector of length **NthT**
- **phiT** → ϕ -steps for the output pattern, ordered in a vector of length **NphT**
- **Q(s, m, n)** → spherical wave coefficients (SWCs), ordered in an array with SWC-indices $s = (1, 2)$ (1st dimension), $m = (0, 1, \dots, N - 1, N, -N, -N + 1, \dots, -1)$ (2nd dimension), and $n = (1, 2, \dots, N)$ (3rd dimension) as array indices; all array elements with $|m| > n$ are assigned a value of zero

A.2 List of Supporting Functions

The function **SN2FFT** discussed above is the main function of the transformation algorithm and the only function that must be called by the user in order to obtain the SWCs and the transformed pattern. Within this function, other (supporting) functions are then called automatically during the transformation process. All functions are listed in the annotated call graph shown in Figure A.1, which illustrates the relationships between functions of the spherical near-to-far-field transformation (SN2FFT) algorithm. Functions of each call chain level in the call graph are marked with a different shade of gray from top-level main function (brightest) to third-level functions (darkest). The call order of the main function is indicated with Roman numerals (i. to iv.), while call orders of first-level functions are indicated with Latin letters (a. to d.). Each function in the graph has an inward-pointing arrow and an outward-pointing arrow together with sets of variable names. The variables next to the inward-pointing arrow indicate the input variables provided to this function by the calling function, while the variables next to the outward-pointing arrow indicate its response, i.e., the output variables. One should note that the first function in the call graph, **get_probe_response_constants**, is called twice. This is done in order to compute both the input and the output probe response constants for the given input/output probe antenna and the given input/output AUT-to-probe distance.

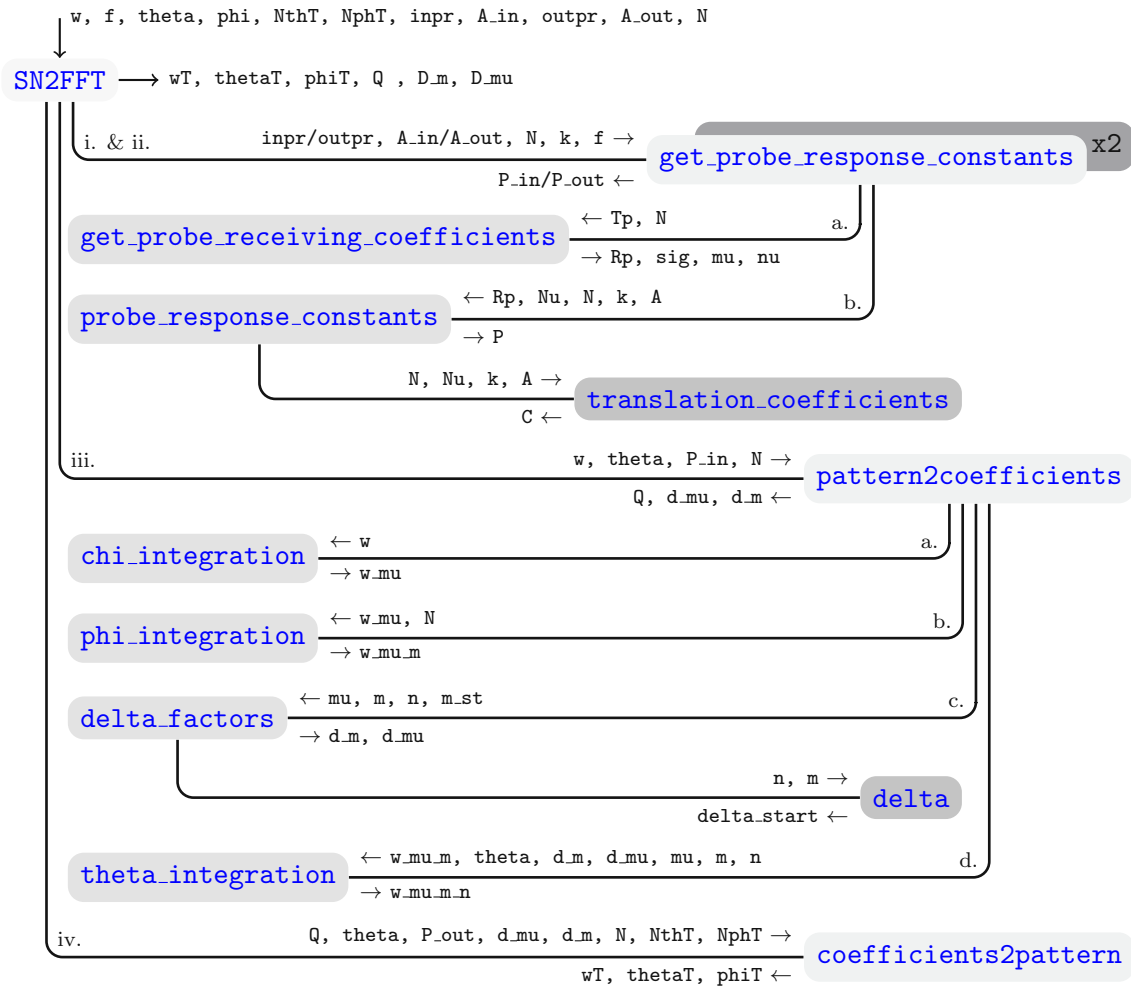


Figure A.1: SN2FFT annotated call graph

These supporting functions will be presented in this section in their respective call order, discussing their functionality, syntax, required inputs, and their outputs.

get_probe_response_constants

Description:

The function loads the precomputed probe receiving coefficients for the selected probe (data for three measurement probes available at the NF range at TU Wien have been stored in a subdirectory of the folder containing all functions of the SN2FFT implementation) or, if an x-oriented dipole is chosen as the probe, calls `get_probe_receiving_coefficients` to compute the probe receiving coefficients from its transmission coefficients. It then calls the function `probe_response_constants` to compute the probe response constants for this probe at the input measurement distance between the probe and the AUT and the maximum polar order N of the AUT, determined according to (2.24).

Syntax:

`P = get_probe_response_constants(pr, A, N, k, f)`

Inputs:

- `pr` → probe name: 'dipole' (ideal x-oriented dipole) or 'RGP10_187' (RGP10 with a 187 mm mast) or 'RGP10_527' (RGP10 with a 527 mm mast) or 'RGP40' (RGP40 dual ridge horn probe antenna)
- `A` → distance between the probe and the AUT
- `N` → maximum polar order of the AUT
- `k` → wavenumber
- `f` → frequency in Hz

Outputs:

- `P(s,mu,n)` → probe response constants, ordered in an array with SWC-indices $s = (1, 2)$ (1st dimension), $\mu = (1, -1)$ (2nd dimension), and $n = (1, 2, \dots, N)$ (3rd dimension) as array indices

get_probe_receiving_coefficients

Description:

Subfunction of the `get_probe_response_constants` function that computes probe receiving coefficients $R_{\sigma\mu\nu}^p$ for $\mu = \pm 1$ (A1) from transmitting coefficients $T_{\sigma\mu\nu}^p$ according to (2.54). Along with the probe receiving coefficients, it returns the vectors `sig` representing the indices σ , `mu` representing the indices μ , and `nu` representing the indices ν for further processing. This function can be used for the computation of receiving coefficients of an arbitrary probe from its SWCs by assuming $v = 1$ in the relation $vT_{smn}^p = Q_{smn}^p$ (2.48).

Syntax:

`[Rp, sig, mu, nu] = get_probe_receiving_coefficients(Tp, N)`

Inputs:

- `Tp(sig,mu,nu)` → probe transmitting coefficients $T_{\sigma\mu\nu}^p$, ordered in an array with spherical wave coefficient (SWC)-indices $\sigma = (1, 2)$ (1st dimension), $\mu = (1, -1)$ (2nd dimension), and $\nu = (1, 2, \dots, \nu_{\max})$ (3rd dimension) as array indices
- `N` → maximum polar order N

Outputs:

- `Rp(sig,mu,nu)` → probe receiving coefficients $R_{\sigma\mu\nu}^p$, which are ordered in an array with SWC-indices $\sigma = (1, 2)$ (1st dimension), $\mu = (1, -1)$ (2nd dimension), and $\nu = (1, 2, \dots, \nu_{\max})$ (3rd dimension) as array indices
- `sig` → denotes the probe's generating function indices σ , ordered in a vector: `sig = 1` (m -function), `sig = 2` (n -function)

- μ → vector of probe azimuthal indices $\mu = (1, -1)$ (probe antenna's equivalent of index m)
- ν → vector of probe polar indices $\nu = (1, 2, \dots, \nu_{\max})$ (probe antenna's equivalent of index n)

probe_response_constants

Description:

This function computes the probe response constants $P_{s\mu n}(kA)$ for the corresponding probe receiving coefficients $R_{\sigma\mu\nu}^p$ of the selected input/output probe with the maximum polar order ν_{\max} for an AUT with the maximum polar order N according to (2.55).

Syntax:

$P = \text{probe_response_constants}(\text{Rp}, \text{Nu}, \text{N}, \text{k}, \text{A})$

Inputs:

- $\text{Rp}(\text{sig}, \mu, \nu)$ → probe receiving coefficients $R_{\sigma\mu\nu}^p$, which are ordered in an array with SWC-indices $\sigma = (1, 2)$ (1st dimension), $\mu = (1, -1)$ (2nd dimension), and $\nu = (1, 2, \dots, \nu_{\max})$ (3rd dimension) as array indices
- Nu → probe's maximum polar order ν_{\max}
- N → AUT's maximum polar order N
- k → wavenumber
- A → distance between the probe and the AUT

Outputs:

- $P(\text{s}, \mu, \text{n})$ → probe response constants, ordered in an array with SWC-indices $s = (1, 2)$ (1st dimension), $m = (1, -1)$ (2nd dimension), and $n = (1, 2, \dots, N)$ (3rd dimension) as array indices

translation_coefficients

Description:

The function computes translation coefficients $C_{\sigma\mu\nu}^{sn(c)}(kA)$ for outward traveling waves ($c = 4$) for probe's azimuthal indices $\mu = \pm 1$ in accordance with (2.34).

Syntax:

$C = \text{translation_coefficients}(\text{N}, \text{Nu}, \text{k}, \text{A})$

Inputs:

- N → AUT's maximum polar order N
- Nu → probe's maximum polar order ν_{\max}

- $k \rightarrow$ wavenumber
- $A \rightarrow$ distance between the probe and AUT

Outputs:

- $\mathbf{C}(\mathbf{sig}, \mathbf{mu}, \mathbf{nu}, \mathbf{s}, \mathbf{n}) \rightarrow$ probe response constants, ordered in a five-dimensional array using the probe's SWC-indices $\sigma = (1, 2)$ (1st dimension), $\mu = (1, -1)$ (2nd dimension), and $\nu = (1, 2, \dots, \nu_{\max})$ (3rd dimension), and the AUT's SWC-indices, $s = (1, 2)$ (4th dimension) and $n = (1, 2, \dots, N)$ (5th dimension) as dimensions, where \mathbf{mu} represents the azimuthal index μ , which is common to both the probe and the AUT

pattern2coefficients

Description:

This function computes the spherical wave coefficients (SWCs) for the provided field pattern $w(\chi, \theta, \phi)$ by calling the subfunctions `chi_integration`, `phi_integration`, and `theta_integration` to transform the field pattern thrice—in χ , ϕ , and θ —and then solving the linear system of equations in (2.65). Additionally, it returns the delta factors $\Delta_{m'\mu}^n$ and $\Delta_{m'm}^n$, computed within the subfunction `delta_factors` according to (2.27), (2.28), and (2.29), which are reused later when computing an output (near- or far-field) pattern. Reusing these coefficients helps reduce the overall computation time of the SN2FFT algorithm.

Syntax:

`[Q, d_m, d_mu] = pattern2coefficients(w, theta, P_in, N)`

Inputs:

- $\mathbf{w}(\mathbf{chi}, \mathbf{theta}, \mathbf{phi}) \rightarrow$ input field pattern $w(\chi, \theta, \phi)$, ordered in an array using indices of vectors `chi` (1st dimension), `theta` (2nd dimension), and `phi` (3rd dimension) as array indices
- $\mathbf{theta} \rightarrow$ θ -steps for the corresponding pattern, ordered in a vector of length K_θ
- $\mathbf{P_in}(\mathbf{s}, \mathbf{mu}, \mathbf{n}) \rightarrow$ input probe response constants $P_{s\mu n}$, ordered in an array using SWC-indices $s = (1, 2)$ (1st dimension), $\mu = (1, -1)$ (2nd dimension), and $n = (1, 2, \dots, N)$ (3rd dimension) as array indices
- $N \rightarrow$ AUT's maximum polar order N

Outputs:

- $\mathbf{Q}(\mathbf{s}, \mathbf{m}, \mathbf{n}) \rightarrow$ spherical wave coefficients, ordered in an array with indices $s = (1, 2)$ (1st dimension), $m = (0, 1, \dots, N-1, N, -N, -N+1, \dots, -1)$ (2nd dimension), and $n = (1, 2, \dots, N)$ (3rd dimension) as array indices; all array elements with $|m| > n$ are assigned a value of zero
- $\mathbf{d_m}(\mathbf{n}, \mathbf{m_st}, \mathbf{m}) \rightarrow$ delta factors $\Delta_{m'm}^n$, saved in an array with indices $n = (1, 2, \dots, N)$ (1st dimension), $m' = (0, 1, \dots, N)$ (2nd dimension), and $m = (0, 1, \dots, N-1, N, -N, -N+1, \dots, -1)$ (3rd dimension) as array indices; all array elements with $|m| > n$ or $|m'| > n$ are assigned a value of zero

- `d_mu(n,m_st,mu)` → delta factors $\Delta_{m'm}^n$, ordered in an array with indices $n = (1, 2, \dots, N)$ (1st dimension), $m' = (0, 1, \dots, N)$ (2nd dimension), and $\mu = (1, -1)$ (3rd dimension) as array indices; all array elements with $|m'| > n$ are assigned a value of zero

chi_integration

Description:

The function is responsible for the first transformation of the sampled input pattern $w(\chi, \theta, \phi)$ over χ . It extends the pattern measured in two orthogonal probe orientations (corresponding to the angles $\chi = 0^\circ$ and $\chi = 90^\circ$) to the full $[0^\circ, 360^\circ)$ range by exploiting symmetries, computes the discrete Fourier transform (DFT) over χ in (2.70) using a fast Fourier transform (FFT), and returns the once transformed field pattern for $\mu = \pm 1$, $w_{\mu=\pm 1}(\theta, \phi)$.

Syntax:

`w_mu = chi_integration(w)`

Inputs:

- `w(chi,theta,phi)` → input field pattern $w(\chi, \theta, \phi)$, ordered in an array using indices of vectors `chi` (1st dimension), `theta` (2nd dimension), and `phi` (3rd dimension) as array indices

Outputs:

- `w_mu(mu,theta,phi)` → once transformed field pattern $w_\mu(\theta, \phi)$ (over χ), ordered in an array using indices of vectors $\mu = (1, -1)$ (1st dimension), `theta` (2nd dimension), and `phi` (3rd dimension) as array indices

phi_integration

Description:

The function is in charge of the second transformation, computing the DFT over ϕ , as described in (2.71), using an FFT. It returns the twice transformed field pattern for $\mu = (1, -1)$ and $m = (0, 1, \dots, N, -N, \dots, -1)$, $w_{\mu m}(\theta)$, discarding any values with $|m| > N$, which are obtained if the pattern is oversampled in ϕ . Note that $M = N$ is assumed according to A2.

Syntax:

`w_mu_m = phi_integration(w_mu, N)`

Inputs:

- `w_mu(mu,theta,phi)` → once transformed field pattern $w_\mu(\theta, \phi)$ (over χ), ordered in an array using indices of vectors $\mu = (1, -1)$ (1st dimension), `theta` (2nd dimension), and `phi` (3rd dimension) as array indices
- `N` → maximum polar order N , since $M = N$ according to A2

Outputs:

- `w_mu_m(mu,theta,m)` → twice transformed field pattern $w_{\mu m}(\theta)$ (over χ and ϕ), ordered in an array using indices of vectors $\mu = (1, -1)$ (1st dimension), `theta` (2nd dimension), and $m = (0, 1, \dots, N, -N, \dots, -1)$ (3rd dimension) as array indices

delta_factors

Description:

The function computes the delta factors $\Delta_{m'\mu}^n$ and $\Delta_{m'm}^n$ for all n , m , μ , and m' . For each n and m/μ pair, the starting delta factor $\Delta_{nm}^n/\Delta_{n\mu}^n$ is first computed by calling the function `delta`. With the help of recursion formula (2.28) and symmetry properties (2.29), all remaining factors are then computed within the function and stored into two three-dimensional arrays. The required function input vectors are generated in the calling function `pattern2coefficients` and are directly related to the given maximum polar order N .

Syntax:

`[d_m, d_mu] = delta_factors(mu, m, n, m_st)`

Inputs:

- `mu` → vector containing all μ indices, $\mu = (1, -1)$
- `m` → vector containing all m indices, $m = (0, 1, \dots, N, -N, \dots, -1)$
- `n` → vector containing all n indices, $n = (1, 2, \dots, N)$
- `m_st` → vector containing all m' indices, $m' = (0, 1, \dots, N)$

Outputs:

- `d_m(n,m_st,m)` → an array containing the delta factors $\Delta_{m'm}^n$ for all indices of vectors `n` (1st dimension), `m_st` (2nd dimension), and `m` (3rd dimension); all array elements with $|m| > n$ or $|m'| > n$ are assigned a value of zero
- `d_mu(n,m_st,mu)` → an array containing the delta factors $\Delta_{m'\mu}^n$ for all indices of vectors `n` (1st dimension), `m_st` (2nd dimension), and `mu` (3rd dimension); all array elements with $|m'| > n$ are assigned a value of zero

delta

Description:

This function uses (2.27) to compute the starting delta factors Δ_{nm}^n (or $\Delta_{n\mu}^n$) for the given index pair n and m (or μ), which are needed for computing all remaining delta factors $\Delta_{m'\neq n,m}^n$ or $\Delta_{m'\neq n,\mu}^n$ with the help of the recursion formula (2.28).

Syntax:

`[delta_start] = delta(n, m)`

Inputs:

- **n** → current polar index n
- **m** → current azimuthal index m (or μ)

Outputs:

- **delta_start** → starting delta factor Δ_{nm}^n (or $\Delta_{n\mu}^n$)

theta_integration

Description:

This function is in charge of the final, third transformation of the input pattern $w(\chi, \theta, \phi)$. It takes the twice transformed pattern $w_{\mu m}(\theta)$, extends it to the full θ -range using (2.72), and computes the Fourier coefficients $b_l^{\mu m}$ from (2.76) and (2.77). It then follows the procedure documented in (2.78) – (2.84) to obtain the thrice transformed radiation pattern, $w_{\mu m}^n$, which is also the output of the function.

Syntax:

`w_mu_m_n = theta_integration(w_mu_m, theta, d_m, d_mu, mu, m, n)`

Inputs:

- **w_mu_m(mu, theta, m)** → twice transformed field pattern $w_{\mu m}(\theta)$ (over χ and ϕ), ordered in an array using indices of vectors $\mu = (1, -1)$ (1st dimension), **theta** (2nd dimension), and $m = (0, 1, \dots, N, -N, \dots, -1)$ (3rd dimension) as array indices
- **theta** → θ -steps for the corresponding pattern, ordered in a vector of length K_θ ; if the vector is truncated, the function extends the range of θ -values to $[0^\circ, 180^\circ]$
- **d_m(n, m_st, m)** → an array containing the delta factors $\Delta_{m'm}^n$ for all indices of vectors **n** (1st dimension), **m_st** (2nd dimension), and **m** (3rd dimension); all array elements with $|m| > n$ or $|m'| > n$ are assigned a value of zero
- **d_mu(n, m_st, mu)** → an array containing the delta factors $\Delta_{m'\mu}^n$ for all indices of vectors **n** (1st dimension), **m_st** (2nd dimension), and **mu** (3rd dimension); all array elements with $|m'| > n$ are assigned a value of zero
- **mu** → vector containing all μ indices, $\mu = (1, -1)$
- **m** → vector containing all m indices, $m = (0, 1, \dots, N, -N, \dots, -1)$
- **n** → vector containing all n indices, $n = (1, 2, \dots, N)$

Outputs:

- **w_mu_m_n(mu, n, m)** → thrice transformed field pattern $w_{\mu m}^n$, ordered in an array using indices of vectors $\mu = (1, -1)$ (1st dimension), $m = (0, 1, \dots, N, -N, \dots, -1)$ (2nd dimension), and $n = (1, 2, \dots, N)$ (3rd dimension) as array indices

coefficients2pattern

Description:

The function computes a radiation pattern, $w_T(\chi, \theta_T, \phi_T)$, from the spherical wave coefficients Q_{smn} as it would be received by an output probe with coefficients P_{out} at a distance A_T (which can be defined either in near or far field). As additional input, the function requires the θ -vector, the maximum polar order N , desired number of points in the transformed data both in θ ($N_{\theta,T}$) and in ϕ ($N_{\phi,T}$), and the delta factors $\Delta_{m'\mu}^n$ and $\Delta_{m'm}^n$.

Syntax:

```
[wT, thetaT, phiT] = coefficients2pattern(Q, theta , P_out, d_mu, d_m, N, NthT, NphT)
```

Inputs:

- **Q(s,m,n)** → spherical wave coefficients, ordered in an array with indices $s = (1, 2)$ (1st dimension), $m = (0, 1, \dots, N-1, N, -N, -N+1, \dots, -1)$ (2nd dimension), and $n = (1, 2, \dots, N)$ (3rd dimension) as array indices; all array elements with $|m| > n$ are assigned a value of zero
- **theta** → θ -steps for the corresponding pattern, ordered in a vector of length K_θ
- **P_out(s,m,n)** → probe response constants, ordered in an array with SWC-indices $s = (1, 2)$ (1st dimension), $m = (0, 1, \dots, N-1, N, -N, -N+1, \dots, -1)$ (2nd dimension), and $n = (1, 2, \dots, N)$ (3rd dimension) as array indices
- **d_m(n,m_st,m)** → an array containing the delta factors $\Delta_{m'm}^n$ for all indices of vectors **n** (1st dimension), **m_st** (2nd dimension), and **m** (3rd dimension); all array elements with $|m| > n$ or $|m'| > n$ are assigned a value of zero
- **d_mu(n,m_st,mu)** → an array containing the delta factors $\Delta_{m'\mu}^n$ for all indices of vectors **n** (1st dimension), **m_st** (2nd dimension), and **mu** (3rd dimension); all array elements with $|m'| > n$ are assigned a value of zero
- **N** → AUT's maximum polar order N
- **NthT** → desired number of equidistant θ -steps in $[0, \pi]$ after transformation
- **NphT** → desired number of equidistant ϕ -steps in $[0, 2\pi)$ after transformation

Outputs:

- **wT(chi,thetaT,phiT)** → output field pattern $w_T(\chi, \theta_T, \phi_T)$, ordered in an array using indices of vectors **chi** (1st dimension), **thetaT** (2nd dimension), and **phiT** (3rd dimension) as array indices
- **thetaT** → vector of equidistant θ -angles in $[0, \pi]$ of the transformed patterns, derived from the desired number of samples **NthT**
- **phiT** → vector of equidistant ϕ -angles in $[0, 2\pi)$ of the transformed patterns, derived from the desired number of samples **NphT**

B Pattern Stitching Method Documentation

This appendix presents the Matlab [44] implementation of the pattern stitching method, the underlying theory of which has been introduced in Chapter 3. With a similar structure as Appendix A, an example of usage will first be presented, giving detailed information on the required input data of the main function governing the pattern stitching procedure. This will be followed by an overview of all the implemented supporting functions required to successfully stitch together truncated field patterns of an antenna under test (AUT).

At this stage, it is important to note that assumptions A1 to A3, made in Appendix A for the implementation of the spherical near-to-far-field transformation (SN2FFT) algorithm, have also been made when implementing the pattern stitching method. In addition to that, the following assumptions were also made:

- A4 The method presupposes equidistant sampling in both θ and ϕ , with the assumption that the samples in ϕ have been obtained over the whole measurement sphere, whereas samples in θ may be truncated at some $\theta_{\text{trunc}} < 180^\circ$.
- A5 Both truncated measurements are assumed to have been measured covering the same part of the measurement sphere (same truncation angle θ_{trunc}), using the same maximum polar order N , and identical sampling in χ , θ , and ϕ . This is necessary for the definition of the overlapping range which is required for the alignment procedure.

B.1 Example of Usage

As explained in Chapter 3, the pattern stitching method has (currently) been implemented for stitching together two truncated field patterns which, when combined, must cover the entire sphere surrounding the AUT. The choice of antenna orientation for the first measurement is arbitrary, while the second measurement must be conducted with the antenna turned over (rotated by 180° in either x - or y -axis) to cover the opposite hemisphere of its radiation sphere. These measurements will be referred to as the top (hemisphere) measurement $w_{\text{top}}(\chi, \theta, \phi)$ and the bottom (hemisphere) measurement $w_{\text{bottom}}(\chi, \theta, \phi)$ hereafter. While the assignment of each measurement to a specific hemisphere is arbitrary, it should be noted that the upper measurement remains fixed in its coordinate system while the

bottom measurement is aligned to the coordinate system of the former during the alignment procedure; this is done using translation and rotation operations on the computed truncated SWCs of the bottom measurement.

To be able to use the FFT/Matrix method for computing the spherical wave coefficients (SWCs), two sample points, 0° and 90° , are required in χ (under the assumption A1). Since the transformation in ϕ is done using an FFT, the same number of equidistant samples as for the SN2FFT is required in the range $0^\circ \leq \phi < 360^\circ$, $K_\phi = 2N + 1$ (assuming A2). In θ , the minimum number of samples required by SN2FFT can also be used, but it is recommended to use an increased number of samples, defined by $K_{\theta,\text{trunc}} \geq N + 1$. As demonstrated in Table 3.1, the increased number of samples helps reduce the condition number $\kappa(\Psi)$. Since a least squares (LS) matrix method is used for the transformation in θ , the samples could theoretically be taken on an irregular, but an equidistant sampling was assumed during implementation (A4). To have an overlapping spherical belt between them, both $w_{\text{top}}(\chi, \theta, \phi)$ and $w_{\text{bottom}}(\chi, \theta, \phi)$ must be acquired following an identical sampling scheme (A5). For correct operation of the method, samples can be acquired with either the minimum number of required samples or with any excessive number of samples, i.e., oversampled. Just as with SN2FFT, the computation presupposes the knowledge of the probe antenna in order to carry out probe correction with its receiving coefficients $R_{\sigma\mu\nu}^p$. For both measurements, the FFT/Matrix method is used twice. In the first step, no singular value (SV) truncation is used and the resulting pattern is compared to the measured pattern by computing the scaled mean square error, which is then used as a signal-to-noise ratio estimate for SV truncation in the second run.

After truncated SWCs for both measurements are obtained, those of the bottom measurement are aligned to those of the upper measurement using the alignment procedure. The procedure attempts to minimize the weighted scaled mean square error (wSMSE) in the overlapping region between measurements in a constrained range of misalignment vectors $\mathbf{v}_M = (\chi_M, \vartheta_M, \varphi_M, x_M, y_M, z_M)$ containing the three Euler angles and the three offset distances. It requires an initial vector $\mathbf{v}_0 = (\chi_0, \vartheta_0, \varphi_0, x_0, y_0, z_0)$, an upper boundary vector $\mathbf{v}_{UB} = (\chi_{UB}, \vartheta_{UB}, \varphi_{UB}, x_{UB}, y_{UB}, z_{UB})$, and a lower boundary vector $\mathbf{v}_{LB} = (\chi_{LB}, \vartheta_{LB}, \varphi_{LB}, x_{LB}, y_{LB}, z_{LB})$. The upper and lower boundaries must be chosen by estimating the maximum offset and rotation from the origin of the coordinate system, while the initial vector can be set to $\mathbf{v}_0 = (0, 0, 0, 0, 0, 0)$ unless additional information on the AUT's position is known.

All steps of the pattern stitching method discussed above can be executed by calling the main function of the pattern stitching algorithm, aptly named `stitch_patterns`. A brief description, the function's syntax, and its input and output parameters will be described in the remainder of this section.

stitch_patterns

Description:

The main function of the pattern stitching method, which takes the measured truncated patterns $w_{\text{top}}(\chi, \theta, \phi)$ and $w_{\text{bottom}}(\chi, \theta, \phi)$, measured at frequency f . For computing truncated SWCs of both measurements, the function requires information on ϕ - and θ -samples, the name of the used probe antenna, the measurement distance A , and the maximum polar

order N . After computing truncated SWCs of both measurements, these can be aligned and stitched together to obtain the stitched field pattern $w_{\text{final}}(\chi, \theta, \phi)$, its SWCs, and the misalignment vector $\mathbf{v}_{\text{opt}} = (\chi_{\text{opt}}, \vartheta_{\text{opt}}, \varphi_{\text{opt}}, x_{\text{opt}}, y_{\text{opt}}, z_{\text{opt}})$. To do so, the initial point, upper bound, and lower bound vectors must be provided for the alignment procedure. Before the alignment procedure starts, the bottom measurement is rotated by 180° about the axis of rotation over which the bottom measurement was rotated before measurement. This information must be provided in the input parameter `rax`. In accordance with Section 4.1.2, the wSMSE minimization procedure can be done in two ways, using either complex field patterns or only the magnitude field pattern information. An additional input parameter `ev` allows for choosing between the two approaches, where assigning the string ‘abs’ instructs the function to use only the magnitude information. Setting `ev` to any other value or leaving it undefined will result in the default wSMSE computation using complex field pattern data.

Syntax:

```
[wfin, Qfin, vopt] = stitch_patterns(wttr, wbtr, f, thtr, phi, pr, A, N,
ev, rax, ub, lb, v0)
```

Inputs:

- `wttr(chi, thtr, phi)` → 3D array containing the truncated field pattern of the top measurement $w_{\text{top}}(\chi, \theta, \phi)$, ordered in an array using indices of vectors `chi` (1st dimension), `thtr` (2nd dimension), and `phi` (3rd dimension) as array indices
- `wbtr(chi, thtr, phi)` → 3D array containing the truncated field pattern of the bottom measurement $w_{\text{bottom}}(\chi, \theta, \phi)$, ordered in an array using indices of vectors `chi` (1st dimension), `thtr` (2nd dimension), and `phi` (3rd dimension) as array indices
- `f` → measurement frequency in Hz
- `thtr` → vector of measurement θ -steps for both patterns, in radians
- `phi` → vector of measurement ϕ -steps for both patterns, in radians
- `pr` → measurement probe name (the following probe antennas have been implemented): ‘dipole’ (ideal x-oriented dipole) or ‘RGP10_187’ (RGP10 with 187 mm mast) or ‘RGP10_527’ (RGP10 with 527 mm mast) or ‘RGP40’ (RGP40 dual ridge horn probe antenna)
- `A` → AUT-to-probe distance A in meters
- `N` → maximum polar order N of both truncated patterns
- `ev` → character string argument, if set to ‘abs’, pattern alignment is done using only magnitude information of both patterns, otherwise complex field patterns are used
- `rax` → defines the rotation axis over which the AUT has been rotated by 180° between the two partial measurements, either ‘x’ or ‘y’ must be set
- `ub` → upper bound for the misalignment vector, contains the Euler angles and translation offsets in the following order: $\mathbf{v}_{\text{UB}} = (\chi_{\text{UB}}, \vartheta_{\text{UB}}, \varphi_{\text{UB}}, x_{\text{UB}}, y_{\text{UB}}, z_{\text{UB}})$

- **lb** → lower bound for the misalignment vector, contains the Euler angles and translation offsets in the following order: $\mathbf{v}_{LB} = (\chi_{LB}, \vartheta_{LB}, \varphi_{LB}, x_{LB}, y_{LB}, z_{LB})$
- **v0** → initial estimate misalignment vector, contains the Euler angles and translation offsets in the following order: $\mathbf{v}_0 = (\chi_0, \vartheta_0, \varphi_0, x_0, y_0, z_0)$

Outputs:

- **wfin(chi,theta,phi)** → stitched field pattern, ordered in an array using indices of vectors **chi** (1st dimension), **theta** (2nd dimension), and **phi** (3rd dimension) as array indices
- **Qfin(s,m,n)** → spherical wave coefficients (SWCs) of the stitched pattern, ordered in an array with SWC-indices $s = (1, 2)$ (1st dimension), $m = (0, 1, \dots, N - 1, N, -N, -N + 1, \dots, -1)$ (2nd dimension), and $n = (1, 2, \dots, N)$ (3rd dimension) as array indices; all array elements with $|m| > n$ are assigned a value of zero
- **vopt** → misalignment vector solution, contains the Euler angles and translation offsets in the following order: $\mathbf{v}_{opt} = (\chi_{opt}, \vartheta_{opt}, \varphi_{opt}, x_{opt}, y_{opt}, z_{opt})$

B.2 List of Supporting Functions

Within the main function, various supporting functions are called in order to compute truncated SWCs of both measurements, align the patterns, and stitch them together. All supporting functions will be documented in the remainder of this chapter, providing a brief description, function syntax, and its input and output variables. For visual aid, first-level functions called by `stitch_patterns` have been illustrated in the annotated call graph in Figure B.1 along with their input and output parameters. The calling order has been

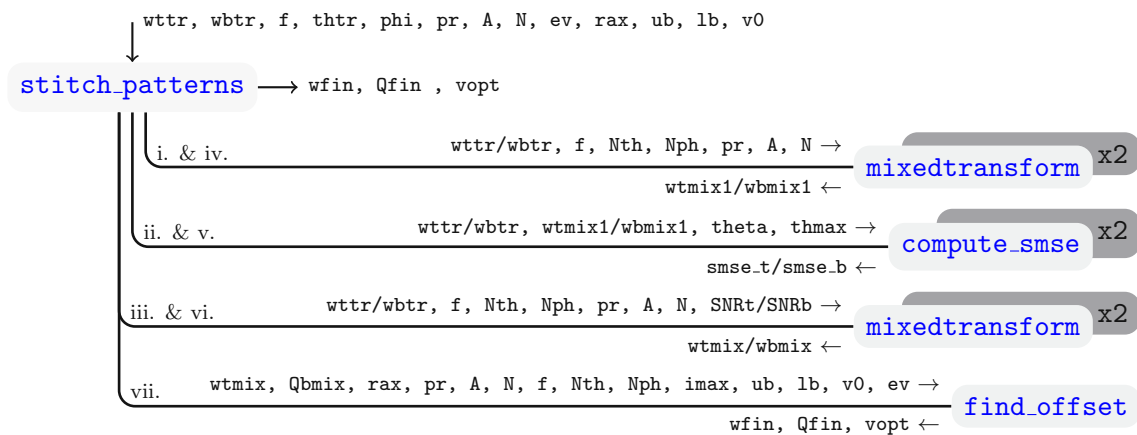


Figure B.1: Pattern stitching method annotated call graph

marked with Roman numerals i to vi., where two numerals were used where the function is called twice to indicate sequences of the first three called functions. From the call graph, one can see that these are called twice. They are used to compute the truncated field patterns and truncated SWCs, which is done separately for the top measurement and the bottom measurement. As explained at the beginning of this section, the truncated

field patterns are first computed without SV truncation to obtain SNR estimates. In the second computation round, these estimates are then used for SV truncation in order to compute realistic SWCs for the transformation algorithm, which is called in the final step. Lower-level functions were omitted from this graph for readability purposes and will be introduced later on.

mixedtransform

Description:

This function covers the first conceptual block of the pattern stitching method, the computation of truncated SWCs, as described in Section 3.2. It computes the truncated SWCs from field patterns truncated in θ using the FFT/Matrix method. To do so, the transmission equation is first constructed by computing the delta factors $\Delta_{m'\mu}^n$ and $\Delta_{m'm}^n$ and the probe response coefficients $P_{s\mu m}$ by calling the `delta_factors` and `get_probe_response_constants` functions presented in Appendix A. The transmission equation is transformed over χ and ϕ using FFTs to obtain the twice-transformed transmission equation (3.5). The remaining transformation in θ is then solved for each polar index m separately. In accordance with findings reported in Section 3.2.4, singular value (SV) truncation has been implemented, for which the function requires an input signal-to-noise ratio (SNR) estimate. This estimate is used to discard very small SVs when computing the pseudoinverse of the coefficient matrix Ξ_m and solving the inverted transmission formula from (3.7). This procedure returns the truncated SWCs Q_{smn}^{mix} are computed. After these are obtained, a classical FT-based expansion to a same-distance field pattern, $w_{\text{mix}}(\chi, \theta, \phi)$, is done using the function `coefficients2pattern` (also presented in Appendix A).

The call order of the subfunctions within the `mixedtransform` function is shown in the call graph in Figure B.2, where Roman numerals and lowercase Latin letters indicate the call order when multiple functions are called within a function. The graph highlights all called functions and their input and output parameters. As can be seen, all called functions are reused functions (marked with a “*” in the graph), implemented for the SN2FFT algorithm presented in Appendix A. They could be reused by the FFT/Matrix method since the only difference between the two computations is the transformation in θ , which is executed directly in the function `mixedtransform`.

Syntax:

```
[wmix,Qmix] = mixedtransform(w, f, theta, NthT, NphT, pr, A, N, SNR)
```

Inputs:

- `w(chi,theta,phi)` → 3D array of the field pattern $w(\chi, \theta, \phi)$, ordered in an array using indices of vectors `chi` (1st dimension), `theta` (2nd dimension), and `phi` (3rd dimension) as array indices
- `f` → measurement frequency in Hz
- `theta` → vector of measurement θ -steps in radians
- `NthT` → desired number of θ -steps in $[0, \pi]$ after transformation

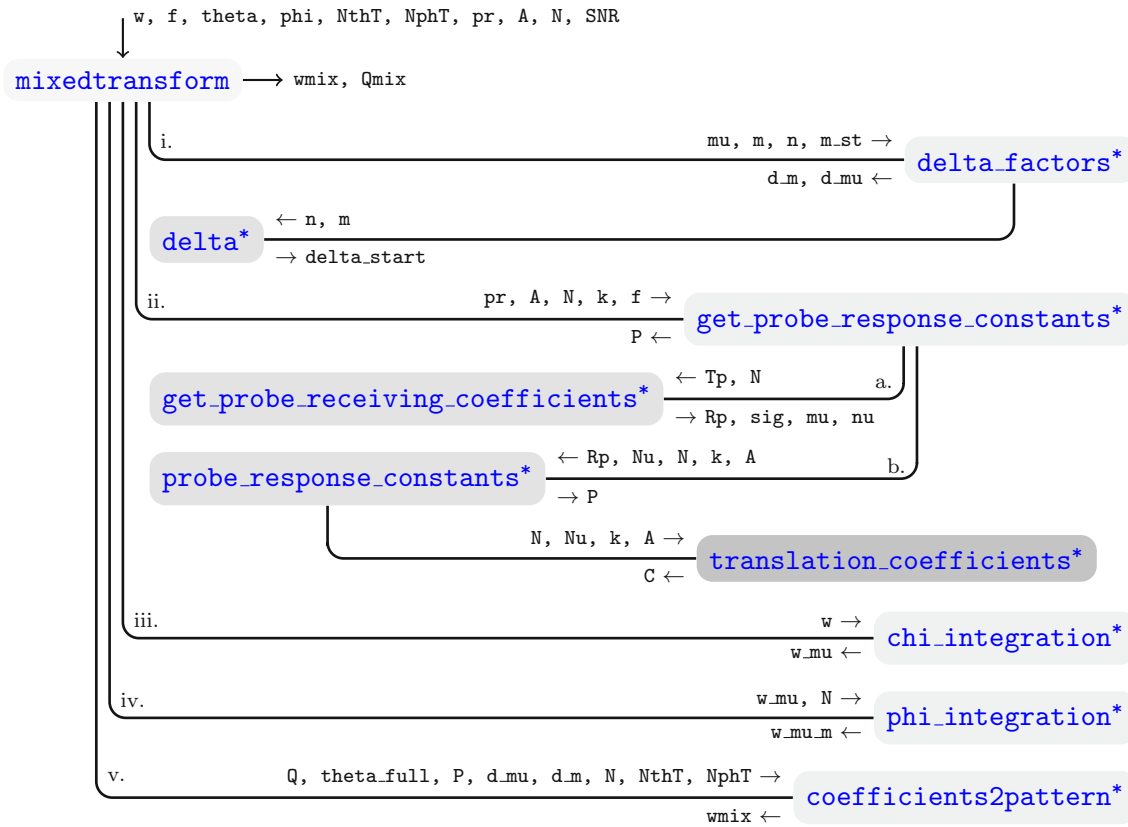


Figure B.2: Mixed transform annotated call graph

- $NphT \rightarrow$ desired number of ϕ -steps in $[0, 2\pi)$ after transformation
- $pr \rightarrow$ measurement probe name (the following probe antennas have been implemented): 'dipole' (ideal x-oriented dipole) or 'RGP10_187' (RGP10 with 187 mm mast) or 'RGP10_527' (RGP10 with 527 mm mast) or 'RGP40' (RGP40 dual ridge horn probe antenna)
- $A \rightarrow$ AUT-to-probe distance A in meters
- $N \rightarrow$ maximum polar order N of both truncated patterns
- $SNR \rightarrow$ signal-to-noise ratio (SNR) estimate needed for singular value (SV) truncation

Outputs:

- $wmix(\chi, \theta, \phi) \rightarrow$ 3D array of the resulting field pattern $w_{mix}(\chi, \theta, \phi)$, ordered in an array using indices of vectors χ (1st dimension), θ (2nd dimension), and ϕ (3rd dimension) as array indices
- $Qmix(s, m, n) \rightarrow$ resulting SWCs Q_{smn}^{mix} , ordered in an array with SWC-indices $s = (1, 2)$ (1st dimension), $m = (0, 1, \dots, N-1, N, -N, -N+1, \dots, -1)$ (2nd dimension), and $n = (1, 2, \dots, N)$ (3rd dimension) as array indices; all array elements with $|m| > n$ are assigned a value of zero

compute_smse

Description:

The function computes the scaled mean square error (SMSE) (3.14) between two input patterns, $w_1(\chi, \theta, \phi)$ and $w_2(\chi, \theta, \phi)$, in the overlapping range of θ -angles between θ_{\min} and θ_{\max} . For indexing purposes, it requires that both patterns are defined starting at $\theta = 0^\circ$ and extend at least up to θ_{\max} . Since only the part between θ_{\min} and θ_{\max} is considered in the computation, any θ -value outside this range can be set to 0 in case of missing data.

Syntax:

```
smse = compute_smse(w1, w2, theta, thmax, thmin)
```

Inputs:

- **w1(chi,theta,phi)**, **w2(chi,theta,phi)** → 3D arrays containing field patterns $w_1(\chi, \theta, \phi)$ and $w_2(\chi, \theta, \phi)$, ordered in an array using indices of vectors **chi** (1st dimension), full-range **theta** (2nd dimension), and **phi** (3rd dimension) as array indices
- **theta** → full-range θ -vector ($0^\circ \leq \theta \leq 180^\circ$)
- **thmax** → largest θ -angle to be considered in the computation
- **thmin** → smallest θ -angle to be considered in the computation

Outputs:

- **smse** → computed SMSE in the overlapping range between both input patterns as defined by the minimum and the maximum θ -angle

find_offset

Description:

This function, along with all the subfunctions that it calls, covers the second and third conceptual blocks of the stitching algorithm, which were presented in Sections 3.3 and 3.4. It takes the field pattern of the top measurement $w_{\text{top,mix}}(\chi, \theta, \phi)$, preprocessed with the FFT/Mixed method, the truncated SWCs of the bottom measurement Q_{smn}^B , and all relevant parameters for the alignment procedure, i.e., rotation axis parameter **rax**, probe name **pr**, measurement distance A , maximum polar order N , frequency f , number of steps in θ and ϕ , information about the truncation angle θ_{trunc} , initial misalignment vector, upper and lower bounds, and the parameter defining whether wSMSE in the overlapping range should be evaluated using complex data or only magnitude information. The function call order within the **find_offset** function is shown in Figure B.3, where input and output parameters of each called function are shown. As in previous call graphs, the call order of functions calling multiple subfunctions are marked with Roman numerals i. to vii. and Latin letters a. and b. Functions called at positions iii., v., and vii. were annotated with additional commentary to clarify exactly which part of the alignment and stitching procedure they cover. In iii., the rotation is done over the rotation axis used during

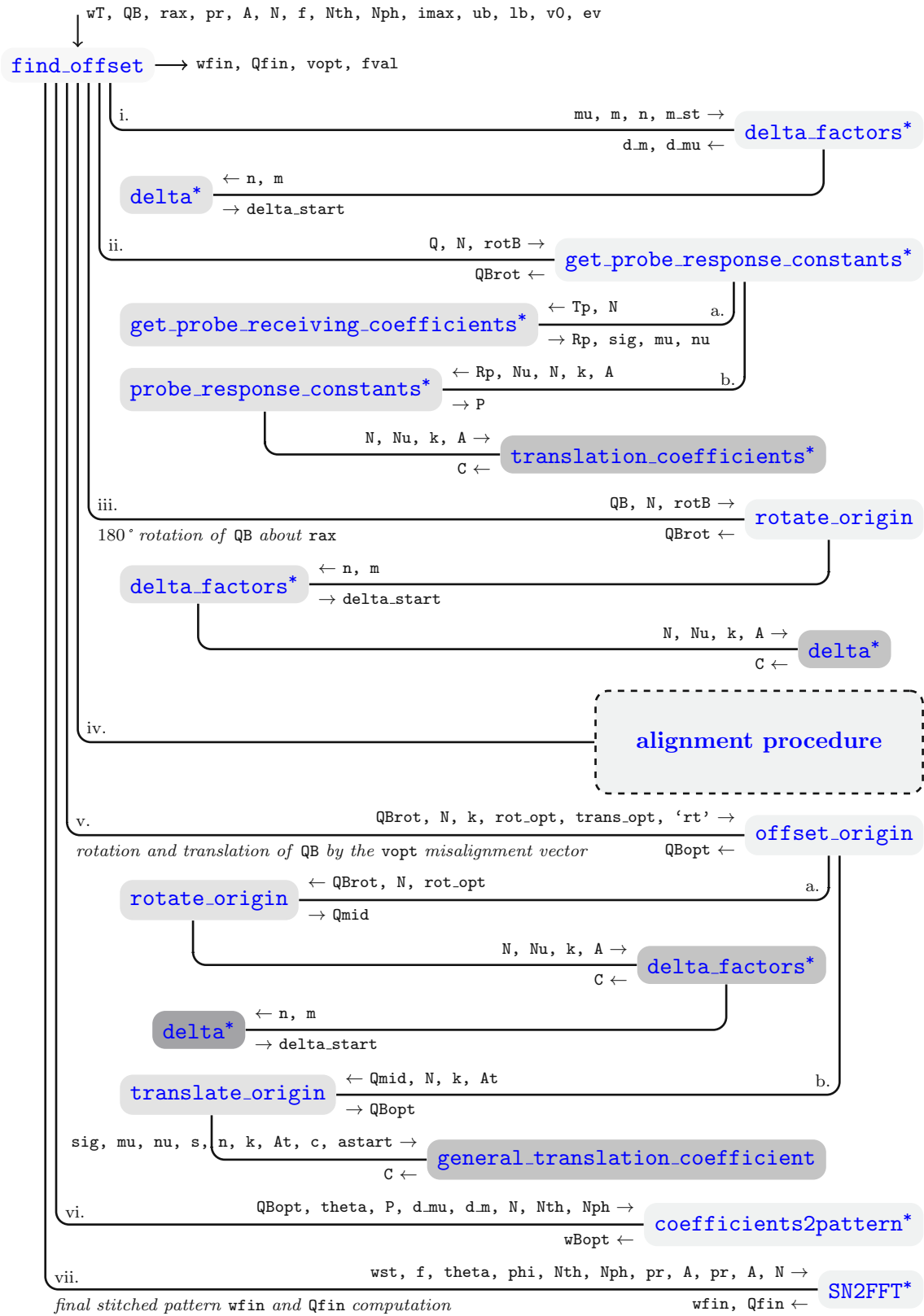


Figure B.3: Pattern alignment annotated call graph

measurement. In step v., the rotation and translation are done with the optimum misalignment vector \mathbf{vopt} , which was found during the alignment procedure called in iv. The call of the spherical near-to-far-field transformation (SN2FFT) algorithm at the final stage is done at the end of the pattern stitching method in order to obtain the final stitched pattern \mathbf{wfin} and its SWCs, which are stored in \mathbf{Qfin} .

The alignment procedure marked in Figure B.3 with a dashed frame, whose details were excluded in the graph, deserves some further attention. For that reason, its detailed operation has been drawn in Figure B.4. This iterative block contains the objective function, `offset_function`, and the optimizer function `fmincon` from Matlab's Optimization Toolbox [44]. The objective function is used to rotate and translate SWCs of the bottom measurement, generate the field pattern $w_{\text{bottom}}^o(\chi, \theta, \phi)$ for the given input misalignment vector, and compute the value of the minimization objective for this misalignment combination, the weighted scaled mean square error (wSMSE). It is called iteratively by the `fmincon` function during the alignment procedure with varying misalignment combinations in order to find the misalignment between the coordinate systems of both measurements. The `fmincon` function is a powerful minimization solver that allows the user to apply different types of inequalities to the problem, including nonlinear constraints [44]. Its general definition is

$$\min_{\mathbf{x}} f(\mathbf{x}) \text{ such that } \begin{cases} c(\mathbf{x}) \leq \mathbf{0} \\ ceq(\mathbf{x}) = \mathbf{0} \\ \mathbf{A} \cdot \mathbf{x} \leq \mathbf{b} \\ \mathbf{Aeq} \cdot \mathbf{x} \leq \mathbf{beq} \\ \mathbf{lb} \leq \mathbf{x} \leq \mathbf{ub} \end{cases},$$

where $c(\mathbf{x})$ and $ceq(\mathbf{x})$ represent nonlinear (in)equality constraints, \mathbf{A} and \mathbf{Aeq} represent linear (in)equality constraints, and \mathbf{lb} and \mathbf{ub} represent the lower and upper bounds of the variable matrix \mathbf{x} . Since the minimization in the case of pattern stitching requires only the upper and lower bound constraints, all other constraints were assigned an empty array, as can be seen on the bottom of Figure B.4. Moreover, some optimizer settings were also changed for the pattern stitching method, as seen on the bottom of the graph. Any optimizer option not explicitly listed in the graph has been set to its default value. The most important among the options were the choice of algorithm, which was set to 'interior-point', and the use of parallel computing for faster results. For more information on the minimization function, the reader is invited to read the supporting Matlab documentation [44].

Syntax:

```
[wfin, Qfin, vopt, fval] = find_offset(wT, QB, rax, pr, A, N, f, Nth, Nph,
imax, ub, lb, v0, flag)
```

Inputs:

- `wT(chi, theta, phi)` → 3D array containing the truncated field pattern of the top measurement $w_{\text{top}}(\chi, \theta, \phi)$, ordered in an array using indices of vectors `chi` (1st dimension), `theta` (2nd dimension), and `phi` (3rd dimension) as array indices
- `QB(s,m,n)` → truncated spherical wave coefficients (SWCs) of the bottom measurement, ordered in an array with SWC-indices $s = (1, 2)$ (1st dimension), $m =$

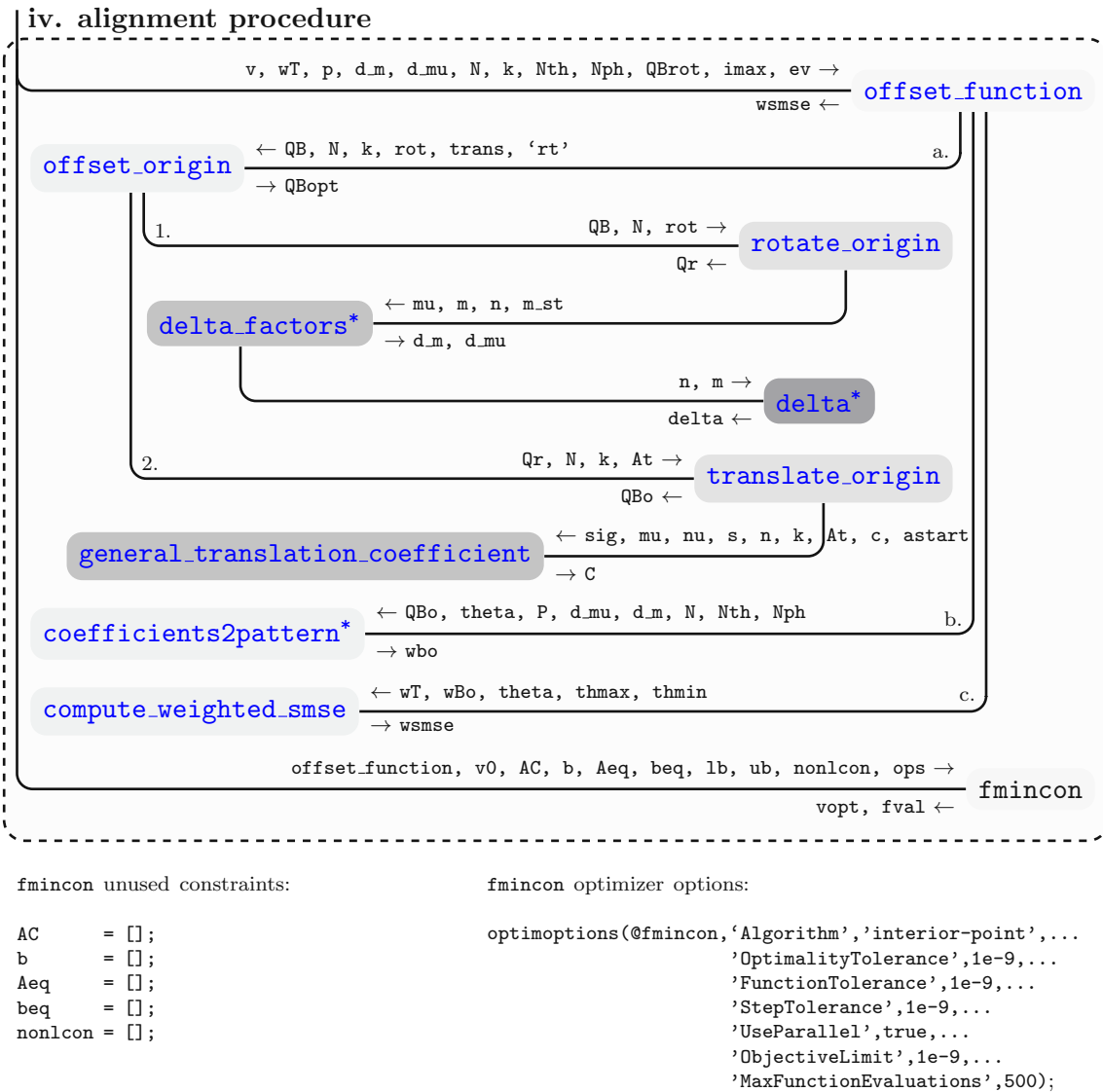


Figure B.4: Alignment procedure annotated call graph

$(0, 1, \dots, N-1, N, -N, -N+1, \dots, -1)$ (2^{nd} dimension), and $n = (1, 2, \dots, N)$ (3^{rd} dimension) as array indices; all array elements with $|m| > n$ are assigned a value of zero

- **rax** → defines the rotation axis over which the AUT has been rotated by 180° between the two partial measurements, either 'x' or 'y' must be set
- **pr** → measurement probe name (the following probe antennas have been implemented): 'dipole' (ideal x-oriented dipole) or 'RGP10_187' (RGP10 with 187 mm mast) or 'RGP10_527' (RGP10 with 527 mm mast) or 'RGP40' (RGP40 dual ridge horn probe antenna)
- **A** → AUT-to-probe distance A in meters
- **N** → maximum polar order N of both truncated patterns

- **f** → measurement frequency in Hz
- **Nth** → number of θ -steps in $[0, \pi]$
- **Nph** → number of ϕ -steps in $[0, 2\pi)$
- **imax** → **theta** index pointing to the truncation angle θ_{trunc}
- **ub** → upper bound for the misalignment vector, contains the Euler angles and translation offsets in the following order: $(\chi_{\text{UB}}, \vartheta_{\text{UB}}, \varphi_{\text{UB}}, x_{\text{UB}}, y_{\text{UB}}, z_{\text{UB}})$
- **lb** → lower bound for the misalignment vector, contains the Euler angles and translation offsets in the following order: $(\chi_{\text{LB}}, \vartheta_{\text{LB}}, \varphi_{\text{LB}}, x_{\text{LB}}, y_{\text{LB}}, z_{\text{LB}})$
- **v0** → initial estimate misalignment vector, contains the Euler angles and translation offsets in the following order: $(\chi_0, \vartheta_0, \varphi_0, x_0, y_0, z_0)$
- **ev** → character string argument, if set to 'abs', pattern alignment is done using only magnitude information of both patterns, otherwise complex field patterns are used

Outputs:

- **wfin(chi, theta, phi)** → stitched field pattern, ordered in an array using indices of vectors **chi** (1st dimension), **theta** (2nd dimension), and **phi** (3rd dimension) as array indices
- **Qfin(s, m, n)** → spherical wave coefficients (SWCs) of the stitched pattern, ordered in an array with SWC-indices $s = (1, 2)$ (1st dimension), $m = (0, 1, \dots, N - 1, N, -N, -N + 1, \dots, -1)$ (2nd dimension), and $n = (1, 2, \dots, N)$ (3rd dimension) as array indices; all array elements with $|m| > n$ are assigned a value of zero
- **vopt** → misalignment vector solution, contains the Euler angles and translation offsets in the following order: $(\chi_{\text{opt}}, \vartheta_{\text{opt}}, \varphi_{\text{opt}}, x_{\text{opt}}, y_{\text{opt}}, z_{\text{opt}})$
- **fval** → minimum wSMSE result in the overlapping region, achieved during pattern alignment

rotate_origin

Description:

The function first computes all delta factors $\Delta_{m/m}^n$ for the given order N by calling the function `delta_factors`, which was presented in Appendix A. These factors are needed to compute rotation coefficients $d_{\mu m}^n(\vartheta_0)$ for rotation over θ from (2.26). Then, the original SWCs Q_{smn} are rotated using (2.32) to obtain the rotated SWCs Q_{smn}^r .

Syntax:

`Qr = rotate_origin(Q, N, rot)`

Inputs:

- $Q(\mathbf{s}, \mathbf{m}, \mathbf{n}) \rightarrow$ SWCs Q_{smn} , ordered in an array with SWC-indices $s = (1, 2)$ (1st dimension), $m = (0, 1, \dots, N - 1, N, -N, -N + 1, \dots, -1)$ (2nd dimension), and $n = (1, 2, \dots, N)$ (3rd dimension) as array indices; all array elements with $|m| > n$ are assigned a value of zero
- $N \rightarrow$ maximum polar order N of the SWCs
- $\text{rot} \rightarrow$ vector $(\chi_0, \vartheta_0, \varphi_0)$ containing the Euler rotation angles

Outputs:

- $Qr(\mathbf{s}, \mathbf{m}, \mathbf{n}) \rightarrow$ rotated SWCs Q_{smn}^r , ordered in an array with SWC-indices $s = (1, 2)$ (1st dimension), $m = (0, 1, \dots, N - 1, N, -N, -N + 1, \dots, -1)$ (2nd dimension), and $n = (1, 2, \dots, N)$ (3rd dimension) as array indices; all array elements with $|m| > n$ are assigned a value of zero

offset_origin

Description:

The function takes the input SWCs Q_{smn} and uses the provided coordinate system offset, defined by the set of Euler angles $(\chi_0, \vartheta_0, \varphi_0)$ and the translation vector (x_0, y_0, z_0) , to transform them into the desired offset SWCs Q_{smn}^o . This is done by calling the functions `rotate_origin` and `translate_origin` in the order defined by the parameter `order`. As discussed in Section 2.2, an arbitrary translation direction (different than $+z$, for which the function `translate_origin` has been defined) is achieved by first rotating the SWCs to align the direction of translation with the $+z$ -axis, translating them, and then rotating them back into the initial orientation.

Syntax:

`Qo = offset_origin(Q, N, k, rot, trans, order)`

Inputs:

- $Q(\mathbf{s}, \mathbf{m}, \mathbf{n}) \rightarrow$ SWCs Q_{smn} , ordered in an array with SWC-indices $s = (1, 2)$ (1st dimension), $m = (0, 1, \dots, N - 1, N, -N, -N + 1, \dots, -1)$ (2nd dimension), and $n = (1, 2, \dots, N)$ (3rd dimension) as array indices; all array elements with $|m| > n$ are assigned a value of zero
- $N \rightarrow$ maximum polar order N of the SWCs
- $k \rightarrow$ wavenumber
- $\text{rot} \rightarrow$ vector $(\chi_0, \vartheta_0, \varphi_0)$ containing the Euler rotation angles
- $\text{trans} \rightarrow$ vector (x_0, y_0, z_0) containing the translation distances in all axes
- $\text{order} \rightarrow$ parameter defining the order of operations: ‘`rt`’ “first rotation and then translation” and ‘`tr`’ “first translation and then rotation”

Outputs:

- $Q_0(\mathbf{s}, \mathbf{m}, \mathbf{n}) \rightarrow$ offset (translated and rotated) SWCs Q_{smn}^o , ordered in an array with SWC-indices $s = (1, 2)$ (1st dimension), $m = (0, 1, \dots, N-1, N, -N, -N+1, \dots, -1)$ (2nd dimension), and $n = (1, 2, \dots, N)$ (3rd dimension) as array indices; all array elements with $|m| > n$ are assigned a value of zero

translate_origin

Description:

The function first computes the recursive formula starting linearization coefficients $a_{n+\nu}$ for all n and ν according to [38, Eqs. (28)]. It then computes all translation coefficients $C_{\sigma\mu\nu}^{sn(c)}(kA_t)$ for a translation distance A_t in $+z$ direction by calling the function `general_translation_coefficient`. Finally, the input SWC matrix \underline{Q} is translated to the new $+z$ -translated origin using (2.41). giving the translated SWC matrix \underline{Q}_t . Additionally, the total power contained in the original and the translated SWCs is computed using (2.22). A warning is returned if the power of the translated SWCs is more than 0.1% below that of original SWCs as this indicates that the considered maximum polar order N is insufficient for such a translation.

Syntax:

`Qt = translate_origin(Q, N, k, At)`

Inputs:

- $Q(\mathbf{s}, \mathbf{m}, \mathbf{n}) \rightarrow$ SWCs Q_{smn} , ordered in an array with SWC-indices $s = (1, 2)$ (1st dimension), $m = (0, 1, \dots, N-1, N, -N, -N+1, \dots, -1)$ (2nd dimension), and $n = (1, 2, \dots, N)$ (3rd dimension) as array indices; all array elements with $|m| > n$ are assigned a value of zero
- $N \rightarrow$ maximum polar order N of the SWCs
- $k \rightarrow$ wavenumber
- $At \rightarrow$ translation distance in meters

Outputs:

- $Qt(\mathbf{s}, \mathbf{m}, \mathbf{n}) \rightarrow$ translated SWCs Q_{smn}^t , ordered in an array with SWC-indices $s = (1, 2)$ (1st dimension), $m = (0, 1, \dots, N-1, N, -N, -N+1, \dots, -1)$ (2nd dimension), and $n = (1, 2, \dots, N)$ (3rd dimension) as array indices; all array elements with $|m| > n$ are assigned a value of zero

general_translation_coefficient

Description:

The function computes a translation coefficient $C_{\sigma\mu\nu}^{sn(c)}(kA_t)$ for a translation distance A_t according to (2.34), for spherical wave functions of type (c), as discussed in Section 2.1.

It uses the recursive formula given in [38, Eqs. (26)] to compute the required linearization coefficients from the starting value `astart`.

Syntax:

`C = general_translation_coefficient(sig, mu, nu, s, n, k, At, c, astart)`

Inputs:

- `sig` → denotes the probe’s generating function indices σ , ordered in a vector: `sig` = 1 (m -function), `sig` = 2 (n -function)
- `mu` → vector of probe azimuthal indices $\mu = (1, -1)$ (probe antenna’s equivalent of index m)
- `nu` → vector of probe polar indices $\nu = (1, 2, \dots, \nu_{\max})$ (probe antenna’s equivalent of index n)
- `s` → denotes the AUT’s generating function indices s , ordered in a vector: `s` = 1 (m -function), `s` = 2 (n -function)
- `n` → vector of AUT’s polar indices $n = (1, 2, \dots, N)$
- `k` → wavenumber
- `At` → translation distance in meters
- `c` → spherical function type: `c` = 1 standing wave, `c` = 3 inward traveling wave, `c` = 4 outward traveling wave
- `astart` → starting linearization coefficient for the recursive formula

Outputs:

- `C` → computed translation coefficient $C_{\sigma\mu\nu}^{sn(c)}(kA_t)$

offset_function

Description:

This is the error function used for the alignment procedure which is executed with varying misalignment vectors during the error minimization process. It takes the current input misalignment vector $v = (\chi_C, \vartheta_C, \varphi_C, x_C, y_C, z_C)$ containing the Euler angles and the translation offsets, uses them to rotate and translate the truncated SWCs of the bottom measurement Q_{smn}^B by calling the `offset_origin` function and then expands these offset SWCs into a field pattern by calling the `coefficients2pattern` function introduced in Appendix A. Finally, the wSMSE in the overlapping range is computed between the resulting bottom pattern and the pattern of the top measurement, $w_T(\chi, \theta, \phi)$. Depending on the set parameter `ev`, this can be done either using only the magnitudes of both patterns or complex field patterns.

Syntax:

`wsmse = offset_function(v, wT, P, d_m, d_mu, N, k, Nth, Nph, QB, imax, ev)`

Inputs:

- \mathbf{v} → current misalignment vector, contains the Euler angles and translation offsets in the following order: $(\chi_C, \vartheta_C, \varphi_C, x_C, y_C, z_C)$
- $\mathbf{wT}(\mathbf{chi}, \mathbf{theta}, \mathbf{phi})$ → 3D array containing the truncated field pattern of the top measurement $w_{\text{top}}(\chi, \theta, \phi)$, ordered in an array using indices of vectors \mathbf{chi} (1st dimension), \mathbf{theta} (2nd dimension), and \mathbf{phi} (3rd dimension) as array indices
- $\mathbf{P}(\mathbf{s}, \mathbf{mu}, \mathbf{n})$ → probe response constants, ordered in an array with SWC-indices $s = (1, 2)$ (1st dimension), $\mu = (1, -1)$ (2nd dimension), and $n = (1, 2, \dots, N)$ (3rd dimension) as array indices
- $\mathbf{d}_m(\mathbf{n}, \mathbf{m_st}, \mathbf{m})$ → an array containing the delta factors $\Delta_{m'm}^n$ for all indices of vectors \mathbf{n} (1st dimension), $\mathbf{m_st}$ (2nd dimension), and \mathbf{m} (3rd dimension); all array elements with $|m| > n$ or $|m'| > n$ are assigned a value of zero
- $\mathbf{d}_{\mu}(\mathbf{n}, \mathbf{m_st}, \mathbf{mu})$ → an array containing the delta factors $\Delta_{m'\mu}^n$ for all indices of vectors \mathbf{n} (1st dimension), $\mathbf{m_st}$ (2nd dimension), and \mathbf{mu} (3rd dimension); all array elements with $|m'| > n$ are assigned a value of zero
- N → maximum polar order N of both truncated patterns
- \mathbf{k} → wavenumber
- N_{θ} → number of θ -steps in $[0, \pi]$
- N_{ϕ} → number of ϕ -steps in $[0, 2\pi]$
- $\mathbf{QB}(\mathbf{s}, \mathbf{m}, \mathbf{n})$ → truncated spherical wave coefficients (SWCs) of the bottom measurement, ordered in an array with SWC-indices $s = (1, 2)$ (1st dimension), $m = (0, 1, \dots, N-1, N, -N, -N+1, \dots, -1)$ (2nd dimension), and $n = (1, 2, \dots, N)$ (3rd dimension) as array indices; all array elements with $|m| > n$ are assigned a value of zero
- \mathbf{imax} → \mathbf{theta} index pointing to the truncation angle θ_{trunc}
- \mathbf{ev} → character string argument, if set to 'abs', pattern alignment is done using only magnitude information of both patterns, otherwise complex field patterns are used

Outputs:

- \mathbf{wsmse} → computed wSMSE in the overlapping range between both input patterns as defined by the minimum and the maximum θ -angle

compute_weighted_smse

Description:

The function computes the weighted scaled mean square error (wSMSE) (3.15) between two input patterns, $w_1(\chi, \theta, \phi)$ and $w_2(\chi, \theta, \phi)$, in the overlapping range of θ -angles between θ_{\min} and θ_{\max} . For indexing purposes, it requires that both patterns are defined starting

at $\theta = 0^\circ$ and at least up to θ_{\max} . Since only the part between θ_{\min} and θ_{\max} is considered in the computation, any θ -value outside this range can be set to 0 in case of missing data.

Syntax:

```
wsmse = compute_weighted_smse(w1, w2, theta, thmax, thmin)
```

Inputs:

- `w1(chi,theta,phi)`, `w2(chi,theta,phi)` → 3D arrays containing field patterns $w_1(\chi, \theta, \phi)$ and $w_2(\chi, \theta, \phi)$, ordered in an array using indices of vectors `chi` (1st dimension), full-range `theta` (2nd dimension), and `phi` (3rd dimension) as array indices
- `theta` → full-range θ -vector ($0^\circ \leq \theta \leq 180^\circ$)
- `thmax` → largest θ -angle to be considered in the computation
- `thmin` → smallest θ -angle to be considered in the computation

Outputs:

- `wsmse` → computed wSMSE in the overlapping range between both input patterns as defined by the minimum and the maximum θ -angle

C Extension of the Stitching Method to Connectorless Devices

The alignment algorithm presented in Section 3.3.2 was implemented for use with classical antenna measurements, where the antennas under test (AUTs) are equipped with a coaxial connector and regular S-parameter measurements are possible. However, the antenna to be measured is often integrated on a printed circuit board (PCB) and is not equipped with a coaxial connector, e.g., when dealing with connectorless internet of things (IoT) devices with an integrated radio frequency (RF) chip and power supply. To cater to connectorless devices, the measurement procedure must therefore be modified. Furthermore, adaptations of the alignment procedure are required in order to be able to process radiation patterns of this type of devices. We first tackled these issues in [59], where the extension of the pattern stitching method to connectorless devices was presented on the example of battery-powered electronic shelf labels (ESLs) with an antenna integrated onto the PCB. A measurement setup for measuring connectorless devices was devised for this purpose and the pattern-stitching method was adapted accordingly. The procedure can be generalized to all kinds of devices under test (DUTs) with integrated antennas, as long as they can be triggered into transmitting mode where a continuous wave (CW) signal is transmitted for a known time. The necessary modifications of the measurement procedure and the required adaptations to the stitching method for processing patterns of connectorless devices measured in this manner are documented in the remainder of this chapter.

C.1 Measurement Setup

Considering the standard measurement setup of a swing arm-over-azimuth test range, which was shown in Figure 3.1, a vector network analyzer (VNA) measurement of the incoming wave received by the probe antenna would suffice to obtain relative magnitude patterns. This, however, does not give us coherent phase information, which is needed for computing the SWCs, without which the pattern stitching method cannot work. In order to obtain a reference signal for coherent phase information, an additional antenna must be used. This reference antenna must always maintain the same distance and orientation with regard to the device under test (DUT). This can be achieved by mounting the reference antenna onto the ϕ -axis rotary stage. The reference antenna is then covered with the

support structure on which the DUT is mounted, as shown in Figure C.1. ROHACELL is used for the support structure because its permittivity closely resembles the permittivity of air and thus aids in minimizing interactions with the DUT and unwanted reflections.

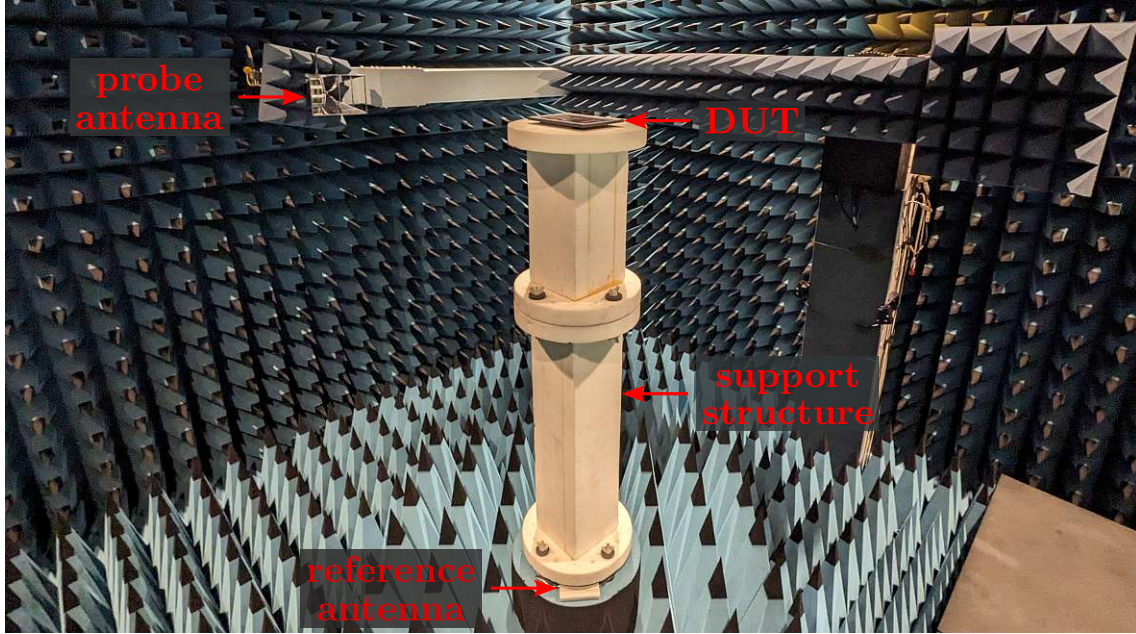


Figure C.1: Placement of the reference antenna, the support structure, the DUT, and the probe antenna when measuring connectorless devices.

Next, the DUT must be set to transmit a CW signal at all frequencies of interest. In order to measure this transmitted signal, a synchronization between the measurement system and the DUT is required. To allow for synchronization, the DUT is programmed such that it waits to receive a wake-up pulse at a chosen frequency and then starts transmitting a CW signal, progressing in a sequence of known durations over all frequencies to be measured.¹

After the DUT is programmed, it is ready to be measured in the antenna test range. The measurement setup schematic of the range containing all crucial measurement equipment is shown in Figure C.2. Using this measurement setup, a synchronized measurement can then be done in the following three steps, marked with 1. to 3. in the schematic:

1. By default, the DUT waits for a wake-up pulse before transmitting a sequence of CW signals of known duration over all measurement frequencies. The position controller (PosC) is connected to the swing arm (θ) and the two rotary stages (ϕ, χ). For every (χ, θ, ϕ) measurement point, the PosC sends a trigger signal to both the signal generator and the VNA once the axes are in position.
2. The signal generator then transmits a CW pulse to the reference antenna via a directional coupler to set the DUT into transmitting mode. At the same time, the VNA uses the trigger to time the start of the measurement sequence over all frequencies.

¹It is important to note that the reference frequency of the measurement equipment generally does not match that of the DUT's internal chip, so the exact frequencies either need to be measured in advance or a sufficiently large VNA IF bandwidth must be used to assure that the signal is captured by the VNA.

3. The VNA measures the received signals on two receivers: On receiver A, the signal received by the probe antenna is measured, while receiver B is connected to the reference antenna via the directional coupler. By measuring the ratio between the signal received at receiver A and the signal received at receiver B (A/B), a phase-coherent radiation pattern is obtained.

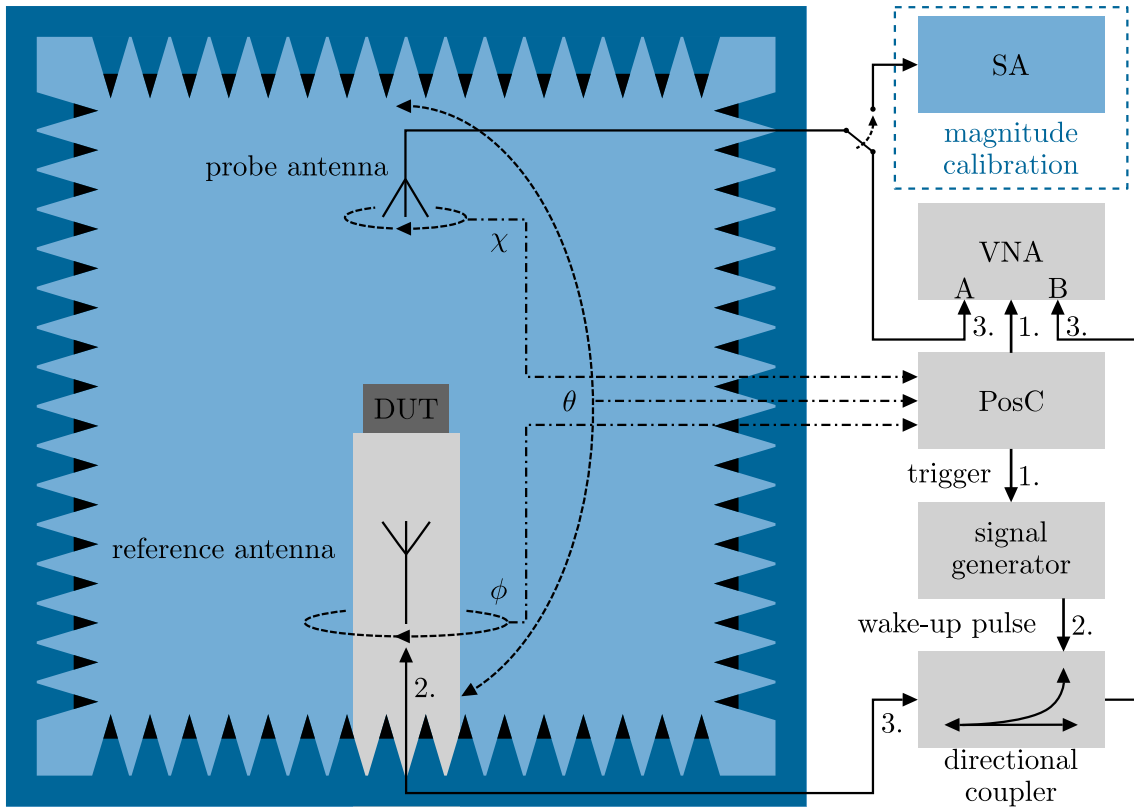


Figure C.2: Measurement setup for connectorless DUTs: antenna range

This measurement procedure gives coherent phase information, but only relative signal levels. To determine parameters such as antenna gain, equivalent isotropic radiated power (EIRP), or total radiated power (TRP), an additional magnitude-calibration measurement is required.

C.2 Magnitude Calibration

While classical two-port measurements allow for gain calibration by substituting the AUT with a standard gain horn (SGH) antenna with a known gain, this is not possible in the case of connectorless test objects. Instead, the absolute power received by the probe antenna can be measured at an arbitrary measurement orientation, $(\chi_0, \theta_0, \phi_0)$. This requires precise knowledge of the probe antenna gain, the measurement distance, as well as cable attenuation between the probe antenna and the measurement port. Since the DUT transmits short, pulsed CW signals, a synchronized spectrum analyzer (SA), which was also included in the measurement setup schematic in Figure C.2, must be used instead

of a power meter to measure the received power. The EIRP can then be derived from the link budget equation:²

$$\text{EIRP}_{\text{dB}} = P_{\text{SA|dB}} + \text{ATT}_{\text{dB}} - G_{\text{probe|dB}} + \text{FSPL}_{\text{dB}} \quad (\text{C.1})$$

In (C.1), P_{SA} is the power measured with the SA, ATT represents both the cable losses on the path from probe antenna to the SA and the SA power correction factor, G_{probe} is the probe gain and FSPL the free-space path loss between the DUT and the probe antenna. Once the EIRP is known, the magnitude of the electric field at the measurement distance d can be calculated:

$$|E_d(\chi_0, \theta_0, \phi_0)| = \sqrt{\frac{2Z_0 \cdot 10^{\frac{\text{EIRP}_{\text{dB}}}{10}}}{4\pi d^2}} \quad (\text{C.2})$$

Finally, the known value of $|E_d|$ at $(\chi_0, \theta_0, \phi_0)$ can be compared to the relative magnitude measured at that same position during the probe/reference relative measurement in order to obtain a correction factor which can then be applied to all measurement points. Since the coordinate systems of both measurements are not perfectly aligned, this of course has to be done separately for each (truncated) measurement.

C.3 Alignment Procedure Adaptation

As mentioned earlier, the magnitude of each measurement is calibrated by measuring the signal power received by the probe antenna at a single measurement point. Ideally, this would bring the two measurements to matching magnitude levels. However, it was observed that this single-point calibration procedure can cause a significant increase of the weighted scaled mean square error (wSMSE) in the overlapping region when inappropriate calibration points are chosen, i.e., points where the antenna radiates poorly and the SNR is low. Moreover, the magnitude calibration does not correct for the change in phase between measurements which occurs because the path to the reference antenna changes when the DUT is turned over.

To tackle these issues, the alignment procedure must be modified accordingly. Specifically, the wSMSE minimization procedure has to be extended by two additional parameters. Parameter m represents the magnitude mismatch, while ψ stands for the phase difference between the two measurements. The radiation pattern of one measurement is then modified in the following simple manner:

$$E_{\text{corrected}}(\chi, \theta, \phi) = m \cdot E(\chi, \theta, \phi) \cdot e^{-j\psi} \quad (\text{C.3})$$

With these adjustments, the method is now capable of compensating for both the magnitude and the phase offset between two measurements during the alignment procedure. The magnitude offset parameter m obtained by the alignment procedure favors the magnitude of the fixed measurement over that of the aligned measurement. Alternatively, the two measurements could also be scaled by \sqrt{m} and \sqrt{m}^{-1} , respectively, which would result in an averaged magnitude calibration.

²The link budget equation used for magnitude calibration requires the probe antenna's gain, G_{probe} , and the free-space path loss, FSPL, for its computation, which are far-field parameters. The calibration is thus valid only for measurements in the far field. While a near-field equivalent of the gain can easily be obtained from the probe's radiation patterns, estimation of the path loss at a given near-field distance requires further analysis, which was not done at this stage.